Contributions to the study of small electronically-commutated axial-flux permanent-magnet machines

Adrian Augustin Pop

N° d'ordre : 210

ÉCOLE CENTRALE DE LILLE

THÈSE

présentée en vue

d'obtenir le grade de

DOCTEUR

En

Spécialité : Génie électrique

par

Adrian Augustin **POP**

DOCTORAT DELIVRE CONJOINTEMENT PAR L'ECOLE CENTRALE DE LILLE (EC-LILLE) ET L'UNIVERSITÉ TECHNIQUE DE CLUJ-NAPOCA (UTC-N), ROUMANIE DANS LE CADRE D'UNE COTUTELLE INTERNATIONALE DE THESE

Titre de la thèse :

Contributions à l'étude des petites machines électriques à aimants permanents, à flux axial et à auto-commutation électronique

Soutenue le 15 décembre 2012 devant le jury d'examen :

Président	**Radu MUNTEANU**, *Professeur des universités, UTC-N, Roumanie*
Rapporteur	**Mohamed GABSI**, *Professeur des universités, Ecole Normale Supérieure de Cachan, France*
Rapporteur	**Stéphane VIVIER**, *Maître de conférences, Université de Technologie de Compiègne, France*
Membre	**Nicolae MUNTEAN**, *Professeur des universités, Université 'POLITEHNICA' de Timişoara, Roumanie*
Membre	**Călin RUSU**, *Professeur des universités, UTC-N, Roumanie*
Co-directeurs de thèse	**Frédéric GILLON**, *Maître de conférences, EC-Lille, France*
	Mircea M. RADULESCU, *Professeur des universités, UTC-N, Roumanie*

Thèse préparée dans le Laboratoire L2EP
École Doctorale SPI 072
PRES Université Lille Nord-de-France

Acknowledgement

This thesis is submitted to the Technical University of Cluj-Napoca and the Ecole Centrale de Lille in fulfillment of legal requirements of Ph.D. Degree in Electrical Engineering.

The thesis was elaborated within the Special Electric Machines and Light Electric Traction (SEMLET) Research Laboratory, Technical University of Cluj-Napoca and the Laboratory of Electrical Engineering and Power Electronics (L2EP), Ecole Centrale de Lille, and supported by the Romanian grant 'Doctoral Studies in engineering sciences for developing the knowledge based society (SIDOC)', POSDRU/88/1.5/S/60078, under the European Social Fund through Sectorial Operational Program Human Resources 2007-2013.

I wish to express my hearty gratitude to Professors Mircea M. Radulescu and Frédéric Gillon, scientific co-supervisors of this thesis, for their competent guidance and untiring support along this work.

I am also thankful to all my Ph.D. colleagues from both Laboratories for their help and collaboration.

I would like to thank the referees and members of the jury of this thesis, Professors Mohamed Gabsi from the Ecole Normale Supérieure de Cachan, France, Stéphane Vivier from the Université de Technologie de Compiègne, France, Nicolae Muntean from the Polytechnic University of Timişoara, Romania, and Radu Munteanu from the Technical University of Cluj-Napoca, Romania, for their valuable comments and suggested improvements.

Finally, I will always be grateful to my family members who have been supportive and encouraging throughout all my years of study.

Cluj-Napoca, October 2012 *Adrian Augustin Pop*

Contents

1. Small electronically-commutated axial-flux permanent-magnet (AFPM) machines

Small electronically-commutated (or *brushless*) *axial-flux permanent-magnet* (AFPM) *machines* have been under keen research interest in the last decade as an alternative to conventional radial-flux PM machines, particularly for low-speed direct-drive applications (e.g. wheel motors and wind generators), due to their advantages of flexible disk (pancake) shape, compact and rugged construction, adjustable flat (plane) airgap, high power density and high torque-to-weight ratio [1-3].

The simplest AFPM machine structure uses an annular, slotted (or slotless) stator, containing the radially-arranged armature windings, and a disk-rotor, carrying PMs that produce the axial flux. The AFPM machine has a larger diameter-to-active-length ratio compared to its radial-flux PM counterpart. As a consequence, when the number of poles increases, the AFPM machine radial active part remains almost unchanged, while the axial length can decrease, so that the torque density increases. A main drawback of the single-stator-single-rotor AFPM structure is the unbalanced axial force between rotor PMs and the stator steel, which leads to thicker rotor disk and complex bearing arrangements.

1.1. Double-sided axial-flux inner-rotor permanent-magnet (AFIPM) machine topologies

Several AFPM machine configurations can be conceived regarding the stator(s) position with respect to the rotor(s) position, and the winding design, which allow selecting the best suited machine structure for a particular application. Among them, double-sided structures, in which the axial forces are balanced, may be built as

- single-rotor-double-stator structure (Fig.1.1), hereafter referred to as *axial-flux inner-rotor permanent-magnet (AFIPM)* machine topology, in which a PM rotor is sandwiched between two slotted (or slotless) stator cores having three-phase windings. For parallel connection of its armature windings, the AFIPM can operate even when one winding breaks down; on the other hand, a series connection is preferred because it can provide equal but opposing axial attractive forces on the rotor.

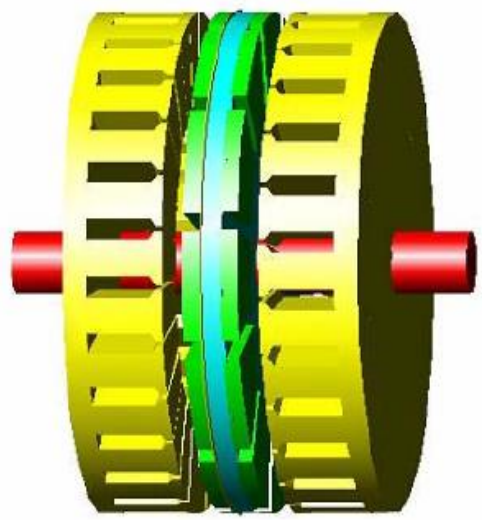

Fig. 1.1. Small single-rotor-double-stator. AFPM (AFIPM) machine topology. (after [2])

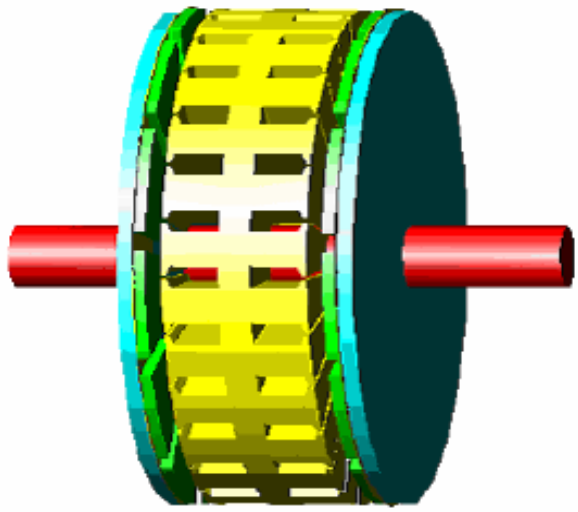

Fig. 1.2. Small single-stator-double-rotor AFPM machine topology. (after [2])

- single-stator-double-rotor structure (Fig.1.2), can have toroidal armature windings; as drawbacks of this structure compared to the AFIPM topology, one may point out that the stator fixture to the frame is more complex, and less space is left for the windings [4, 5]. In the axial flux permanent magnet machine two kinds of rotor can be used:

- axially-magnetized PMs are mounted on both surfaces of the inner-rotor disk (Fig.1.1), so that the basic magnetic flux flows axially through the PM-rotor disk (Fig.1.3, *a*);
- circumferentially-magnetized PMs are buried inside the rotor disk, in which case the main flux flows circumferentially along the PM-rotor disk (Fig.1.3, *b*).

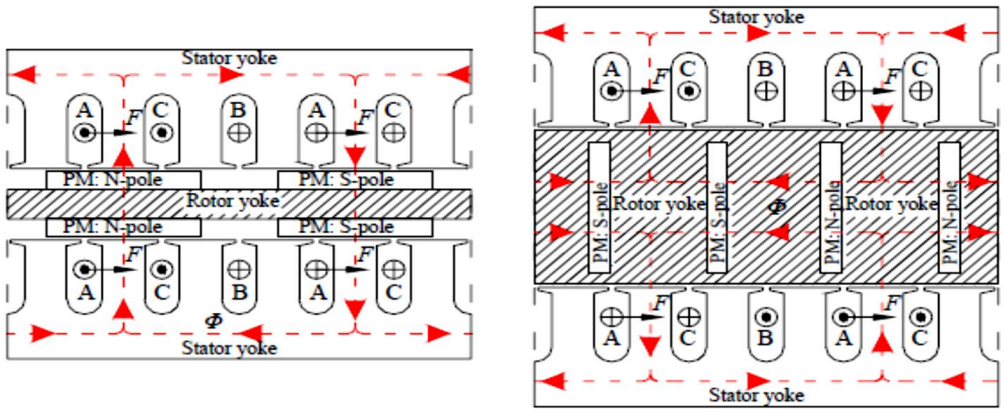

Fig. 1.3. Basic magnetic flux paths in small AFIPM machine structures (a) with surface-mounted rotor-PMs and (b) with buried rotor-PMs (after [3]).

Ideally, coreless rotor can be used for the AFIPM structure with surface-mounted rotor-PMs, since the magnetic flux travels through the PMs from one stator to another. This makes the manufacturing of the PM-rotor very simple and inexpensive, and is also favourable in low-inertia drive applications.

Comparative to its surface-mounted PM-rotor counterpart, the AFIPM machine structure with buried rotor-PMs has much thicker rotor disk, which consequently reduces the power density of the machine for the same outer stators, and increases the leakage flux at PM ends, because the PMs are surrounded by ferromagnetic material. Armature reaction is then higher in buried-PM structure than in surface-mounted-PM one. As an advantage, the buried-PM topology better protects the rotor PMs against mechanical stress, wear and demagnetization.

Slotted stators in the AFIPM machine increase notably the amplitude of the airgap flux density due to shorter airgap. This reduces the required amount of rotor-PMs, which yields savings in the AFIPM machine cost. Moreover, copper losses in slotted-stator AFIPM machines are lower than those of their slotless-stator counterpart. On the other hand, the use of slotted-stator armature winding results in significant cogging torque and content of harmonics in the back-emf waveform. Both problems may be tackled efficiently from the design point of view.

References [6,7] advocate the application of slotted-stator concentrated (fractional-slot) armature winding in AFIPM machines. When open stator slots and concentrated windings are used, prefabricated coils can simply be inserted around the stator teeth, and the winding process becomes very low-cost. Furthermore, the space needed by the end-windings and thus the Joule losses are minimized. However, due to the discrete position of concentrated-winding coils in stator-armature slots there are space harmonic components in the armature-reaction m.m.f. produced by the concentrated winding. The ‘main harmonic component’ is that whose wavelength is equal to the rotor pole-pair pitch, i.e. whose order is equal to the number of rotor pole-pairs. Only this main harmonic component of the stator-armature m.m.f (and not the fundamental or first-harmonic component) is torque-producing harmonic, as being synchronous with the rotor, and thus interacting with the PM-rotor excitation field to produce the continuous PM-alignment torque. Conversely, all other stator spatial slot harmonic mmf components

rotate at speeds that are different from the rotor speed, and they can induce losses in the stator teeth and yoke, as well as in the rotor laminations and PMs, with undesired side-effects, such as the risk of possible thermal demagnetization of the rotor-PMs. Therefore, distributed three-phase winding design with integral slot/pole/phase number is an often choice for small AFIPM machines in direct-drive low-speed applications.

Through particular winding design AFIPM machines may have back-emfs of sinusoidal shape, in which case sine-wave current supply is recommended to avoid the occurrence of pulsating torques, or of trapezoidal waveform, when rectangular-current supply is required for smooth electromagnetic torque production.

1.2. Small AFIPM machine prototype

A small AFIPM machine prototype has been constructed to benchmark further research work of this thesis. It has a solid-iron rotor disk with surface-mounted Nd-Fe-B PMs, glued on both sides. Special PM-rotor construction has been adopted, by manufacturing reasons, with two distinct PMs for each rotor pole, i.e. one of rectangular flat shape, the other one loaf-shaped (Fig.1.4).

Each of the twin slotted stators is made of steel-sheet (M400-50A) rolled in circular form, and carries a three-phase distributed armature-winding inserted in the 25 slots (Fig.1.5).

Fig. 1.4. Photograph of the rotor-PM arrangement of the small AFIPM machine built prototype.

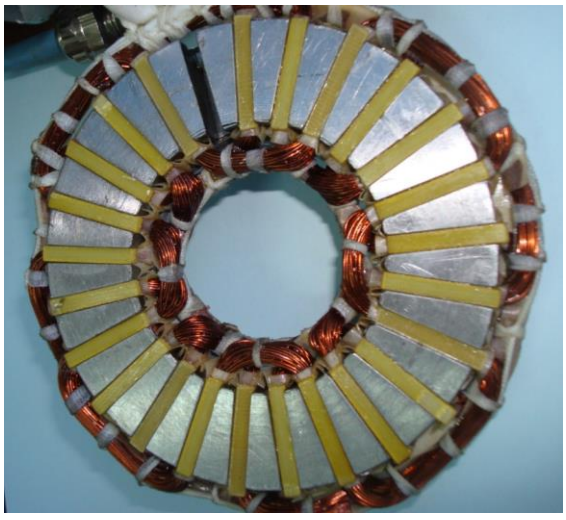

Fig. 1.5. Photograph of one of the two slotted stators with three-phase distributed armature-winding of the small AFIPM machine built prototype.

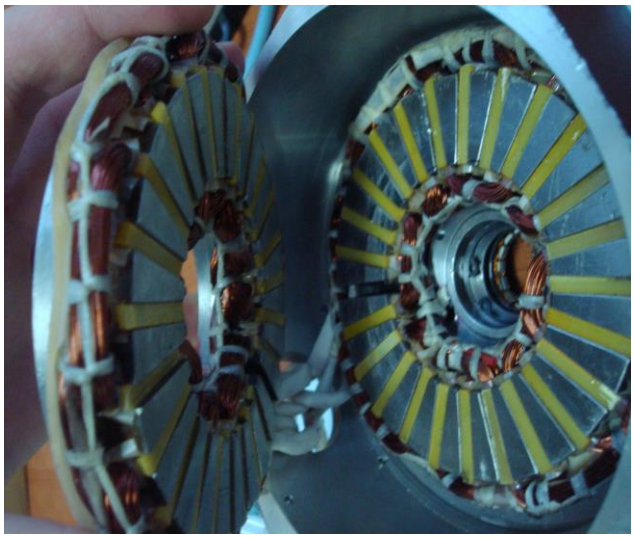

Fig. 1.6. Photograph of the two slotted stators with series-connected three-phase armature windings.

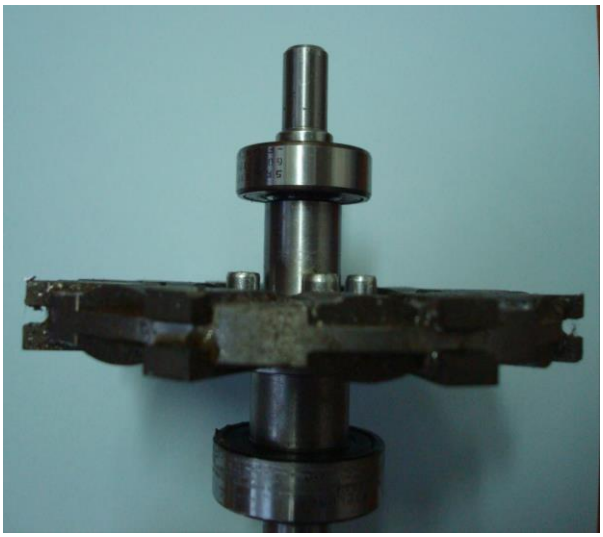

Fig. 1.7. Photograph of the PM-rotor assembly, the rotor shaft and the two bearings of different size.

One stator slot is left empty by manufacturing reasons. The two three-phase armature windings are connected in series (Fig.1.6), and for each of them star-connection is used to avoid circulating currents.

The rotor shaft and the two bearings of different size (Fig.1.7) are made from steel (OL 38). For separating the two stators and for increasing the stiffness of the whole machine structure, a steel spacer is used.

All the machine specifications are presented in Table 3.1.

1.3. Outline of the thesis

The research work contained in this thesis is concerned with small brushless AFIPM machines having surface-mounted Nd-Fe-B rotor-PMs and three-phase slotted-stator distributed armature windings, which are most suitable for low-speed direct-drive applications. The primary reasons are that, the fixture of external stators may be arranged easily, and the axial loading of bearings is rather small due to the internal rotor topology. However, in direct-drive applications, the electromagnetic torque quality being an important issue, the AFIPM machine designer has to fulfill the task of minimizing the torque pulsations as a sum of cogging (or detent) torque and torque ripple [4, 8]. Cogging torque originates from the tendency of rotor-PMs to align themselves with the minimum reluctance path given by the relative position between

rotor and stator. Torque ripple arises from distortion of the sinusoidal back-emf and armature-winding current. Primarily, the electromagnetic torque quality issue in small brushless AFIPM machines can be addressed by minimizing cogging torque and back-emf harmonic contents from the design point of view.

In this context, the first objective of the thesis is to propose an analytical approach to the preliminary electromagnetic design of the small AFIPM machine, whose results are then confronted with the design data of the machine prototype purposely built in the early stage of the thesis work.

The second objective of the research is to develop a two-dimensional finite-element field modeling for further design optimization of the considered small AFIPM machine for torque quality improvement by rotor-PM shape modification.

The last objective of this thesis is to carry out extensive experiments and tests on the small AFIPM machine prototype, in order to validate its finite-element numerical modeling, as well as to check the feasibility of its electronic commutation and basic control scheme.

The thesis is structured in five chapters whose short presentation is given herewith.

Chapter 1 briefly reviews small double-sided AFPM machine candidate topologies for low-speed direct-drive applications, and addresses the features of small AFIPM machines in such applications through a three-phase machine prototype built to be further studied in the thesis.

In **Chapter 2**, an analytical preliminary design based on general AFPM machine sizing equations is proposed for the small three-phase AFIPM machine prototype, which is then used to ascertain the dimensioning results and to enable further research study of the thesis.

Chapter 3 is the backbone of the thesis, developing the two-dimensional finite-element field modeling and design optimization of the small prototype AFIPM machine with the view to reducing the airgap flux density space-harmonics and the cogging torque by rotor-PM shape modification. The original finite-element numerical model is validated against experimental measurements on the small AFIPM machine prototype.

Chapter 4 presents the results obtained with a dedicated laboratory set-up built to experimentally characterize and check the proper operation of the small three-phase

AFIPM machine prototype under electronic self-commutation and basic control.

In the **last chapter**, general conclusions of the thesis research are drawn, main original contributions of the author are emphasized, and some hints for future research are provided.

Selected references

[1]. J.F. Gieras, R.-J. Wang, M.J. Kamper, *Axial-flux permanent-magnet brushless machines,* 2nd Edition, Springer, The Netherlands, 2008.

[2]. K. Sitapati, R. Krishnan, Performance comparisons of radial and axial field, permanent-magnet, brushless machines, *IEEE Trans. Ind. Applicat.*, Vol. 37 (2001), No. 5, pp. 1219-1226.

[3]. A. Parviainen, *Design of axial-flux permanent-magnet low-speed machines and performance comparison between radial-flux and axial-flux machines*, Ph.D. Thesis, Lappeenranta University of Technology, Finland, 2005.

[4] M. Aydin, S. Huang, T.A. Lipo, Torque quality and comparison of internal and external rotor axial flux surface-magnet disc machines, *IEEE Trans. Ind. Electron.*, Vol. 53 (2006), No. 3, pp. 822-830.

[5] A. Mahmoudi, N.A. Rahim, W.P. Hew, TORUS and AFIR axial-flux permanent-magnet machines: A comparison via finite element analysis, *Int. Rev. Modell. Simul*., Vol. 4 (2011), No. 2, pp. 624-631.

[6] Hanne Jussila *et al.*, Concentrated winding axial flux permanent magnet motor for industrial use, *Proc. 19th Int. Conf. Electr. Mach. – ICEM 2010*, Rome, Italy, 2010, CD-ROM, 5 pp.

[7] A. Di Gerlando *et al*., Axial flux PM machines with concentrated armature windings: design analysis and test validation of wind energy generators, *IEEE Trans. Ind. Electron.*, Vol. 58 (2011), No. 9, pp. 3795-3805.

[8] D.A. Gonzalez, J.A. Tapia, A.L. Bettancourt, Design consideration to reduce cogging torque in axial flux permanent-magnet machines, *IEEE Trans. Magn.*, Vol. 43 (2007), No. 8, pp. 3435-3440.

2. Analytical preliminary design of small AFIPM machines based on general sizing equations

In this chapter, general sizing equations of AFPM machines are employed in an analytical approach to the determination of main dimensions of three-phase small AFIPM machine under study. The built machine prototype is used to benchmark the preliminary design results.

2.1. General sizing equations of AFPM machines

Assuming negligible stator-armature leakage inductance and resistance, the output mechanical power for an AFPM machine can be expressed as [1 - 4]

$$P_{out} = \frac{m}{T}\eta\int_0^T e_{ph}(t)\cdot i_{ph}(t)\,\mathrm{d}t = mk_p\eta\hat{E}_{ph}\hat{I}_{ph}, \tag{2.1}$$

where $e_{ph}(t)$ and $\hat{E}_{ph}$ are the stator-armature phase back-emf and its amplitude (or peak value), respectively; $i_{ph}(t)$ and $\hat{I}_{ph}$ denote the stator-armature phase current and its amplitude, respectively; η, m and T represent the machine efficiency, the total number of phases on the slotted stator(s) and the period of one back-emf cycle, respectively; k_p is termed the electric power waveform factor, defined by

$$k_p = \frac{1}{T}\int_0^T \frac{e_{ph}(t)\cdot i_{ph}(t)}{\hat{E}_{ph}\hat{I}_{ph}}\,\mathrm{d}t. \tag{2.2}$$

For AFPM machines, the amplitude of the phase back-emf in (2.1) has the following form:

$$\hat{E}_{ph} = k_e N_{ph}\frac{f}{p}(1-\lambda^2)D_o^2\hat{B}_g, \tag{2.3}$$

where k_e is the back-emf factor, i.e. the armature-winding distribution factor; N_{ph} denotes the number of turns in series per armature-winding phase; f represents the mains electrical frequency; p defines the number of machine pole-pairs; D_i , D_o are the

diameters of the inner and outer surfaces of the AFPM machine, respectively, $\lambda = D_i / D_o$ being the inner-to-outer diameter ratio; $\hat{B}_g$ represents the peak value of the magnetic flux density in the airgap (magnetic loading).

In order to emphasize the effect of the armature-winding phase current waveform, the factor

$$k_i = \frac{\hat{I}_{ph}}{I_{ph,\mathrm{rms}}} = [\frac{1}{T}\int_0^T (\frac{i_{ph}(t)}{\hat{I}_{ph}})^2 \,\mathrm{d}t]^{-1/2} \tag{2.4}$$

is introduced with $I_{ph,\mathrm{rms}}$ denoting the armature-phase current rms value. The peak value of the armature-winding phase current is thus given by

$$\hat{I}_{ph} = \frac{\pi}{4} k_i \frac{(1+\lambda) D_o}{m_{ph} N_{ph}} \hat{A}, \tag{2.5}$$

where $\hat{A}$ represents the peak value of the line armature-winding current density per stator active surface (electrical loading); since it is a radial function, it is expressed at the average diameter diameter of the airgap in (2.5); m_{ph} denotes the number of armature-winding phases per stator (e.g. in the case of a double- or multiple-stator machine topology).

With (2.3) and (2.5) in (2.1), the general sizing equation of AFPM machines takes the form of

$$P_{out} = \frac{\pi}{4} \frac{m}{m_{ph}} \frac{f}{p} k_e k_i k_p \eta (1+\lambda)(1-\lambda^2) D_o^3 (\hat{A}\hat{B}_g). \tag{2.6}$$

The electromagnetic torque density of AFPM machines results from (2.6) as

$$\xi_{Te} = \frac{P_{out}}{\omega_m} \cdot \frac{1}{\frac{\pi}{4} D_{tot}^2 L_{tot}}, \tag{2.7}$$

where ω_m defines the rotor angular speed; D_{tot} is the total machine outer diameter, including the stator-armature outer diameter and the protrusion of the end-windings from the stator-core stack in the radial direction; L_{tot} represents the total axial length of the

machine, including the stack axial length(s) of the stator(s) and the protrusion of the end-windings from the stator-core stack in the axial direction.

By examination of the output power expression (2.6) for AFPM machines, the following remarks can be made :

- the outer diameter D_o of the machine, which is its most important dimensional parameter, is proportional to $\sqrt[3]{P_{out}}$, so that, it decreases rather slowly with the reduction of the output power; this is why small-power AFPM machines have relatively large diameters;
- the developed electromagnetic torque is proportional to D_o^3; for given outer diameter and electrical and magnetic loadings, it is determined by the value of diameter ratio λ ;
- the ratio λ has also significant effect on AFPM machine characteristics; for given electrical and magnetic loadings its optimal value depends on the rated power, number of pole pairs, mains electrical frequency, material properties etc.;
- from the armature-winding phase back-emf and current waveforms for a particular AFPM machine, factors k_i and k_p in the sizing equation may be determined, as shown in references [2, 4].

2.2. Analytical approach to the preliminary design of the small AFIPM machine under study

The above-stated general sizing equation can readily be applied to the small AFIPM machine under study. The outer surface diameter D_o is obtained by particularizing (2.6), i.e.

$$D_o = \left[\frac{8}{\pi^2} \frac{p}{f} \frac{P_{out}}{k_i k_p \eta (1+\lambda)(1-\lambda^2)(\hat{A}\hat{B}_g)} \right]^{1/3}, \qquad (2.8)$$

where it was accounted for that, in this case, $k_e = \pi/4$ and $m / m_{ph} = 6/3 = 2$.

The total outer diameter of the considered AFIPM machine is given by

$$D_{tot} = D_o + 2W_{Cu}, \tag{2.9}$$

where the protrusion of the end-winding from the stator-core stack, in radial direction is assumed as half the value of the stator-pole inner arc, i.e.

$$W_{Cu} = \frac{1}{2p} \cdot \frac{\pi}{4}(\lambda D_o) = \frac{\pi}{8}\frac{\lambda D_o}{p}. \tag{2.10}$$

The total axial length of the AFIPM machine can be expressed as:

$$L_{tot} = L_r + 2L_s + 2g, \tag{2.11}$$

where the rotor axial length sums the rotor-core and rotor-PM contributions, i.e.

$$L_r = L_{r,core} + 2L_{PM} = \frac{B_u}{B_{r,core}} \cdot \frac{\pi}{8}\frac{(1+\lambda)D_o}{p} + \frac{\mu_{r,PM}\hat{B}_g}{B_{rem} - \frac{k_f}{k_d}\hat{B}_g} k_C g \tag{2.12}$$

with $B_{r,core}$, the flux density in the rotor-disk core; B_u, the attainable flux density on the surface of the rotor-PM; $\mu_{r,PM}$ and B_{rem}, the relative permeability and the remanent flux density of the rotor-PM material, respectively; k_d and k_f, the leakage flux factor and the peak-value-corrected radial-airgap-flux-density factor of the AFIPM machine, respectively; g, the airgap axial length; k_C, the Carter factor, which takes into account the fact that large airgap length in front of the stator-slot and a small one in front of the stator-tooth makes the airgap flux density position dependent; for AFPM machines, k_C can be expressed as [1, 6] :

$$k_C = \frac{t}{t - \gamma g}, \quad \gamma = \frac{4}{\pi}\left[\frac{W_{so}}{2g}\tan^{-1}\left(\frac{W_{so}}{2g}\right) - \ln\sqrt{1+\left(\frac{W_{so}}{2g}\right)^2}\right], \tag{2.13}$$

g and W_{so} being the average slot-pitch and the slot-opening, respectively.

The stator axial length sums the stator-core axial length and the stator-slot depth, i.e.

$$L_s = L_{s,core} + L_{s,slot}, \tag{2.14}$$

where

$$L_{s,core} = \frac{\hat{B}_g}{B_{s,core}} \cdot \frac{\pi}{4} \frac{\alpha_p (1+\lambda) D_o}{p}, \quad L_{s,slot} = \frac{\hat{A}}{2 J_{slot} k_{Cu}} \cdot \frac{1+\lambda}{\lambda} \tag{2.15}$$

with $B_{s,core}$, the flux density in the stator core; α_p, the ratio of the average airgap flux density to the peak value of the airgap flux density; J_{slot}, the stator-slot current density; k_{Cu}, the copper-fill factor.

The above-established expressions of analytical dimensioning of AFIPM machines have been used in the design and construction of the small three-phase AFIPM machine prototype described in Chapter 1 of this thesis. The following given design specifications and chosen design parameters have been considered in determining the main dimensions of the small AFIPM machine prototype listed in Table 2.1:

$P_{out} = 300$ [W]; $f = 100$ [Hz]; $\hat{A} = 8000$ [A/m]; $\hat{B}_g = 0.7$ [T]; $\lambda = 0.5$; $\eta = 0.8$;
$B_{rem} = 1.17$ [T]; $\mu_{r,PM} = 1.05$; $B_{s,core} = B_{r,core} = 1.25$ [T]; $B_u = 1.1$ [T]; $J_{slot} = 5$ [A/mm^2];
$g = 1$ [mm]; $k_i = \sqrt{2}$; $k_p = 0.5$; $k_{Cu} = 0.4$; $k_f = 0.9$; $k_d = 0.8$; $\alpha_p = 0.8$.

Table 2.1. Main results of analytical dimensioning of the small AFIPM prototype

Number of armature-winding phases	3
Number of stator slots	24
Number of rotor poles	8
Stator outer diameter [mm]	100
Stator inner diameter [mm]	50
Stator-core height [mm]	20
Stator-slot depth [mm]	10
Stator-slot width [mm]	4
Air gap length [mm]	1
Rotor outer diameter [mm]	100
Rotor axial length with PM [mm]	10

2.3. Conclusions

In this chapter, an analytical approach has been proposed for dimensioning of double-sided AFPM machines by means of general sizing equations. It has been proved that the inner-to-outer diameter ratio λ has a strong effect on the power and torque density of AFIPM machines, and that its optimal value is highly dependent on the machine topology.

The analytical preliminary design has been used for determining the main dimensions of rotor and stator components of a small three-phase AFIPM machine prototype, which has been constructed to enable further research study of this thesis.

Selected references

[1] J.F. Gieras, R.-J. Wang, M.J. Kamper, *Axial-flux permanent-magnet brushless machines,* 2nd Edition, Springer, The Netherlands, 2008.

[2] S. Huang *et al*., A comparison of power density for axial flux machines based on the general purpose sizing equation, *IEEE Trans. Energy Convers*., Vol. 14 (1999), No. 2, pp. 185-192.

[3] S. Gholamian, M. Ardebili, K. Abbaszadeh, Analytic and FEM evaluation of power density for various types of double-sided axial flux slotted PM motors, *Int. J. Appl. Eng. Res*., Vol. 3(2008), No. 6, pp. 749-762.

[4] W.-Y. Jo *et al*., Design and analysis of axial flux permanent magnet synchronous machine, *J. Electr. Engng. Technol*., Vol. 2 (2007), No.1, pp. 61-67.

[5] J.R. Bumby *et al*., Electromagnetic design of axial flux permanent magnet machines, *IEE Proc. – Electr. Power Appl.*, Vol. 151 (2004), No. 2, pp. 151–160.

[6] A. Parviainen, *Design of axial-flux permanent-magnet low-speed machines and performance comparison between radial-flux and axial-flux machines*, Ph.D. Thesis, Lappeenranta University of Technology, Finland, 2005.

3. Finite-element modeling and design optimization of the small AFIPM machine prototype

3.1. Introduction

A model allows describing the performance of a device. It can be more or less powerful, depending on the designer experience. From another point of view, a model may also represent a simulation of a physical phenomenon, or it can represents several physical phenomena, which can be assembled together in order to achieve a multi-physics modeling. The models can be divided into two categories: analytical and numerical.

- **Analytical model**

An analytical model is a set of mathematical equations describing physical phenomena of a device. It provides information on the performance from input parameters. The analytical model can provide very useful results, which can be used in the optimization process. To build an analytical model, one needs to have a good knowledge of the device. The construction of an analytical model can be usually long. Empirical coefficients, assumptions and simplifications on phenomena must be often integrated. The results obtained by analytical model are often less accurate than those provided by a numerical model. The analytical models are frequently used in the early stages of the design. The numerical model is then used to validate or adjust the preliminary analytical results.

- **Finite element model**

Unlike the analytical modeling, the numerical one, e.g. the finite-element modeling, can take into account the complex geometries. The design requirements may thus be met precisely. Another facility provided by finite-element-based software is that it can be connected with other programs in order to analyze multi-physics phenomena. In the following, finite-element models are preferred because of the complexity of AFIPM machine topology under study, and because the design optimization can be connected directly to the finite-element modeling.

The design optimization process of electric machines is typically sequenced as shown in Fig.3.1. First, design specifications are collected and analyzed. Then the design optimization is formulated as a mathematical problem. The problem is solved using algorithms, and finally the results are analyzed. The solution depends a lot on designer experience.

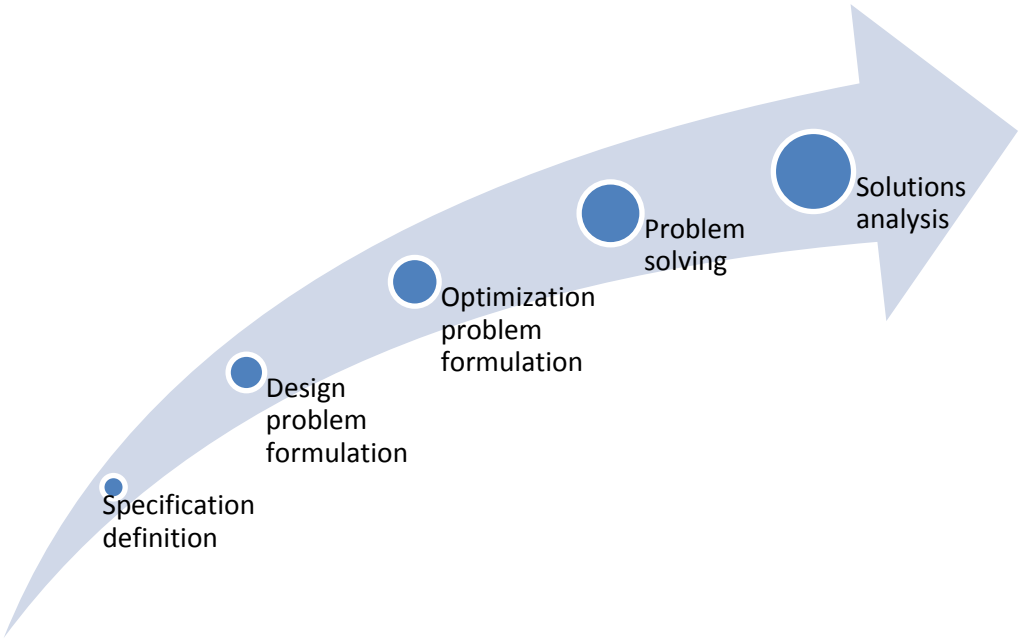

Fig. 3.1. General development of the design optimization process.

- ***Specification definition***

This phase consists in collecting design requirements and needs. Specification extends from non-technical to technical issues. This phase is essential for the design optimization process because all design teams (engineering, marketing, etc.) are involved and must work together to elaborate all needs, requirements and design objectives.

- ***Design problem formulation***

Design variables are controlled by designer during the design process in order to achieve desired performances expressed by design criteria. Design parameters are assigned to specific values. In early design stage, the design problem may consist of a large number of design variables but very few design parameters, since the system is not well known. More the knowledge on the system the design gains, more design

variables are fixed. A design problem can be solved using different techniques. Optimization is only one of them.

- ***Optimization problem formulation***

After establishing the design problem, the optimization problem can be formulated by expressing the limitations, constraints and objectives. A good knowledge of the model is needed to formulate a reasonable problem of optimization.

- ***Problem solving***

The selection of the optimization method depends on its nature, as well as on the execution time and model robustness. There is no optimization algorithm that works universally for all optimization problems, so it is necessary to search for the best suited optimization method.

- ***Analysis of results***

Once the problem is solved, the results have to be analyzed. Now, it is time to designers to make a decision. It is essential for the designer to analyze the variables, constraints and objectives to verify the results. When the optimization problem does not converge it is necessary to return to the formulation stage of the design problem.

In what follows, an overview of the optimization techniques used to solve complex system design problems is presented.

Optimization technique is a general tool that helps designers to manage complexity of design problems. Such a complexity is mainly due to existence of interactions between disciplines and between physical or functional subsystems. These interactions are usually difficult to manage because of the increased number of design parameters.

The *Global System* approach considers the whole system as a single unit. The system modeling may consist of several models, which are launched sequentially or solved using numerical method. In any case, the system model is considered as a whole black-box model. The global system design problem is formulated as a single optimization problem. Therefore, all subsystems are optimized simultaneously. This is a traditional approach, commonly used in engineering optimal design. Two such conventional optimization algorithms are presented.

3.1.1. Single-objective optimization

Two popular algorithms for single-objective optimization are presented. The first one is the *Sequential Quadratic Programming* (SQP), and the second one is the *Genetic Algorithm* (GA). GA is a global optimization algorithm, whereas SQP is a local method. Each algorithm has specific advantages and drawbacks.

- **Sequential Quadratic Programming (SQP) algorithm**

SQP algorithm is one of the most accurate gradient algorithms. It enables solving nonlinear constrained optimization problems. SQP includes directly objective and constraint functions into its optimum solution search process. It relies on a profound theoretical foundation and provides powerful algorithmic tools for the solution of large-scale technologically-relevant problems [1].

Let us consider the application of the SQP methodology to nonlinear optimization problems (NLP) of the form:

$$\begin{gathered} minimize\ f(x) \\ over\ x \epsilon \mathbb{R}^n \\ subject\ to\ h(x) = 0 \\ g(x) \leq 0, \end{gathered} \tag{3.1}$$

where $f: \mathbb{R}^n \to \mathbb{R}$ is the objective functional, while the functions $h: \mathbb{R}^n \to \mathbb{R}^m$ and $h: \mathbb{R}^n \to \mathbb{R}^p$ describe the equality and inequality constraints. The NLP contains as special cases linear and quadratic programming problems, when *f* is linear or quadratic, and the constraint functions *h* and *g* are affine.

Gradient and derivative can be computed by symbolic math, when it is possible. This increases robustness of algorithm. However, this symbolic derivative calculation may not always be possible. Finite difference method can be used, but it increases significantly the number of function calls. SQP method is efficient in the following conditions.

- Problem is not of too high dimensions, otherwise the problem becomes highly multimodal, and SQP is trapped into local optima. Moreover, the number of function

evaluations is increased rapidly in high-dimensional problem, if finite difference is used to compute gradient.

- Computation of gradient can be obtained with rather high precision. Convergence speed depends on gradient precision.
- Problem is smooth and scaled. Design variables must be scaled in order to ensure a correct operation of algorithm.

As SQP uses gradient information, it has difficulties to find the global optimum, if the problem has several optima. The similar problem is stated in the case of noisy function with one or several true optima.

- **Genetic algorithm (GA)**

Gas are among the most popular Evolutionary Algorithms (EAs). GAs are stochastic algorithms, whose search methods are based on Darwin's theory of natural selection [2, 3]. Like other EAs, GA applies selection operators and variation operators or search operators (called *genetic operators* in GAs' case) to a set of individuals (design vector). Fitness value is assigned to each individual. The fitness depends on objective function, and represents how good the individual is. The set of individuals or population is treated simultaneously and improved from actual generation (iteration) to the next one.

Two classical genetic operators are used: mutation and crossover [4]. The mutation operators transform an individual. The crossover operators use two or more parents to create a child (called *offspring*) for the next generation.

GAs are known as global optimization algorithms as they are less sensitive to noisy functions and able to solve multimodal problems.

One of the main advantages of GAs is that they can handle discrete and non-classable variables. This is not possible with an algorithm using gradient information. However, some of GA drawbacks can be revealed.

- GAs are likely unable to find high-accurate results compared with a deterministic algorithm, such as SQP, since GAs cannot ensure optimality. Stopping criteria are usually the maximum number of generations.

- GAs usually requires high number of function calls due to their global search characteristic. However, since GAs work with population, they can be parallelized easily. This decreases significantly the computation time.

As already mentioned, SQP and GA have their own advantages and drawbacks. To summarize, SQP requires less number of objectives and constraint function calls than GA. It can also find accurate optimum results, as it is deterministic algorithm. However, due to the fact that SQP uses gradient information in its search algorithm, it tends to be trapped in local optima, and suffers from noise in objective or constraint functions. In contrast, GAs search more globally, and have more chance to find global optimum.

3.1.2. Multi-objective optimization

One should realize that in the real life, most of engineering design problems are multi-criteria or multi-objective. To optimize such design problems, engineer may simplify the multi-objective design problems, and formulate them as single-objective optimization problems due to limited performance of early developed optimization algorithms. Only the most important criterion is selected as sole objective function. The others are fixed as parameter or constraint limit. It is important to note that this process is done during the optimization problem formulation phase. This approach is called '*a priori method*'.

This chapter is further devoted to finite-element modeling and design optimization of the small AFIPM machine prototype under study with a view to reducing its back-emf harmonics and electromagnetic torque pulsations.

Primarily, the origins of harmonics in an AFIPM machine are recalled. They are either temporal, for external variables (such as current, voltage or torque) or spatial, for internal quantities. An original approach to reducing the harmonics of the airgap flux density is developed. It uses finite-element parameterized model in conjunction with design optimization technique. Numerical simulations are first performed for slotless stator and then for the real slotted stator.

3.2. Harmonic analysis of AFIPM machine

Usually, one speaks about electric machines harmonics in terms of unwanted spectral components in the current and emf waveforms. However, electric machines being electromechanical converters, it is important to analyze the airgap flux-density harmonics distribution.

In an AFIPM machine, the shaft torque contains three components:

- the mutual (or PM-alignment) torque due to the interaction between the armature flux and the magnet flux;
- the reluctance torque due to the rotor saliency;
- the cogging (or detent) torque due to the interaction between the rotor-PM field and stator slots.

The first two torque components have a non-zero average value with a pulsating component, while the cogging torque component is a zero-current oscillating torque with a null average value.

The torque pulsations can have two distinct origins: cogging torque and torque ripple due to the interaction between the stator-armature mmf and the airgap flux harmonics. Unlike the cogging torque, the torque ripple is load-dependent. It can be reduced by modifying the number of stator slots, the number of poles, the slot-opening width, etc.

3.2.1. Back-emf harmonics

The back-emf, at no load, is generated by the rotor-PM flux linking the stator armature winding. One can schematize the process (Fig.3.2) in a block-diagram showing the flux density path from the magnetization up to the dynamically-induced back-emf. At each passing from one block to another, the harmonic contents of a certain electromagnetic quantity make changes depending on the block type.

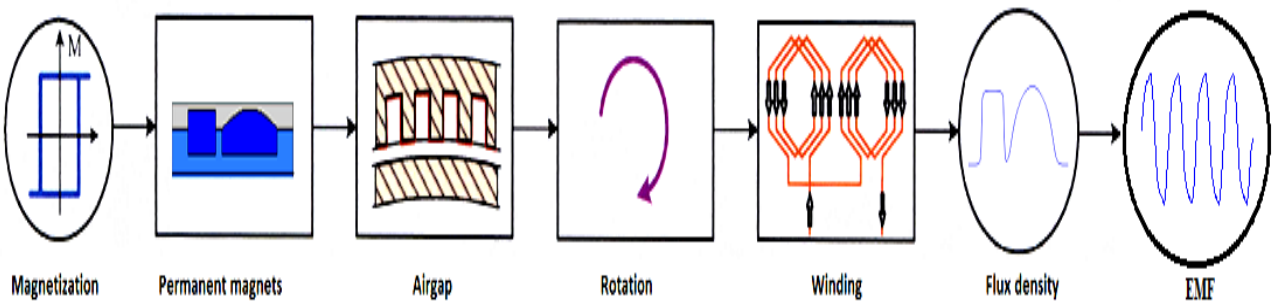

Fig. 3.2. Back-emf waveform generation process.

One can change the back-emf harmonic contents by acting on the rotor-PM size and shape, i.e. changing their height, length or other geometrical parameters. Fig. 3.3, *a* shows the line back-emf waveform for the small AFIPM prototype machine operating in generator mode, at the rated speed of 1500 [rpm]. The simulation has been done for an entire rotation of the machine. The harmonic content of the back-emf waveform is presented in Fig. 3.3, *b*. It can be noticed, that the 4th harmonic has the largest impact on the harmonics distribution. This back-emf dominant harmonic can be reduced by shape modification of rotor-PMs.

In order to evaluate quickly the distribution of back-emf harmonics, only one of its periods is used (Fig.3.4). Thus, the design optimization process will be shorter.

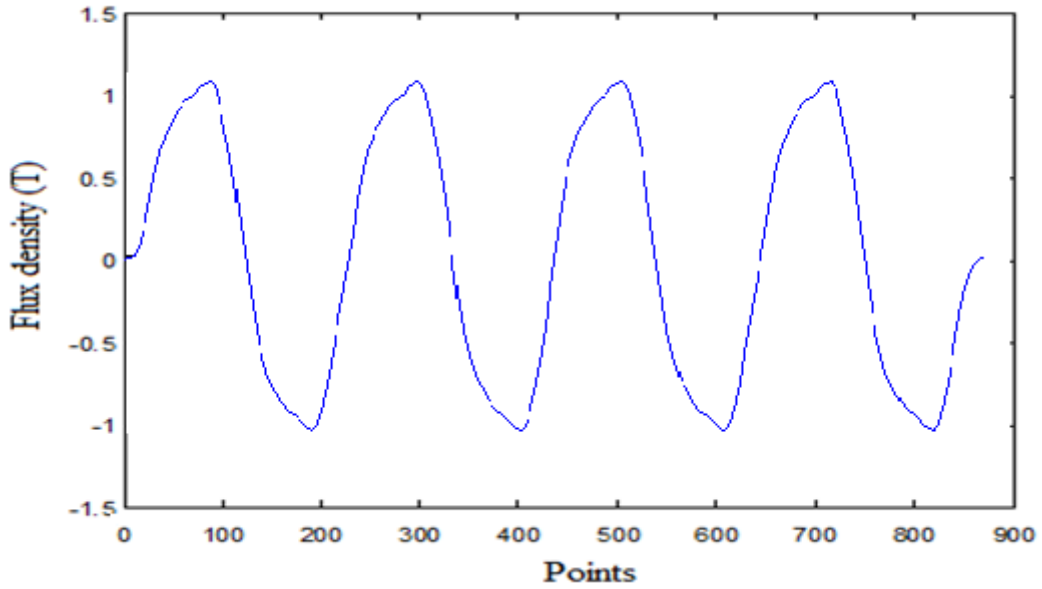

(a)

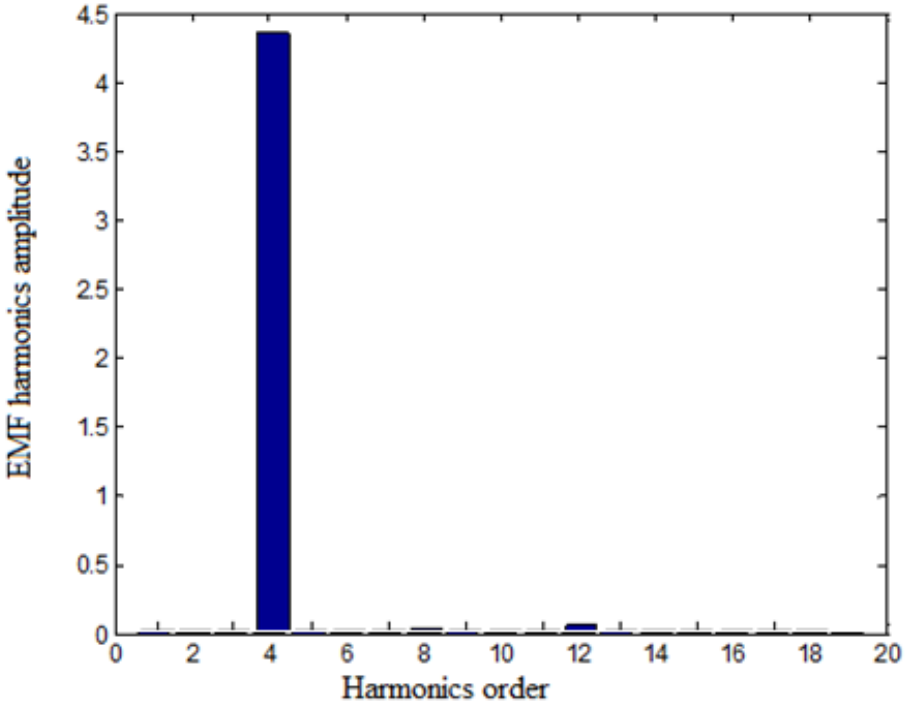

(b)

Fig. 3.3. Back-emf waveform (a), and its harmonics distribution (b), at rated speed and no-load.

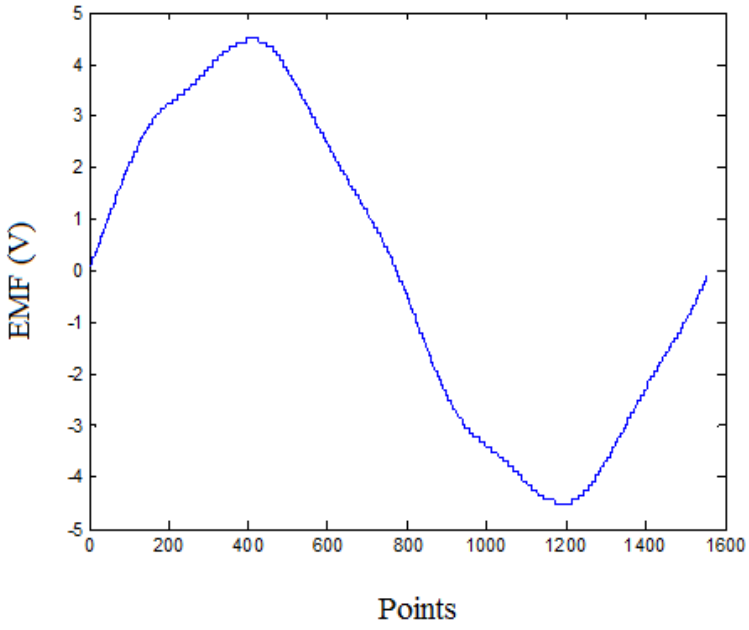

(a)

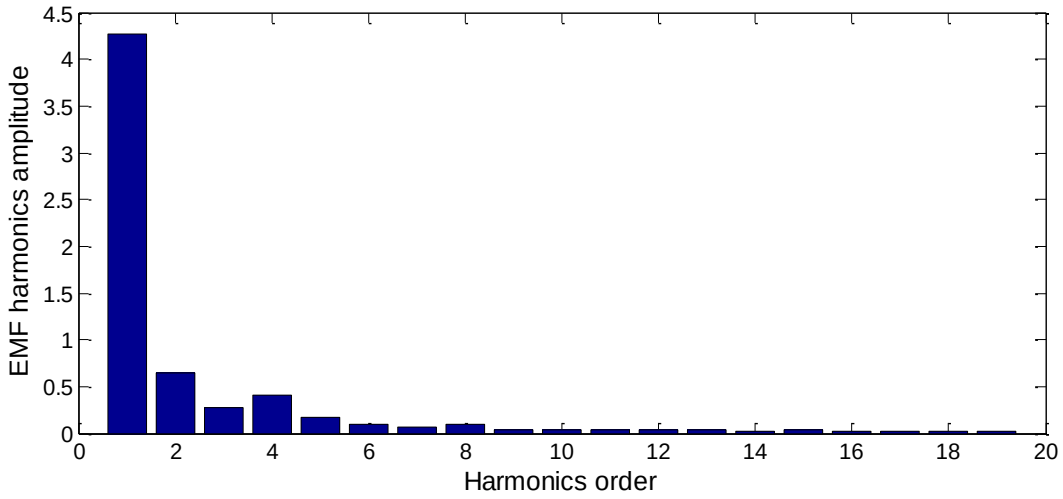

(b)

Fig. 3.4. Back-emf waveform (a), and its harmonic distribution (b), for a single period, at rated speed and no-load.

It can be seen that the distribution of back-emf harmonics has different repartition as a function of the signal period. For the entire period, the 4th harmonic has the largest impact on the harmonics distribution. For one period, the back-emf simulation shows that there are several new harmonics that appear. The first-harmonic has the main impact, compared to the 2nd, 3rd, 4th and 5th harmonics.

3.2.2. Airgap flux-density harmonics

Case of slotless stator with rectangular-shaped magnets

The airgap flux density depends on the shape of rotor-PMs and stator teeth. In Fig.3.5, the effect of PM openings α_m on the airgap flux-density waveform, for a slotless-stator AFIPM machine topology, is presented. The airgap flux-density distribution for the slotless machine is presented in Fig. 3.6. It can be seen, that the flux density waveform has a rectangular shape, due to the rotor-PM geometry. Spectral analysis of this waveform gives for the *h*–order harmonic the expression:

$$B_h = \frac{4}{\pi h} B_{max} \sin\left(\frac{h\alpha_m}{2}\right) \text{ with } 0 \leq \alpha_m \leq \pi. \quad (3.2)$$

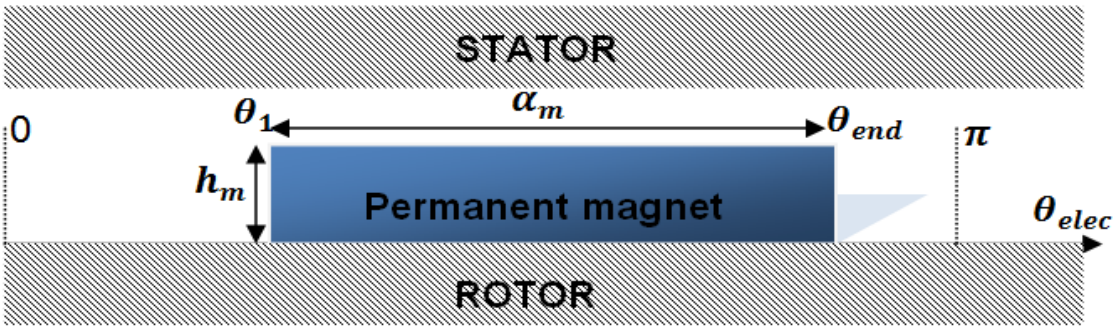

Fig. 3.5 One-pole representation for a slotless-stator AFIPM machine.

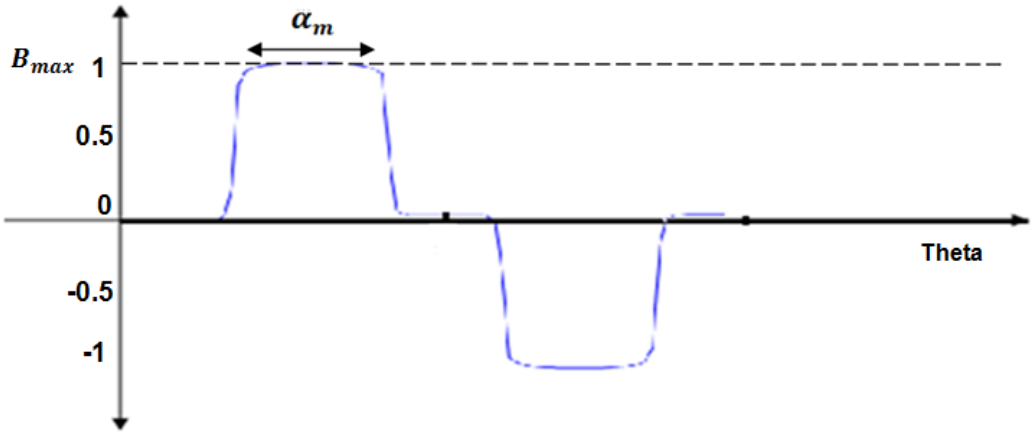

Fig. 3.6 Airgap flux-density distribution for a slotless-stator AFIPM machine.

Case of slotless-stator AFIPM machine with rectangular- and arc-shaped magnets

For the AFIPM under study, it can be noticed that there are 8 poles and for each one there are two different shaped magnets. This particular construction is simulated for a slotless stator case. Thus, the real waveform of the flux density can be extracted.

The flux density waveform representation for the entire slotless-stator machine is displayed in Fig.3.7. The flux density waveform reaches the maximum value of 1.1 [T], as shown in Fig. 3.8. The results are obtained by using the finite element model.

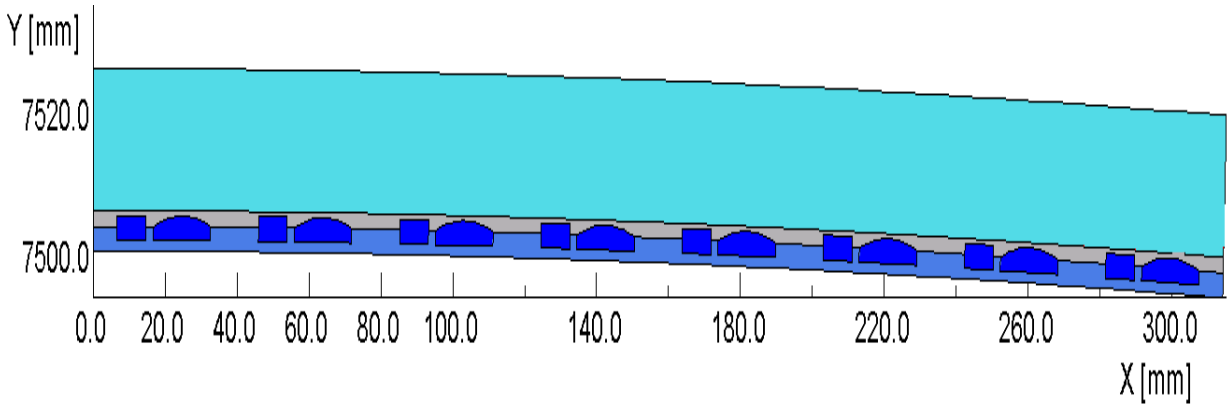

Fig. 3.7. Representation of the slotless-stator AFIPM machine.

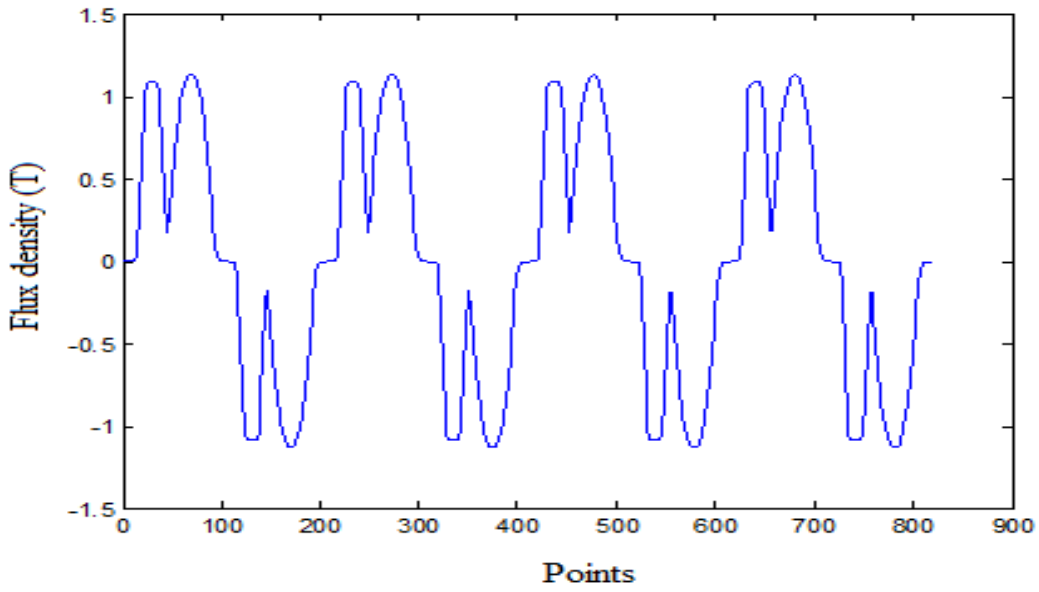

Fig. 3.8. Airgap flux-density distribution for the slotless-stator AFIPM machine.

One intends to search for design optimization techniques, which allow reducing or even eliminating undesired harmonics from the airgap flux-density waveform without altering the slotless-stator design. The flux density harmonics are presented in Fig. 3.9. It can be noticed that the 4th harmonic has the largest impact on the flux-density harmonics distribution.

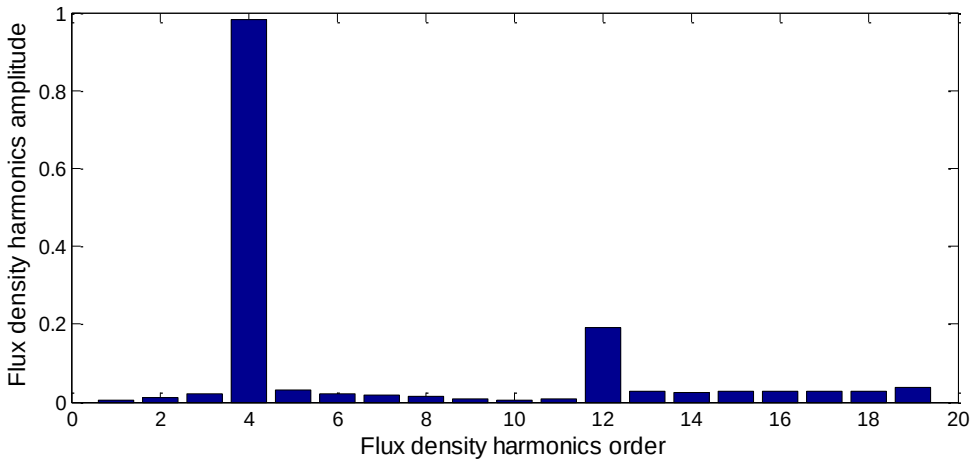

Fig. 3.9. Harmonics distribution for the 8-pole slotless-stator AFIPM machine.

Case of slotted-stator AFIPM machine with rectangular- and arc-shaped magnets

In order to visualize the slotting effects the airgap flux density was computed for a slotted machine Fig. 3.10. It can be seen that the airgap flux density drops in the areas where magnets meet the stator slots Fig. 3.11. This particular construction is made with 25 slots and it can be seen that there is an unused slot. Thus the flux density has a special waveform. The flux density harmonics have a similar distribution with the case of slotless machine Fig. 3.12. The difference between these two different representations is made by the harmonics amplitude.

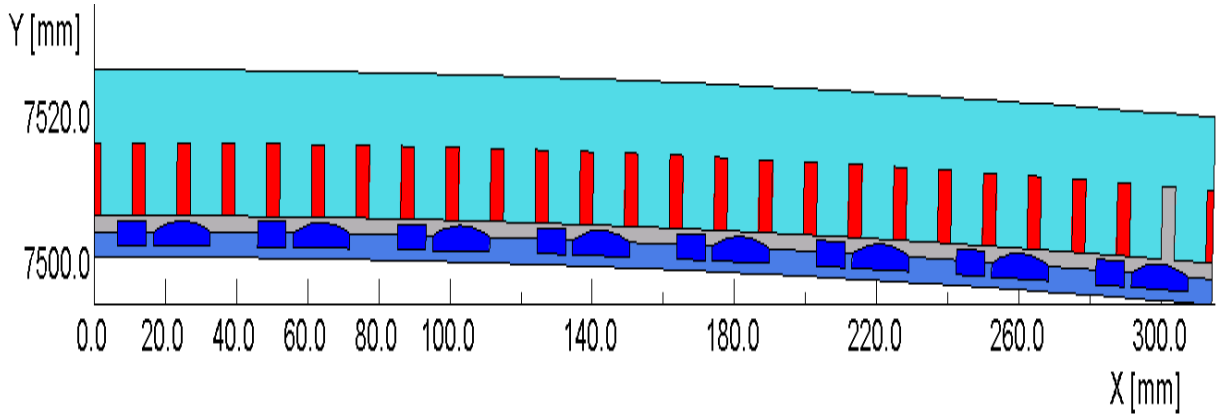

Fig. 3.10. Representation of the slotted-stator AFIPM machine.

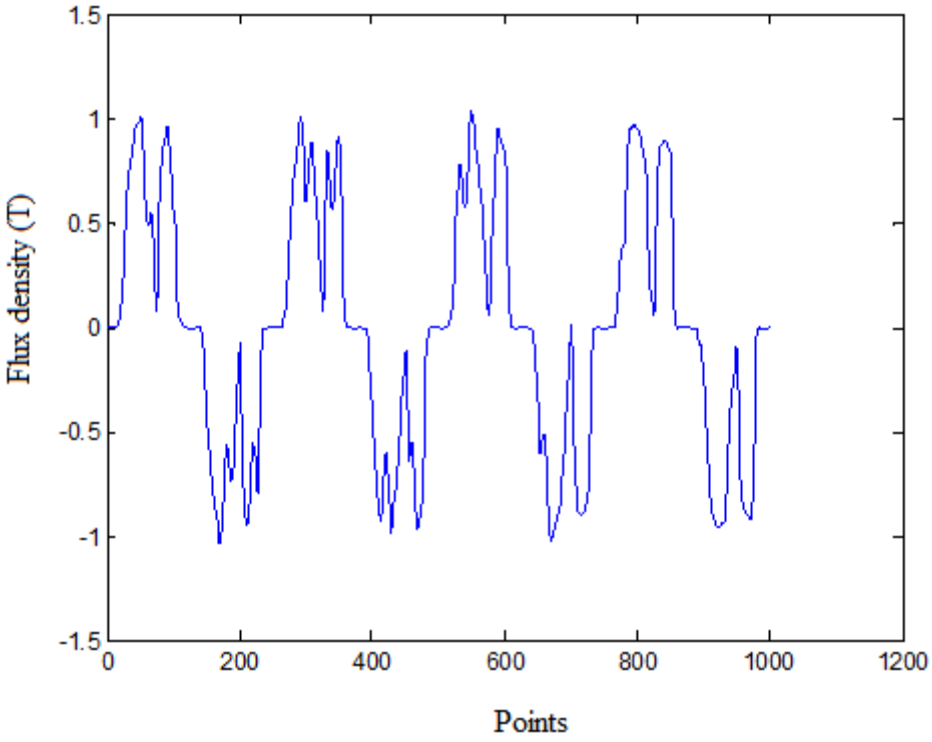

Fig. 3.11. Airgap flux-density distribution for the slotted-stator AFIPM machine.

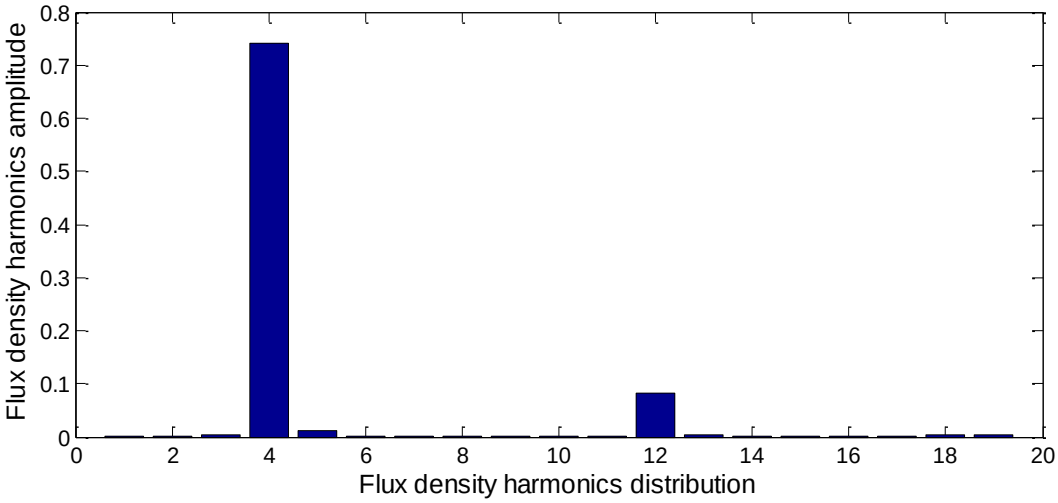

Fig. 3.12. Harmonics distribution for the 8-pole slotted-stator AFIPM machine.

3.2.3. Simplified waveform of airgap flux density

In the following, it is the aim to apply the proposed technique to shape optimization of rotor-PMs. The assumption to be taken into account is that the airgap flux density has a waveform, which is the image of the shape of rotor-PMs, i.e.

$$B_{e_{max}} = \left(\mu_0 \frac{h_m}{h_m + e}\right) M \ , \tag{3.3}$$

where *M* represents the PM magnetization, and h_m the PM height.

In Fig. 3.13, the case of an AFIPM machine with surface-mounted rotor-PMs, constant airgap thickness, constant PM height and two-pole symmetry, is considered. In contrast, Fig. 3.14 shows the case of the AFIPM under study, where there is no two-pole symmetry, thus leading to different airgap flux-density amplitudes from one pole to another. The computations are performed using numerical tools.

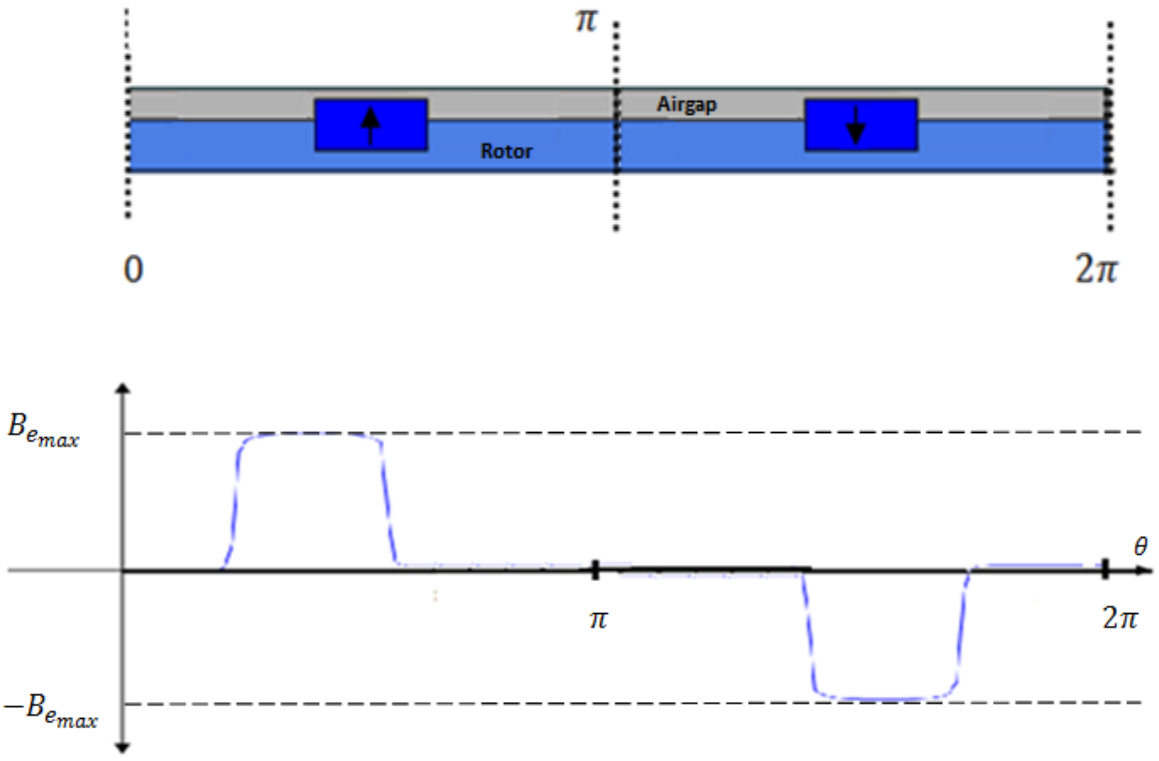

Fig. 3.13. AFIPM machine with two-pole symmetry.

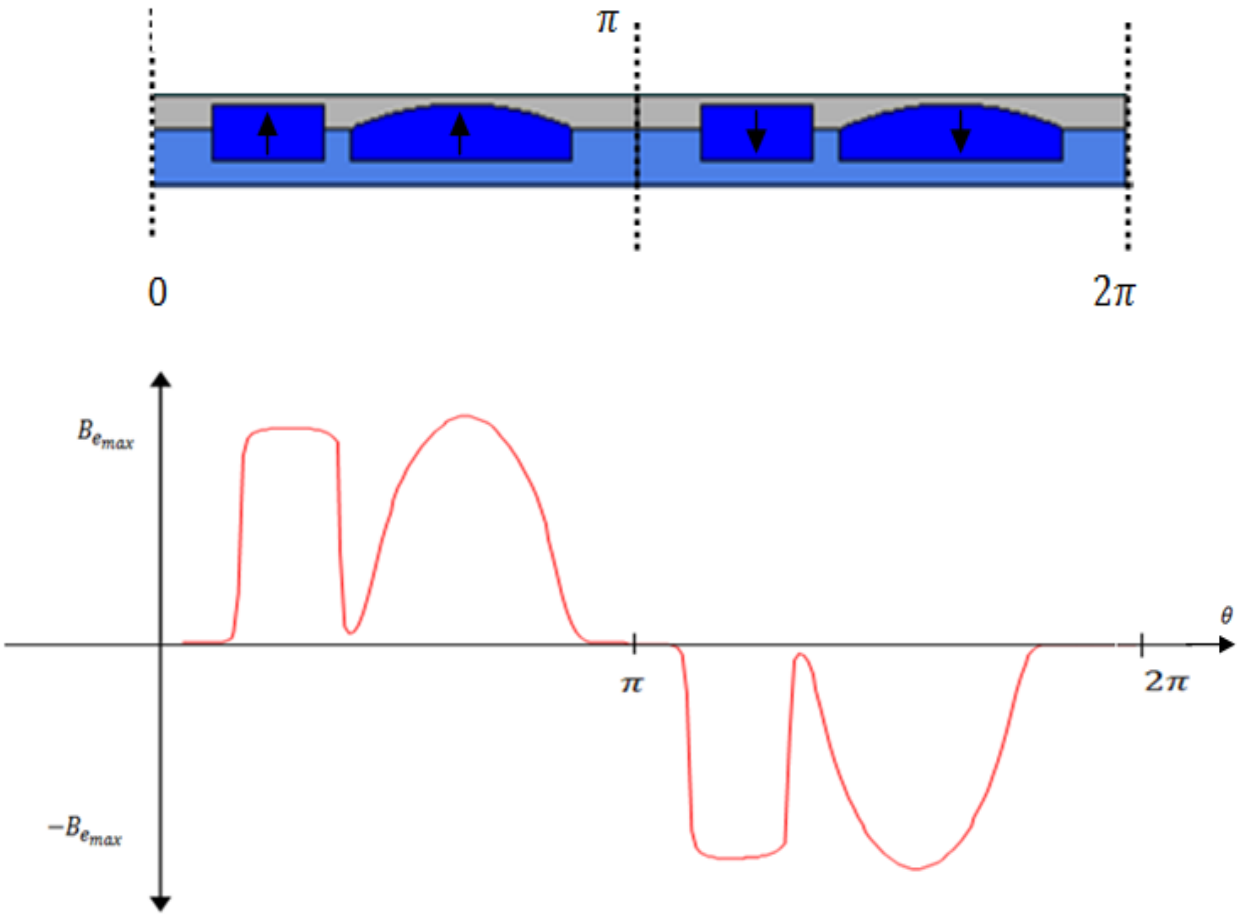

Fig. 3.14. AFIPM machine under study without two-pole symmetry.

In what follows, the AFIPM machine topology without two-pole symmetry and different shape of the two PMs per pole, is further studied. The airgap remains constant, and the airgap flux-density waveform is the image of the rotor-PM shape. Hence, the airgap flux-density waveform can be studied starting from the spectral function providing by the rotor-PM geometry.

A sequence of *N* PM-blocks for a half electric period is considered in Fig. 3.15. The angles $\theta_1, \theta_2, \theta_3, \ldots, \theta_{2N}$ define the PM sizes and positions. It is to be pointed out, that the function *f(θ)* contains both sine and cosine term, as well as odd harmonics. By using the Fourier-series decomposition, it can be expressed, in spectral form, as

$$f(\theta) = \frac{\theta_0}{2} + \sum_{n=1}^{\infty}(a_n \cos(n\theta) + b_n \sin(n\theta)),$$

$$a_n = \frac{2}{\pi}\left\{\int_{\theta_1}^{\theta_2} B_m \cos(n\theta)\, d\theta + \int_{\theta_3}^{\theta_4} B_m \sin(\theta - \theta_3)\cos(n\theta) d\theta\right\}, \quad (3.4)$$

$$b_n = \frac{2}{\pi}\left\{\int_{\theta_1}^{\theta_2} B_m \sin(n\theta)\, d\theta + \int_{\theta_3}^{\theta_4} B_m \sin(\theta - \theta_3)\sin(n\theta) d\theta\right\}.$$

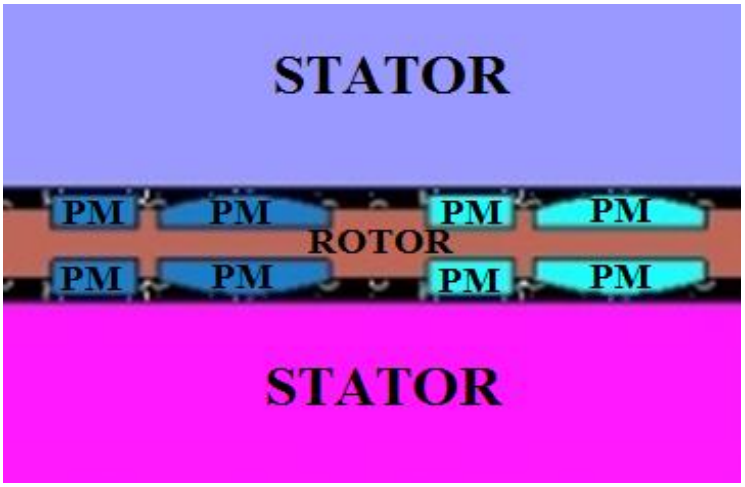

(a)

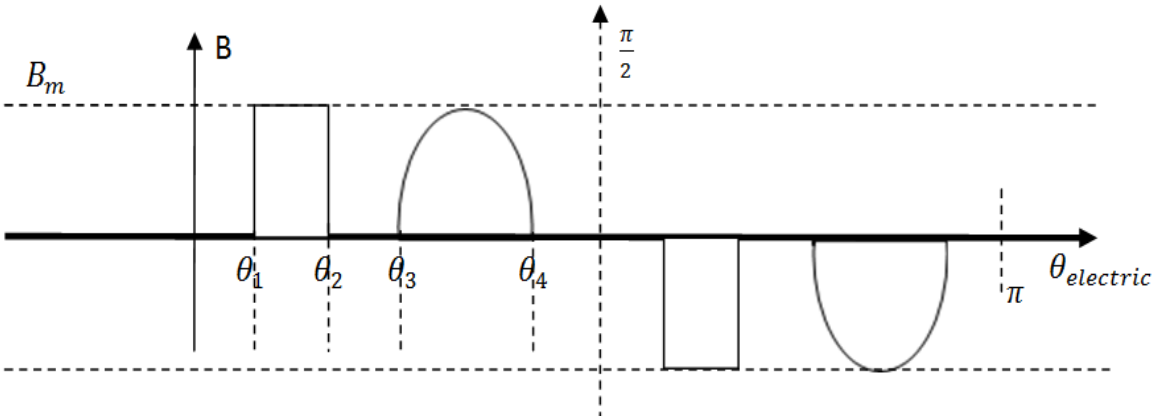

(b)

Fig. 3.15. AFIPM machine design (a) and airgap flux-density representation (b).

It is aimed at determining the angles $\theta_1, \theta_2, \theta_3, \ldots, \theta_N$ to ensure a certain level of the fundamental harmonic and to eliminate unwanted harmonics.

In Fig. 3.16, the airgap flux-density spectral optimization, starting with an analytical model, is presented. This model ensures the rotor-PM shape with reduced content of harmonics.

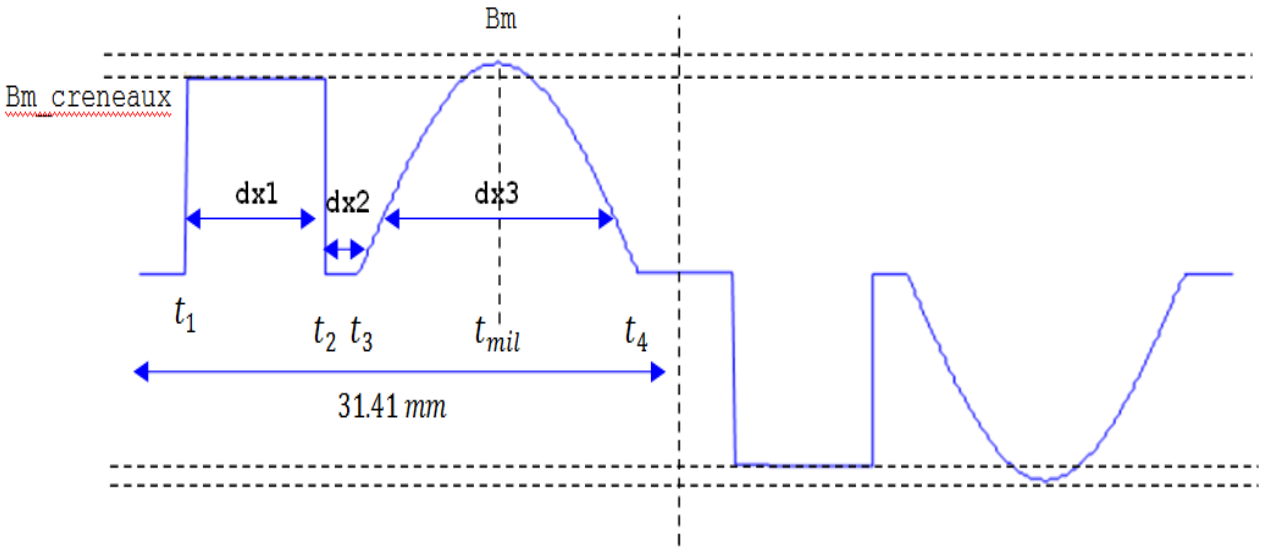

Fig. 3.16. Analytical model of the airgap flux-density distribution.

The development of this analytical airgap flux-density model will be explained in more detail in Section 3.6. It will be used in order to obtain a quick inside look on the harmonics distribution. This analytical model is faster in computation time than the finite element (FE) model. Solutions of both models will be compared and applied to the optimization process.

3.3. Finite-element modeling and analysis of AFIPM machine

The first quality criterion imposed is the minimization of disturbances. These are induced by torque pulsations, which generate noise and vibrations, damaging the mechanical system and also causing premature aging of the machine. Such disturbances can be mitigated by reducing the airgap flux-density harmonics.

3.3.1. Investigation tools

With the development of computational tools, one cannot imagine the modeling process without using a PC. The same thing is happening with the optimization process of AFIPM machines.

There are various techniques used to model electromechanical devices. The resulting models are more or less precise, depending on their complexity. The modeling tools are selected according to the objectives imposed for the study and based on the time required to perform calculations, which strongly depends on the modeling method used and the amount of computer resources.

A first solution to investigate the electromagnetic and thermal phenomena in electrical machines is the use of analytical methods. These methods are used by machine designers, especially when large quantities of figures should be tested. It considerably reduces the design computation time.

These analytical methods use the basic mathematical equations, which directly describe physical phenomena, or equivalent circuits. When a new machine has to be designed, it is necessary to make a detailed analysis of electromagnetic and thermal behaviours. In this case, one uses numerical methods, allowing more accurate results.

The most commonly used method in this field is the finite element analysis (FEA), which is used to solve electromagnetic field problems, especially when the complex machine geometry and non-linear characteristics of materials are to be taken into account. There are two different FEAs: the 2D and the 3D. The accuracy of both FEAs depends on the element size, whereas the calculation time depends on the FE number. If the discretization mesh is sufficiently fine, the results obtained by FEA are highly accurate, allowing the possibility to visualize many physical quantities, which are difficult to measure: flux densities, forces, torques, temperature gradients etc. Compared to analytical method, FEA requires more data processing resources, which is an important inconvenient.

Many programs that employ FEA have been developed and are commercially available. In the following, the Opera package [5], for the 2D-FEA modeling, and JMAG-Studio [6], for the 3D-FEA model, are used. Matlab software [7] is also used to interconnect Opera FE-model with the optimization algorithms. Opera is lunched from Matlab by using special line codes developed in the Laboratory L2EP of Lille. The analysis results will be compared with experimental measurements. The models development and their validation are presented in the following sections.

3.3.2. 3-D finite element modeling and analysis

JMAG-Studio is an electromagnetic field analysis software package that supports the design and development of motors, actuators, circuit components etc. It has been used by many companies and universities since 1983. JMAG-Studio has a long track record of use for analyzing electric machines and other rotating electromagnetic devices. JRI Solutions is constantly improving JMAG-Studio by incorporating features provided by the latest technology developed through research and accumulated analysis expertise.

JMAG-Studio is linked to the popular mid-range CAD product SolidWorks [8] through a powerful link function. In order to analyze the AFIPM machine flux-density distribution, the 3D field model is constructed. Because of the complex 3D-shaped model of the AFIPM machine, the geometry is firstly designed in Solid Works, while material and condition settings are maintained in JMAG-Studio. The ability to implement simulation calculation immediately after design revision facilitates design assessments on a more rapid cycle. The link between SolidWorks and JMAG-Studio is presented in Fig. 3.17.

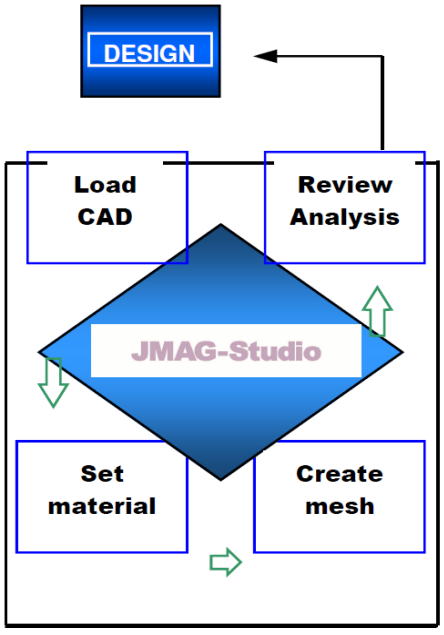

Fig. 3.17. Link between SolidWorks and JMAG-Studio. [6]

In the brushless AFIPM machine under study, the magnetic circuit having 3D flux paths, the magnetic field analysis uses 3D model to evaluate the machine electromagnetic quantities, parameters and performances. The entire 3D field model is shown in Fig. 3.18.

The AFIPM machine specifications are presented in Table 3.1.

For the physical properties of machine active materials, one can use digital data provided by industry, as indicated in Table 3.2.

Table 3.1. Specifications of the brushless AFIPM machine under study

Winding phase number	3	
Number of rotor pole pairs	4	
Rated phase current	36	A
Phase resistance	0.036023	Ohm
Winding connection	Star connection	
PM thickness	3.5	mm
PM length	20	mm
Number of stator slots	25	
Airgap thickness	0.75	mm
Stator-stack outer diameter	100	mm
Stator-stack inner diameter	80	mm
Number of phase-winding turns	48	
Rotor outer diameter [mm]	100	mm
Rotor axial length	10	mm
Stator-slot depth [mm]	10	mm
Stator-yoke axial length	20	mm

Table 3.2. Properties of AFIPM machine active materials

Stator	Isotropic magnetic steel sheet M400-50A
Permanent magnet	Nd-Fe-B 35SH
Rotor	OL 38
Winding	Electrolytic copper

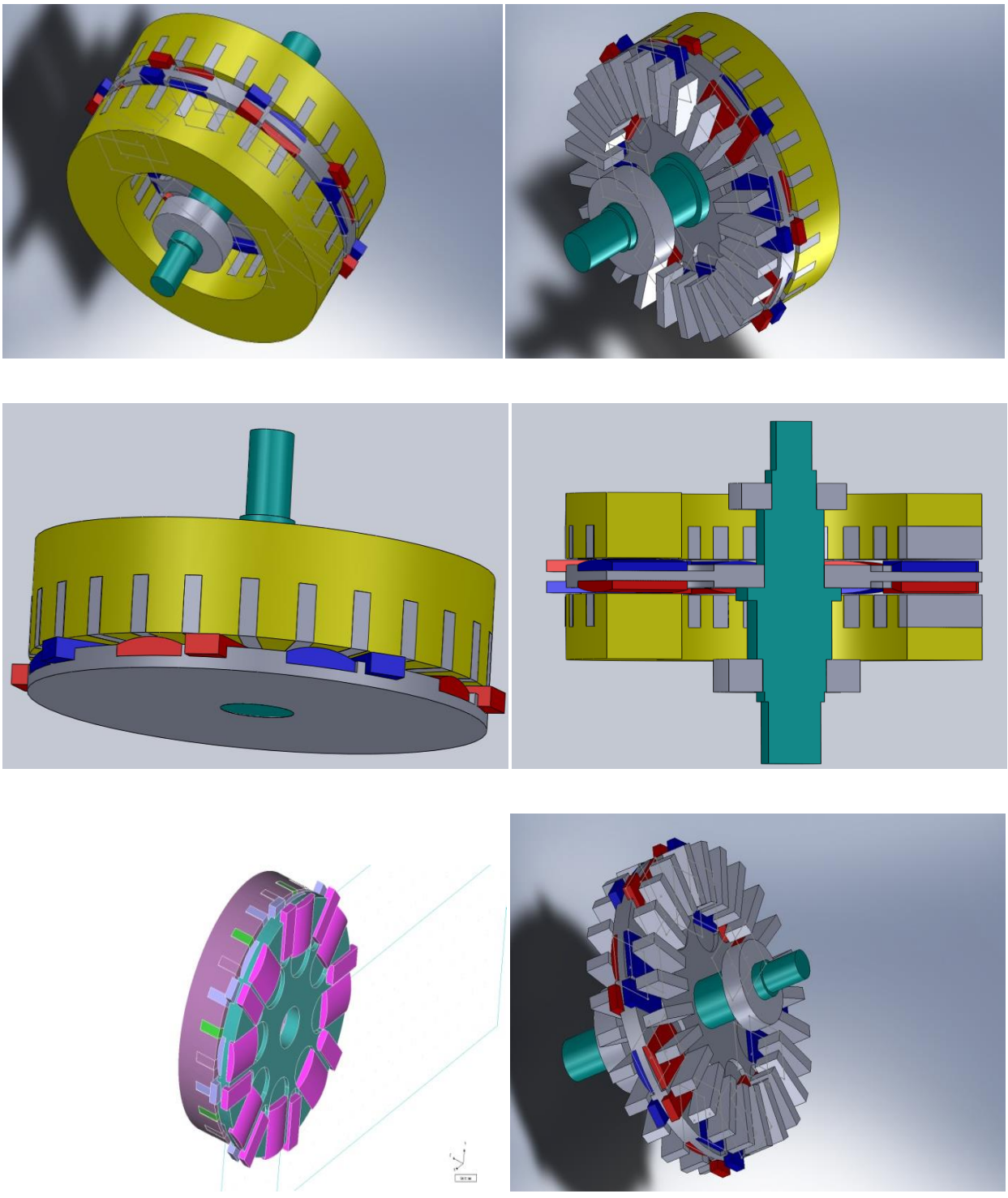

Fig. 3.18. Magnetic circuit parts of the AFIPM machine prototype topology under study.

- **Permanent magnet model**

When multiple magnets are represented by two layers, the FE discretization mesh may not be able to represent the pole area correctly. As a result, FEA is made for two different magnets. The first layer of rotor-PMs is thus on one side of the rotor, and the other PM layer is on the opposite side of rotor. The magnetization directions are opposite for the two PM layers in respect to each rotor pole.

The PMs used in FE simulation are of Nd-Fe-B 35SH (Appendix 1) with axial magnetization, linear material, and coercive force of 868000 [A/m], as shown in Fig.3.19.

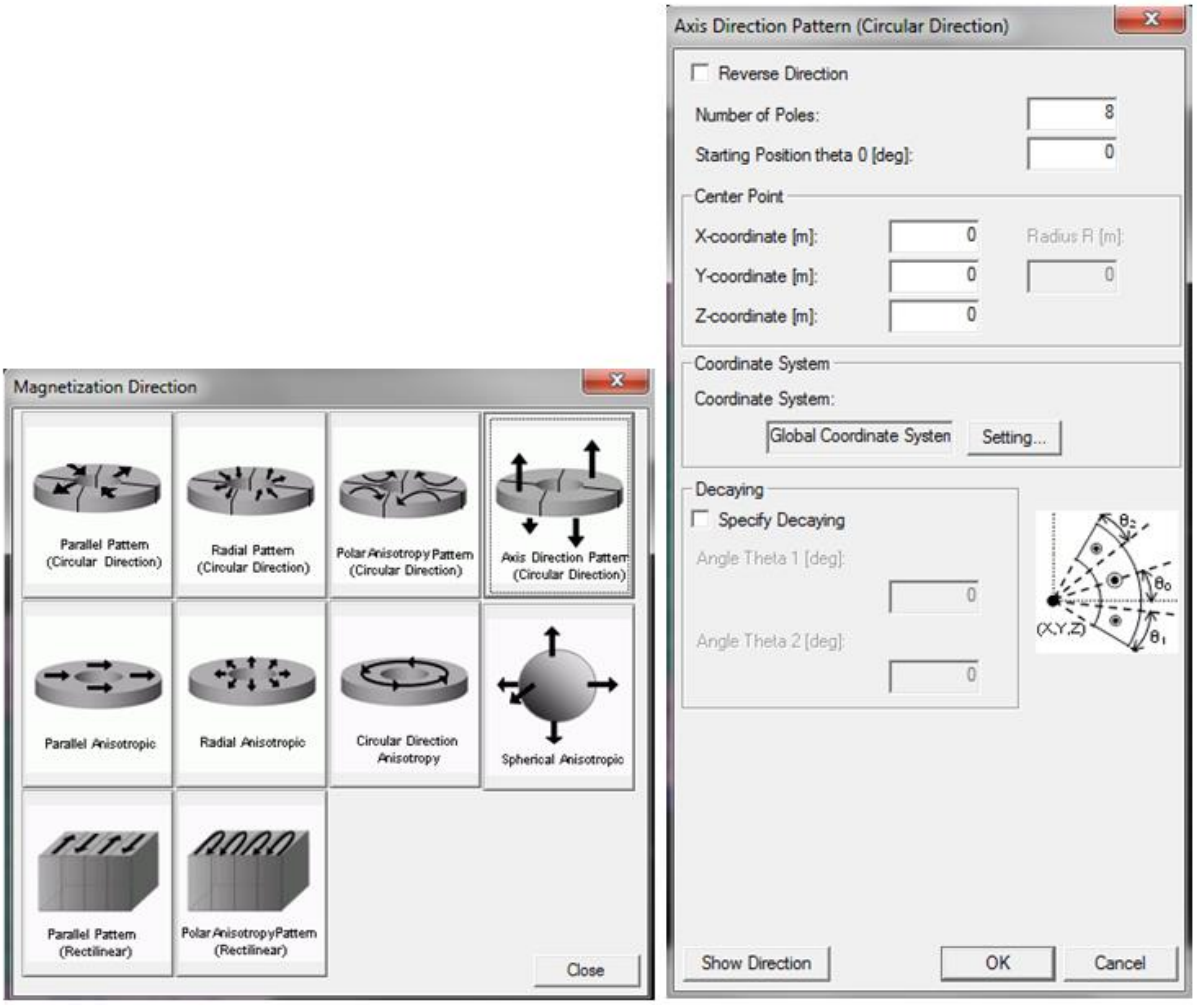

Fig. 3.19. Setting the rotor-PM features using JMAG-Studio facilities [6].

- **Stator model**

One stator of the AFIPM machine consists only of one long lamination rolled in circular form illustrated in Fig. 3.20. This means that the stator slot-pitch shortens towards the inner radius of the stator stack. Therefore, the manufacturing of the stator is somewhat more difficult than of the stators in the radial-flux machines. On the other hand, the rotor is usually very simple and the flat shape of the magnets is easy to manufacture.

For the stator, the isotropic magnetic steel sheet was chosen. The steel sheet used for this machine is M400-50A (Appendix 2).

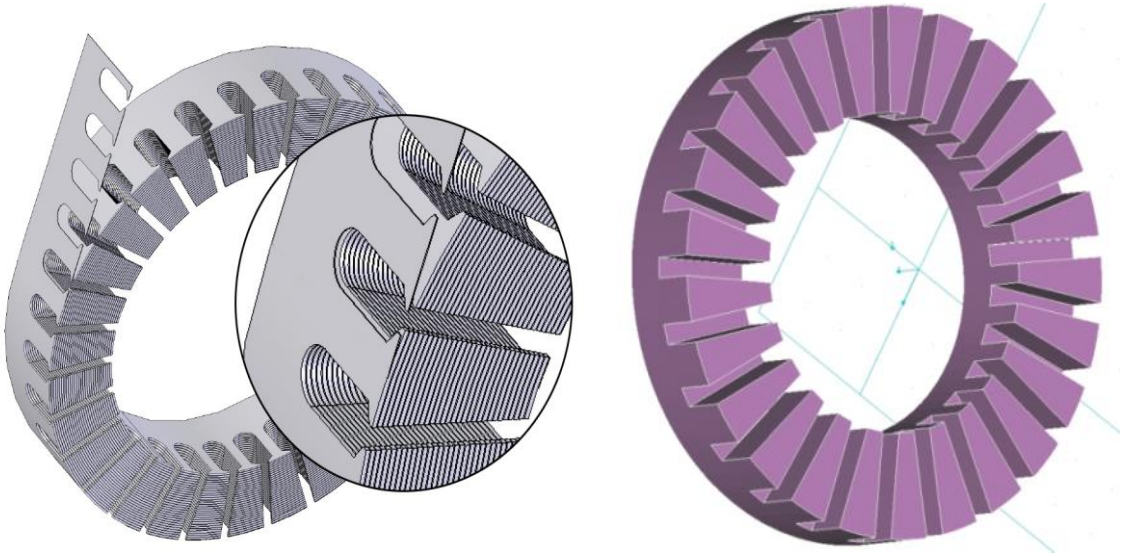

Fig. 3.20. AFIPM-machine stator lamination rolled into circular form.

- **Rotor model**

For the rotor of Fig. 3.21, the iron-part properties were imported from external database by choosing OL38 sheets.

- **Air region**

In this analysis the radius of the mesh model including the air region is set at 0.75 mm. The element size of the opposing faces of the air gap between the rotor and the stator needs to be uniform so as to ensure accuracy of the analysis. In this analysis the mesh is generated automatically at each step using a function, or so called patch mesh function.

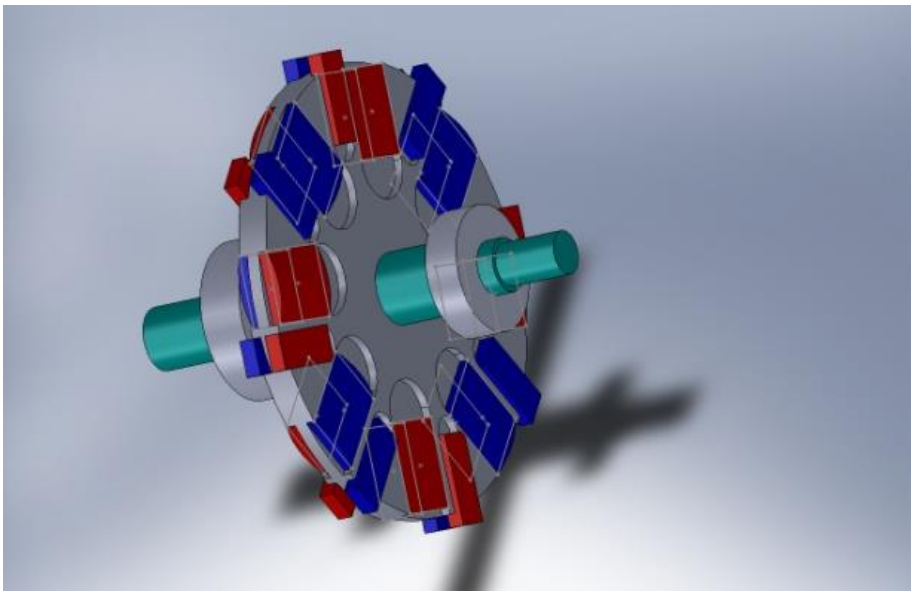

Fig. 3.21. Setting the PM-rotor geometry.

- **FE discretization mesh generation**

The element size of the PM region facing the airgap and opposing faces of coils is set to be small, so that a fine FE mesh is generated in these field regions. When the permeance is uniform, the mesh in the opposing faces of the airgap between the sandwiched rotor and stators must be uniform; otherwise, the analysis cannot be run accurately.

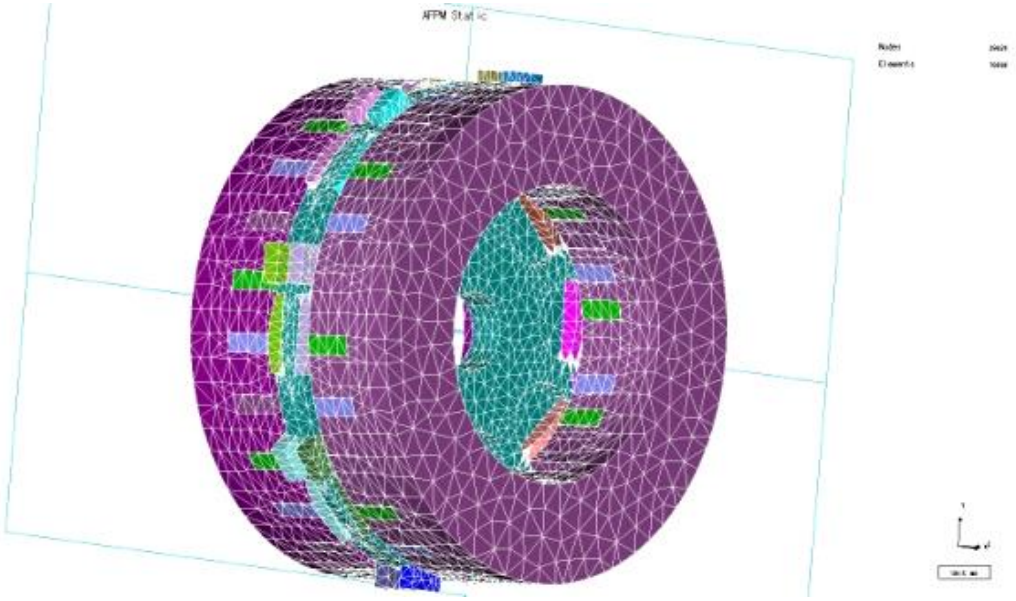

Fig. 3.22. Creating the 3D FE discretization mesh.

To include the effect of the rotor movement, the FE mesh in the airgap (Fig. 3.22) needs to be matched. However, since it is difficult to generate it manually, the mesh is generated automatically at each step during FEA using the patch mesh function.

- **Analysis conditions**

Transient response analysis is used since the electromagnetic force and the rotor position are time-variant.

Step

For the rotor to rotate one degree per step, the time interval is set depending on the rotational speed, which is set to 1500 rpm (25 rps) for rated conditions. The time interval is calculated accordingly, i.e. 1/(1500/60 rps x 360 degrees) = 1/9000 seconds.
The analysis being run for a half period of the electric cycle (mechanical angle of 45 degrees), the number of steps is set to 46 to include the initial starting position.

Motion

The motion condition is set on the coils. The center of rotation is the origin (0,0,0), and the direction of *Z*-axis rotation is set as (*X, Y, Z*) = (0,0,1).

3-D FEA results

- **Magnetic flux-density distribution**

The magnetic flux density is distributed in the axial direction due to the particular structure of the AFIPM machine (Fig. 3.23).

- **Flux density distribution for the slotless-stator AFIPM machine**

In order to visualize the airgap flux-density distribution, FE simulation for the slotless-stator AFIPM machine is performed (Fig. 3.24).

- **Magnetization analysis**

This tool specifies the magnetization on rotor-PMs according to the direction of the axial field generated by the magnets (Fig. 3.25).

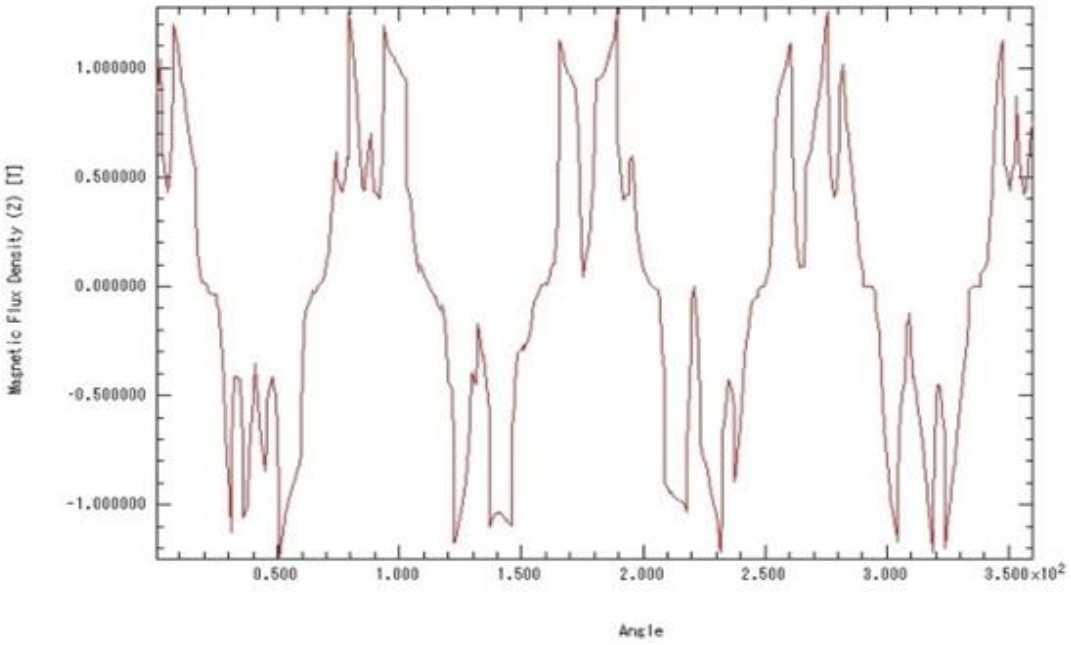

Fig. 3.23. Flux-density B_z – component distribution from 3D FEA.

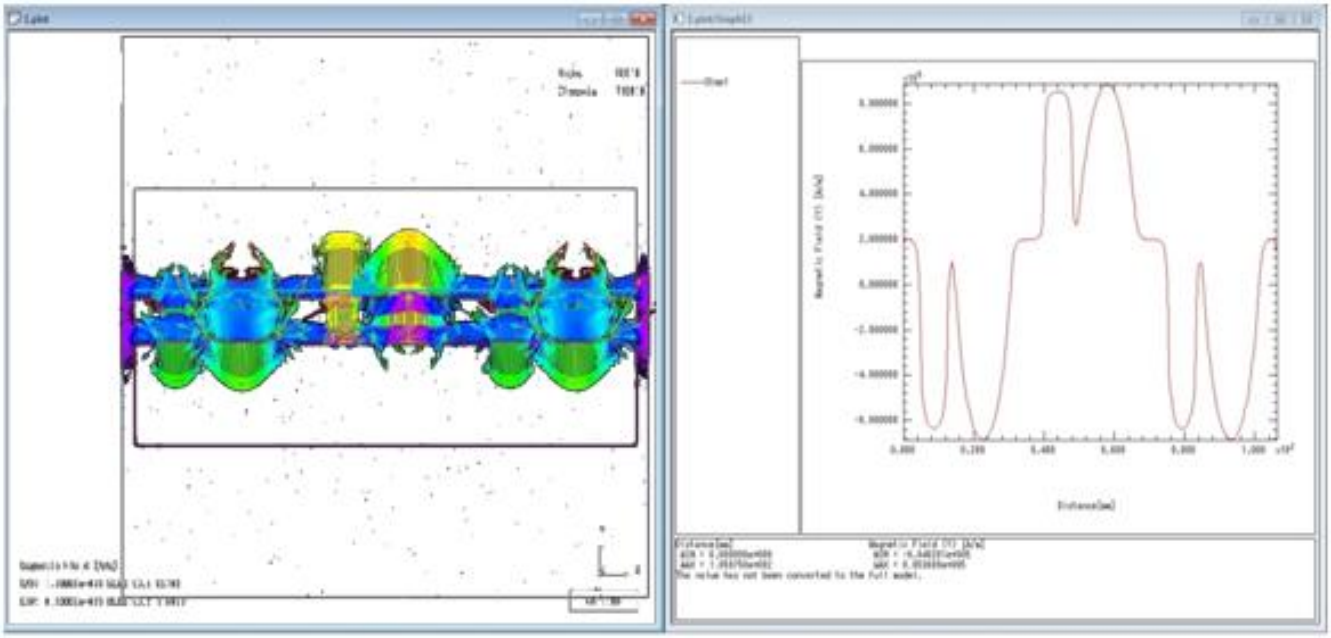

Fig. 3.24. Airgap flux-density distribution for slotless-stator AFIPM machine.

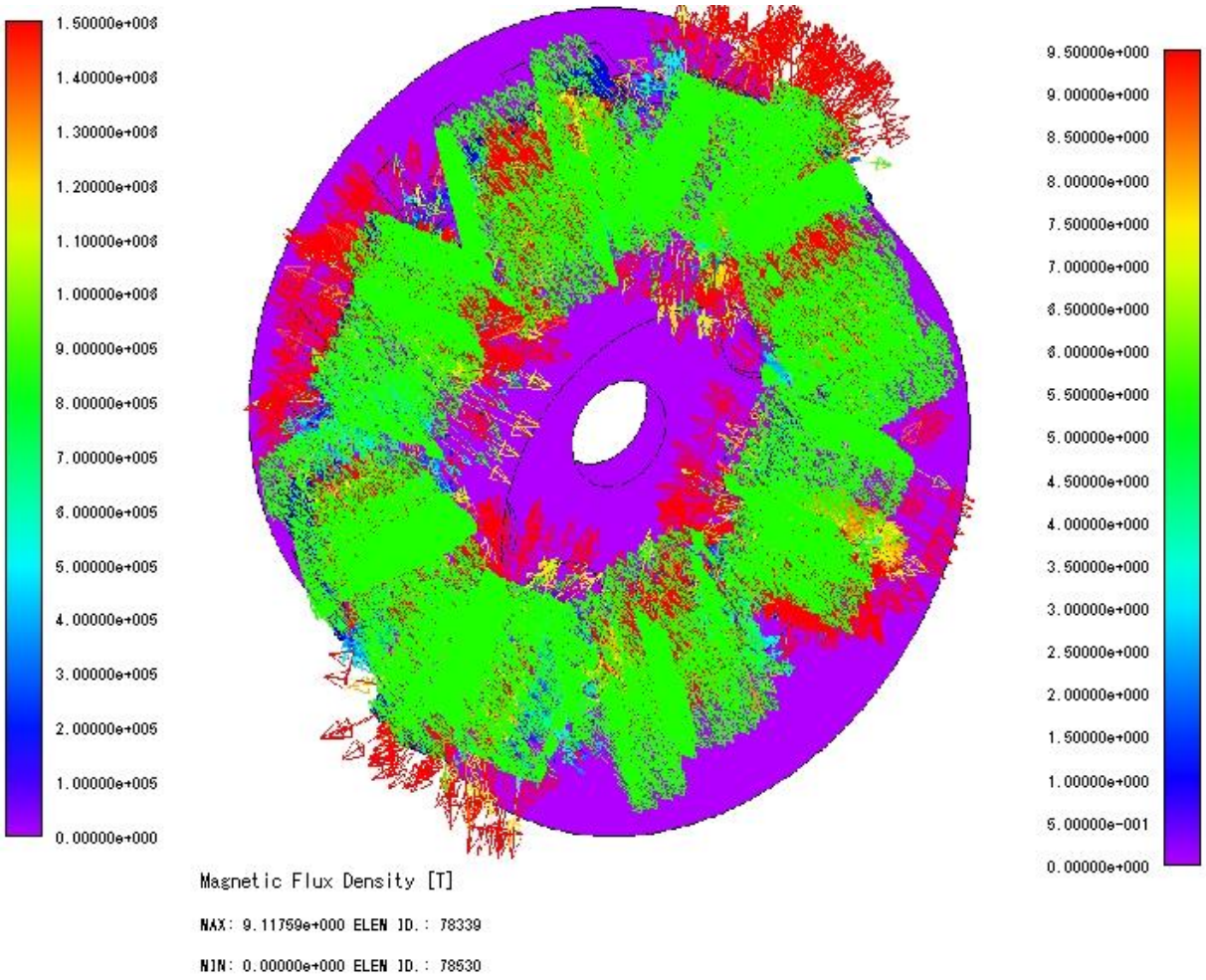

Fig. 3.25. Rotor-PM magnetization distribution.

3.3.3. 2-D finite-element modeling and analysis

In the AFIPM machine modeling, the fastness and accuracy of computations are very important aspects. By using FEA, it is possible to consider 3-D structure of the machine, but performing the computations is often too time-consuming. In order to evaluate quickly the performance of AFIPM machine, the 2-D FE modeling and analysis, which are usually carried out on the average radius of the machine, is a time-saving option, especially if the machine model will further be optimized. The basic idea of the design method is to subdivide the AFIPM machine structure into independent computation planes, and to use the average radius of the machine as a design plane.

In AF machines, the airgap flux density is an important design parameter, having notable effect on the machine characteristics. Therefore, in order to optimize the machine performance, the airgap flux density must be determined properly [9].

To tackle this problem, a transformation 3D - 2D will be used to transform the AFIPM machine in a linear equivalent structure, which is then analyzed using 2D models, easier to use and more faster in computation time.

This transformation is performed in the following manner (Fig. 3.26): one can take into consideration that the AFIPM machine is composed of several linear machines, each of them being given by a straight parallel cut to the axis of the machine for a given diameter.

Initially, the 3D geometry of the AFIPM machine is transformed to a 3D linear model (Fig. 3.26, *b*), which is then reduced to several 2D models (Fig. 3.26, *c*). 2D-FE simulations can be performed only using the ST-module (magnetostatic analysis) of Opera-2D software.

To take into account the rotor movement, the time-variation of currents and the coupling with external supplying circuits, Opera-2D RM module may be used, although this module is associated with radial-airgap topologies. Hence, an axial-to-radial transformation is done by using radial and circular construction lines for the equivalent radial machine. The disc-rotor model is built with constant PM width / pole-pitch ratio for all diameters of the AFIPM machine, and thus the PM angular width becomes constant.

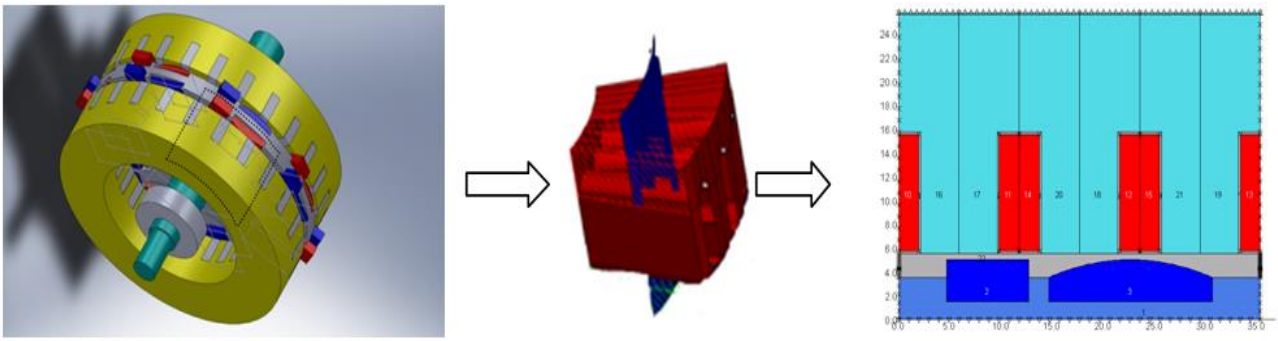

(a) *(b)* *(c)*

Fig. 3.26. (a) Structure of the AFIPM machine under study; (b) 3-D FE-model for one magnetic pole; (c) 3-D model reduced to 2-D representative plane.

The stator-slot width is constant throughout the radial dimension of the machine, but for different diameters the angular widths of slots and teeth are variable. This requires multiple divisions for several diameters. The slots edges of the AFIPM machine are parallel.

Since the axial-to-radial transformation does not change the slot geometry, the equivalent radial structures will have the airgap diameters equal to the section diameter of the AFIPM machine, multiplied by a ratio (called *linearity ratio*) chosen in such a way that the obtained structure will be almost equivalent to the linear structure obtained by the axial-to-linear transformation.

For AFIPM machine modeling, 2D FE models are used by considering the axial-to-radial transformation of Fig. 3.27, in order to benefit from Opera-2D RM module, which takes the rotor movement into account.

Periodicity conditions are well accepted by Opera-2D RM module, and therefore 3D axial-to-2D radial transformation is used for the small AFIPM machine under study.

The stator teeth and slots appear straight, as is the case of axial-airgap structure. The new model is limited by the number of nodes and maximum elements allowed by the software used.

Starting from the average diameter of the AFIPM machine, one may determine the diameter of the equivalent radial structure. Knowing the airgap diameter and the different geometrical parameters of the machine (airgap thickness, height and width of

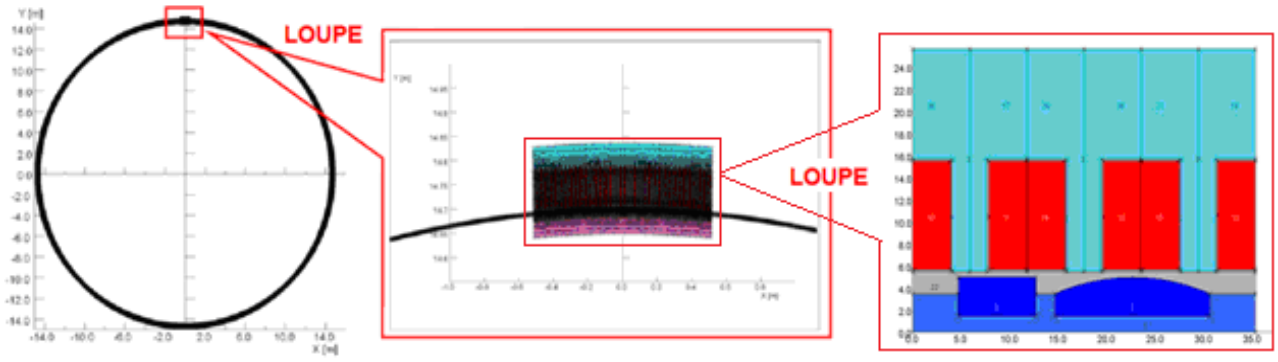

(a) *(b)*

Fig. 3.27. (a) 3D axial-to-2D radial transformation; (b) 2D radial equivalent structure.

slots, height and width of magnets, periodicity conditions) the different radii and angles for the geometrical structure construction of the equivalent radial-airgap machine are obtained.

The construction can be performed using files completely parameterized. Such files also allow using specific commands to define *B*(*H*) characteristics for different magnetic materials: magnets, stator laminations, rotor yoke. The parameterized files contain pre-processing, and post-processing commands. They can help optimizing the machine design by direct FE optimization method. The characteristics of the materials are provided in the Appendices.

The OPERA-2D RM module uses an airgap region defined by the user in order to separate the stationary and rotating parts of the model. The airgap surrounding areas must be circular. To avoid numerical problems, the real airgap model must be divided into several layers. In the present case, the airgap is divided into three layers, the first fixed to the stator, the second fixed to the rotor, while the third, placed in the middle of the other two, represents the airgap region defined by the system. As can be seen in Fig. 3.28, the region "gap" is the entire mesh circumference of the airgap. The region sides located near the airgap have a fine FE-discretization (Fig. 3.29).

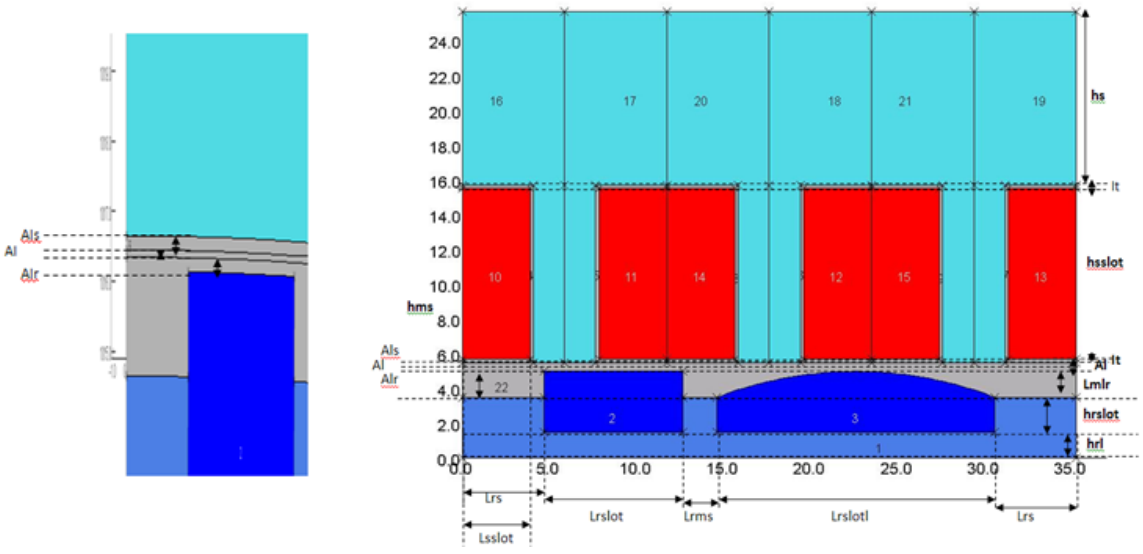

Fig. 3.28. Division of airgap layers for proper use of Opera-2D RM module.

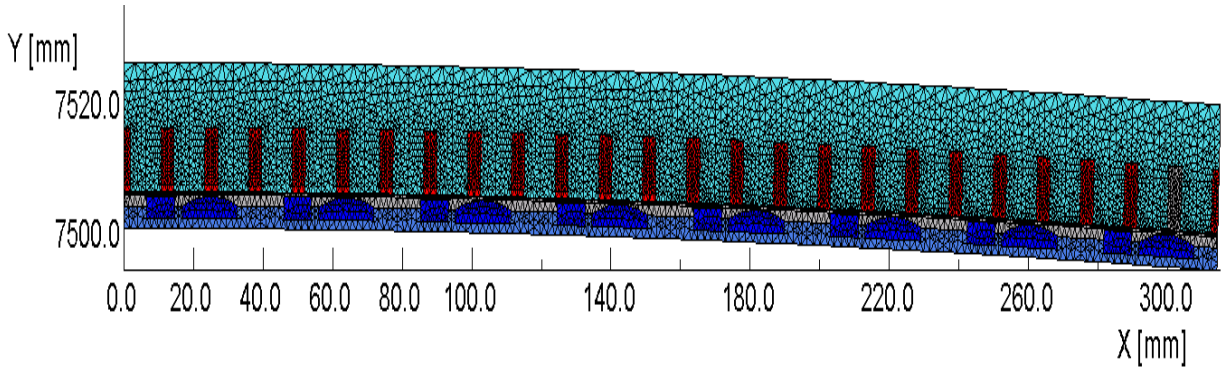

Fig. 3.29. FE discretization mesh for the equivalent 2D radial model of AFIPM machine.

The boundary conditions allow reducing the size of 2D models by taking into account the magnetic periodicities and the axial symmetry of AFIPM machine. This means that for the equivalent 2D radial model, the boundary conditions are (Fig. 3.30):

- cyclic symmetry conditions on the left and right ends of the model (magnetic vector potential at FE nodes on both sides has the same amplitude and sign);
- on the stator upper boundary, there is a Dirichlet boundary condition;
- on the rotor lower boundary, there is a homogeneous Neumann boundary condition.

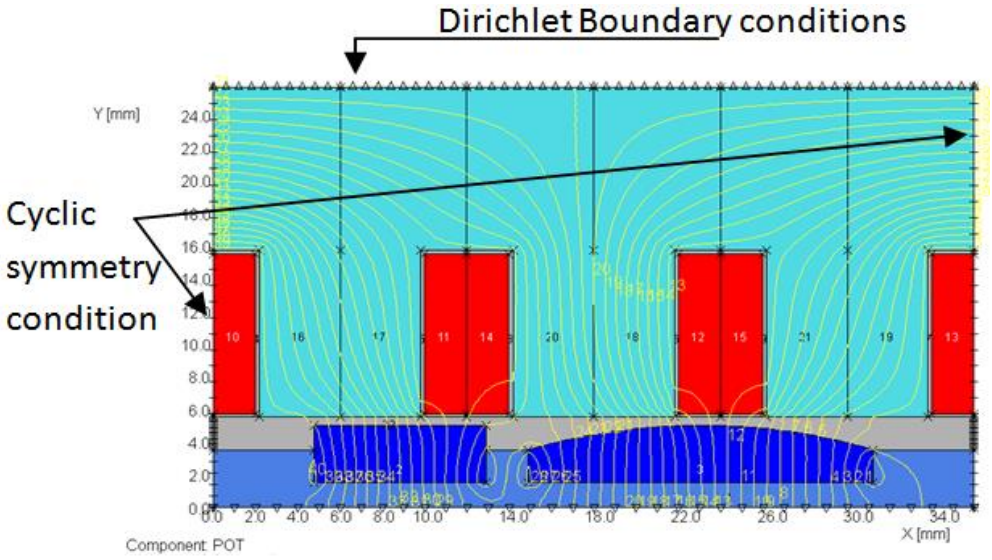

Fig. 3.30. Boundary conditions for the equivalent 2D radial model of AFIPM machine.

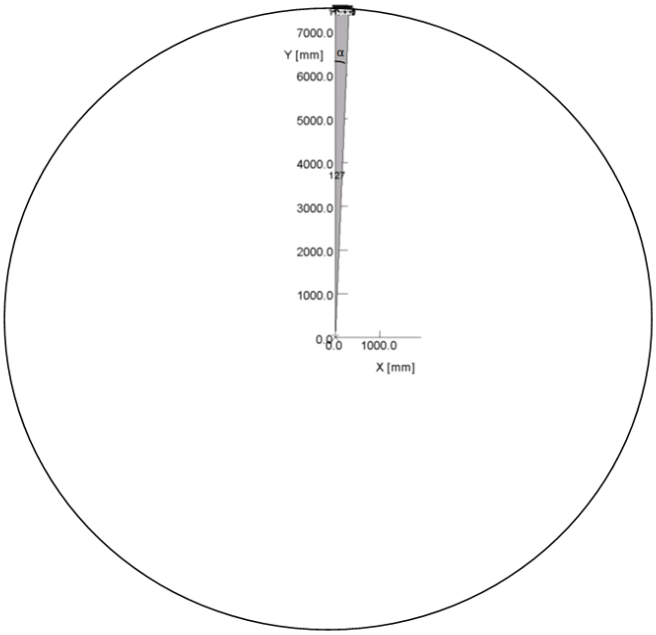

Fig. 3.31. AFIPM machine symmetry considered for 2D FE simulations.

In order to properly use the Opera-2D RM module, the symmetry of the FE-simulated part of the AFIPM machine is that shown by Fig. 3.31, where the phase winding is connected in series on both sides of the stator. One conductor is placed in each slot. In the 2D radial model, the phase winding is considered by using the external circuit features. Each coil is characterized by two conductors ‘go and return’, and each conductor is defined by the number of turns and the length. As the airgap of the equivalent radial-flux machine is placed far from the origin, the obtained back-emf is divided by the number of symmetries. Fig. 3.32 reveals the conductors of different phases and the winding direction. Each phase can be connected with other external circuit elements.

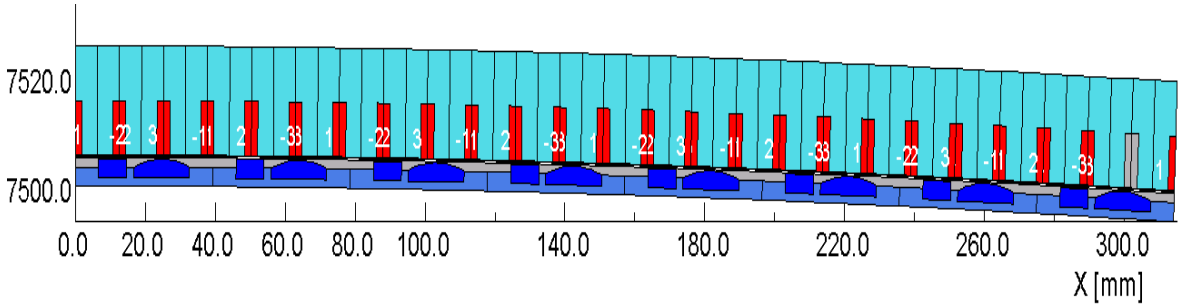

Fig. 3.32. Conductors of different phases and winding direction for AFIPM machine 2D-FE simulations.

For open-circuit FE simulations using Opera-2D software, each phase is connected in series with a high-value resistor (1 MΩ). The software provides the phase currents of very low values allowing to evaluate the no-load (open-circuit) back-emfs.

When the RM module is used, the software delivers the field computation results at different time-periods, as specified by the user. One rotor movement is shown in Fig. 3.33.

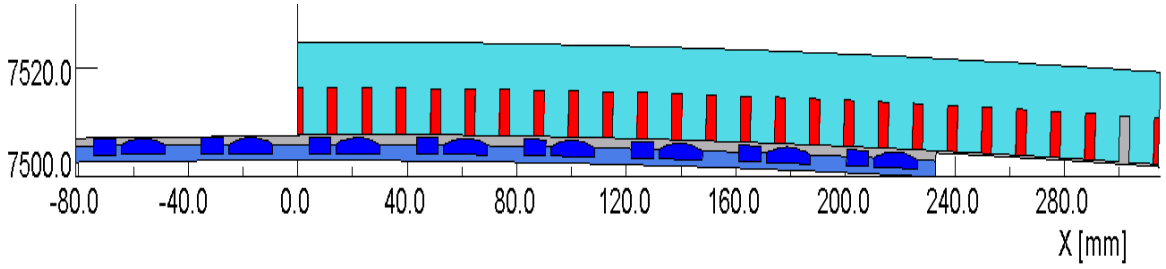

Fig. 3.33. Rotor movement performed using Opera-2D RM module.

The flux-line distribution is displayed in Fig. 3.34. It can be observed that the potential lines leave one pole and enter to the closest one, so that 50% of the flux produced by each rotor-PM passes through the airgap, slots, stator yoke and closes onto adjacent PMs. The other half of flux lines crosses the rotor yoke and closes onto the PM placed on the other side of the rotor.

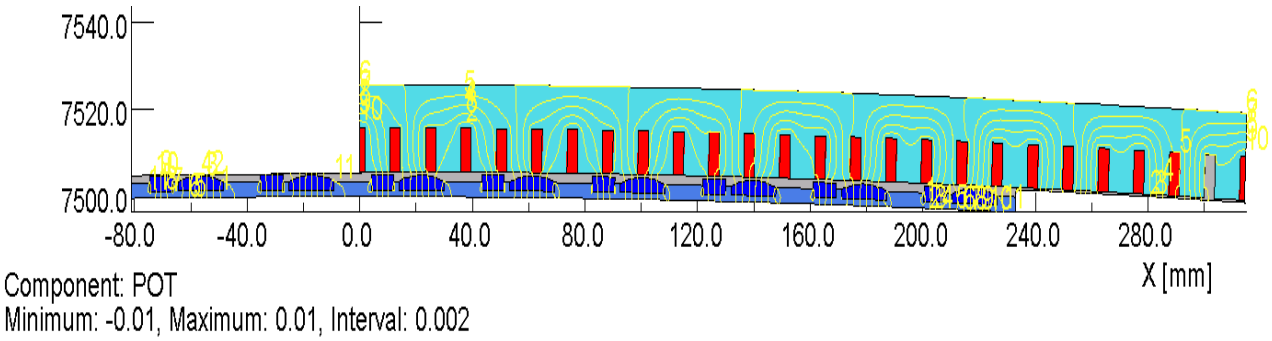

Fig. 3.34. Magnetic flux-line distribution as a result of 2D-FE simulation.

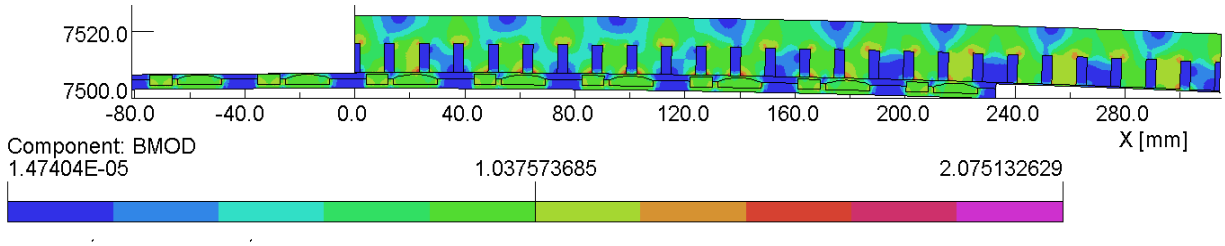

Fig. 3.35. Magnetic flux density representation

Magnetic flux-density map at open-circuit (no-load) conditions is represented in Fig. 3.35. The maximum magnetic flux density in stator tooth is achieved when the tooth axis is aligned with the rotor-PM axis, however, without revealing any magnetic saturation.

Airgap flux-density harmonics for slotless stator

By modifying the space harmonics distribution of both airgap flux density and back-emf one can improve the electromagnetic torque feature of the AFIPM machine.

With that end in view, FE simulations are performed for a slotless-stator machine, the impact of slots on the flux density repartition being disregarded, in the first instance (Fig. 3.36). This technique considers the time-space distribution of electromagnetic variables, so that it enables to identify the cross-coupling between different spatial and temporal field harmonics. Therefore, it provides a very meaningful

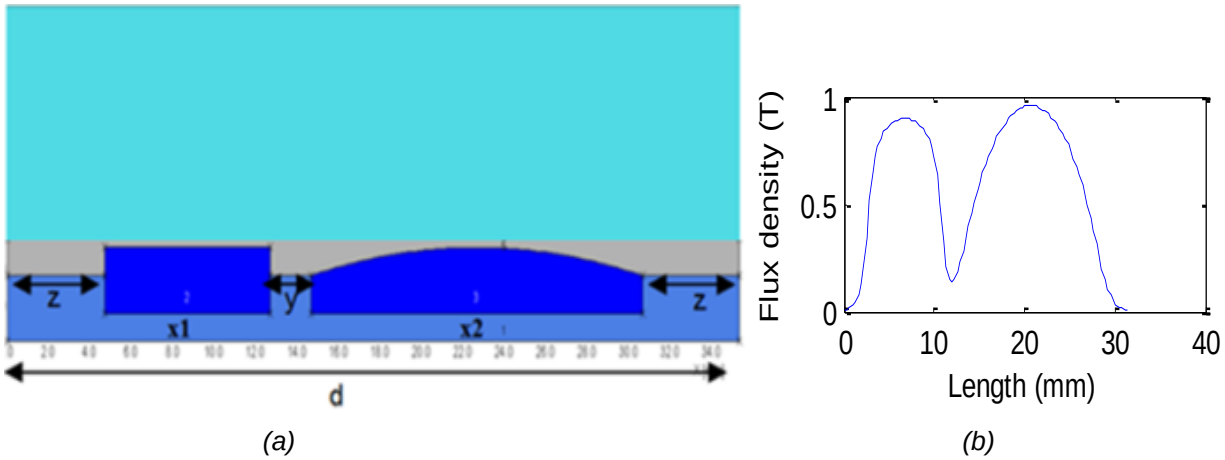

(a) *(b)*

Fig. 3.36. (a) One-pole representation of the AFIPM machine topology; (b) flux density distribution for a half-period.

insight into the correlation of different design variables with machine performances.

The airgap flux density produced by rectangular and sinusoidal magnets in surface-mounted AFPM machines, neglecting the slotting effect, is a square and sinusoidal waveform consisting of all odd harmonics.

It can be seen that due to the rotor-PM shape, the flux density distribution has an unsymmetrical distribution. Therefore, an entire period needs to be taken into account.

The flux density distribution in the AFIPM machine under study for an entire period is presented in Fig. 3.37. FE simulations are carried out under open-circuit (no-load) conditions in order to handle the airgap flux pattern.

A fast Fourier transform (FFT) is used to obtain the airgap flux-density harmonic spectrum. Fig. 3.38 shows that the first-order harmonic and then the fifth-order harmonic are dominant. Third- and seventh-order harmonics in the airgap flux-density spectrum are also significant. Only the harmonic orders less than 50 are considered in Fig. 3.38. The 5th harmonic is of 0.35 relative amplitude compared to the fundamental. In their turn, the 3rd, 7th and 13th harmonics have relative amplitudes of 0.21, 0.18 and 0.12, respectively. All other harmonics have relative amplitudes below 0.1. As the considered three-phase AFIPM machine topology is balanced and symmetrical, there are no even-order harmonics.

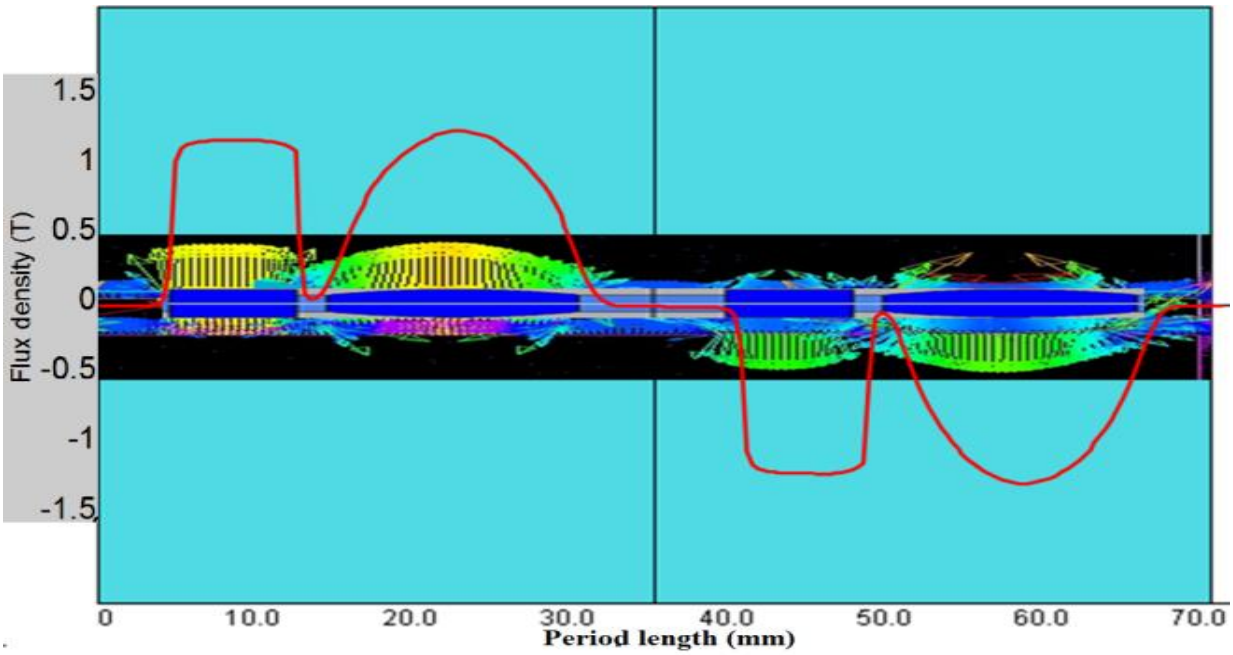

Fig. 3.37. Flux density distribution in the airgap of slotless-stator AFIPM machine.

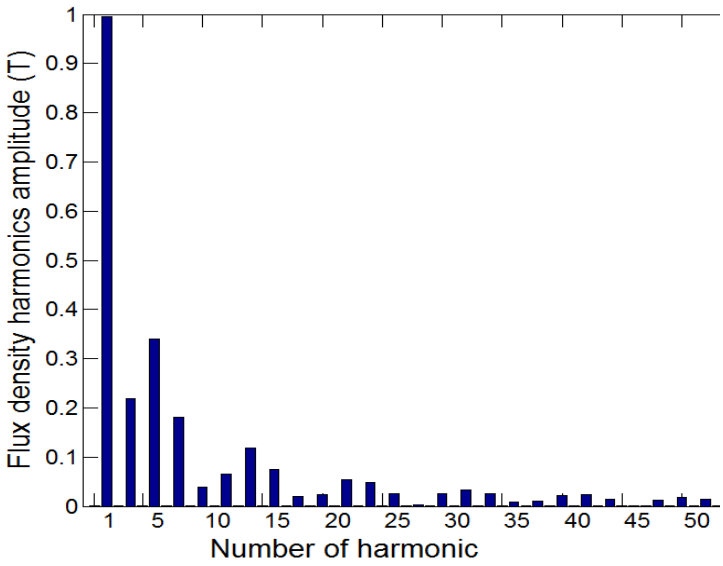

Fig. 3.38. Airgap flux-density harmonic spectrum of the AFIPM.

Effect of stator slotting

The effect of stator slots on the open-circuit (no-load) magnetic flux distribution is investigated. The airgap flux density always drops at stator slot-openings, and this effect has a significant influence on the values of flux and back-emf. For this reason, it is important to accurately model the airgap flux density.

The rotor-PM distribution is depicted in Fig.3.39.

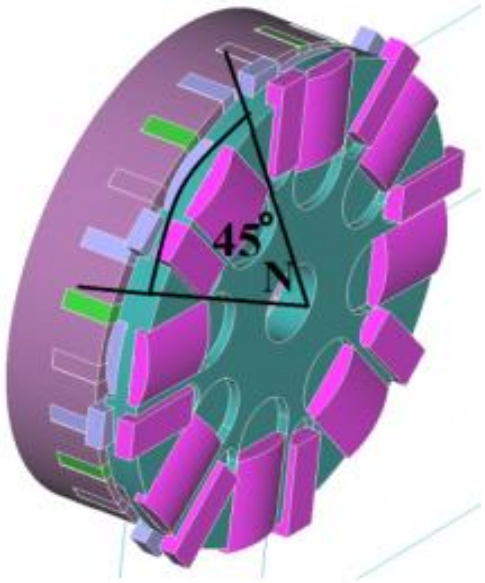

Fig. 3.39. One of the two stators and the rotor with its PM arrangement for AFIPM machine under study.

In order to reduce the time of the simulation, just one pole pitch of the structure was simulated, by setting the boundary conditions specified with reference to Fig. 3.30.

The maximum flux of a certain pole is obtained when a rotor-PM centerline is coincident with that of a stator tooth. Accordingly, the integration of the positive flux pulse under the tooth gives the maximum flux per pole.

The 2D representation of one pole of the AFIPM machine, and the open-circuit (no-load) magnetic flux distribution in the airgap are shown in Fig. 3.40. The angular variation of the airgap flux density due to rectangular- and arc-shaped rotor-PMs for one pole is shown in this figure. *A* and *A'* represent the winding of the phase *A*, and *B* denotes the PM-created flux density in the airgap. By superposing the flux density distribution upon the AFIPM machine geometry, one may emphasize the effect of the stator slots on the flux density waveform.

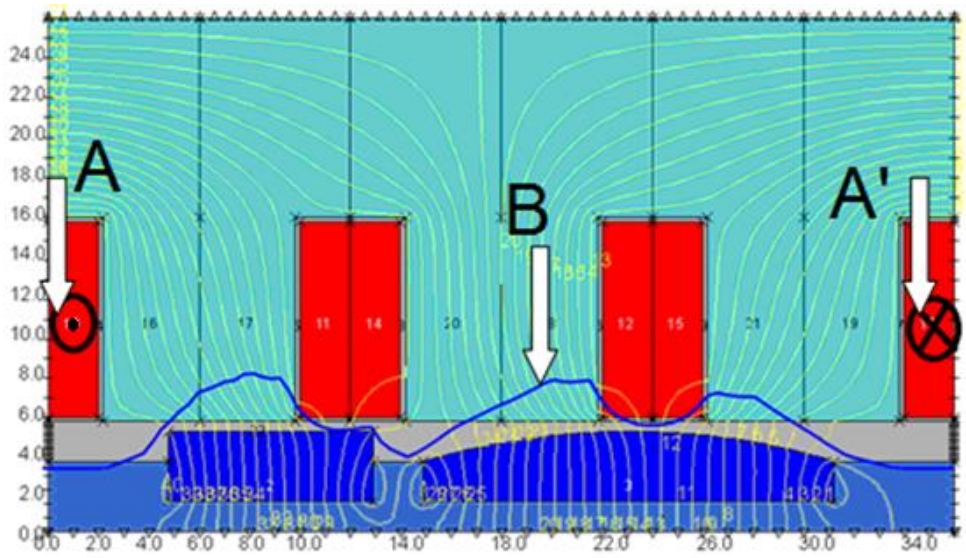

Fig. 3.40. No-load magnetic flux distribution for one PM-rotor pole.

The first airgap flux-density distribution is due to the rotor-PM of rectangular shape, while the second one is due to the arc-shaped PMs. The stator slotting effect has a large impact on the flux density distribution. It can be seen the flux density decreasing in the areas where the flux density crosses the slots. Moreover, the flux density amplitude is oscillating due to stator-slotting effect. From FE simulations, the magnetic flux distribution in the airgap (Fig. 3.41) and stator core (Fig. 3.42) is obtained.

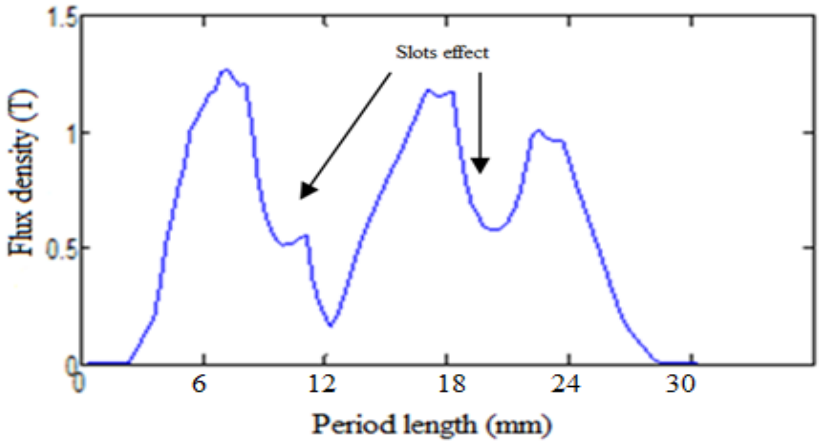

Fig. 3.41. Airgap flux density due to rotor-PMs.

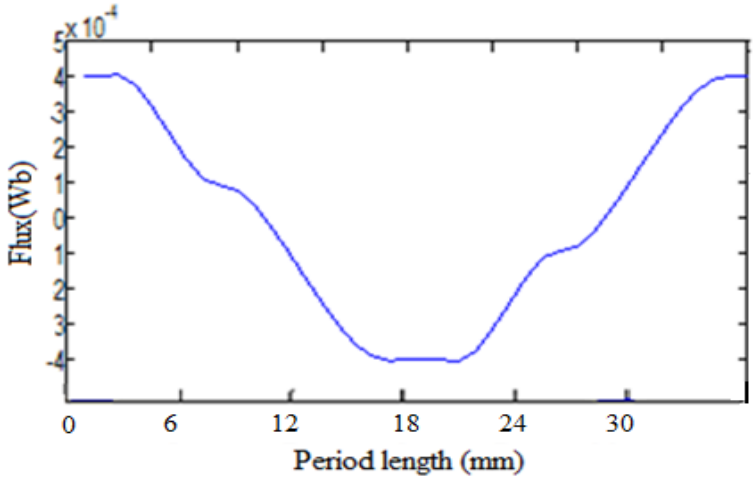

Fig. 3.42. Magnetic flux density in the stator core.

Finally, the phase back-emf is calculated as the time-derivative of magnetic flux (Fig. 3.43).

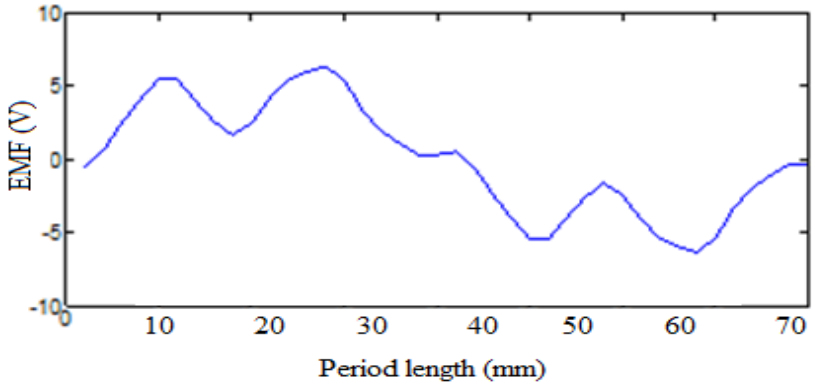

Fig. 3.43. FE-computed back-emf waveform.

3.4. Analytical field modeling of AFIPM machine

The analytical field model of AFIPM machine gives a quick inside look regarding the flux-density harmonics distribution, and enables reduction of the computation time compared with FE modeling and analysis.

The model is developed in Matlab by using trigonometric functions and nonlinear regression, as detailed in Appendix 3.

The airgap flux-density waveform results obtained from FE simulations and from the analytical field model are compared in Fig. 3.44, in order to check their relative accuracy. Since it is revealed that the results of both models are in good agreement, there are jointly used in the rotor-PM shape optimization in view of minimizing undesired airgap flux-density harmonics, which exist in the small AFIPM machine design.

An important analytical model simulation result concerns the back-emf waveform (Fig. 3.45). It is to be pointed out that the pole pitch is $\frac{2\cdot\pi}{8}$, whereas the coil pitch is $\frac{2\cdot\pi}{25}\cdot 3$. The phase difference between coil pitch and magnetic pole is 1.8 degrees.

Winding coils with a phase shift of 1.8 degrees allow making an analytical estimation of the phase back-emf (Fig. 3.46). It is to be observed that its waveform is close to a sinusoidal function of time.

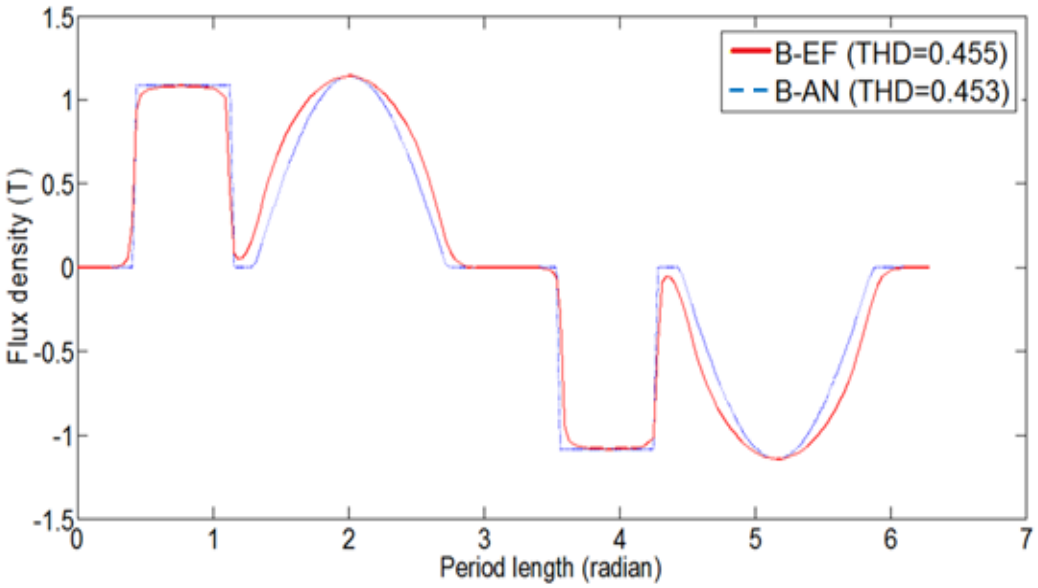

Fig. 3.44. Airgap flux density distribution of the AFIPMM.

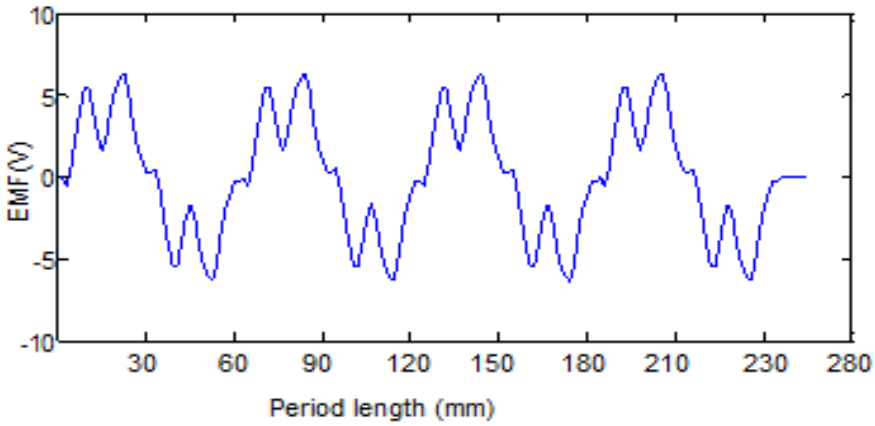

Fig. 3.45. Analytically-obtained open-circuit (no-load) back-emf waveform.

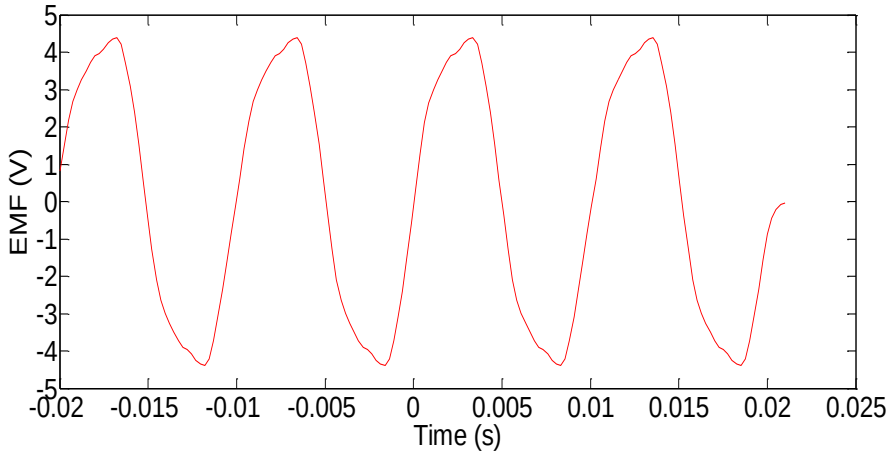

Fig. 3.46. Analytically-obtained open-circuit (no-load) back-emf vs. time.

3.5. Reduction of airgap flux-density space harmonics of AFIPM machine by rotor-PM shape optimization

3.5.1. FE model-based optimization

In order to reduce undesired airgap flux-density space harmonics, several steps have to be pursued. In Fig. 3.47, the coupling of the SQP optimization algorithm and the FE model in Opera-2D software is emphasized. The roles of different modules of Fig. 3.47 are defined in Table 3.3.

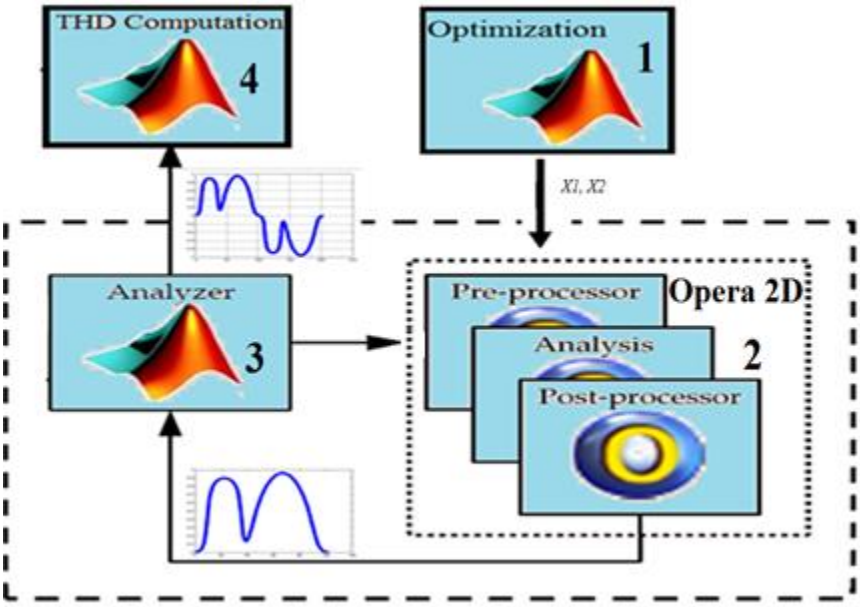

Fig. 3.47. Optimization process using FE model.

Table 3.3. Role of different modules in optimization process using FE model and analysis

Module	Role
(1)SQP optimization	perform optimization on a low-budget of FE model evaluations
(2)Opera-2D	perform FE model evaluation (pre, post-processing and analysis)
(3)Analyzer	launch FE model evaluation, recompose the flux density signal and export the results to THD computation block
(4)THD computation	Fast Fourier Transformation (FFT-Matlab) and THD computation

The optimization process is launched within Matlab. The SQP algorithm makes regular calls to the FE model of AFIPM machine, throughout a Matlab developed interface. The FE model evaluation is done using the FE model-based optimization in Opera-2D software.

The FE model evaluation implies three distinct phases: pre-processing (the mesh is generated for the given geometrical configuration), analysis (a static analysis (ST) is performed for the model, generating a file of results) and post-processing (analysis results are extracted and made available to the Matlab model launching function by the

Matlab-Opera interface). Depending on the geometrical configuration, one FE model evaluation (pre-processing, analysis and post-processing) takes about 15 seconds.

Matlab model exports the results to the analyzer. The flux density waveform is recomposed for the entire period. Then, it is subjected to Fast Fourier Transformation (FFT) for the total harmonic distortion (THD) computation. Once the optimization process has finished, the optimization results are handled and analyzed in Matlab environment.

The electromagnetic torque developed by the AFIPM machine is often affected by harmonics of various origins, such as

- space harmonics of the stator mmf due to the non-sinusoidal distribution of the stator (armature) phase windings;
- space harmonics caused by the presence of stator slots;
- time harmonics related to the power electronic supply, and affecting the stator current.

Space harmonics in AFIPM machines are the main concern of this thesis. Starting from a simplified model, but enough accurate and fast, a rotor-PM shape optimization technique allowing to reduce the airgap flux-density space harmonics is proposed and fully described.

The electromagnetic torque pulsations of AFIPM machines are the result of interaction between back-emf harmonics and current harmonics. Back-emf harmonics are due to armature winding distribution and to rotor-PM shape. Minimizing the airgap flux-density and back-emf space harmonics will notably improve the quality of the developed electromagnetic torque.

Supposing ideal stator winding distribution, the back-emf can be expressed as

$$e = n\frac{\partial \phi}{\partial t} = n\frac{\partial \int BdS}{\partial t} = n\frac{\partial \int BLRd\theta}{\partial t} = n\frac{\partial \int BLRd\theta}{\partial t}\frac{dt}{d\theta}\Omega = nB(\theta)LR\Omega, \qquad (3.5)$$

where ϕ is the flux density in the airgap, R, the radius of the rotor, L, the axial length and Ω, the rotor angular speed of the AFIPM machine.

Disregarding the stator-winding distribution effect, the back-emf space harmonics are those of the airgap flux-density. To reduce these harmonics by managing the THD, rotor-PM shape optimization may be applied, as further described.

FE model-based optimization using Opera-2D software with parameterized mesh for configuration of the AFIPM machine under study is thus developed.

It consists of three parts called “pre-processor”, “processor”, and “post-processor”. The *pre-processor* is used to draw the geometry of AFIPM machine, to define materials and field model boundaries. A parameterized model of the machine is built with the following tasks.

a) Draw: one pole of slotless-stator AFIPM machine is represented.

b) Materials: physical characteristics of the geometric domains previously drawn in their assigning properties (magnetic linear, nonlinear) are assigned.

c) Boundary conditions: Dirichlet, Neumann and periodicity conditions are applied to the contour lines of the geometry.

The pre-processing file is lunched in Matlab using the following command line:

```
“pre = '"C:\Program Files\Vector Fields\Opera 13.0\bin\pp.exe"';
PrjPath = D:\Optimization\Optimization_plate-forme\Mono\';
PrjFilePre = sprintf('%spre.comi',PrjPath);”
```

Firstly, Opera-2D is lunched with the first command line, and then the project path is initialized. The pre processing operation needs to be lunched in “local” mode by the enabling command line:

```
“dos(sprintf('%s ''%s'' /local /%s',pre,PrjFilePre));”
```

The *processor* is the part where the partial differential equation is solved on discrete form. For the case of nonlinear problem, the processor solves in iterative way until the required precision is reached. The processor makes possible to find magnetic potential vector values in each node of the FE discretization mesh, and then to compute the magnetic flux density distribution. The file containing the corresponding parameterized command lines is defined in Appendix 4.

After a finite element model has been prepared and checked, boundary conditions have been applied, and the model has been solved, it is time to investigate the results of the analysis. This activity is known as the post-processing phase of the finite element method.

The *post-processor* is the part where the results are analyzed. A visualization aspect is often useful for the comprehension of results. The command line, which enables to lunch the post-processing line is

```
"dos(sprintf('%s ''%s'' /local /%s',post,PrjFilePost))".
```

In this case the objective of the post-processing file is to re-direct the airgap flux pattern to the output file. The information regarding the airgap flux density waveform is stocked in a text file. The command line, which enables the export of flux density waveform in a table form is

```
  "READ FILE='fluxdensity.rm' CASE=1 GEOMETRY=YES
$OPEN 1 'D:output.txt' OVERWRITE +REDIRECT"
```

The *analyzer* is used for re-composing the flux density waceform for an entire period. Also this block serves as interface between FE model and Matlab. The results are then exported to the THD computation block.

The THD of a quantity waveform is a measurement of the harmonic distortion and is defined as the ratio of the sum of the powers of all harmonic components to the power of the fundamental frequency:

$$THD = \frac{\sqrt{\sum_{h=3,5,7\ldots13}^{\infty} B_h^2}}{\sqrt{B_1^2}}. \tag{3.6}$$

Because of the low permeability (comparable to that of air) of rotor-PMs, the airgap flux density waveform depends on the shape and size of rotor-PMs. Therefore, a rotor-PM shape optimization technique is introduced allowing minimization of space harmonics existing in the airgap flux-density waveform of the AFIPM machine under study. It is schematically represented in Fig. 3.48.

The mono-objective optimization problem is formulated as

$$\begin{cases} \min THD(x_1, x_2) \\ x_{1\min} \le x_1 \le x_{1\max} \\ x_{2\min} \le x_2 \le x_{2\max} \end{cases}. \tag{3.7}$$

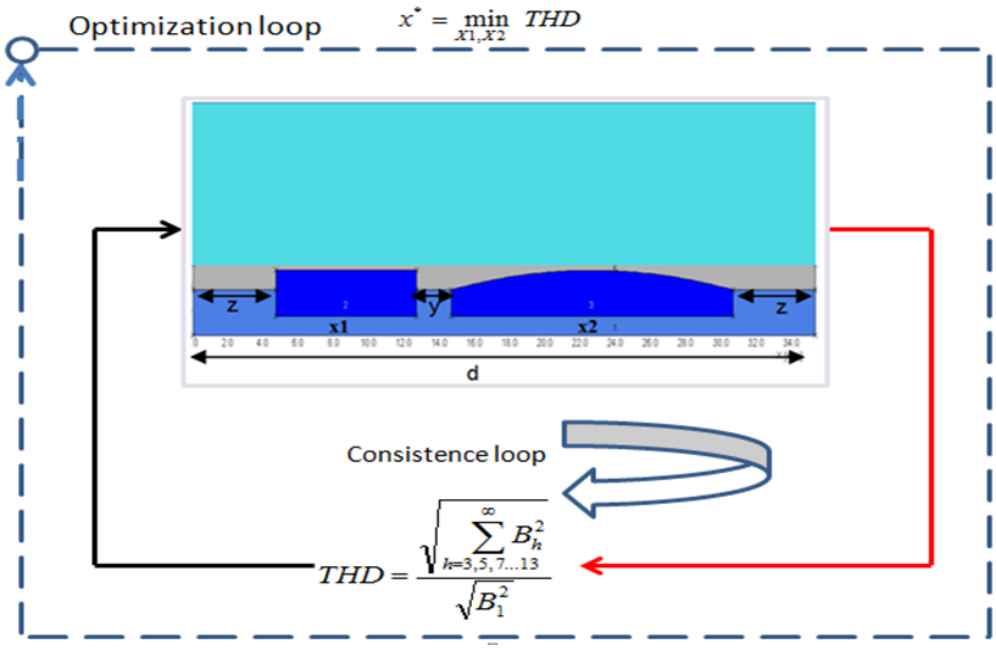

Fig. 3.48. Mono-objective optimization problem.

3.5.2. Analytical model-based optimization

In order to reduce the space harmonics of the airgap flux density an analytical model is also developed [9], as a computation time-saving option.

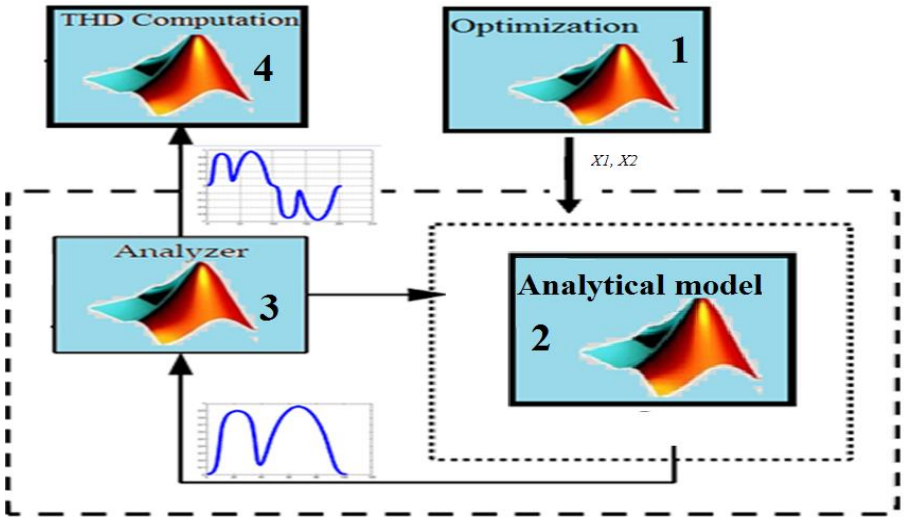

Fig. 3.49. Optimization process using analytical model.

In Fig. 3.49, the coupling of the SQP optimization algorithm and the analytical model of AFIPM machine is outlined. The optimization process is similar to that based on the FE model. Hence, for checking the effectiveness of both models, their solutions are compared in terms of convergence (Fig. 3.50). It can be seen that for both models the convergence tendency for optimum solutions is quite the same. However, for high THD values, the FE model-based optimization is in advantage.

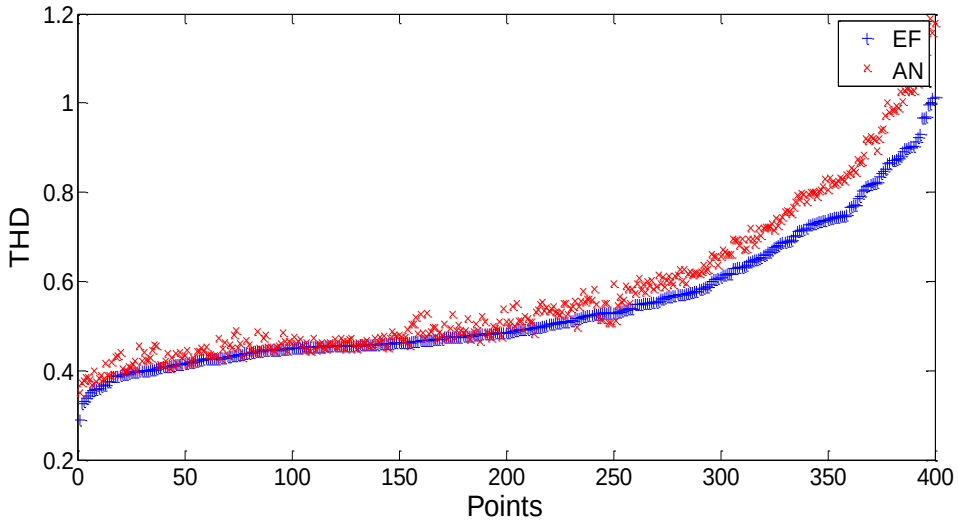

Fig. 3.50. Comparative convergence of FE model-based and analytical model-based optimization solutions.

3.6. Design optimization results

Mono-objective SQP optimization

SQP optimization technique has been applied to identify optimal rotor-PM design in order to reduce the THD of the airgap flux-density waveform. In Table 3.4, SQP optimization results are presented.

The length *X1* of the first rotor-pole PM is reduced to 2 mm and the length *X2* of the second rotor-pole PM is increased to 19 mm. The airgap flux density produced by both shape-optimized rotor-pole PMs is represented in Fig. 3.51. It can be pointed out that the THD is minimized to 0.27 value for the FE model, and to 0.33 value for the analytical model.

Table 3.4. SQP optimization results

Parameters	Rated values	Variation interval	Optimized values	Units
x1	8	2<x1<10	2	mm
x2	16	3<x2<19	19	mm
y	1.95	1.95	constant	mm
z	computed	computed	computed	mm
d	31.41	31.41	constant	mm
THD (FE model)	0.455	-	0.27	-
THD (analytical model)	0.453	-	0.33	-

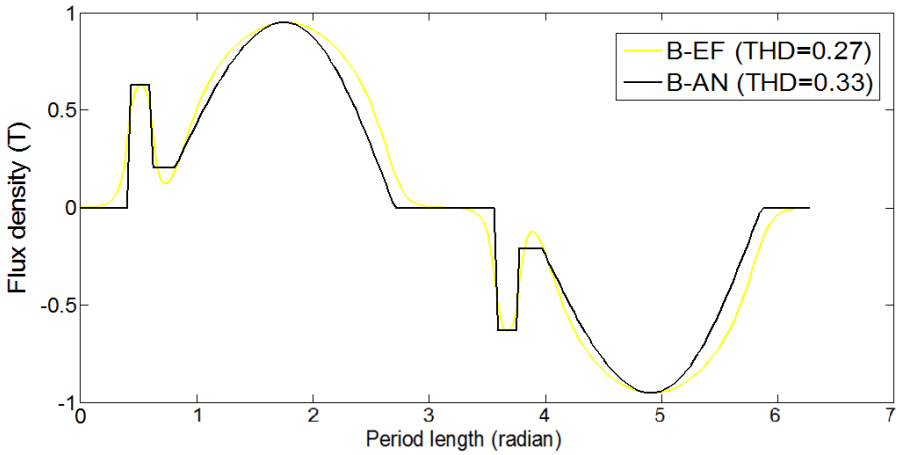

Fig. 3.51. SQP optimization results for the airgap flux density waveform of AFIPM machine by using FE model (B-EF) and analytical model (B-AN), respectively.

In Fig. 3.52, the space-harmonic spectrum of the airgap flux density is displayed as a result of the non-optimized design using FE model and analytical model, respectively, as well as of the SQP-optimization design also using FE model and analytical model, respectively. It is clearly noticeable that the first odd harmonics are succesfully reduced, as well as the THD by the rotor-PM shape design optimization of the AFIPM machine under study.

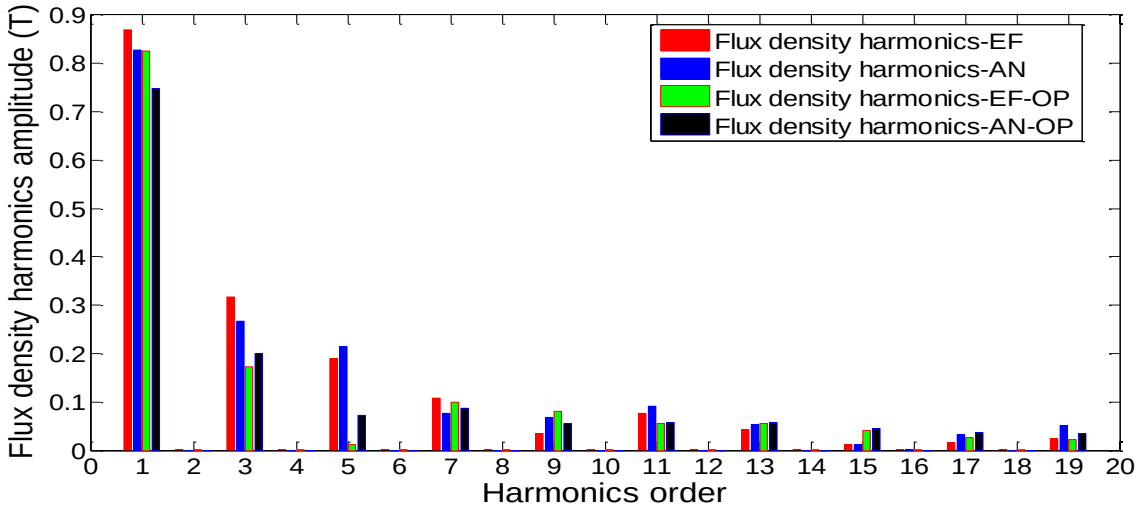

Fig. 3.52. Frequency spectrum of the airgap flux-density space harmonics as a result of the non-optimized design and SQP-optimization design (OP), respectively, both designs using FE model (EF) and analytical model (AN).

In Figs. 3.53 and 3.54, the influence of *X1* and *X2* geometric variables to the optimized THD is graphically represented for the FE model and the analytical model, respectively. It can be observed that the SQP optimization process for both FE and analytical models aims at reducing the length of the first rotor-pole PM and increasing the length of the second rotor-pole PM. Blue regions represent the good solutions, whereas red regions, the unusable solutions.

Bi-objective GA optimization

The purpose of this section is to achieve design optimization with the following two objectives:

- minimizing the THD of the airgap flux density waveform;
- minimizing the amplitude of odd space harmonics and maximizing the fundamental of the airgap flux density waveform.

The bi-objective function is thus defined by

$$F_{obj} = \begin{bmatrix} \sqrt{\sum_{h=3,5,7...13}^{\infty} B_h^2} = Numerator \\ \left(\sqrt{B_1^2}\right) = Deno\,min\,ator \end{bmatrix}, \qquad (3.8)$$

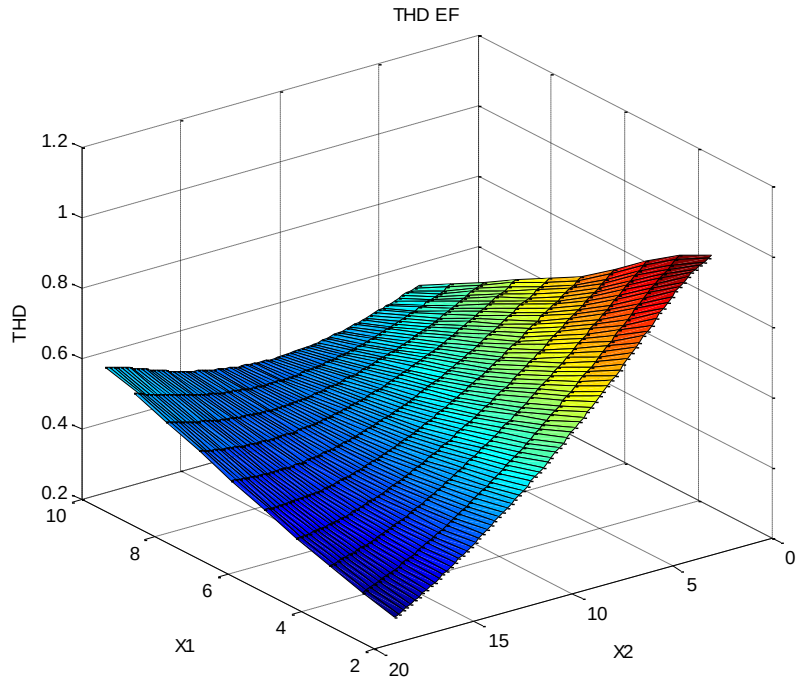

Fig. 3.53. Optimized THD representation as a function of *X*1 and *X*2 variables, for the FE model.

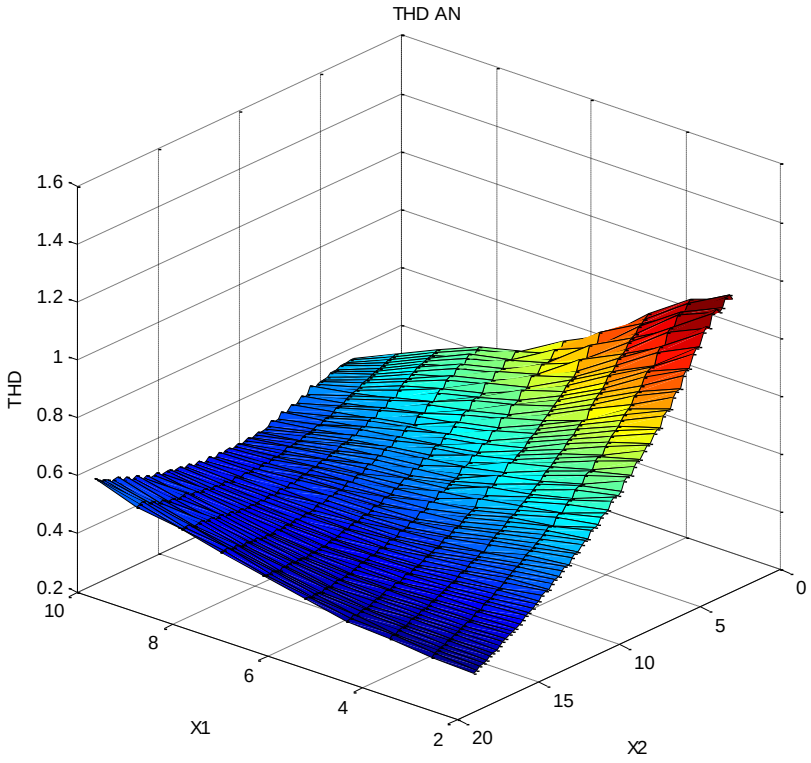

Fig. 3.54. Optimized THD representation as a function of *X*1 and *X*2 variables, for the analytical model.

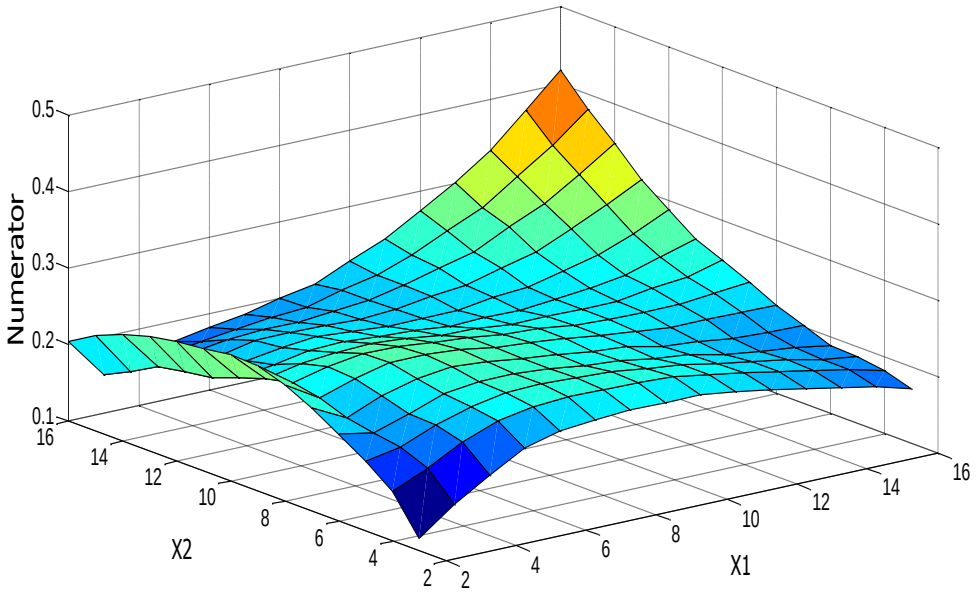

Fig. 3.55. Representation of bi-objective function *Numerator* vs. rotor-PM lengths *X*1 and *X*2.

where *Numerator* is represented as a function of rotor-PM length in Fig. 3.55.

With this in view, bi-objective GA optimization of the rotor-PM shape using the FE model of AFIPM machine is proposed and lunched for the geometrical variables specified in Table 3.5.

Table 3.5. Geometric variables for GA optimization of rotor-PM design

Geometric variables	Rated values	Variation interval	Units	
x1	8	2<x1<16	mm	First magnet length
x2	16	2.99<x2<16	mm	Second magnet length
y	1.95	1.95	mm	Distance between magnets
z	-	-	mm	Left and right extremities of the rotor pole
d	33.34	33.34	mm	Length of one rotor-pole

GA design optimization results are displayed in Fig. 3.56, where the 3D Pareto front for the bi-objective optimization problem is emphasized. The dots marked with (blue) circles are Pareto solutions, while the (red) stars are the tested points. It can be seen that the extreme Pareto front intersection provides a relative solution for the two

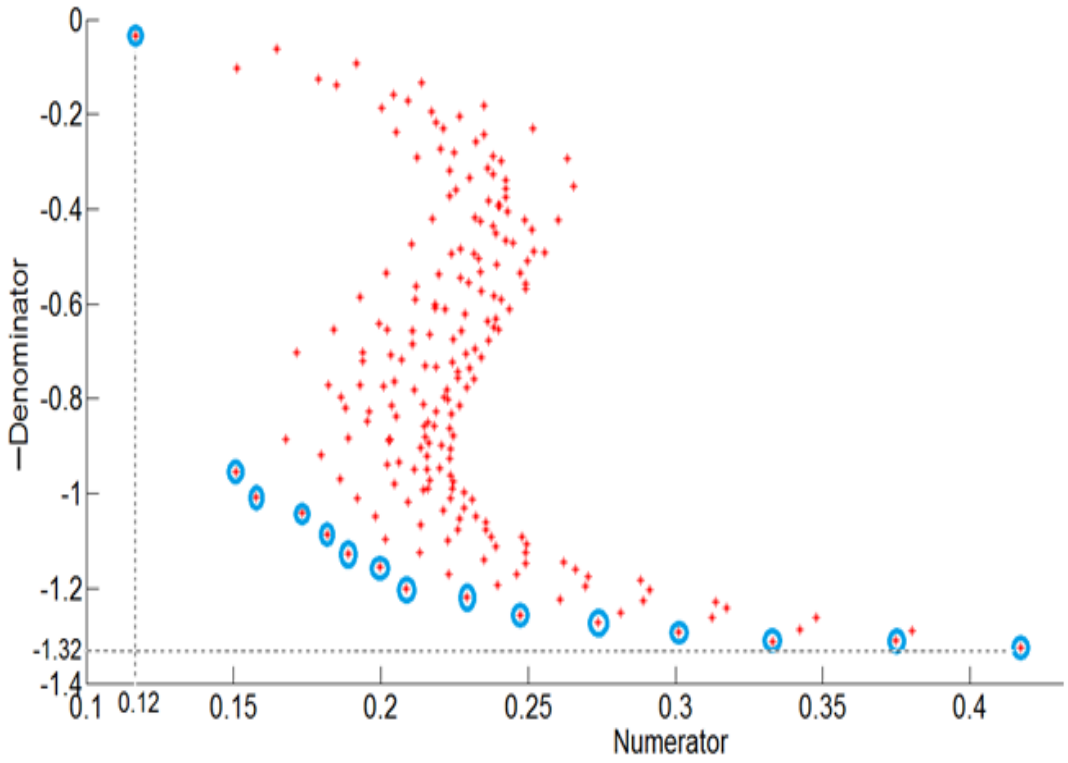

Fig. 3.56. 3D Pareto front for the considered bi-objective GA optimization problem.

search objectives of the GA optimization, i.e. the *Numerator* is reduced to 0.12, while the *Denominator* is increased to 1.32.

3.7. Conclusions

In order to solve the problem of modeling and design optimization of the small prototype AFIPM machine, axial-to-radial FE transformation has been proposed and used. A special analytical method for back-emf computation has been provided. FE field models have been developed in order to predict the AFIPM machine airgap flux-density distribution. FE-computed and analytical results for the open-circuit (no-load) back-emf have been compared providing full consistency.

The reduction of the space harmonic content of the airgap flux density waveform by rotor-PM shape optimization has been proposed and applied to the small AFIPM machine prototype under study. The analytical model was developed in order to have

quick insight on the flux density distribution, and thus to compare the obtained results with the FE model results.

Mono-objective SQP optimization and bi-objective GA optimization techniques have been developed and successfully applied to rotor-PM design for reducing low odd-order harmonics and increasing the fundamental of airgap flux-density and back-emf waveforms of the small AFIPM machine under study.

Selected references

[1] http://www.math.uh.edu/~rohop/fall_06/Chapter4.pdf

[2] J. Dreo, A. Pe, P. Siarry, and E. Taillard. Metaheuristics for Hard Optimization Methods and Case Studies. Springer Verlag, 2006.

[3] Z. Michalewicz, *Genetic algorithms + data structures = evolution programs*, Springer, London, UK, 3rd edition, 1996.

[4] S. Kreuawan, *Modelling and optimal design in railway applications*, Ph.D. Thesis, Ecole Centrale de Lille, France, 2011.

[5] http://www.cobham.com/about-cobham/aerospace-and-security/abouts/antenna systems/kidlington.aspx

[6] http://www.jmag-international.com/products/studio_designer/index_studio.html

[7] http://www.mathworks.com/products/matlab/

[8] http://www.solidworks.com/

[9] A. Egea *et al*., "Analytic model of axial flux permanent magnet machines considering spatial harmonics", *Proc. International Symposium on Power Electronics, Electrical Drives, Automation and Motion – SPEEDAM,* 2010.

[10] **A.A. Pop**, F. Gillon, M.M. Radulescu, "Modelling and permanent-magnet shape optimization of an axial-flux machine", *Proc. XXth International Conference Electrical Machines - ICEM2012,* pp.357-363 (included in IEEE Xplore database).

[11] **A.A. Pop**, F. Gillon, M.M. Radulescu, "Space harmonics modeling of an axial-flux permanent-magnet machine", *Proc. Conférence Européenne sur les Méthodes Numériques en Electromagnétisme – NUMELEC 2012*, Marseille, France, CD-ROM.

4. Experimental characterization and basic control of the small brushless AFIPM machine prototype

4.1. Experimental characterization of the small AFIPM machine

A comparison between FE-computed flux-related values and the experimental ones is provided. Hence, no-load tests were performed under open-circuit (generator-mode) conditions using the DC machine drive as a prime mover Fig. 4.1. The no-load test was done to experimentally evaluate the back-emf, and to measure the armature-winding resistance and inductance.

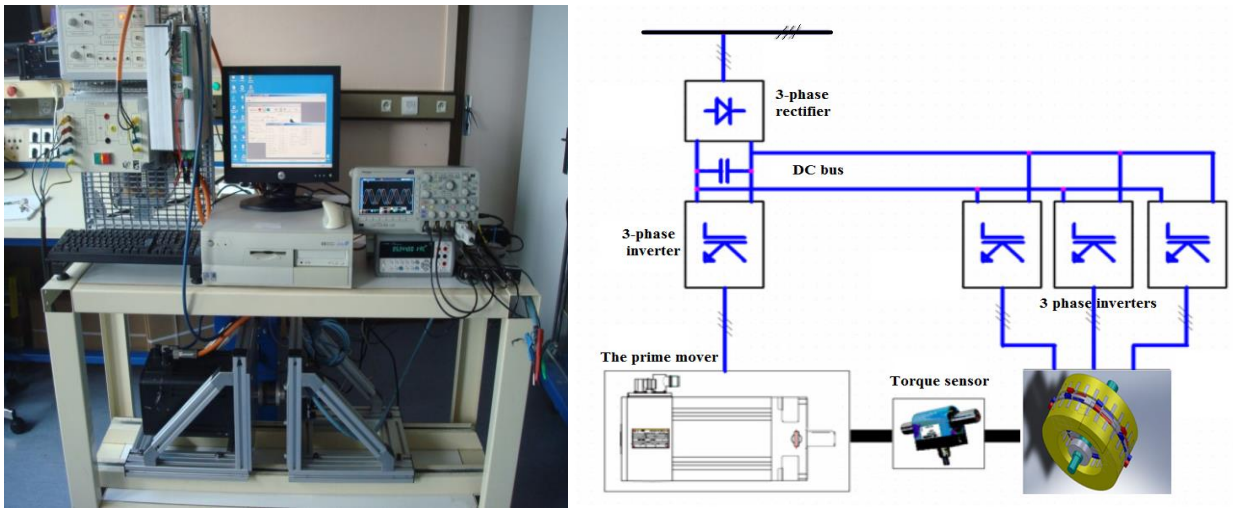

Fig. 4.1. Experimental set-up.

The back-emf measurements were carried out for a rated speed of 1500 [rpm]. The voltage measurements are made with the high-precision voltage oscilloscope probe. The test results captured on the oscilloscope are presented in Fig.4.2. It can be seen that there are three-phase winding back-emf measurements. For this test, at 1500 rpm, with the machine turning in generator mode, the value of back-emf is approximately 4.5 V/phase.

The open-circuit (no-load) stator-phase back-emfs, for clockwise and counter-clockwise rotation, are displayed in Figs. 4.3 and 4.4, respectively. It can be seen that the back-emf waveform shape changes in function of rotation sense. In the case of the

machine operating in generator mode and clockwise rotation, the top of the waveform is orientated to the left. For the case where the machine is in counter-clockwise rotation, the top of the waveform is orientated to the right.

Both back-emf waveforms are comparatively shown in Fig. 4.5. Both tests are in good agreement. The difference between them consists only on the machine rotation sense. In its turn, the FE-computed stator-phase back-emf (using Opera-2D software) is presented in Fig. 4.6.

In order to compare experimental results with FE simulation results, both back-emf waveforms are superposed in Fig. 4.7, providing good agreement [4].The tests were performed with the machine turning in clockwise direction.

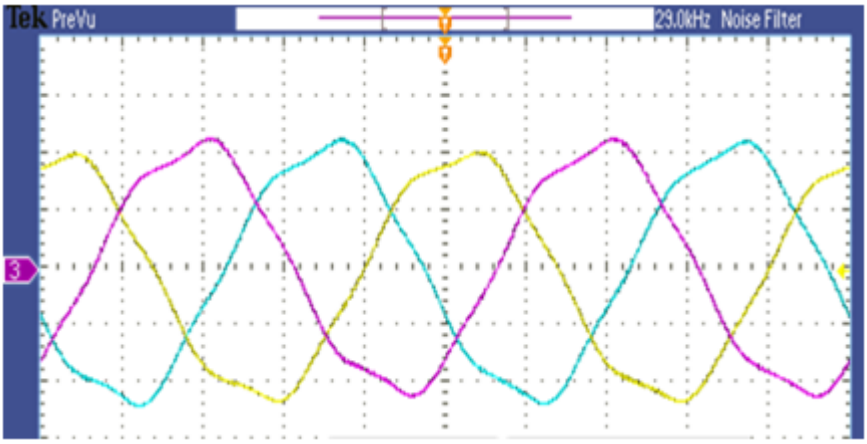

Fig. 4.2. Experimental open-circuit (no-load) back-emf waveforms of the three armature-phases.

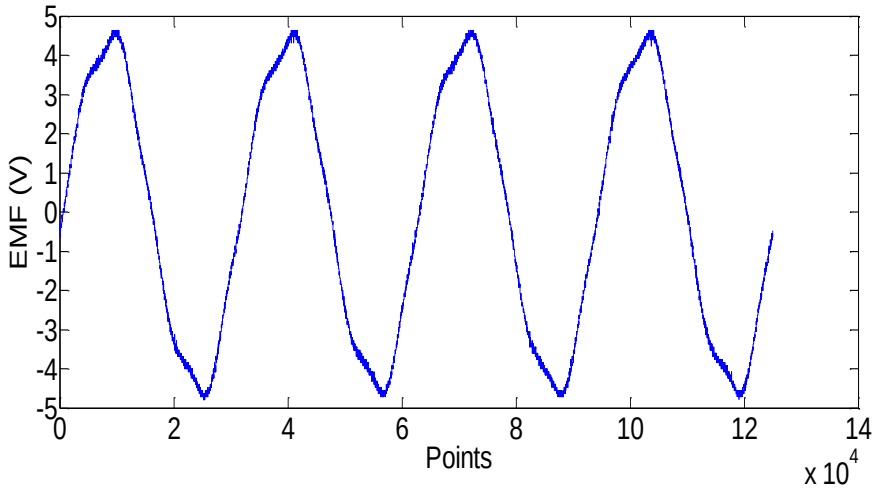

Fig. 4.3. Experimental open-circuit (no-load) stator-phase back-emf for clockwise rotation.

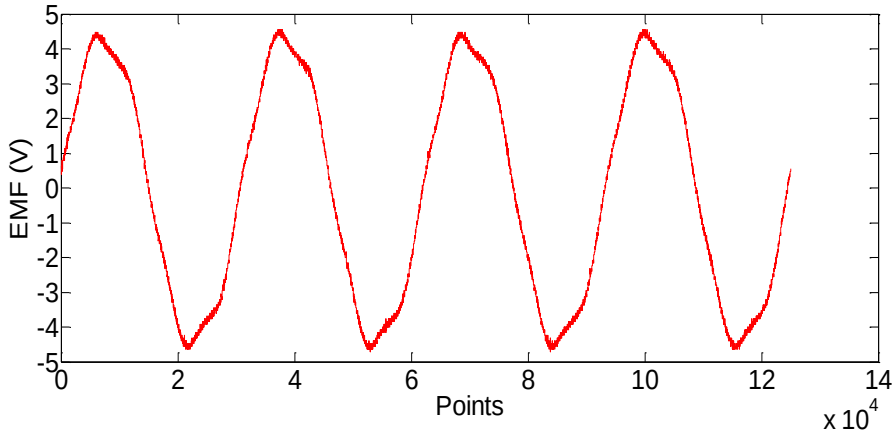

Fig. 4.4. Experimental open-circuit (no-load) stator-phase back-emf for counter-clockwise rotation.

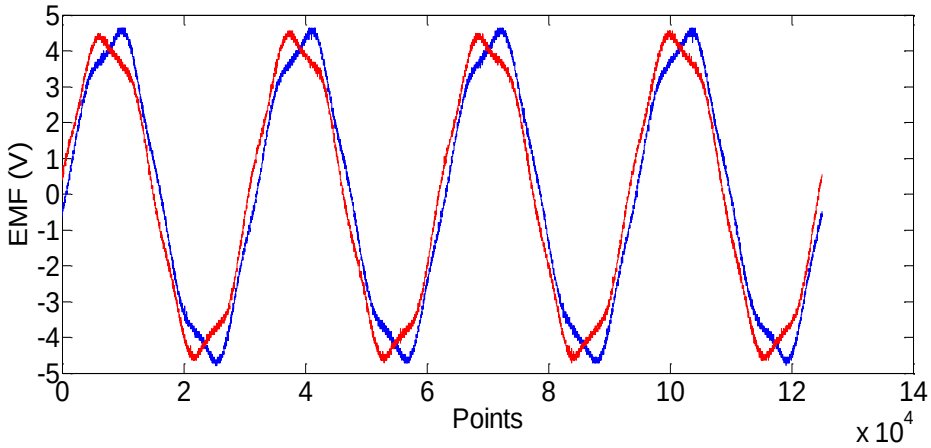

Fig. 4.5. Comparative experimental open-circuit (no-load) back-emfs for clockwise and counter-clockwise rotation.

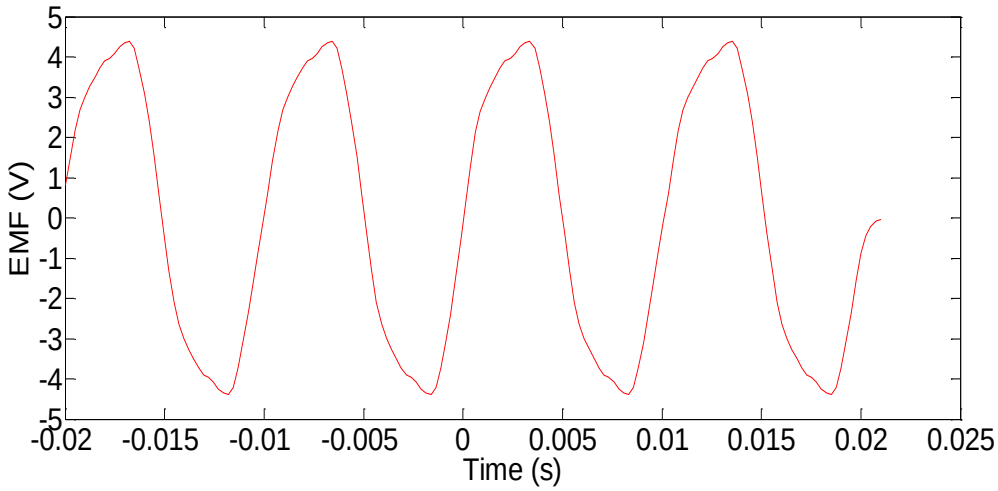

Fig. 4.6. FE-computed open-circuit (no-load) phase back-emf..

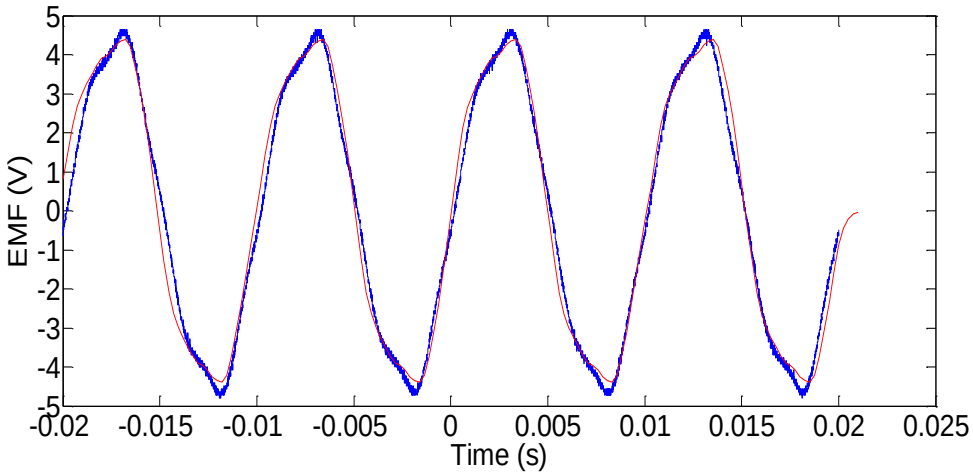

Fig. 4.7. Experimental vs. FE-computed back-emfs under open-circuit (no-load) condition.

In order to find the connection between the speed and the back-emf value there was made several measurements. The rotor speed vs. back-emf characteristic is linear, as attested by Fig. 4.8. The electromotive force obtained in this figure is multiplied with $\sqrt{3}$ in order to obtain the composed electromotive force. The coefficient which enables to find the relation between the speed and electromotive force is now performed. The value of this coefficient is 0.0021. If we multiply the speed with this coefficient we obtain the value of electromotive force. The computation gives us the certitude of good measurements.

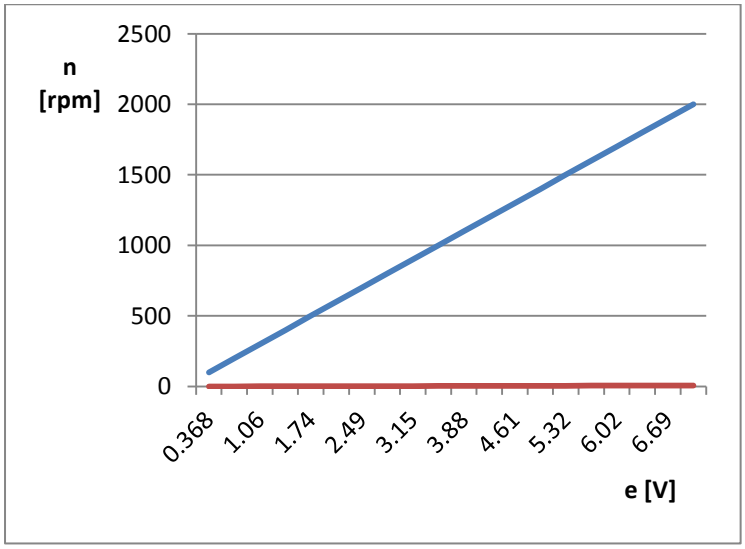

N (tr /min)	F (Hz)	$E(V)$
500	33.21	1.03
1000	66.46	2.05
1500	99.77	3.15
2000	132.9	4.30

Fig. 4.8. Rotor speed vs. back-emf.

Different measurements were also made in order to characterize the small AFIPM machine prototype under study.

1) Resistance measurements

Current (A)	Voltage(V)	Resistance calculated (Ω)
2	0.12	0.06
5	0.302	0.0604
7	0.428	0.06114

3) Inductance measurements

	Unit	Value	Value	Value	Value
*U*1 (rms)	V	133,8 mV	281,8 mV	0,41 V	0,55 V
*I*1 (rms)	A	2.07 A	4.34 A	6.37 A	8.65
*P*1	W	276.93 mW	1200 mW	2.61 W	4.62 V
*S*1	VA	0.28 VA	1.22 VA	2.67 VA	5.44 V
*Q*1	VAR	0.05 Var	0.23 Var	0.52 Var	0.97 Var
λ	ind	0.98	0.98	0.98	0.98
L (computed)	H	3.71^{e}-5	3.88^{e}-5	4.08^{e}-5	4.12^{e}-5

4) Electromagnetic torque measurements

In order to perform the dynamic tests, an experimental set-up has been assembled. A conventional three-phase synchronous machine is used to drive the small AFIPM machine prototype. Both machines are directly coupled on the same shaft, and torque sensor is used to measure the electromagnetic torque. The driving machine is fed from a three-phase AC-DC-AC converter. The test is made with the prototype operating in generator mode with a preset resistive load (Fig. 4.9). With the prime mover at 1500 [rpm], one obtains the current of 29.89 [A/phase]. For this speed one finds that the torque has approximately the value of 2 Nm (Fig. 4.10).

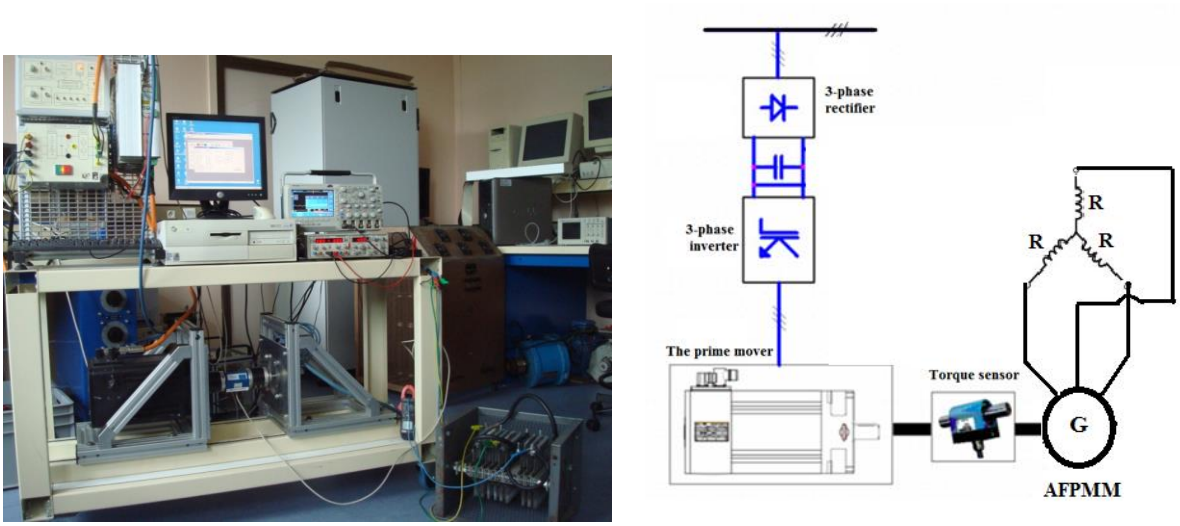

Fig. 4.9. The test bench for the small AFIPM machine in generator mode with resistive load.

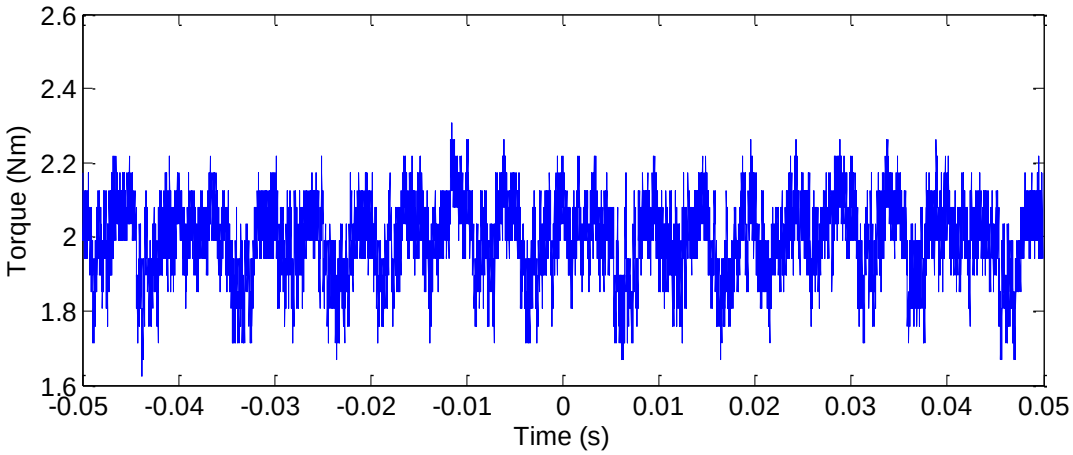

Fig. 4.10. Torque measurements for the small AFIPM machine in generator mode with resistive load.

4.2. Electronic commutation and basic control of the small AFIPM machine

The power electronic converter supplying the small AFIPM machine consists of a three-phase full-bridge voltage-source inverter with six commutation modules (each represented by an IGBT (or MOSFET) associated with an antiparallel freewheeling diode) connected to a DC source through a DC-link circuit. In its turn, the basic-electronic-control part has the proper duty of commutation logic suitable to decode the rotor-position feedback signals into the inverter switching pattern.

Each stator-phase current is fed by direct means of one inverter leg, so that current commutations are synchronized with appropriate rotor positions; this enables the coupling of both electronic switching and position-sensing functions, which are carried out in distinct subsystems of the brushless AFIPM machine. The 120-electrical degree block-commutation pattern is considered here, meaning that each of the six inverter power switches conducts stator-armature phase current for one-third (i.e. 120 electrical degrees) of an electrical cycle. The small AFIPM machine can be operated in two modes by 120-electrical-degree block-commutation pattern: with or without armature-current regulation.

In the AFIPM machine operation by *120-electrical-degree block-commutation pattern without armature-current regulation* [1, 2], each electrical cycle of 360 electrical degrees can be divided into six sectors of 60 electrical degrees in accordance with the position information provided by Hall sensors, resolvers or optical encoders. Here, the Baumer incremental encoder BHK 16 (Appendix 5) is used (Fig.4.11).

Fig. 4.11. Incremental encoder mounted on the small AFIPM machine rotor-shaft.

In its turn, each sector of 60 electrical degrees can be sub-divided into two intervals: (i) a commutation interval, when current flows in all three armature phases, followed by (ii) a conduction interval, when two armature phases are energized, the third one being disconnected (also referred to as being inactive or idle).

The stator-armature mmf, produced by the currents of two series-connected armature phases, jumps forward 60 electrical degrees, every time when an inverter-commutation order is driven by the rotor-position sensors for energizing a pair of armature-winding phases. The electromagnetic torque is developed by the tendency of

reducing the angular displacement between the positions of the armature mmf and of the PM-rotor mmf, respectively, so that the rotor is forced into a continuous rotational motion for aligning the two mmfs. At the next switching instant, at which the rotor gets to within 60 electrical degrees of being aligned, the armature mmf moves again forward 60 electrical degrees in a discrete fashion. This, in turn, maximizes to 120 electrical degrees the angular displacement between armature and rotor mmfs, thus increasing the torque. The process of rotor motion towards aligned position is repeated by keeping this mmf angular displacement at an average value of 90 electrical degrees. Hence, a pulsating torque profile vs. angular rotor position results.

For AFIPM machine operation by *120-electrical-degree block-commutation pattern with armature-current regulation* [3, 4], the actual phase currents are sensed and compared to their rectangular-current references using three independent phase hysteresis comparators. The inverter power-switches are driven directly by the hysteresis-comparator output signals, so that armature-phase currents exhibit a quasi-square waveform, being forced to follow their references within the hysteresis band. Armature-current regulation by phase hysteresis comparators is commonly used because of its simple implementation and fast dynamic response in transient states.

During the commutation interval, the hysteresis-current-regulated inverter-fed AFIPM machine operation is quite similar to that for unregulated armature current.

On the contrary, during the subsequent conduction interval of the electrical cycle, the hysteresis-current-regulated AFIPM machine operation is different from that for unregulated armature current. According to machine operation by 120-electrical-degree block-commutation pattern with armature-current regulation, each inverter power switch is conducting for two consecutive 60-electrical-degree sectors per electrical cycle.

4.3. Description of the experimental hardware and software

The inverter topology has an important influence on the choice of the electronic commutation and control scheme. The choice of inverter used to supply the small AFIPM machine is influenced by technical and economic constraints imposed by the application. The inverter used for experimental tests here is an SEMITEACH Semikron inverter -

IGBT 1.3 [kW] three-phase full-bridge (Fig.4.12). The maximum current supply of the bridge is 30 [A] for a voltage of 440 [V]. The six switches are accessible through six BNC ports. Three other ports BNC offer recovery of error signals originated from inverter. The supply of the inverter drivers is made in the range 0 ... 15V. The command signals of the six switches are in the range 0 ... 15V. Thus, a card processing domain signals, up to 15 [V], and protection against short-circuits is built to make the link between the experimental set-up and the inverter (Appendix 6). The card diagram is provided in Appendix 7.

The practical implementation of the commutation pattern and basic control scheme for the small AFIPM machine prototype is carried out using dSPACE 1104 platform (Fig. 4.13).

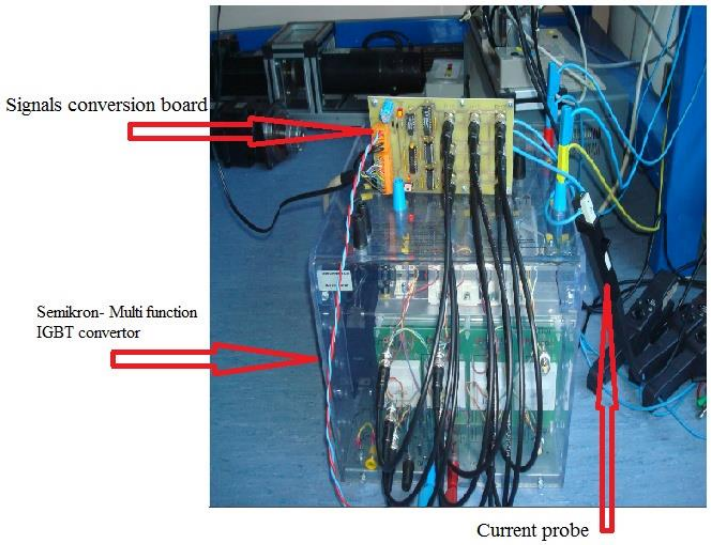

Fig. 4.12. Semiteach Semikron three-phase full-bridge inverter.

The experimental system dSPACE 1104 is used to interface the control program with the inputs / outputs of the motor-converter ensemble.

The integration of command software with the "hardware" components (the three-phase bridge inverter, the AFIPM machine and the incremental encoder) is done using two elements:

- The software implementation in real-time "Real-Time Interface RTI" that provides the blocks required to interface the dSpace system with developed MATLAB / Simulink programs. RTI library contains blocks of real-time communication.

- experimentation and testing software "ControlDesk " which allows to manage the tests in real time.

The basic control scheme is implemented in MATLAB / Simulink using the information provided by the incremental encoder via the RTI blocks acquisition. Starting from the rotor position the control strategy is applied and the six states of the switches of the three phase bridge inverter are obtained. These blocks replace the system models

Fig. 4.13. dSPACE 1104 platform.

to build the HIL (Hardware-in-loop) programs. dSPACE Card receives incremental encoder signals and sends the control signals to the six commutators of the inverter. The error signals of the three arms of the inverter are recovered to integrate the protection of the inverter in the control program.

Values of the DC-link and phase currents and voltages are recorded by the ADC communication ports.

The test bench also consists of (Fig.4.14):

- Tektronix DPO2014 digital oscilloscope with 5 channels of acquisition. The oscilloscope is used with three voltage probes and three current probes
- Two multimeters Agilent 34405A
- power source
- computer with Matlab / Simulink 6.5, the RTI library and experiments management software ControlDesk.

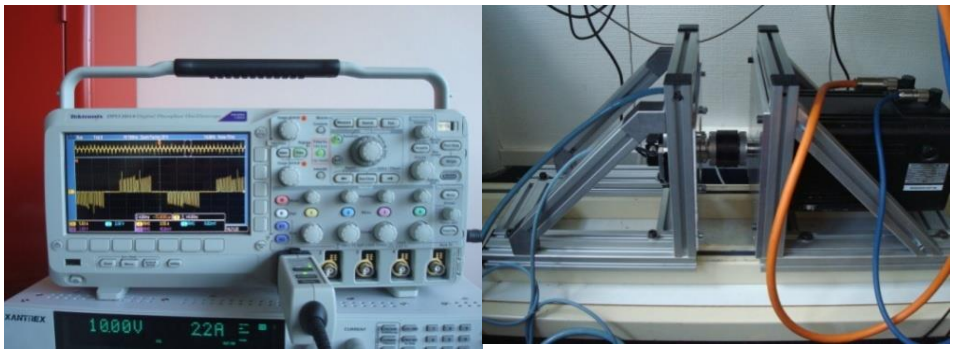

(a) *(b)*

Fig. 4.14. (a) Digital oscilloscope; (b) test bench with the small AFIPM machine prototype.

The simulation integration step is fixed and equal to 1e-4 seconds and the (Runge - Kutta) solver is used. This configuration allows real time program execution on the used dSPACE system.

The main program can be divided into four major subparts:

- recovery of the inverter error signals ("Inverter error")
- management of motor starting up phase ("Start")
- management of the motor dynamic operation phase ("Run")
- transformation of command technique in to signal for the inverter ("Command")

In addition to these four major parts, in the main program (Fig.4.15) one finds the RTI blocks for the inputs controling on the dSPACE ADC ports for recording the measured voltages and currents (DS1104ADC_C5 and _C6).

The signals are multiplied with the multiplication coefficients of the used probes. "Master switch" variable, whose default value is zero, controls the operating status of the system.

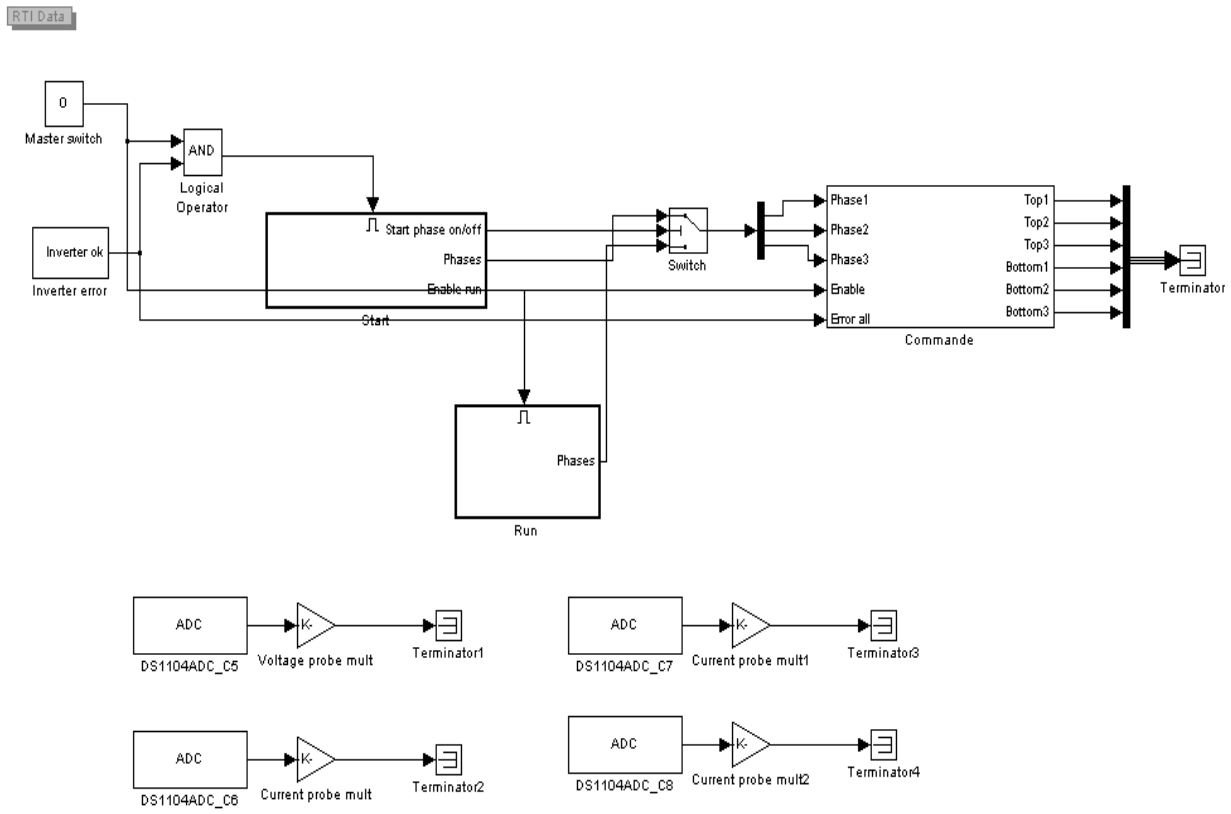

Fig. 4.15. Main program implementation.

The error signals are sent initially to the protection card. The interest for the error block is to inform the experimentation environment if an error exists on the inverter arm in order to stop the control program. The starting up motor subprogram (Fig.4.16.) has the objective of fixing the rotor into a certain position considered position 0. The sub-program "Enabled" meaning that it will be executed only when the main program allows. The sub-program has three outputs:

- "Start phase on / off" - signaling the state of the starting up phase and may have a value of 0 or 1.
- "Enable run" - signal for starting the dynamic operation phase at the end of the starting up phase
- "Phases" - the alimentation status of the three phases during the starting up phase

The sub-program mesure 300 iteration step when the starting up phase is active. During this period, phase 1 and phase 3 are supplied to set the rotor in certain position.

By the end of this period, the rotor position is initialized to zero (using the block "Rotor position reset") to give a reference point for switching technology at the stage of dynamic operation phase. Also, the variable "Enable run" becomes equal to 1 and the sub-program "Run" continues with the switching technique.

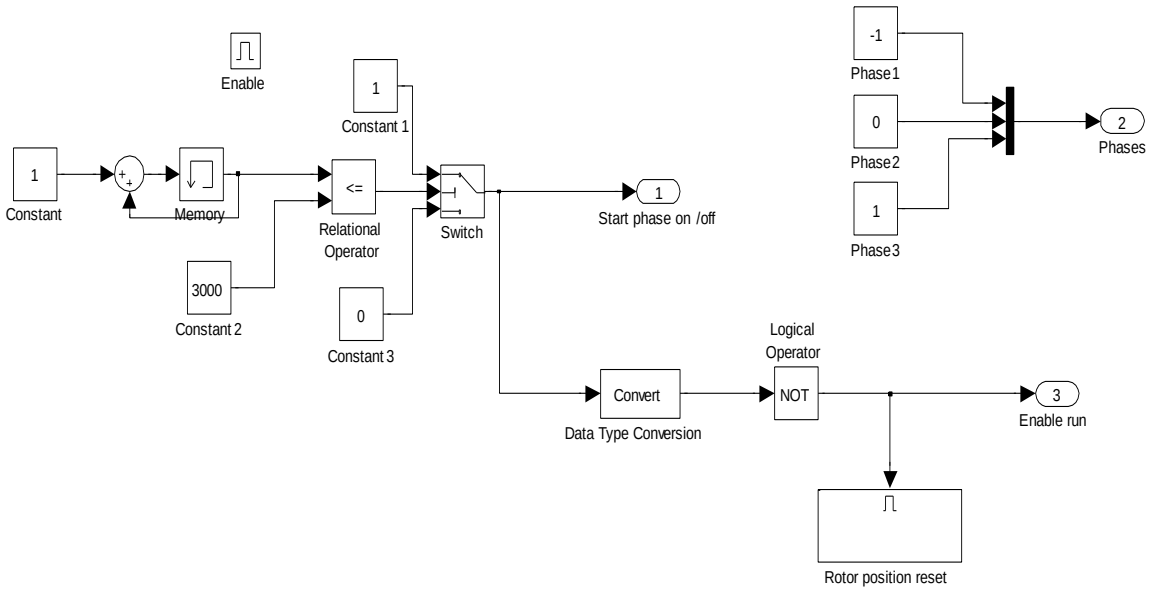

Fig. 4.16. "Start" sub-program

The sub-program "Start" is active only during the first 300 times iteration from the beginning of the execution of simulation. The sub-program motor control during the dynamic operation phase "Run" is shown in Fig. 4.17.

It is an "enabled" program type which starts when the start-up phase is over. It includes three sub-programs:

"Encoder" - is the component designed to manage the communication interface with the incremental encoder through the RTI blocks (Fig.4.18.). Thus, the block is DS1104ENC_POS_C1 make the interpretation of the pulses provided by the encoder. Those signals are multiplied with the specific resolution of the encoder (600 lines in this case) to obtain the position in degrees and the speed in rot / min. Also, the switching variable γ is integrated into this sub-program to gap the switching times with the number of degree specified by the optimization results. "EncoderMaster Setup" is a specific block in the RTI library used to define the parameters of the incremental encoder.

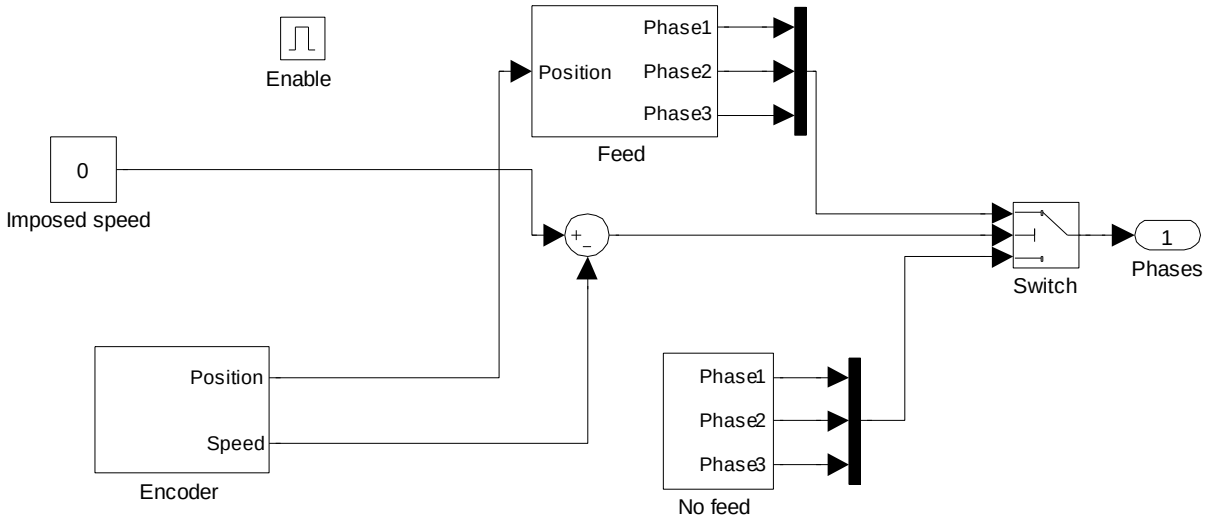

Fig. 4.17. "Run" sub-program.

"Feed" - is the sub-program designed to recover the supply status of the three phases starting from the real rotor position (Fig.4.19). Thus the program uses the table constructed before the experiment ("offline") containing the states of the three phases from 0 to 360 degrees. The domain is divided into 6 sections of 60 electrical degrees and the blocks of "pre-look-up" identifying the section where the rotor is located at a certain iteration step. This information is passed to the interpolation block with "pre-look-up" which provide the information for each stage of its supply status in the domain of {-1, 1, 0} which means that a power supply has negative polarity, positive or no supply, respectively.

"No feed" is the sub-program used to disconnect the power supply for all three phases if the rotor speed exceeds the speed imposed or the inverter signalizes an error. The alternation between phases of supply and non-supply("Feed" and "no feed") is given by the difference between the imposed speed ("Imposed speed") that can be varied in the simulation program, and the actual speed block identified by "Encoder " block. Finally, the position information is sent to the DAC output of the card dSPACE to be visualized on an analog format. The output of this subprogram is represented by the power supply status (positive, negative or zero) of the three phases of the inverter.

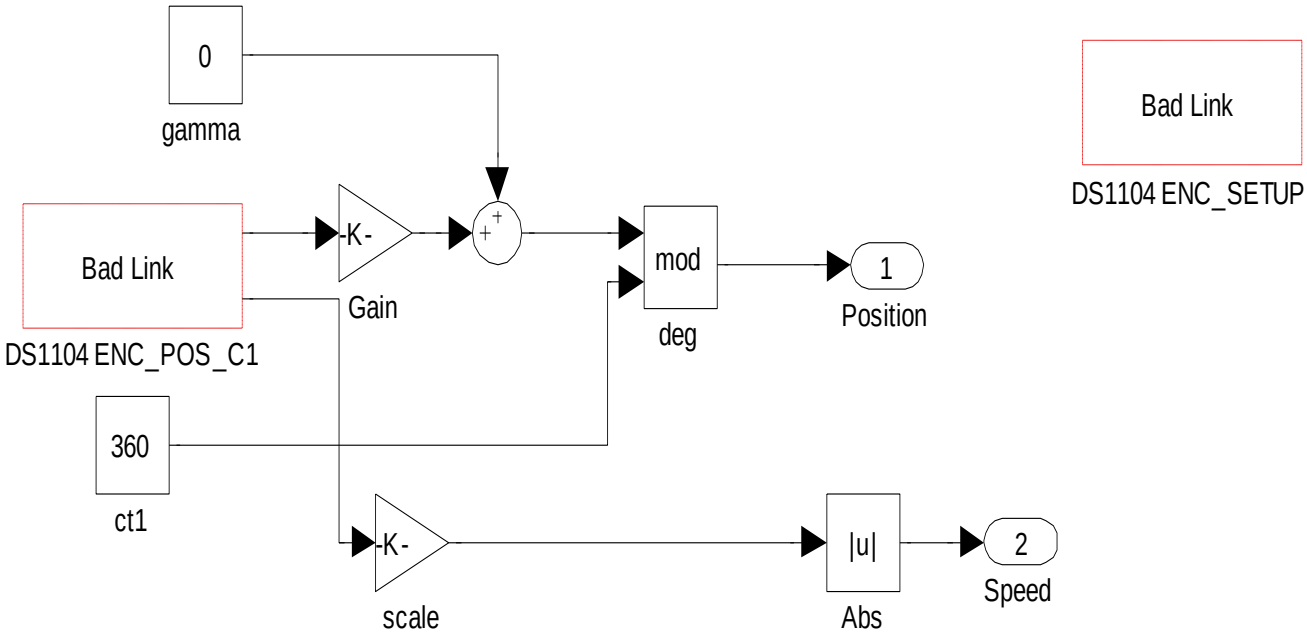

Fig. 4.18. " Encoder " subroutine

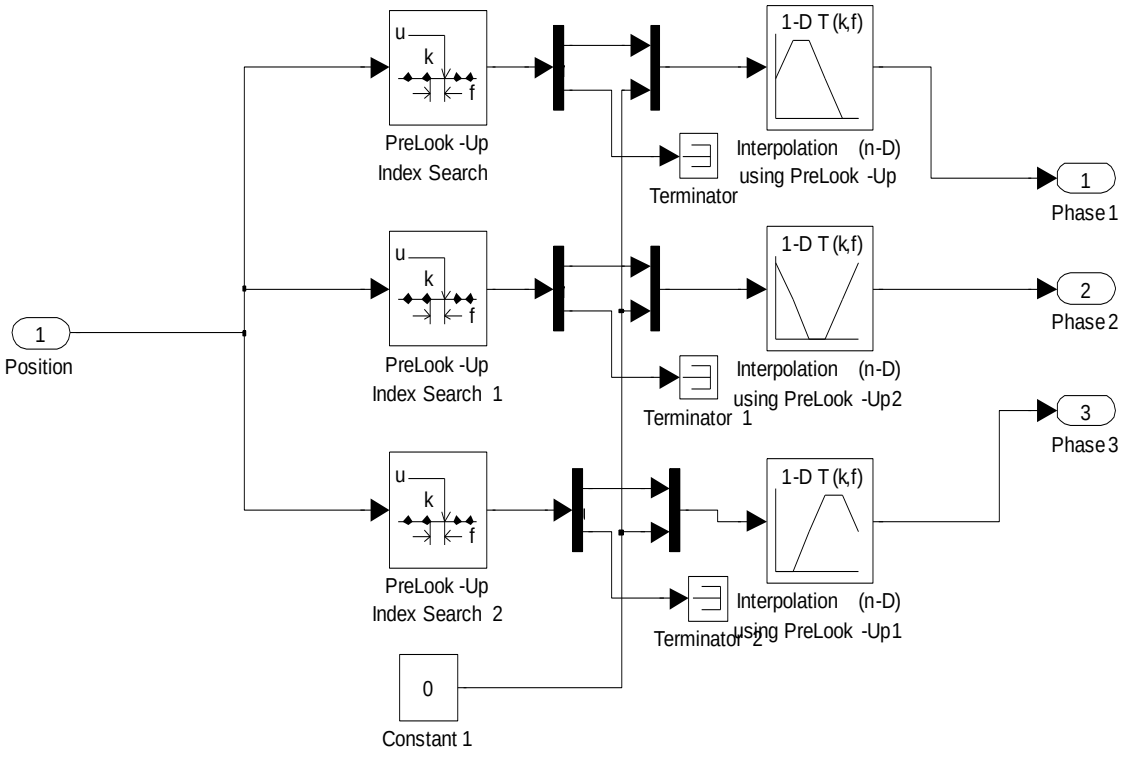

Fig. 4.19. "Feed" sub-program.

The subprogram "Commande" (Fig.4.20) uses the information about the alimentation status of the three phases (provided either by the starting up subprogram or by the dynamic operation subprograme) and sends the information in a binary format to the six switches of the inverter.

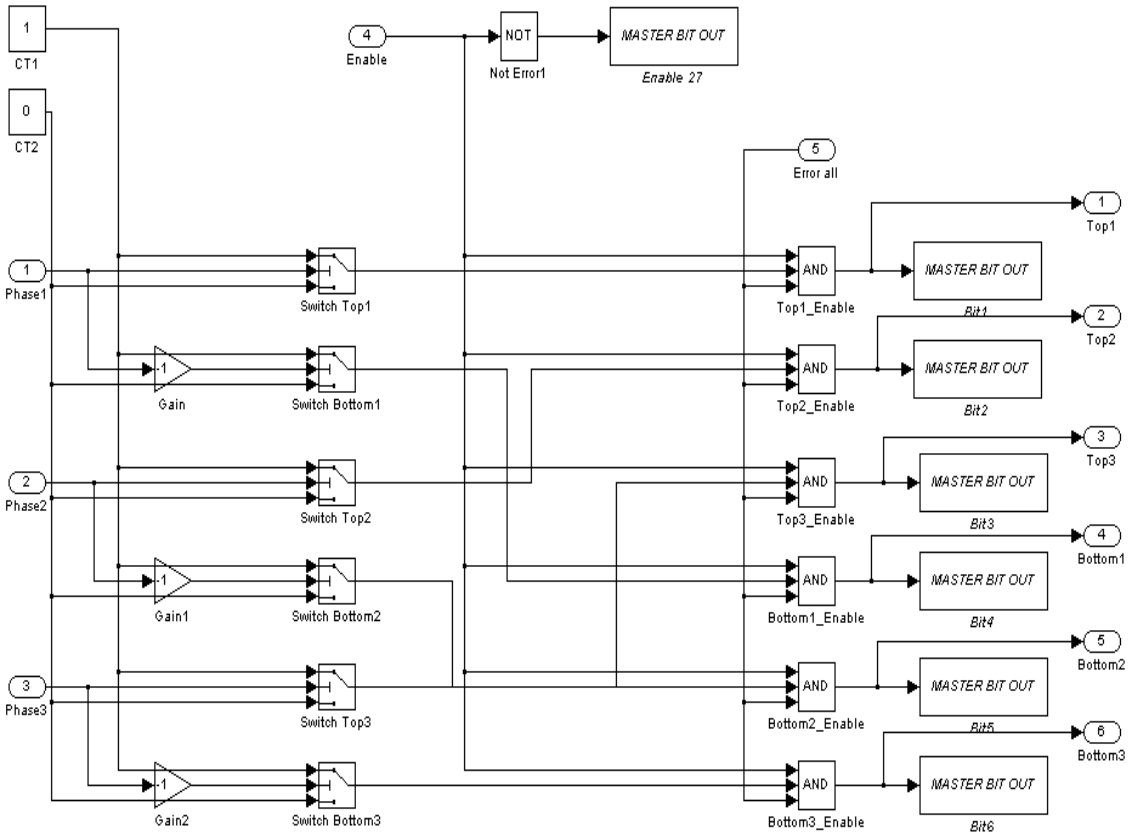

Fig. 4.20. "Commande" sub-program.

4.4. Experimental results

The digital controller (conduction-angle control) was implemented with the real-time interface system dSPACE. The dSPACE system assists research and development by interfacing powerful engineering software, MATLAB/SIMULINK, to external hardware such as electric motors or power electronic converters. Therefore, the controller was created in the SIMULINK platform. dSPACE was then used to control the operation of

the electric drive system via its Control Desk (Fig.4.21). Once all the components were designed and assembled, were interfaced to form the final experimental setup.

The software is organized in the experiment form of containing the program, the communication interface with the program ("layout") and the links between the different variables and interface components of the dSpace system.

The variables defined in the control program can be displayed and edited using the graphical interface. The variables changed in real time are:

- "Master switch" variable that allows starting and stopping of the engine control strategy. This variable can be set to 0 or 1.
- "Imposed speed" - controls the imposed speed of the motor. The speed variation is limited in the range [0 ... 3000 rpm].
- "Gamma" - defined the offset of the feeding strategy compared to the zero point. This variable is limited in the (mechanical) range [-5 ° ... 5 °].

  Additional variables are displayed in the experiment interface :

  - inverter error states
  - engine operation state.
  - the measured voltages and currents
  - the rotor position and speed

The tests were made for commanded speeds of 500 [rpm] (Fig.4.22.), 1000 [rpm] (Fig. 4.23.), 1500 [rpm] (Fig. 4.24.) and 2000 [rpm] (Fig. 4.25.), respectively. For the test made at 500 rpm the current have a value of 2.92A and the voltage 4V. At 1000 rpm the current absorbed by the machine is increased at a value of 4.19A and the voltage at 6V. In order to increase the speed at 1500 rpm the machine needs a current of 6.24A and a voltage of 6.24V. The dc current absorbed by the machine grows depending on speed.

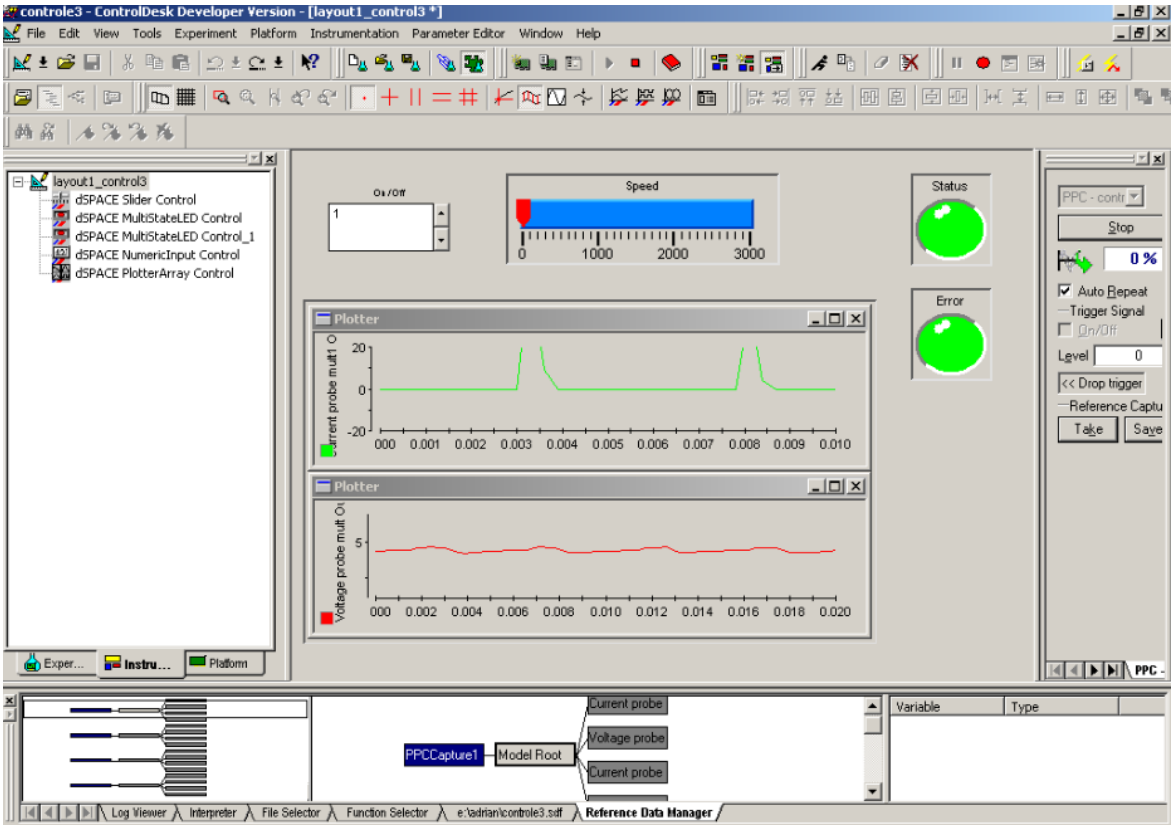

Fig. 4.21. Control desk program.

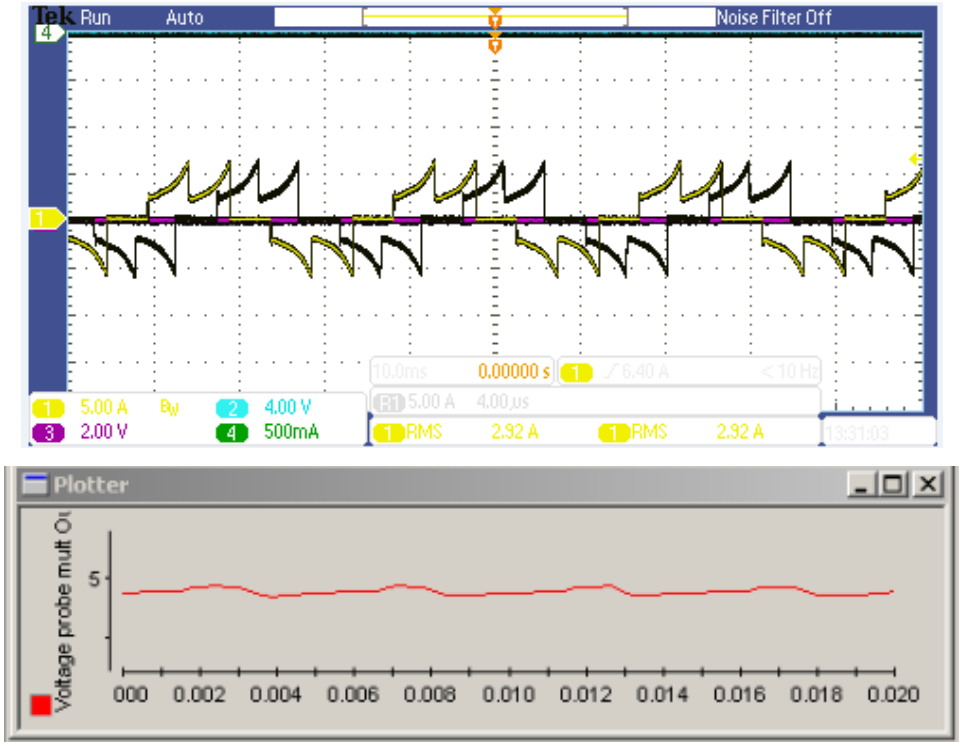

Fig. 4.22. Current and voltage results for 500 [rpm].

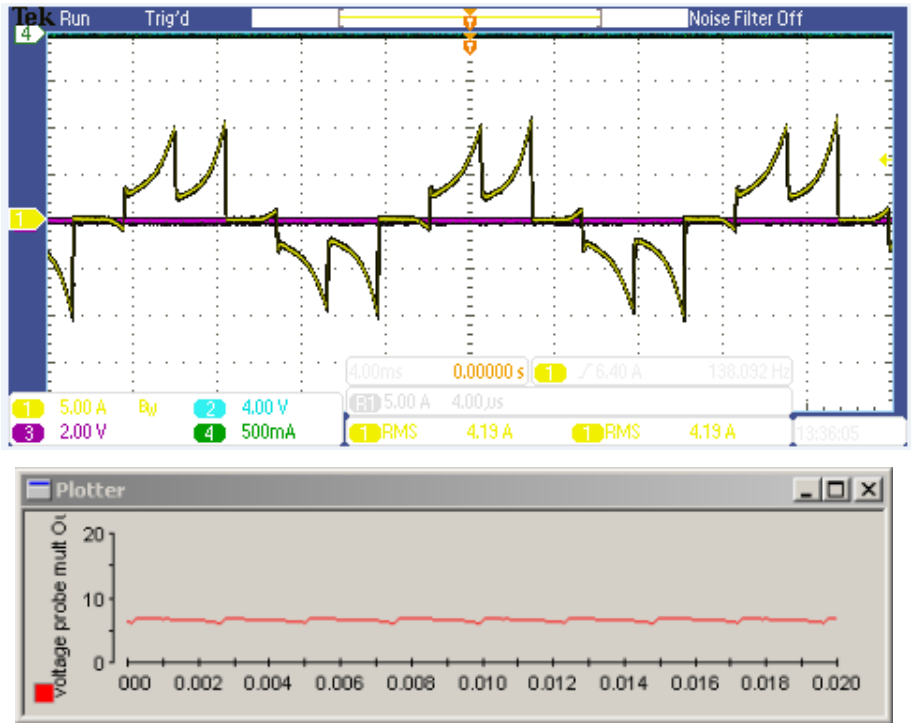

Fig. 4.23. Current and voltage results for 1000 [rpm].

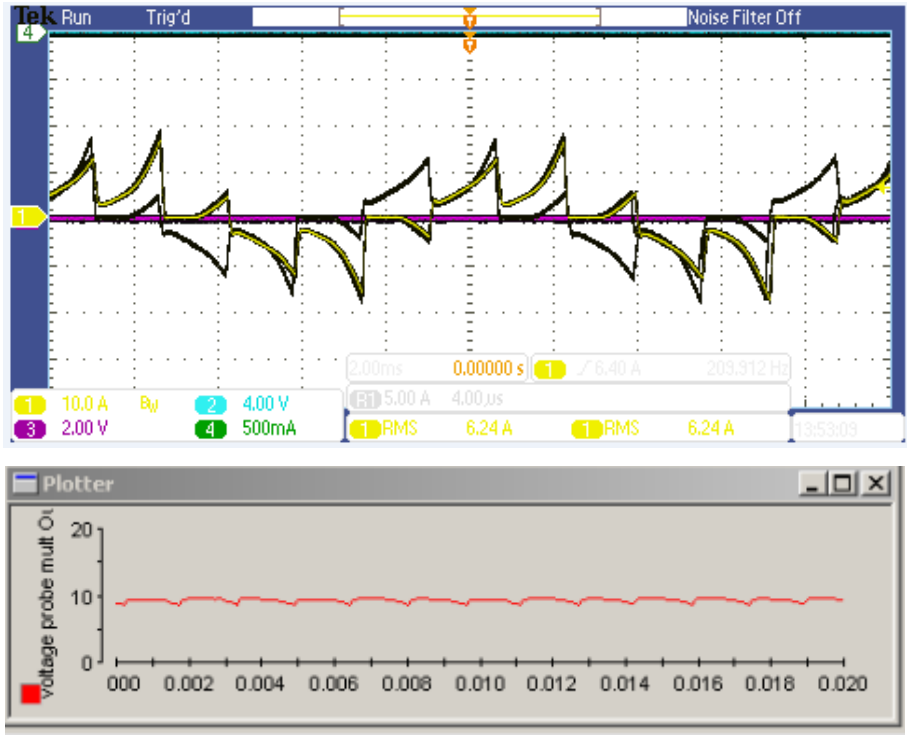

Fig. 4.24. Current and voltage results for 1500 [rpm].

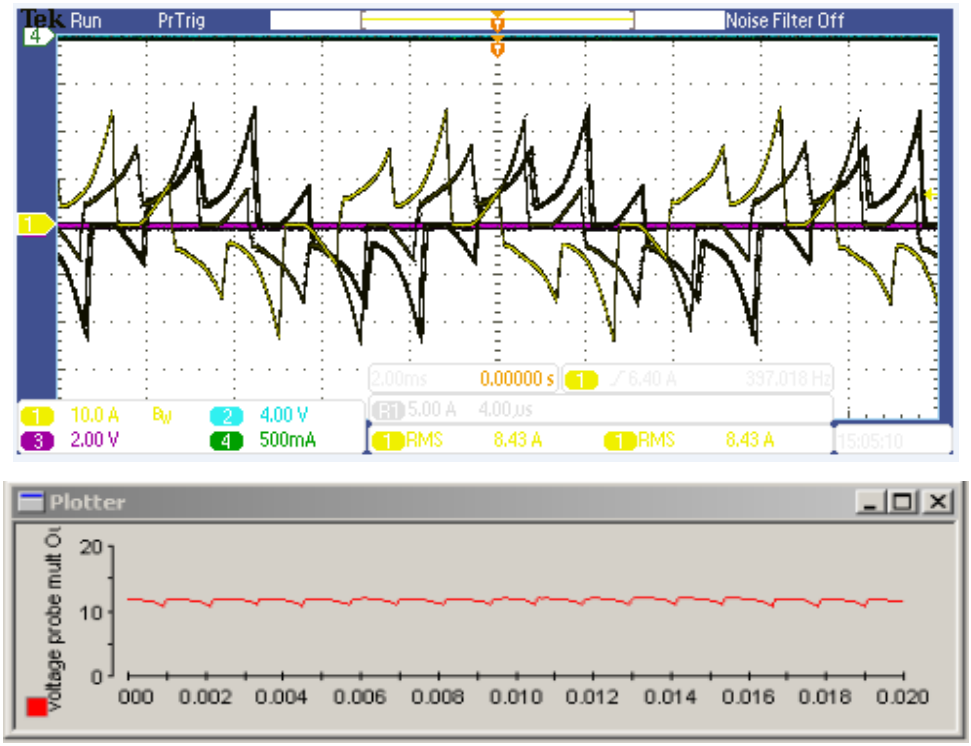

Fig. 4.25. Current and voltage results for 2000 [rpm].

4.5. Conclusions

In this chapter, the experimental study of the small AFIPM machine prototype has been carried out. A test bench comprising the small AFIMP machine prototype, the three-phase inverter and the electronic control components has purposely been built.

Firstly, the prototype AFIPM machine has been experimentally characterized. Then, electronic commutation pattern and basic control scheme for the inverter-fed AFIMP machine have been implemented. Lastly, extensive experiments on dSPACE 1104 platform have been performed in real-time for the AFIPM machine prototype from standstill up to 2000 [rpm] rotor speed.

Selected references

[1] J.F. Gieras, R.-J. Wang, M.J. Kamper, *Axial-flux permanent-magnet brushless machines*, 2nd Edition, Springer, The Netherlands, 2008, Ch. 7

[2] T.J. Sokira, W. Jaffe, *Brushless DC motors: electronic commutation and controls*, TAB Books Inc., USA, 1990.

[3] S.D. Sudhoff, P.C. Krause, Operation modes of the brushless DC motor with a 120º inverter, *IEEE Trans. Energy Convers*., Vol. 5 (1990), pp. 558–564.

[4] K.A. Corzine, S.D. Sudhoff, H.J. Hegner, Analysis of a current-regulated brushless DC drive, *IEEE Trans. Energy Convers*., Vol. 10 (1995), pp.438-445.

[5] M. Allan, I.J. Kemp, Commutation strategies for the DC brushless motor, *Proc. IEE Conf. Electr. Mach. Drives – EMD 1993*, London, UK, pp. 133-138.

[6] I. Lar, M.M. Radulescu, E. Ritchie, **A.A. Pop**, Current control methods for grid-side three-phase PWM voltage-source inverter in distributed generation systems, *Proc. 13th Int. Conf. Optimiz. Electr. Electron. Equipm. – OPTIM 2012*, Brasov, Romania, 2012 (Paper published in IEEE Xplore database).

[7] TMS320C240, TMS320F240 DSP controllers from Texas Instruments *http://www.ti.com/lit/an/bpra055/bpra055.pdf*

5. General conclusions

The main objectives of this thesis were (i) analytical preliminary design based on general AFPM machine sizing equations for the single-rotor-double-stator topology of a small three-phase AFIPM machine; (ii) development of 2D FE model for analysis and design optimization of the small three-phase AFIPM machine prototype in view of improving the electromagnetic torque quality by modifying shape and size of rotor-PMs; (iii) experimental characterization, validation of FE modeling and analysis, as well as implementation of electronic self-commutation and basic control of the small three-phase AFIPM machine prototype.

The major contributions brought by the author to the present research work are the following:

- design of a nonconventional disc-rotor topology with two different-shape PMs on each pole for the small AFIPM machine;
- analytical pre-dimensioning of the discoid electromechanical structure of AFIPM machines based on deriving power and torque density from the general sizing equation;
- 2D FE-based electromagnetic modeling of the small AFIPM machine prototype accounting for its nonconventional geometry, stator slotting and rotor movement;
- rotor-PM geometric optimization in view of minimizing the airgap flux-density space harmonics by using SQP and GA techniques;
- conceiving and building of a test bench for experimental characterization of the small three-phase AFIPM machine prototype and implementation on dSPACE platform of its electronic self-commutation and basic control scheme adapted to the full-bridge voltage-source inverter supply.

As future developments of the thesis research work, it is suggested

- to investigate the AFIPM machine behaviour in generating mode for small-scale distributed electric energy production with renewable sources;
- to address the multi-objective design optimization of AFIPM machine with nonconventional double-sided topology;

- to implement sensorless techniques for electronic self-commutation of small AFIPM machine in both generating and motoring operation modes;
- to extend the real-time simulations and experiments to vector control and direct torque control of AFIPM machines operating in traction drives.

Appendix 1. Properties of rotor permanent magnets

Magnetic properties of Sintered NdFeB magrets:					
Grade	Remanence	Coercive Force	Intrinsic Coercive Force	Max. energy product	Max. Operating Temperature
	Br	Hcb	Hcj	(BH) max	Tw
	mT	kA/m	kA/m	kJ/m3	
	(kGs)	(kOe)	(kOe)	(MGOe)	
N35	1170-1220	≥ 868	≥ 955	263-287	80 °C
	(11.7-12.2)	(≥ 10.9)	(≥ 12)	(33-36)	
N38	1220-1250	≥ 899	≥ 955	287-310	80 °C
	(12.2-12.5)	(≥ 11.3)	(≥ 12)	(36-39)	
N40	1250-1280	≥ 907	≥ 955	302-326	80 °C
	(12.5-12.8)	(≥ 11.4)	(≥ 12)	(38-41)	
N42	1280-1320	≥ 915	≥ 955	318-342	80 °C
	(12.8-13.2)	(≥ 11.5)	(≥ 12)	(40-43)	
N45	1320-1380	≥ 923	≥ 955	342-366	80 °C
	(13.2-13.8)	(≥ 11.6)	(≥ 12)	(43-46)	
N48	1380-1420	≥ 923	≥ 955	366-390	80 °C
	(13.8-14.2)	(≥ 11.6)	(≥ 12)	(46-49)	
N50	1400-1450	≥ 796	≥ 876	382-406	80 °C
	(14.0-14.5)	(≥ 10.0)	(≥ 11)	(48-51)	
N52	1430-1480	≥ 796	≥ 876	398-422	80 °C
	(14.3-14.8)	(≥ 10.0)	(≥ 11)	(50-53)	
33M	1130-1170	≥ 836	≥ 1114	247-263	100 °C
	(11.3-11.7)	(≥ 10.5)	(≥ 14)	(31-33)	
35M	1170-1220	≥ 868	≥ 1114	263-287	100 °C
	(11.7-12.2)	(≥ 10.9)	(≥ 14)	(33-36)	
38M	1220-1250	≥ 899	≥ 1114	287-310	100 °C
	(12.2-12.5)	(≥ 11.3)	(≥ 14)	(36-39)	
35SH	1170-1220	≥ 876	≥ 1592	263-287	150 °C
	(11.7-12.2)	(≥ 11.0)	(≥ 20)	(33-36)	

Appendix 2. Stator lamination properties

Typical data for SURA® M400-50A

T	W/kg at 50 Hz	VA/kg at 50 Hz	A/m at 50 Hz	W/kg at 100 Hz	W/kg at 200 Hz	W/kg at 400 Hz	W/kg at 1000 Hz	W/kg at 2500 Hz
0,1	0,02	0,07	32,6	0.07	0.16	0,48	2.12	8.64
0,2	0,09	0,18	43,5	0.26	0.64	1,80	7.49	30.1
0,3	0,19	0,33	50,8	0.54	1.35	3,77	15.3	62.7
0,4	0,31	0,50	57,2	0.88	2.25	6,29	25.7	109
0,5	0,46	0,69	63,4	1.27	3.33	9,37	39.0	172
0,6	0,62	0,91	69,9	1.73	4.58	13,1	56.1	256
0,7	0,81	1,16	77,3	2.24	6.03	17,5	77.1	367
0,8	1,01	1,46	86,0	2.80	7.68	22,7	103.1	509
0,9	1,24	1,81	97,2	3.44	9.58	28,8	135.0	685
1,0	1,49	2,23	113,2	4.15	11.7	35,9	173.3	899
1,1	1,76	2,79	137,8	4.95	14.2	44,2	218.8	1155
1,2	2,09	3,60	180,2	5.85	17.0	53,8	272.4	1453
1,3	2,46	5,07	269,5	6.88	20.2	64,9	334.6	1793
1,4	2,96	8,80	516,8	8.18	23.8	77,4	405.6	2130
1,5	3,57	21,6	1307	9.82	28.3	91,7	488.4	
1,6	4,38	57,2	3180					
1,7	5,02	128	6361					
1,8	5,47	243	10890					

Loss at 1.5 T , 50 Hz, W/kg	3,57
Loss at 1.0 T , 50 Hz, W/kg	1,49
Anisotropy of loss, %	8
Magnetic polarization at 50 Hz	
H = 2500 A/m, T	1,59
H = 5000 A/m, T	1,68
H = 10000 A/m, T	1,79
Coercivity (DC), A/m	50
Relative permeability at 1.5 T	1050
Resistivity, μΩcm	42
Yield strength, N/mm²	325
Tensile strength, N/mm²	465
Young's modulus, RD, N/mm²	200 000
Young's modulus, TD, N/mm²	210 000
Hardness HV5 (VPN)	165

RD represents the rolling direction
TD represents the transverse direction
Values for yield strength (0.2 % proof strength) and tensile strength are given for the rolling direction
Values for the transverse direction are approximately 5% higher

cogent
Surahammars Bruks AB

Oct 2009

Appendix 3. Analytical field model description

```
function  sorties = model_static_analytic (entrees,npt)
 %% couplage Modele EF2D du moteur a flux axial avec Matlab
%% fait par Adrian POP 6.06.2011 Ecole Centrale de Lille
dx1=entrees(1);
dx2=entrees(2);
dx3=entrees(3);
 %% Entrees
t1=(31.41-( dx1+dx2+dx3 ) )/2;
t2=t1+dx1;
t3=t2+dx2;
t4=t3+dx3;
 tmil=(t3+t4)/2;
Bm=-0.0018*dx3+0.9851;
 Bm_creneaux=0.0312*dx1+0.0722*dx2-3.3673e-4+0.4225;
Binter=-5.4564e-6*dx1+0.0575*dx2-8.1322e-4*dx3+0.1075;
   % passage des paramètres en radian
  t1=t1*pi/31.41;
  t2=t2*pi/31.41;
  t3=t3*pi/31.41;
  t4=t4*pi/31.41;
  tmil=tmil*pi/31.41;
  dt=t4-t3;
  % fonction créneaux
  f1=@(x) (t1<x & x<t2)*Bm_creneaux;
  finter=@(x) (t2<x & x<t3)*Binter;
  % fonction sinus, moitiée gauche
f2=@(x) (t3<x & x<tmil)*( (Bm-Binter)*sin( pi*(x-t3)/dt ) +Binter );
   % fonction sinus, moitiée droite
  f3=@(x) (tmil<x & x<t4)*Bm*sin( pi*(t4-x)/dt );
   % fonction du signal sur une demie-période
   f=@(x) f1(x)+finter(x)+f2(x)+f3(x);
  xxx=linspace(0,pi,npt);
    % vecteur de la fonction signal
  g=zeros(2*length(xx),1);
   for i=1:length(xx)
    g(i)=f(xx(i));
end
g(length(xx)+1:end)=-g(1:length(xx));
  sorties=g;
 end
```

Appendix 4. Pre-processing file description

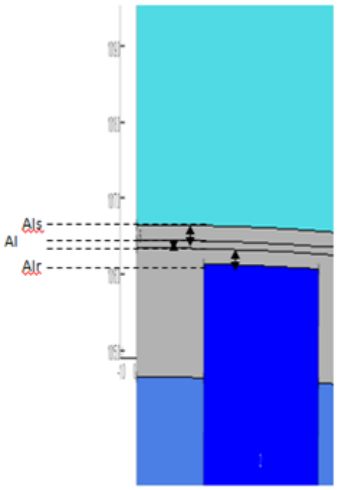

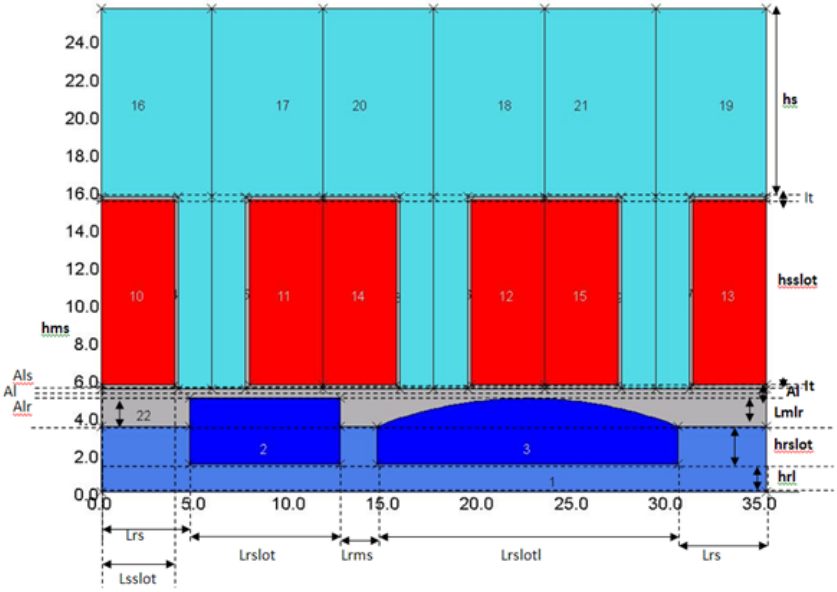

/ Setting the Pre Processor Environment
/ Setting Units
UNITS LENGTH=MM FLUX=TESLA FIELD=AM POTENTIAL=WBM CONDUCTIVITY=SM DENSITY=AM2 FORCE=NEWTON ENERGY=JOULE POWER=WATT MASS=KG
/ Setting View
/ Solution type
/ Setting Region properties
/model quadratic
SET FIELD=MAGNETIC SYMMETRY=XY AUTOMATIC=YES ELEMENT=QUADRATIC
$STRING NAME=YESORNO VALUE=YES

/ Lire les valeurs d'entree du dimensionnement : hrl hrslot hms Al Lrs Lrslot Lrms Lrslotl Lmlr hs hsslot Lsslot It Alr Als

$ open 2 D:\Adrian\Optimization_Cosmo\Slot-simulation-rotativ-entire\inputs.txt read
$ read 2 #hrl_update #hrslot_update #hms_update #Al_update #Lrs_update #Lrslot_update #Lrms_update #Lrslotl_update #Lmlr_update #hs_update #hsslot_update #Lsslot_update #Alr_update #Als_update

$ close 2

Definir les parametres de dimmensionnement moteur axial

$PARAMETER NAME=#hrl VALUE=#hrl_update
$PARAMETER NAME=#hrslot VALUE=#hrslot_update
$PARAMETER NAME=#hms VALUE=#hms_update
$PARAMETER NAME=#Al VALUE=#Al_update
$PARAMETER NAME=#Lrs VALUE=#Lrs_update
$PARAMETER NAME=#Lrslot VALUE=#Lrslot_update
$PARAMETER NAME=#Lrms VALUE=#Lrms_update
$PARAMETER NAME=#Lrslotl VALUE=#Lrslotl_update
$PARAMETER NAME=#Lmlr VALUE=#Lmlr_update
$PARAMETER NAME=#hs VALUE=#hs_update
$PARAMETER NAME=#hsslot VALUE=#hsslot_update
$PARAMETER NAME=#Lsslot VALUE=#Lsslot_update
/++ $PARAMETER NAME=#It VALUE=#It_update
$PARAMETER NAME=#Alr VALUE=#Alr_update
$PARAMETER NAME=#Als VALUE=#Als_update

$PARAMETER NAME=#R1 VALUE=10E6
$PARAMETER NAME=#U VALUE=0
$PARAMETER NAME=#teta VALUE=0.3

```
 $PARAMETER NAME=#Re VALUE=(#Lrs+#Lrslot+#Lrms+#Lrslotl+#Lrs)/tand(#teta)

/++ $PARAMETER NAME=#tetatot VALUE=atand(((#Lrs+#Lrslot+#Lrms+#Lrslotl+#Lrs)*8)/(#Re+#hrl+#hrslot+#hms+#Alr))
$PARAMETER NAME=#tetahsslot VALUE=atand((#Lsslot)/(#Re+#hrl+#hrslot+#hms+#Alr+#Al+#Als+#hsslot))
$PARAMETER NAME=#tetacoil VALUE=atand(#Lsslot/(#Re+#hrl+#hrslot+#hms+#Alr+#Al+#Als+#hsslot))
$PARAMETER NAME=#tetapot VALUE=atand((#Lrs+#Lrslot+#Lrms+#Lrslotl+#Lrs)/(#Re+#hrl+#hrslot+#hms+#Alr+#Al/2))
$PARAMETER NAME=#tetapot2 VALUE=atand((#Lrs+#Lrslot+#Lrms+#Lrslotl+#Lrs)/(#Re+#hrl+#hrslot+#Lmlr+#Alr+#Al/2))
$PARAMETER NAME=#x0 VALUE=(#Re+#hrl+#hrslot+#hms+#Alr+#Al/2)*tand(#tetapot)
$PARAMETER NAME=#x1 VALUE=(#Re+#hrl+#hrslot+#Lmlr+#Alr+#Al/2)*tand(#tetapot2)
$PARAMETER NAME=#x VALUE=(tand(#teta))*(#Re+#hrl+#hrslot+#hms+#Alr+#Al+#Als+#hsslot+#hs)
$PARAMETER NAME=#tetamax VALUE=atand(#x/(#Re+#hrl+#hrslot+#hms+#Alr+#Al+#Als+#hsslot+#hs))
$PARAMETER NAME=#tetatotal VALUE=#tetamax*8
$PARAMETER NAME=#tetatooth VALUE=(#tetatotal/25)/2
$PARAMETER NAME=#tetahms VALUE=atand((#Lrs)/(#Re+#hrl+#hrslot+#hms))
$PARAMETER NAME=#tetahmsr VALUE=atand((#Lrs+#Lrslot)/(#Re+#hrl+#hrslot+#hms))
$PARAMETER NAME=#tetaLrsr VALUE=atand((#Lrs+#Lrslot+#Lrms+#Lrslotl)/(#Re+#hrl+#hrslot))
$PARAMETER NAME=#tetaLrms VALUE=atand((#Lrs+#Lrslot+#Lrms)/(#Re+#hrl+#hrslot))
$PARAMETER NAME=#tetaLrslot VALUE=atand((#Lrs+#Lrslot)/(#Re+#hrl+#hrslot))
$PARAMETER NAME=#tetaLrsl VALUE=atand(#Lrs/(#Re+#hrl+#hrslot))
$PARAMETER NAME=#tetaLrslott VALUE=atand((#Lrs+#Lrslot)/(#Re+#hrl+#hrslot+#hms))
$PARAMETER NAME=#tetaLmlr VALUE=atand((#Lrs+#Lrslot+#Lrms+#Lrslotl/2)/(#Re+#hrl+#hrslot+#Lmlr))

/-----------------------------------------------------
/Conditions:
/(#Lrslotl/2)>=#Lmlr
/Run the analysis two times for overwriting the file!!!
/-----------------------------------------------------

/---------------------------------------
/ROTOR steel design for one polar step
/---------------------------------------

DRAW +DEFAULTS SHAPE=POLYGON TOLERANCE=5.0E-05 MATERIAL=4 PERM=2500 DENS=0 CONDUCTIVITY=0
PHASE=0 VELOCITY=0 N=0 SYMMETRY=0 XCEN=0 YCEN=0 ANGLE=0 NX=1 DX=0 NY=1 DY=0 ROTATIONS=1
TROTATION=0 MIRROR=NO
POLYGON -RELATIVE POLAR=YES RADIUS=#Re THETA=90 OPTION=TEXT +DATA
/#Lrs+#Lrslot+#Lrms+#Lrslotl+#Lrs
POLYGON -RELATIVE POLAR=YES RADIUS=#Re THETA=90-#teta LINESHAPE=CURVATURE CURVATURE=1/#Re
OPTION=TEXT +DATA -SIZE N=20 BIAS=0.5 F=DV
/x=#Lrs+#Lrslot+#Lrms+#Lrslotl+#Lrs y=#Re+#hrl+#hrslot
POLYGON -RELATIVE POLAR=YES RADIUS=#Re+#hrl+#hrslot THETA=90-#teta  LINESHAPE=CURVATURE CURVATURE=0
OPTION=TEXT +DATA -SIZE N=3 BIAS=0.5 F=NO
/x=#Lrs+#Lrslot+#Lrms+#Lrslotl y=#Re+#hrl+#hrslot
POLYGON -RELATIVE POLAR=YES RADIUS=#Re+#hrl+#hrslot THETA=90-#tetaLrsr LINESHAPE=CURVATURE CURVATURE=-
1/(#Re+#hrl+#hrslot)  OPTION=TEXT +DATA -SIZE N=5 BIAS=0.5 F=NO
/x=#Lrs+#Lrslot+#Lrms+#Lrslotl y=#Re+#hrl
POLYGON -RELATIVE POLAR=YES RADIUS=#Re+#hrl THETA=90-#tetaLrsr LINESHAPE=CURVATURE CURVATURE=0
OPTION=TEXT +DATA -SIZE N=2 BIAS=0.5 F=NO
/x=#Lrs+#Lrslot+#Lrms y=#Re+#hrl
POLYGON -RELATIVE POLAR=YES RADIUS=#Re+#hrl THETA=90-#tetaLrms LINESHAPE=CURVATURE CURVATURE=-
1/(#Re+#hrl) OPTION=TEXT +DATA N=10 BIAS=0.5 F=NO
/x=#Lrs+#Lrslot+#Lrms y=#Re+#hrl+#hrslot
POLYGON -RELATIVE POLAR=YES RADIUS=#Re+#hrl+#hrslot THETA=90-#tetaLrms LINESHAPE=CURVATURE
CURVATURE=0 OPTION=TEXT +DATA N=2 BIAS=0.5 F=NO
/x=#Lrs+#Lrslot y=#Re+#hrl+#hrslot
POLYGON -RELATIVE POLAR=YES RADIUS=#Re+#hrl+#hrslot THETA=90-#tetahmsr LINESHAPE=CURVATURE
CURVATURE=-1/(#Re+#hrl+#hrslot) OPTION=TEXT +DATA N=2 BIAS=0.5 F=NO
/x=#Lrs+#Lrslot y=#Re+#hrl
POLYGON -RELATIVE POLAR=YES RADIUS=#Re+#hrl THETA=90-#tetahmsr LINESHAPE=CURVATURE CURVATURE=0
OPTION=TEXT +DATA N=2 BIAS=0.5 F=NO
POLYGON -RELATIVE POLAR=YES RADIUS=#Re+#hrl THETA=90-#tetahms LINESHAPE=CURVATURE CURVATURE=-
1/(#Re+#hrl) OPTION=TEXT +DATA N=8 BIAS=0.5 F=NO
/x=#Lrs y=#Re+#hrl+#hrslot
POLYGON -RELATIVE POLAR=YES RADIUS=#Re+#hrl+#hrslot THETA=90-#tetahms LINESHAPE=CURVATURE
CURVATURE=0 OPTION=TEXT +DATA N=2 BIAS=0.5 F=NO
/x=0 y=#Re+#hrl+#hrslot
POLYGON -RELATIVE POLAR=YES RADIUS=#Re+#hrl+#hrslot THETA=90 LINESHAPE=CURVATURE CURVATURE=-
1/(#Re+#hrl+#hrslot) OPTION=TEXT +DATA N=5 BIAS=0.5 F=NO
POLYGON OPTION=close LINESHAPE=CURVATURE CURVATURE=0 +DATA N=3 BIAS=0.5 F=NO
```

```
TEST REG1=1 REG2=* POINTS=BOTH QUERY=NO SIDES=UNDER MATCH=YES DRAW=NO

/----------------------------------------
/ SMALLER MAGNET design for one polar step
/----------------------------------------

TEST REG1=1 REG2=* POINTS=BOTH QUERY=NO SIDES=UNDER MATCH=NO DRAW=NO

DRAW +DEFAULTS SHAPE=POLYGON TOLERANCE=5.0E-05 MATERIAL=3 PERM=1 DENS=0 CONDUCTIVITY=0 PHASE=90
VELOCITY=0 N=0 SYMMETRY=0 XCEN=0 YCEN=0 ANGLE=0 NX=1 DX=0 NY=1 DY=0 ROTATIONS=1 TROTATION=0
MIRROR=NO

POLYGON -RELATIVE POLAR=YES RADIUS=#Re+#hrl THETA=90-#tetahms OPTION=TEXT +DATA
POLYGON -RELATIVE POLAR=YES RADIUS=#Re+#hrl+#hrslot THETA=90-#tetahms LINESHAPE=CURVATURE
CURVATURE=0 OPTION=TEXT +DATA N=1 BIAS=0.5 F=NO
POLYGON -RELATIVE POLAR=YES RADIUS=#Re+#hrl+#hrslot+#hms THETA=90-#tetahms LINESHAPE=CURVATURE
CURVATURE=0 OPTION=TEXT +DATA N=1 BIAS=0.5 F=NO
POLYGON -RELATIVE POLAR=YES RADIUS=#Re+#hrl+#hrslot+#hms THETA=90-#tetahmsr LINESHAPE=CURVATURE
CURVATURE=1/(#Re+#hrl+#hrslot+#hms) OPTION=TEXT +DATA N=5 BIAS=0.5 F=NO
POLYGON -RELATIVE POLAR=YES RADIUS=#Re+#hrl+#hrslot THETA=90-#tetahmsr LINESHAPE=CURVATURE
CURVATURE=0 OPTION=TEXT +DATA N=1 BIAS=0.5 F=NO
POLYGON -RELATIVE POLAR=YES RADIUS=#Re+#hrl THETA=90-#tetahmsr LINESHAPE=CURVATURE CURVATURE=0
OPTION=TEXT +DATA N=1 BIAS=0.5 F=NO
POLYGON OPTION=close LINESHAPE=CURVATURE CURVATURE=0 +DATA

/----------------------------------------
/LARGER MAGNET design for one single regions
/----------------------------------------
TEST REG1=1 REG2=* POINTS=BOTH QUERY=NO SIDES=UNDER MATCH=NO DRAW=NO

DRAW +DEFAULTS SHAPE=POLYGON TOLERANCE=5.0E-05 MATERIAL=3 PERM=1 DENS=0 CONDUCTIVITY=0 PHASE=90
VELOCITY=0 N=0 SYMMETRY=0 XCEN=0 YCEN=0 ANGLE=0 NX=1 DX=0 NY=1 DY=0 ROTATIONS=1 TROTATION=0
MIRROR=NO

POLYGON -DATA LINESHAPE=MIDSIDE
POLYGON -RELATIVE POLAR=YES RADIUS=#Re+#hrl+#hrslot THETA=90-#tetaLrsr OPTION=TEXT +DATA
POLYGON -RELATIVE POLAR=YES RADIUS=#Re+#hrl+#hrslot+#Lmlr THETA=90-#tetaLmlr OPTION=TEXT +DATA N=15
BIAS=0.5 F=NO
POLYGON -RELATIVE POLAR=YES RADIUS=#Re+#hrl+#hrslot THETA=90-#tetaLrms  OPTION=TEXT +DATA
POLYGON -DATA LINESHAPE=STRAIGHT
POLYGON -RELATIVE POLAR=YES RADIUS=#Re+#hrl THETA=90-#tetaLrms OPTION=TEXT +DATA
POLYGON -RELATIVE POLAR=YES RADIUS=#Re+#hrl THETA=90-#tetaLrsr OPTION=text +DATA
POLYGON OPTION=close +DATA

/----------------------------------------
/Drawing the COILS
/----------------------------------------

TEST REG1=1 REG2=* POINTS=BOTH QUERY=NO SIDES=UNDER MATCH=YES DRAW=YES

DRAW SHAPE=POLYGON,
DRAW +DEFAULTS SHAPE=POLYGON TOLERANCE=5.0E-05 MATERIAL=1 PERM=1 DENS=0 CONDUCTIVITY=0 PHASE=0
VELOCITY=0 N=0 SYMMETRY=0 XCEN=0 YCEN=0 ANGLE=0 NX=1 DX=0 NY=1 DY=0 ROTATIONS=1 TROTATION=0
MIRROR=NO

$IF #hrl+#hrslot+#hms GE #hrl+#hrslot+#Lmlr

POLYGON -RELATIVE POLAR=YES RADIUS=#Re+#hrl+#hrslot+#hms+#Alr+#Al+#Als THETA=90 OPTION=TEXT +DATA
POLYGON -RELATIVE POLAR=YES RADIUS=#Re+#hrl+#hrslot+#hms+#Alr+#Al+#Als THETA=90-#tetacoil
LINESHAPE=CURVATURE CURVATURE=1/(#Re+#hrl+#hrslot+#hms+#Alr+#Al+#Als) OPTION=TEXT +DATA -SIZE N=2
BIAS=0.5 F=NO
POLYGON -RELATIVE POLAR=YES RADIUS=#Re+#hrl+#hrslot+#hms+#Alr+#Al+#Als+#hsslot THETA=90-#tetacoil
LINESHAPE=CURVATURE CURVATURE=0 OPTION=TEXT +DATA -SIZE N=10 BIAS=0.5 F=NO
POLYGON -RELATIVE POLAR=YES RADIUS=#Re+#hrl+#hrslot+#hms+#Alr+#Al+#Als+#hsslot THETA=90
LINESHAPE=CURVATURE CURVATURE=-1/(#Re+#hrl+#hrslot+#hms+#Alr+#Al+#Als+#hsslot) OPTION=TEXT +DATA -SIZE N=2
BIAS=0.5 F=NO
POLYGON OPTION=close LINESHAPE=CURVATURE CURVATURE=0 +DATA N=10 BIAS=0.5 F=NO
  $else
    $if #hrl+#hrslot+#Lmlr GT #hrl+#hrslot+#hms
POLYGON -RELATIVE POLAR=YES RADIUS=#Re+#hrl+#hrslot+#Lmlr+#Alr+#Al+#Als THETA=90 OPTION=TEXT +DATA
```

```
POLYGON -RELATIVE POLAR=YES RADIUS=#Re+#hrl+#hrslot+#Lmlr+#Alr+#Al+#Als THETA=90-#tetacoil
LINESHAPE=CURVATURE CURVATURE=1/(#Re+#hrl+#hrslot+#Lmlr+#Alr+#Al+#Als) OPTION=TEXT +DATA -SIZE N=2
BIAS=0.5 F=NO
POLYGON -RELATIVE POLAR=YES RADIUS=#Re+#hrl+#hrslot+#Lmlr+#Alr+#Al+#Als+#hsslot THETA=90-#tetacoil
LINESHAPE=CURVATURE CURVATURE=0 OPTION=TEXT +DATA -SIZE N=10 BIAS=0.5 F=NO
POLYGON -RELATIVE POLAR=YES RADIUS=#Re+#hrl+#hrslot+#Lmlr+#Alr+#Al+#Als+#hsslot THETA=90
LINESHAPE=CURVATURE CURVATURE=-1/(#Re+#hrl+#hrslot+#Lmlr+#Alr+#Al+#Als+#hsslot) OPTION=TEXT +DATA -SIZE N=2
BIAS=0.5 F=NO
POLYGON OPTION=close LINESHAPE=CURVATURE CURVATURE=0 +DATA N=10 BIAS=0.5 F=NO
$end if
 $end if

/----------------------------------------
/++ /Drawing the ISOLATION
/++ /----------------------------------------
/++ DRAW SHAPE=POLYGON,
/++ DRAW +DEFAULTS SHAPE=POLYGON TOLERANCE=5.0E-06 MATERIAL=0 PERM=1 DENS=0 CONDUCTIVITY=0
PHASE=0 VELOCITY=0 N=0 SYMMETRY=0 XCEN=0 YCEN=0 ANGLE=0 NX=1 DX=0 NY=1 DY=0 ROTATIONS=1
TROTATION=0 MIRROR=NO
/++
/++ $IF #hrl+#hrslot+#hms GE #hrl+#hrslot+#Lmlr
/++ POLYGON -RELATIVE POLAR=YES RADIUS=#Re+#hrl+#hrslot+#hms+#Alr+#Al+#Als THETA=90 OPTION=TEXT +DATA
/++ POLYGON -RELATIVE POLAR=YES RADIUS=#Re+#hrl+#hrslot+#hms+#Alr+#Al+#Als THETA=90-#tetahsslot
LINESHAPE=CURVATURE CURVATURE=1/(#Re+#hrl+#hrslot+#hms+#Alr+#Al+#Als) OPTION=TEXT +DATA -SIZE N=3
BIAS=0.5 F=NO
/++ POLYGON -RELATIVE POLAR=YES RADIUS=#Re+#hrl+#hrslot+#hms+#Alr+#Al+#Als+#It+#hsslot+#It THETA=90-#tetahsslot
LINESHAPE=CURVATURE CURVATURE=0 OPTION=TEXT +DATA -SIZE N=12 BIAS=0.5 F=NO
/++ POLYGON -RELATIVE POLAR=YES RADIUS=#Re+#hrl+#hrslot+#hms+#Alr+#Al+#Als+#It+#hsslot+#It THETA=90
LINESHAPE=CURVATURE CURVATURE=-1/(#Re+#hrl+#hrslot+#hms+#Alr+#Al+#Als+#It+#hsslot+#It) OPTION=TEXT +DATA -
SIZE N=3 BIAS=0.5 F=NO
/++ POLYGON -RELATIVE POLAR=YES RADIUS=#Re+#hrl+#hrslot+#hms+#Alr+#Al+#Als+#It+#hsslot THETA=90
LINESHAPE=CURVATURE CURVATURE=0 OPTION=TEXT +DATA -SIZE N=1 BIAS=0.5 F=NO
/++ POLYGON -RELATIVE POLAR=YES RADIUS=#Re+#hrl+#hrslot+#hms+#Alr+#Al+#Als+#It+#hsslot THETA=90-#tetacoil
LINESHAPE=CURVATURE CURVATURE=1/(#Re+#hrl+#hrslot+#hms+#Alr+#Al+#Als+#It+#hsslot+#It) OPTION=TEXT +DATA -
SIZE N=2 BIAS=0.5 F=NO
/++ POLYGON -RELATIVE POLAR=YES RADIUS=#Re+#hrl+#hrslot+#hms+#Alr+#Al+#Als+#It THETA=90-#tetacoil
LINESHAPE=CURVATURE CURVATURE=0 OPTION=TEXT +DATA -SIZE N=8 BIAS=0.5 F=NO
/++ POLYGON -RELATIVE POLAR=YES RADIUS=#Re+#hrl+#hrslot+#hms+#Alr+#Al+#Als+#It THETA=90
LINESHAPE=CURVATURE CURVATURE=1/(#Re+#hrl+#hrslot+#hms+#Alr+#Al+#Als+#It) OPTION=TEXT +DATA -SIZE N=2
BIAS=0.5 F=NO
/++ POLYGON OPTION=close LINESHAPE=CURVATURE CURVATURE=0 +DATA N=1 BIAS=0.5
/++   $else
/++     $if #hrl+#hrslot+#Lmlr GT #hrl+#hrslot+#hms
/++ POLYGON -RELATIVE POLAR=YES RADIUS=#Re+#hrl+#hrslot+#Lmlr+#Alr+#Al+#Als THETA=90 OPTION=TEXT +DATA
/++ POLYGON -RELATIVE POLAR=YES RADIUS=#Re+#hrl+#hrslot+#Lmlr+#Alr+#Al+#Als THETA=90-#tetahsslot
LINESHAPE=CURVATURE CURVATURE=1/(#Re+#hrl+#hrslot+#Lmlr+#Alr+#Al+#Als) OPTION=TEXT +DATA -SIZE N=3
BIAS=0.5 F=NO
/++ POLYGON -RELATIVE POLAR=YES RADIUS=#Re+#hrl+#hrslot+#Lmlr+#Alr+#Al+#Als+#It+#hsslot+#It THETA=90-#tetahsslot
LINESHAPE=CURVATURE CURVATURE=0 OPTION=TEXT +DATA -SIZE N=12 BIAS=0.5 F=NO
/++ POLYGON -RELATIVE POLAR=YES RADIUS=#Re+#hrl+#hrslot+#Lmlr+#Alr+#Al+#Als+#It+#hsslot+#It THETA=90
LINESHAPE=CURVATURE CURVATURE=-1/(#Re+#hrl+#hrslot+#Lmlr+#Alr+#Al+#Als+#It+#hsslot+#It) OPTION=TEXT +DATA -
SIZE N=3 BIAS=0.5 F=NO
/++ POLYGON -RELATIVE POLAR=YES RADIUS=#Re+#hrl+#hrslot+#Lmlr+#Alr+#Al+#Als+#It+#hsslot THETA=90
LINESHAPE=CURVATURE CURVATURE=0 OPTION=TEXT +DATA -SIZE N=1 BIAS=0.5 F=NO
/++ POLYGON -RELATIVE POLAR=YES RADIUS=#Re+#hrl+#hrslot+#Lmlr+#Alr+#Al+#Als+#It+#hsslot THETA=90-#tetacoil
LINESHAPE=CURVATURE CURVATURE=1/(#Re+#hrl+#hrslot+#Lmlr+#Alr+#Al+#Als+#It+#hsslot+#It) OPTION=TEXT +DATA -
SIZE N=2 BIAS=0.5 F=NO
/++ POLYGON -RELATIVE POLAR=YES RADIUS=#Re+#hrl+#hrslot+#Lmlr+#Alr+#Al+#Als+#It THETA=90-#tetacoil
LINESHAPE=CURVATURE CURVATURE=0 OPTION=TEXT +DATA -SIZE N=8 BIAS=0.5 F=NO
/++ POLYGON -RELATIVE POLAR=YES RADIUS=#Re+#hrl+#hrslot+#Lmlr+#Alr+#Al+#Als+#It THETA=90
LINESHAPE=CURVATURE CURVATURE=1/(#Re+#hrl+#hrslot+#Lmlr+#Alr+#Al+#Als+#It) OPTION=TEXT +DATA -SIZE N=2
BIAS=0.5 F=NO
/++ POLYGON OPTION=close LINESHAPE=CURVATURE CURVATURE=0 +DATA N=1 BIAS=0.5
/++ $end if
/++  $end if
/++

/----------------------------------------
/Drawing the TOOTH
/----------------------------------------
```

```
DRAW SHAPE=POLYGON,
DRAW +DEFAULTS SHAPE=POLYGON TOLERANCE=5.0E-05 MATERIAL=5 PERM=2500 DENS=0 CONDUCTIVITY=0
PHASE=0 VELOCITY=0 N=0 SYMMETRY=0 XCEN=0 YCEN=0 ANGLE=0 NX=1 DX=0 NY=1 DY=0 ROTATIONS=1
TROTATION=0 MIRROR=NO

$IF #hrl+#hrslot+#hms GE #hrl+#hrslot+#Lmlr
POLYGON -RELATIVE POLAR=YES RADIUS=#Re+#hrl+#hrslot+#hms+#Alr+#Al+#Als THETA=90-#tetahsslot
LINESHAPE=CURVATURE CURVATURE=0 OPTION=TEXT +DATA -SIZE N=5 BIAS=0.5 F=NO
POLYGON -RELATIVE POLAR=YES RADIUS=#Re+#hrl+#hrslot+#hms+#Alr+#Al+#Als THETA=90-#tetatooth
LINESHAPE=CURVATURE CURVATURE=1/(#Re+#hrl+#hrslot+#hms+#Alr+#Al+#Als) OPTION=TEXT +DATA -SIZE N=8
BIAS=0.5 F=NO
POLYGON -RELATIVE POLAR=YES RADIUS=#Re+#hrl+#hrslot+#hms+#Alr+#Al+#Als+#hsslot+#hs THETA=90-#tetatooth
LINESHAPE=CURVATURE CURVATURE=0 OPTION=TEXT +DATA -SIZE N=15 BIAS=0.5 F=NO
POLYGON -RELATIVE POLAR=YES RADIUS=#Re+#hrl+#hrslot+#hms+#Alr+#Al+#Als+#hsslot+#hs THETA=90
LINESHAPE=CURVATURE CURVATURE=-1/(#Re+#hrl+#hrslot+#hms+#Alr+#Al+#Als+#hsslot+#hs) OPTION=TEXT +DATA -SIZE
N=2 BIAS=0.5 F=V V=0
POLYGON -RELATIVE POLAR=YES RADIUS=#Re+#hrl+#hrslot+#hms+#Alr+#Al+#Als+#hsslot THETA=90
LINESHAPE=CURVATURE CURVATURE=0 OPTION=TEXT +DATA -SIZE N=7 BIAS=0.5 F=NO
POLYGON -RELATIVE POLAR=YES RADIUS=#Re+#hrl+#hrslot+#hms+#Alr+#Al+#Als+#hsslot THETA=90-#tetahsslot
LINESHAPE=CURVATURE CURVATURE=1/(#Re+#hrl+#hrslot+#hms+#Alr+#Al+#Als+#hsslot+#hs) OPTION=TEXT +DATA -SIZE
N=3 BIAS=0.5 F=NO
POLYGON OPTION=close LINESHAPE=CURVATURE CURVATURE=0 +DATA N=10 BIAS=0.5 F=NO
  $else
    $if #hrl+#hrslot+#Lmlr GT #hrl+#hrslot+#hms
POLYGON -RELATIVE POLAR=YES RADIUS=#Re+#hrl+#hrslot+#Lmlr+#Alr+#Al+#Als THETA=90-#tetahsslot
LINESHAPE=CURVATURE CURVATURE=0 OPTION=TEXT +DATA -SIZE N=5 BIAS=0.5 F=NO
POLYGON -RELATIVE POLAR=YES RADIUS=#Re+#hrl+#hrslot+#Lmlr+#Alr+#Al+#Als THETA=90-#tetatooth
LINESHAPE=CURVATURE CURVATURE=1/(#Re+#hrl+#hrslot+#Lmlr+#Alr+#Al+#Als) OPTION=TEXT +DATA -SIZE N=8
BIAS=0.5 F=NO
POLYGON -RELATIVE POLAR=YES RADIUS=#Re+#hrl+#hrslot+#Lmlr+#Alr+#Al+#Als+#hsslot+#hs THETA=90-#tetatooth
LINESHAPE=CURVATURE CURVATURE=0 OPTION=TEXT +DATA -SIZE N=15 BIAS=0.5 F=NO
POLYGON -RELATIVE POLAR=YES RADIUS=#Re+#hrl+#hrslot+#Lmlr+#Alr+#Al+#Als+#hsslot+#hs THETA=90
LINESHAPE=CURVATURE CURVATURE=-1/(#Re+#hrl+#hrslot+#Lmlr+#Alr+#Al+#Als+#hsslot+#hs) OPTION=TEXT +DATA -SIZE
N=2 BIAS=0.5 F=V V=0
POLYGON -RELATIVE POLAR=YES RADIUS=#Re+#hrl+#hrslot+#Lmlr+#Alr+#Al+#Als+#hsslot THETA=90
LINESHAPE=CURVATURE CURVATURE=0 OPTION=TEXT +DATA -SIZE N=7 BIAS=0.5 F=NO
POLYGON -RELATIVE POLAR=YES RADIUS=#Re+#hrl+#hrslot+#Lmlr+#Alr+#Al+#Als+#hsslot THETA=90-#tetahsslot
LINESHAPE=CURVATURE CURVATURE=1/(#Re+#hrl+#hrslot+#Lmlr+#Alr+#Al+#Als+#hsslot+#hs) OPTION=TEXT +DATA -SIZE
N=3 BIAS=0.5 F=NO
POLYGON OPTION=close LINESHAPE=CURVATURE CURVATURE=0 +DATA N=10 BIAS=0.5 F=NO
$end if
 $end if

COPY REG1=4 REG2=5 DX=0 DY=0 MIRROR=NO THETA=-#tetatooth
MOVE REG1=6 REG2=7 DX=0 DY=0 MIRROR=YES THETA=90
MOVE REG1=6 REG2=7 DX=0 DY=0 MIRROR=NO THETA=-3*#tetatooth

/++ EDIT REG1=6 REG2=6 OPTION=SIDE NUMBER=4 F=NO NEIGHBOURS=YES
/++ EDIT REG1=8 REG2=8 OPTION=SIDE NUMBER=4,8 F=NO NEIGHBOURS=YES
/++ EDIT REG1=7 REG2=7 OPTION=SIDE NUMBER=4 F=NO NEIGHBOURS=YES

COPY REG1=4 REG2=7 DX=0 DY=0 MIRROR=NO THETA=-2*#tetatooth
COPY REG1=4 REG2=7 DX=0 DY=0 MIRROR=NO THETA=-4*#tetatooth
COPY REG1=4 REG2=7 DX=0 DY=0 MIRROR=NO THETA=-6*#tetatooth
COPY REG1=4 REG2=7 DX=0 DY=0 MIRROR=NO THETA=-8*#tetatooth
COPY REG1=4 REG2=7 DX=0 DY=0 MIRROR=NO THETA=-10*#tetatooth
COPY REG1=4 REG2=7 DX=0 DY=0 MIRROR=NO THETA=-12*#tetatooth
COPY REG1=4 REG2=7 DX=0 DY=0 MIRROR=NO THETA=-14*#tetatooth
GROUP ACTION=CREATE NAME=Stator
GROUP ACTION=ADD NAME=STATOR REG1=4 REG2=* MATERIAL=ALL NOT=ANY
 COPY REG1=STATOR REG2=* DX=0 DY=0 MIRROR=NO THETA=-#tetatooth*16
GROUP ACTION=CREATE NAME=Stator1
GROUP ACTION=ADD NAME=STATOR1 REG1=36 REG2=* MATERIAL=ALL NOT=ANY
COPY REG1=STATOR1 REG2=* DX=0 DY=0 MIRROR=NO THETA=-#tetatooth*16
GROUP ACTION=CREATE NAME=Stator2
GROUP ACTION=ADD NAME=STATOR2 REG1=4 REG2=7 MATERIAL=ALL NOT=ANY
COPY REG1=STATOR2 REG2=* DX=0 DY=0 MIRROR=NO THETA=-#tetatooth*48

/++ Grouping the rotor regions
```

```
GROUP ACTION=CREATE NAME=Rotor
GROUP ACTION=ADD NAME=ROTOR REG1=1 REG2=3 MATERIAL=ALL NOT=ANY
COPY REG1=ROTOR REG2=3 DX=0 DY=0 MIRROR=NO THETA=-#teta
COPY REG1=ROTOR REG2=3 DX=0 DY=0 MIRROR=NO THETA=-#teta*2
COPY REG1=ROTOR REG2=3 DX=0 DY=0 MIRROR=NO THETA=-#teta*3
COPY REG1=ROTOR REG2=3 DX=0 DY=0 MIRROR=NO THETA=-#teta*4
COPY REG1=ROTOR REG2=3 DX=0 DY=0 MIRROR=NO THETA=-#teta*5
COPY REG1=ROTOR REG2=3 DX=0 DY=0 MIRROR=NO THETA=-#teta*6
COPY REG1=ROTOR REG2=3 DX=0 DY=0 MIRROR=NO THETA=-#teta*7

/changing the region properties
MODIFY REG1=105 REG2=106 MATERIAL=3 PERM=1 CONDUCTIVITY=0 PHASE=-90 ERASE=NO
MODIFY REG1=111 REG2=112 MATERIAL=3 PERM=1 CONDUCTIVITY=0 PHASE=-90 ERASE=NO
MODIFY REG1=117 REG2=118 MATERIAL=3 PERM=1 CONDUCTIVITY=0 PHASE=-90 ERASE=NO
MODIFY REG1=123 REG2=124 MATERIAL=3 PERM=1 CONDUCTIVITY=0 PHASE=-90 ERASE=NO

/----------------------------------------
/Creating the air gap near to rotor
/----------------------------------------

DRAW +DEFAULTS SHAPE=POLYGON TOLERANCE=5.0E-05 MATERIAL=0 PERM=1 DENS=0 CONDUCTIVITY=0 PHASE=0
VELOCITY=0 N=0 SYMMETRY=0 XCEN=0 YCEN=0 ANGLE=0 NX=1 DX=0 NY=1 DY=0 ROTATIONS=1 TROTATION=0
MIRROR=NO
TEST REG1=1 REG2=* POINTS=NONE SIDES=NO DRAW=NO

/++ $IF #hrl+#hrslot+#hms GE #hrl+#hrslot+#Lmlr

POLYGON -RELATIVE POLAR=YES RADIUS=#Re+#hrl+#hrslot+#hms+#Alr THETA=90 OPTION=TEXT +DATA  BIAS=0.5 F=NO
POLYGON -RELATIVE POLAR=YES RADIUS=#Re+#hrl+#hrslot THETA=90 N=3 OPTION=TEXT +DATA -SIZE F=SYMMETRY
 POLYGON -RELATIVE POLAR=YES RADIUS=#Re+#hrl+#hrslot THETA=90-#tetahms N=4 OPTION=TEXT +DATA F=NO
POLYGON -RELATIVE POLAR=YES RADIUS=#Re+#hrl+#hrslot+#hms THETA=90-#tetahms N=1 OPTION=TEXT +DATA F=NO
POLYGON -RELATIVE POLAR=YES RADIUS=#Re+#hrl+#hrslot+#hms THETA=90-#tetahmsr N=8 OPTION=TEXT +DATA F=NO
POLYGON -RELATIVE POLAR=YES RADIUS=#Re+#hrl+#hrslot THETA=90-#tetahmsr N=1 OPTION=TEXT +DATA F=NO
POLYGON -RELATIVE POLAR=YES RADIUS=#Re+#hrl+#hrslot THETA=90-#tetaLrms N=1 OPTION=TEXT +DATA  F=NO
POLYGON -DATA LINESHAPE=MIDSIDE
POLYGON -RELATIVE POLAR=YES RADIUS=#Re+#hrl+#hrslot+#Lmlr THETA=90-#tetaLmlr N=8  OPTION=TEXT +DATA F=NO
 POLYGON -RELATIVE POLAR=YES RADIUS=#Re+#hrl+#hrslot THETA=90-#tetaLrsr N=8 OPTION=TEXT +DATA F=NO
 POLYGON -DATA LINESHAPE=STRAIGHT
POLYGON -RELATIVE POLAR=YES RADIUS=#Re+#hrl+#hrslot THETA=90-#teta N=4 OPTION=TEXT +DATA -SIZE N=2
BIAS=0.5 F=NO


/Second pole
 POLYGON -RELATIVE POLAR=YES RADIUS=#Re+#hrl+#hrslot THETA=90-(#teta+#tetahms) OPTION=TEXT +DATA F=NO
POLYGON -RELATIVE POLAR=YES RADIUS=#Re+#hrl+#hrslot+#hms THETA=90-(#teta+#tetahms)  OPTION=TEXT +DATA
F=NO
POLYGON -RELATIVE POLAR=YES RADIUS=#Re+#hrl+#hrslot+#hms THETA=90-(#teta+#tetahmsr)  OPTION=TEXT +DATA
F=NO
POLYGON -RELATIVE POLAR=YES RADIUS=#Re+#hrl+#hrslot THETA=90-(#teta+#tetahmsr) OPTION=TEXT +DATA F=NO
POLYGON -RELATIVE POLAR=YES RADIUS=#Re+#hrl+#hrslot THETA=90-(#teta+#tetaLrms)  OPTION=TEXT +DATA  F=NO
POLYGON -DATA LINESHAPE=MIDSIDE
POLYGON -RELATIVE POLAR=YES RADIUS=#Re+#hrl+#hrslot+#Lmlr THETA=90-(#teta+#tetaLmlr)   OPTION=TEXT +DATA
F=NO
 POLYGON -RELATIVE POLAR=YES RADIUS=#Re+#hrl+#hrslot THETA=90-(#teta+#tetaLrsr) OPTION=TEXT +DATA F=NO
 POLYGON -DATA LINESHAPE=STRAIGHT
POLYGON -RELATIVE POLAR=YES RADIUS=#Re+#hrl+#hrslot THETA=90-#teta*2 OPTION=TEXT +DATA -SIZE N=2 BIAS=0.5
F=NO


/Third pole
 POLYGON -RELATIVE POLAR=YES RADIUS=#Re+#hrl+#hrslot THETA=90-(#teta*2+#tetahms) OPTION=TEXT +DATA F=NO
POLYGON -RELATIVE POLAR=YES RADIUS=#Re+#hrl+#hrslot+#hms THETA=90-(#teta*2+#tetahms)  OPTION=TEXT +DATA
F=NO
POLYGON -RELATIVE POLAR=YES RADIUS=#Re+#hrl+#hrslot+#hms THETA=90-(#teta*2+#tetahmsr)  OPTION=TEXT +DATA
F=NO
POLYGON -RELATIVE POLAR=YES RADIUS=#Re+#hrl+#hrslot THETA=90-(#teta*2+#tetahmsr) OPTION=TEXT +DATA F=NO
POLYGON -RELATIVE POLAR=YES RADIUS=#Re+#hrl+#hrslot THETA=90-(#teta*2+#tetaLrms)  OPTION=TEXT +DATA  F=NO
POLYGON -DATA LINESHAPE=MIDSIDE
```

```
POLYGON -RELATIVE POLAR=YES RADIUS=#Re+#hrl+#hrslot+#Lmlr THETA=90-(#teta*2+#tetaLmlr)   OPTION=TEXT +DATA
F=NO
 POLYGON -RELATIVE POLAR=YES RADIUS=#Re+#hrl+#hrslot THETA=90-(#teta*2+#tetaLrsr) OPTION=TEXT +DATA F=NO
 POLYGON -DATA LINESHAPE=STRAIGHT
POLYGON -RELATIVE POLAR=YES RADIUS=#Re+#hrl+#hrslot THETA=90-#teta*3 OPTION=TEXT +DATA -SIZE N=2 BIAS=0.5
F=NO

/Forth pole
 POLYGON -RELATIVE POLAR=YES RADIUS=#Re+#hrl+#hrslot THETA=90-(#teta*3+#tetahms) OPTION=TEXT +DATA F=NO
POLYGON -RELATIVE POLAR=YES RADIUS=#Re+#hrl+#hrslot+#hms THETA=90-(#teta*3+#tetahms)  OPTION=TEXT +DATA
F=NO
POLYGON -RELATIVE POLAR=YES RADIUS=#Re+#hrl+#hrslot+#hms THETA=90-(#teta*3+#tetahmsr)  OPTION=TEXT +DATA
F=NO
POLYGON -RELATIVE POLAR=YES RADIUS=#Re+#hrl+#hrslot THETA=90-(#teta*3+#tetahmsr) OPTION=TEXT +DATA F=NO
POLYGON -RELATIVE POLAR=YES RADIUS=#Re+#hrl+#hrslot THETA=90-(#teta*3+#tetaLrms)  OPTION=TEXT +DATA  F=NO
POLYGON -DATA LINESHAPE=MIDSIDE
POLYGON -RELATIVE POLAR=YES RADIUS=#Re+#hrl+#hrslot+#Lmlr THETA=90-(#teta*3+#tetaLmlr)   OPTION=TEXT +DATA
F=NO
 POLYGON -RELATIVE POLAR=YES RADIUS=#Re+#hrl+#hrslot THETA=90-(#teta*3+#tetaLrsr) OPTION=TEXT +DATA F=NO
 POLYGON -DATA LINESHAPE=STRAIGHT
POLYGON -RELATIVE POLAR=YES RADIUS=#Re+#hrl+#hrslot THETA=90-#teta*4 OPTION=TEXT +DATA -SIZE N=2 BIAS=0.5
F=NO

/Fifth pole
 POLYGON -RELATIVE POLAR=YES RADIUS=#Re+#hrl+#hrslot THETA=90-(#teta*4+#tetahms) OPTION=TEXT +DATA F=NO
POLYGON -RELATIVE POLAR=YES RADIUS=#Re+#hrl+#hrslot+#hms THETA=90-(#teta*4+#tetahms)  OPTION=TEXT +DATA
F=NO
POLYGON -RELATIVE POLAR=YES RADIUS=#Re+#hrl+#hrslot+#hms THETA=90-(#teta*4+#tetahmsr)  OPTION=TEXT +DATA
F=NO
POLYGON -RELATIVE POLAR=YES RADIUS=#Re+#hrl+#hrslot THETA=90-(#teta*4+#tetahmsr) OPTION=TEXT +DATA F=NO
POLYGON -RELATIVE POLAR=YES RADIUS=#Re+#hrl+#hrslot THETA=90-(#teta*4+#tetaLrms)  OPTION=TEXT +DATA  F=NO
POLYGON -DATA LINESHAPE=MIDSIDE
POLYGON -RELATIVE POLAR=YES RADIUS=#Re+#hrl+#hrslot+#Lmlr THETA=90-(#teta*4+#tetaLmlr)   OPTION=TEXT +DATA
F=NO
 POLYGON -RELATIVE POLAR=YES RADIUS=#Re+#hrl+#hrslot THETA=90-(#teta*4+#tetaLrsr) OPTION=TEXT +DATA F=NO
 POLYGON -DATA LINESHAPE=STRAIGHT
POLYGON -RELATIVE POLAR=YES RADIUS=#Re+#hrl+#hrslot THETA=90-#teta*5 OPTION=TEXT +DATA -SIZE N=2 BIAS=0.5
F=NO

/Sixth pole
 POLYGON -RELATIVE POLAR=YES RADIUS=#Re+#hrl+#hrslot THETA=90-(#teta*5+#tetahms) OPTION=TEXT +DATA F=NO
POLYGON -RELATIVE POLAR=YES RADIUS=#Re+#hrl+#hrslot+#hms THETA=90-(#teta*5+#tetahms)  OPTION=TEXT +DATA
F=NO
POLYGON -RELATIVE POLAR=YES RADIUS=#Re+#hrl+#hrslot+#hms THETA=90-(#teta*5+#tetahmsr)  OPTION=TEXT +DATA
F=NO
POLYGON -RELATIVE POLAR=YES RADIUS=#Re+#hrl+#hrslot THETA=90-(#teta*5+#tetahmsr) OPTION=TEXT +DATA F=NO
POLYGON -RELATIVE POLAR=YES RADIUS=#Re+#hrl+#hrslot THETA=90-(#teta*5+#tetaLrms)  OPTION=TEXT +DATA  F=NO
POLYGON -DATA LINESHAPE=MIDSIDE
POLYGON -RELATIVE POLAR=YES RADIUS=#Re+#hrl+#hrslot+#Lmlr THETA=90-(#teta*5+#tetaLmlr)   OPTION=TEXT +DATA
F=NO
 POLYGON -RELATIVE POLAR=YES RADIUS=#Re+#hrl+#hrslot THETA=90-(#teta*5+#tetaLrsr) OPTION=TEXT +DATA F=NO
 POLYGON -DATA LINESHAPE=STRAIGHT
POLYGON -RELATIVE POLAR=YES RADIUS=#Re+#hrl+#hrslot THETA=90-#teta*6 OPTION=TEXT +DATA -SIZE N=2 BIAS=0.5
F=NO

/Seventh pole
 POLYGON -RELATIVE POLAR=YES RADIUS=#Re+#hrl+#hrslot THETA=90-(#teta*6+#tetahms) OPTION=TEXT +DATA F=NO
POLYGON -RELATIVE POLAR=YES RADIUS=#Re+#hrl+#hrslot+#hms THETA=90-(#teta*6+#tetahms)  OPTION=TEXT +DATA
F=NO
POLYGON -RELATIVE POLAR=YES RADIUS=#Re+#hrl+#hrslot+#hms THETA=90-(#teta*6+#tetahmsr)  OPTION=TEXT +DATA
F=NO
POLYGON -RELATIVE POLAR=YES RADIUS=#Re+#hrl+#hrslot THETA=90-(#teta*6+#tetahmsr) OPTION=TEXT +DATA F=NO
POLYGON -RELATIVE POLAR=YES RADIUS=#Re+#hrl+#hrslot THETA=90-(#teta*6+#tetaLrms)  OPTION=TEXT +DATA  F=NO
POLYGON -DATA LINESHAPE=MIDSIDE
POLYGON -RELATIVE POLAR=YES RADIUS=#Re+#hrl+#hrslot+#Lmlr THETA=90-(#teta*6+#tetaLmlr)   OPTION=TEXT +DATA
F=NO
 POLYGON -RELATIVE POLAR=YES RADIUS=#Re+#hrl+#hrslot THETA=90-(#teta*6+#tetaLrsr) OPTION=TEXT +DATA F=NO
 POLYGON -DATA LINESHAPE=STRAIGHT
POLYGON -RELATIVE POLAR=YES RADIUS=#Re+#hrl+#hrslot THETA=90-#teta*7 OPTION=TEXT +DATA -SIZE N=2 BIAS=0.5
F=NO
```

```
/eight pole
 POLYGON -RELATIVE POLAR=YES RADIUS=#Re+#hrl+#hrslot THETA=90-(#teta*7+#tetahms) OPTION=TEXT +DATA F=NO
POLYGON -RELATIVE POLAR=YES RADIUS=#Re+#hrl+#hrslot+#hms THETA=90-(#teta*7+#tetahms)  OPTION=TEXT +DATA
F=NO
POLYGON -RELATIVE POLAR=YES RADIUS=#Re+#hrl+#hrslot+#hms THETA=90-(#teta*7+#tetahmsr)  OPTION=TEXT +DATA
F=NO
POLYGON -RELATIVE POLAR=YES RADIUS=#Re+#hrl+#hrslot THETA=90-(#teta*7+#tetahmsr) OPTION=TEXT +DATA F=NO
POLYGON -RELATIVE POLAR=YES RADIUS=#Re+#hrl+#hrslot THETA=90-(#teta*7+#tetaLrms)  OPTION=TEXT +DATA  F=NO
POLYGON -DATA LINESHAPE=MIDSIDE
POLYGON -RELATIVE POLAR=YES RADIUS=#Re+#hrl+#hrslot+#Lmlr THETA=90-(#teta*7+#tetaLmlr)   OPTION=TEXT +DATA
F=NO
 POLYGON -RELATIVE POLAR=YES RADIUS=#Re+#hrl+#hrslot THETA=90-(#teta*7+#tetaLrsr) OPTION=TEXT +DATA F=NO
 POLYGON -DATA LINESHAPE=STRAIGHT
POLYGON -RELATIVE POLAR=YES RADIUS=#Re+#hrl+#hrslot THETA=90-#teta*8 OPTION=TEXT +DATA -SIZE N=2 BIAS=0.5
F=NO
POLYGON -RELATIVE POLAR=YES RADIUS=#Re+#hrl+#hrslot+#hms+#Alr THETA=90-#teta*8  OPTION=TEXT +DATA -SIZE
N=3 F=SYMMETRY
POLYGON OPTION=CLOSE LINESHAPE=CURVATURE CURVATURE=-1/(#Re+#hrl+#hrslot+#hms+#Alr) N=200 F=NO

/----------------------------------------
/Creating the air gap near to stator
/----------------------------------------
DRAW +DEFAULTS SHAPE=POLYGON TOLERANCE=5.0E-06 MATERIAL=0 PERM=1 DENS=0 CONDUCTIVITY=0 PHASE=0
VELOCITY=0 N=0 SYMMETRY=0 XCEN=0 YCEN=0 ANGLE=0 NX=1 DX=0 NY=1 DY=0 ROTATIONS=1 TROTATION=0
MIRROR=NO

$IF #hrl+#hrslot+#hms GE #hrl+#hrslot+#Lmlr

POLYGON -RELATIVE POLAR=YES RADIUS=#Re+#hrl+#hrslot+#hms+#Alr+#Al+#Als THETA=90 OPTION=TEXT +DATA
POLYGON -RELATIVE POLAR=YES RADIUS=#Re+#hrl+#hrslot+#hms+#Alr+#Al THETA=90 LINESHAPE=CURVATURE
CURVATURE=0 OPTION=TEXT +DATA N=1 BIAS=0.5 F=SYMMETRY
POLYGON -RELATIVE POLAR=YES RADIUS=#Re+#hrl+#hrslot+#hms+#Alr+#Al THETA=90-(#teta*8) LINESHAPE=CURVATURE
CURVATURE=1/(#Re+#hrl+#hrslot+#hms+#Alr+#Al) OPTION=TEXT +DATA N=200 BIAS=0.5 F=NO
 POLYGON -RELATIVE POLAR=YES RADIUS=#Re+#hrl+#hrslot+#hms+#Alr+#Al+#Als THETA=90-(#teta*8)
LINESHAPE=CURVATURE CURVATURE=0 OPTION=TEXT +DATA N=1 BIAS=0.5 F=NO
POLYGON -RELATIVE POLAR=YES RADIUS=#Re+#hrl+#hrslot+#hms+#Alr+#Al+#Als THETA=90 LINESHAPE=CURVATURE
CURVATURE=-1/(#Re+#hrl+#hrslot+#hms+#Alr+#Al+#Als) OPTION=TEXT +DATA N=200 BIAS=0.5 F=NO
 POLYGON OPTION=close N=5 BIAS=0.5 F=SYMMETRY

$else
  $if #hrl+#hrslot+#Lmlr GT #hrl+#hrslot+#hms
POLYGON -RELATIVE POLAR=YES RADIUS=#Re+#hrl+#hrslot+#Lmlr+#Alr+#Al THETA=90 OPTION=TEXT +DATA
POLYGON -RELATIVE POLAR=YES RADIUS=#Re+#hrl+#hrslot+#Lmlr+#Alr+#Al THETA=90-(#teta*8) LINESHAPE=CURVATURE
CURVATURE=1/(#Re+#hrl+#hrslot+#Lmlr+#Alr+#Al) OPTION=TEXT +DATA N=200 BIAS=0.5 F=NO
POLYGON -RELATIVE POLAR=YES RADIUS=#Re+#hrl+#hrslot+#Lmlr+#Alr+#Al+#Als THETA=90-(#teta*8)
LINESHAPE=CURVATURE CURVATURE=0 OPTION=TEXT +DATA N=1 BIAS=0.5 F=SYMMETRY
POLYGON -RELATIVE POLAR=YES RADIUS=#Re+#hrl+#hrslot+#Lmlr+#Alr+#Al+#Als THETA=90 LINESHAPE=CURVATURE
CURVATURE=-1/(#Re+#hrl+#hrslot+#Lmlr+#Alr+#Al+#Als) OPTION=TEXT +DATA N=200 BIAS=0.5 F=NO
POLYGON OPTION=close N=1 BIAS=0.5 F=SYMMETRY
$end if
$end if

/++ /----------------------------------------
/++ /Middle airgap automatic generation
/++ /----------------------------------------
/++ GAP INCLUDE=ONE SYMMETRY=360/(#teta*8) RADIUS=#Re+#hrl+#hrslot+#hms+#Alr+#Al/2 SLICES=1 SKEW=0 SKEW2=0
BACKGROUND=YES N=#Re+#hrl+#hrslot+#hms+#Alr+#Al/2

$IF #hrl+#hrslot+#hms GE #hrl+#hrslot+#Lmlr
GAP INCLUDE=YES RADIUS=#Re+#hrl+#hrslot+#hms+#Alr+#Al/2 SYMMETRY=360/(#teta*8)
$else
  $if #hrl+#hrslot+#Lmlr GT #hrl+#hrslot+#hms
GAP INCLUDE=YES RADIUS=#Re+#hrl+#hrslot+#Lmlr+#Alr+#Al/2 SYMMETRY=360/(#teta*8)
$end if
$end if

/++ /change the properties for the conductor regions
MODIFY 4, MATE=1, PERM=1,DENS=0,COND=0,PHAS=0,VELO=0 N=1 SYMMETRY=0
MODIFY 6, MATE=1, PERM=1,DENS=0,COND=0,PHAS=0,VELO=0 N=2 SYMMETRY=0
```

MODIFY 8, MATE=1, PERM=1,DENS=0,COND=0,PHAS=0,VELO=0 N=3 SYMMETRY=0
MODIFY 10, MATE=1, PERM=1,DENS=0,COND=0,PHAS=0,VELO=0 N=4 SYMMETRY=0
MODIFY 12, MATE=1, PERM=1,DENS=0,COND=0,PHAS=0,VELO=0 N=5 SYMMETRY=0
MODIFY 102, MATE=1, PERM=1,DENS=0,COND=0,PHAS=0,VELO=0 N=6 SYMMETRY=0
MODIFY 14, MATE=1, PERM=1,DENS=0,COND=0,PHAS=0,VELO=0 N=7 SYMMETRY=0
MODIFY 16, MATE=1, PERM=1,DENS=0,COND=0,PHAS=0,VELO=0 N=8 SYMMETRY=0

/PHASE B
MODIFY 18, MATE=1, PERM=1,DENS=0,COND=0,PHAS=0,VELO=0 N=9 SYMMETRY=0
MODIFY 20, MATE=1, PERM=1,DENS=0,COND=0,PHAS=0,VELO=0 N=10 SYMMETRY=0

/ PHASE C
MODIFY 22, MATE=1, PERM=1,DENS=0,COND=0,PHAS=0,VELO=0 N=11 SYMMETRY=0
MODIFY 24, MATE=1, PERM=1,DENS=0,COND=0,PHAS=0,VELO=0 N=12 SYMMETRY=0

/ pHASE A
MODIFY 26, MATE=1, PERM=1,DENS=0,COND=0,PHAS=0,VELO=0 N=13 SYMMETRY=0
MODIFY 28, MATE=1, PERM=1,DENS=0,COND=0,PHAS=0,VELO=0 N=14 SYMMETRY=0

/ PHASE B
MODIFY 30, MATE=1, PERM=1,DENS=0,COND=0,PHAS=0,VELO=0 N=15 SYMMETRY=0
MODIFY 32, MATE=1, PERM=1,DENS=0,COND=0,PHAS=0,VELO=0 N=16 SYMMETRY=0

/PHASE C
MODIFY 34, MATE=1, PERM=1,DENS=0,COND=0,PHAS=0,VELO=0 N=17 SYMMETRY=0
MODIFY 36, MATE=1, PERM=1,DENS=0,COND=0,PHAS=0,VELO=0 N=18 SYMMETRY=0

/ pHASE A

MODIFY 38, MATE=1, PERM=1,DENS=0,COND=0,PHAS=0,VELO=0 N=19 SYMMETRY=0
MODIFY 40, MATE=1, PERM=1,DENS=0,COND=0,PHAS=0,VELO=0 N=20 SYMMETRY=0
/ PHASE B
MODIFY 42, MATE=1, PERM=1,DENS=0,COND=0,PHAS=0,VELO=0 N=21 SYMMETRY=0
MODIFY 44, MATE=1, PERM=1,DENS=0,COND=0,PHAS=0,VELO=0 N=22 SYMMETRY=0

/ PHASE C
MODIFY 46, MATE=1, PERM=1,DENS=0,COND=0,PHAS=0,VELO=0 N=23 SYMMETRY=0
MODIFY 48, MATE=1, PERM=1,DENS=0,COND=0,PHAS=0,VELO=0 N=24 SYMMETRY=0

/ pHASE A
MODIFY 50, MATE=1, PERM=1,DENS=0,COND=0,PHAS=0,VELO=0 N=25 SYMMETRY=0
MODIFY 52, MATE=1, PERM=1,DENS=0,COND=0,PHAS=0,VELO=0 N=26 SYMMETRY=0
/ PHASE B
MODIFY 54, MATE=1, PERM=1,DENS=0,COND=0,PHAS=0,VELO=0 N=27 SYMMETRY=0
MODIFY 56, MATE=1, PERM=1,DENS=0,COND=0,PHAS=0,VELO=0 N=28 SYMMETRY=0
/ PHASE C
MODIFY 58, MATE=1, PERM=1,DENS=0,COND=0,PHAS=0,VELO=0 N=29 SYMMETRY=0
MODIFY 60, MATE=1, PERM=1,DENS=0,COND=0,PHAS=0,VELO=0 N=30 SYMMETRY=0
/ pHASE A
MODIFY 62, MATE=1, PERM=1,DENS=0,COND=0,PHAS=0,VELO=0 N=31 SYMMETRY=0
MODIFY 64, MATE=1, PERM=1,DENS=0,COND=0,PHAS=0,VELO=0 N=32 SYMMETRY=0
/ PHASE B
MODIFY 66, MATE=1, PERM=1,DENS=0,COND=0,PHAS=0,VELO=0 N=33 SYMMETRY=0
MODIFY 68, MATE=1, PERM=1,DENS=0,COND=0,PHAS=0,VELO=0 N=34 SYMMETRY=0
/ PHASE C
MODIFY 70, MATE=1, PERM=1,DENS=0,COND=0,PHAS=0,VELO=0 N=35 SYMMETRY=0
MODIFY 72, MATE=1, PERM=1,DENS=0,COND=0,PHAS=0,VELO=0 N=36 SYMMETRY=0
/ pHASE A
MODIFY 74, MATE=1, PERM=1,DENS=0,COND=0,PHAS=0,VELO=0 N=37 SYMMETRY=0
MODIFY 76, MATE=1, PERM=1,DENS=0,COND=0,PHAS=0,VELO=0 N=38 SYMMETRY=0
/ PHASE B
MODIFY 78, MATE=1, PERM=1,DENS=0,COND=0,PHAS=0,VELO=0 N=39 SYMMETRY=0
MODIFY 80, MATE=1, PERM=1,DENS=0,COND=0,PHAS=0,VELO=0 N=40 SYMMETRY=0
/ PHASE C
MODIFY 82, MATE=1, PERM=1,DENS=0,COND=0,PHAS=0,VELO=0 N=41 SYMMETRY=0
MODIFY 84, MATE=1, PERM=1,DENS=0,COND=0,PHAS=0,VELO=0 N=42 SYMMETRY=0
/ pHASE A
MODIFY 86, MATE=1, PERM=1,DENS=0,COND=0,PHAS=0,VELO=0 N=43 SYMMETRY=0
MODIFY 88, MATE=1, PERM=1,DENS=0,COND=0,PHAS=0,VELO=0 N=44 SYMMETRY=0
/ PHASE B

```
MODIFY 90, MATE=1, PERM=1,DENS=0,COND=0,PHAS=0,VELO=0 N=45 SYMMETRY=0
 MODIFY 92, MATE=1, PERM=1,DENS=0,COND=0,PHAS=0,VELO=0 N=46 SYMMETRY=0
/ PHASE C
MODIFY 94, MATE=1, PERM=1,DENS=0,COND=0,PHAS=0,VELO=0 N=47 SYMMETRY=0
 MODIFY 96, MATE=1, PERM=1,DENS=0,COND=0,PHAS=0,VELO=0 N=48 SYMMETRY=0

/ /external circuit for the conductors

/ /Phase A
 EXTERNAL
DEFINE TYPE=FILAMENTARY SYMMETRY=1 LENGTH=20 VOLT=#U PHASE=0 RESISTANCE=#R1 INDUCTANCE=0
CAPACITANCE=0 INITIALCAPVOLT=0
CONDUCTOR=1 SENSE=GO TURNS=2 UNIT=0 FUNCTION=ADD
CONDUCTOR=6 SENSE=GO TURNS=2 UNIT=0 FUNCTION=ADD
CONDUCTOR=7 SENSE=RETURN TURNS=2 UNIT=0 FUNCTION=ADD
CONDUCTOR=8 SENSE=RETURN TURNS=2 UNIT=0 FUNCTION=ADD
CONDUCTOR=13 SENSE=GO TURNS=2 UNIT=0 FUNCTION=ADD
CONDUCTOR=14 SENSE=GO TURNS=2 UNIT=0 FUNCTION=ADD
CONDUCTOR=19 SENSE=RETURN TURNS=2 UNIT=0 FUNCTION=ADD
CONDUCTOR=20 SENSE=RETURN TURNS=2 UNIT=0 FUNCTION=ADD
CONDUCTOR=25 SENSE=GO TURNS=2 UNIT=0 FUNCTION=ADD
CONDUCTOR=26 SENSE=GO TURNS=2 UNIT=0 FUNCTION=ADD
CONDUCTOR=31 SENSE=RETURN TURNS=2 UNIT=0 FUNCTION=ADD
CONDUCTOR=32 SENSE=RETURN TURNS=2 UNIT=0 FUNCTION=ADD
CONDUCTOR=37 SENSE=GO TURNS=2 UNIT=0 FUNCTION=ADD
CONDUCTOR=38 SENSE=GO TURNS=2 UNIT=0 FUNCTION=ADD
CONDUCTOR=43 SENSE=RETURN TURNS=2 UNIT=0 FUNCTION=ADD
CONDUCTOR=44 SENSE=RETURN TURNS=2 UNIT=0 FUNCTION=ADD

 FUNCTION=QUIT

/Phase B
DEFINE TYPE=FILAMENTARY SYMMETRY=1 LENGTH=20 VOLT=#U PHASE=0 RESISTANCE=#R1 INDUCTANCE=0
CAPACITANCE=0 INITIALCAPVOLT=0
CONDUCTOR=2 SENSE=RETURN TURNS=2 UNIT=0 FUNCTION=ADD
CONDUCTOR=3 SENSE=RETURN TURNS=2 UNIT=0 FUNCTION=ADD
CONDUCTOR=9 SENSE=GO TURNS=2 UNIT=0 FUNCTION=ADD
CONDUCTOR=10 SENSE=GO TURNS=2 UNIT=0 FUNCTION=ADD
CONDUCTOR=15 SENSE=RETURN TURNS=2 UNIT=0 FUNCTION=ADD
CONDUCTOR=16 SENSE=RETURN TURNS=2 UNIT=0 FUNCTION=ADD
CONDUCTOR=21 SENSE=GO TURNS=2 UNIT=0 FUNCTION=ADD
CONDUCTOR=22 SENSE=GO TURNS=2 UNIT=0 FUNCTION=ADD
CONDUCTOR=27 SENSE=RETURN TURNS=2 UNIT=0 FUNCTION=ADD
CONDUCTOR=28 SENSE=RETURN TURNS=2 UNIT=0 FUNCTION=ADD
CONDUCTOR=33 SENSE=GO TURNS=2 UNIT=0 FUNCTION=ADD
CONDUCTOR=34 SENSE=GO TURNS=2 UNIT=0 FUNCTION=ADD
CONDUCTOR=39 SENSE=RETURN TURNS=2 UNIT=0 FUNCTION=ADD
CONDUCTOR=40 SENSE=RETURN TURNS=2 UNIT=0 FUNCTION=ADD
CONDUCTOR=45 SENSE=GO TURNS=2 UNIT=0 FUNCTION=ADD
CONDUCTOR=46 SENSE=GO TURNS=2 UNIT=0 FUNCTION=ADD

FUNCTION=QUIT

//Phase C
DEFINE TYPE=FILAMENTARY SYMMETRY=1 LENGTH=20 VOLT=#U PHASE=0 RESISTANCE=#R1 INDUCTANCE=0
CAPACITANCE=0 INITIALCAPVOLT=0
CONDUCTOR=4 SENSE=GO TURNS=2 UNIT=0 FUNCTION=ADD
CONDUCTOR=5 SENSE=GO TURNS=2 UNIT=0 FUNCTION=ADD
CONDUCTOR=11 SENSE=RETURN TURNS=2 UNIT=0 FUNCTION=ADD
CONDUCTOR=12 SENSE=RETURN TURNS=2 UNIT=0 FUNCTION=ADD
CONDUCTOR=17 SENSE=GO TURNS=2 UNIT=0 FUNCTION=ADD
CONDUCTOR=18 SENSE=GO TURNS=2 UNIT=0 FUNCTION=ADD
CONDUCTOR=23 SENSE=RETURN TURNS=2 UNIT=0 FUNCTION=ADD
CONDUCTOR=24 SENSE=RETURN TURNS=2 UNIT=0 FUNCTION=ADD
CONDUCTOR=29 SENSE=GO TURNS=2 UNIT=0 FUNCTION=ADD
CONDUCTOR=30 SENSE=GO TURNS=2 UNIT=0 FUNCTION=ADD
CONDUCTOR=35 SENSE=RETURN TURNS=2 UNIT=0 FUNCTION=ADD
CONDUCTOR=36 SENSE=RETURN TURNS=2 UNIT=0 FUNCTION=ADD
CONDUCTOR=41 SENSE=GO TURNS=2 UNIT=0 FUNCTION=ADD
CONDUCTOR=42 SENSE=GO TURNS=2 UNIT=0 FUNCTION=ADD
```

```
CONDUCTOR=47 SENSE=RETURN TURNS=2 UNIT=0 FUNCTION=ADD
CONDUCTOR=48 SENSE=RETURN TURNS=2 UNIT=0 FUNCTION=ADD

FUNCTION=QUIT

QUIT

/ Changing the side properties

  EDIT REG1=1 REG2=1 OPTION=SIDE NUMBER=12  F=SYMMETRY  NEIGHBOURS=YES
/++ EDIT REG1=5 REG2=5 OPTION=SIDE NUMBER=8  F=SYMMETRY  NEIGHBOURS=YES
EDIT REG1=4 REG2=4 OPTION=SIDE NUMBER=4  F=SYMMETRY  NEIGHBOURS=YES
 EDIT REG1=5 REG2=5 OPTION=SIDE NUMBER=4  F=SYMMETRY  NEIGHBOURS=YES
EDIT REG1=6 REG2=6 OPTION=SIDE NUMBER=4  F=SYMMETRY  NEIGHBOURS=YES

/++ EDIT REG1=152 REG2=152 OPTION=SIDE NUMBER=8  F=SYMMETRY  NEIGHBOURS=YES

/++ EDIT REG1=152 REG2=152 OPTION=SIDE NUMBER=4  F=SYMMETRY  NEIGHBOURS=YES
/++  EDIT REG1=153 REG2=153 OPTION=SIDE NUMBER=4 F=SYMMETRY  NEIGHBOURS=YES
EDIT REG1=126 REG2=126 OPTION=SIDE NUMBER=3  F=SYMMETRY  NEIGHBOURS=YES
EDIT REG1=126 REG2=126 OPTION=SIDE NUMBER=1  F=SYMMETRY  NEIGHBOURS=YES
EDIT REG1=102 REG2=102 OPTION=SIDE NUMBER=4  F=SYMMETRY  NEIGHBOURS=YES
EDIT REG1=103 REG2=103 OPTION=SIDE NUMBER=4  F=SYMMETRY  NEIGHBOURS=YES
EDIT REG1=122 REG2=122 OPTION=SIDE NUMBER=2  F=SYMMETRY  NEIGHBOURS=YES

/++ EDIT REG1=172 REG2=172 OPTION=SIDE NUMBER=2  F=SYMMETRY  NEIGHBOURS=YES
/++ EDIT REG1=176 REG2=176 OPTION=SIDE NUMBER=3  F=SYMMETRY  NEIGHBOURS=YES
/++
/++ EDIT REG1=151 REG2=151 OPTION=SIDE NUMBER=4  F=SYMMETRY  NEIGHBOURS=YES

/Rotor

/CHANGING THE MATERIAL PROPERTIES FOR THE UNUSED SLOT
MODIFY REG1=98 MATERIAL=0 PERM=1 ERASE=NO
MODIFY REG1=100 MATERIAL=0 PERM=1 ERASE=NO

/++ Connect symetric boundaries
/++   SYMMETRY ANGLE=#teta*8 CONNECTION=NEGATIVE DELETE=YES

/----------------------------------------
/Inserting the BH curve for magnets
/----------------------------------------

 ADD  H=-915000, B=0
ADD H=-686250, B=0.3050
ADD H=-457500, B=0.6100
ADD H=-228750, B=0.9150
 ADD H=0, B=1.22
QUIT

/------------------------------------------------------------

BHDATA MENU=RESET
BHDATA MATERIAL=4 TYPE=SAME MENU=SET
BHDA
LOAD FILE='C:\Program Files\Vector Fields\Opera 13.0\bh\default.bh'
QUIT

BHDATA MENU=RESET
BHDATA MATERIAL=5 TYPE=SAME MENU=SET
BHDA
LOAD FILE='C:\Program Files\Vector Fields\Opera 13.0\bh\default.bh'
QUIT

/----------------------------------------
/Model check
/----------------------------------------
CHECK

TEST REG1=1 REG2=* POINTS=BOTH QUERY=NO SIDES=UNDER MATCH=YES DRAW=NO
```

```
/----------------------------------------
/Model reconstruction
/----------------------------------------

SECTION FIXEDASPECT=YES
RECONST XMIN=1 XMAX=-1

/----------------------------------------
/Mesh generation in background
/----------------------------------------

MESH=NO BACKGROUND=NO ERASE=YES FILL=REGION NODES=CORNERS LABEL=REGION AXES=YES

MESH +ERRORCHECK TOLERANCE=5.0E-6 -DISPLAY | NO

/----------------------------------------
/Analysis type
/----------------------------------------

 SOLVE TYPE=RM
$do #increment 0 360 1

$end do


DRIV NUMB=1 TYPE=DEFAULT +SGUI
DRIVE TYPE=DC
DRIV NUMB=2 TYPE=DEFAULT +SGUI
DRIVE TYPE=DC
DRIV NUMB=3 TYPE=DEFAULT +SGUI
DRIVE TYPE=DC
DRIV NUMB=4 TYPE=DEFAULT +SGUI
DRIVE TYPE=DC


LOGFILE LOGGING=SOLUTION COL1=TTIME COL2=rmtorque COL3=e1 COL4=e2 COL5=e3 COL6=i1 COL7=i2 COL8=i3
COL9=rmspeed COL10=rmangle

/ Adaptive steep

/++ DATA LINEAR=NO TOLERANCE=1.0E-03 NITERATION=31 TSTYPE=FIXED TSTEP=7.407407e-7 MOTIONTYPE=FIXED
RMVEL=1500

/++ DATA LINEAR=YES TSTYPE=ADAPTIVE TSINITIAL=0 TSTOLERANCE=1.0E-03 MOTIONTYPE=FIXED RMVEL=20
/++ DATA LINEAR=YES TSTYPE=FIXED TSTEP=2.0000e-004 MOTIONTYPE=FIXED RMVEL=1500/(360/(#teta*8))
DATA LINEAR=NO TOLERANCE=1.0E-03 NITERATION=100 TSTYPE=FIXED TSTEP=5.5556e-005 MOTIONTYPE=FIXED
RMVEL=1500/(360/(#teta*8))
QUIT

/++ DATA LINEAR=NO TOLERANCE=1.0E-03 NITERATION=31 TSTYPE=FIXED TSTEP=1.851851e-7 MOTIONTYPE=FIXED
RMVEL=1500
/++ QUIT

/Writing the file and starting analysis
/++ write FILE='D:\Adrian\Optimization_Cosmo\Slot-simulation-rotativ-entire\Slot-simulation-rotativ-entire_new.op2' +SOLVENOW
write FILE='Slot'


/----------------------------------------
/Starting the RM analysis
/----------------------------------------
/++ WRITE FILE='D:\Adrian\Optimization_Cosmo\Slot-simulation-rotativ-entire.op2' +SOLVENOW

  /$OS OPERAANL WRD2=SOLVE WRD3='D:\Adrian\Optimization_Cosmo\Slot-simulation-rotativ-entire\Slot-simulation-rotativ-
entire.op2' WRD4=FORE

 /END
```

Appendix 5. Incremental encoder for rotor position detection

Incremental encoders

Mini series end shaft ø12 mm, hollow shaft ø6 mm
Resolution 10...2048 pulses

BHK

BHK with end shaft

Features

- **Mini encoder with end shaft or hollow shaft**
- **Optical sensing**
- **Resolution max. 2048 ppr**
- **Housing ø40 mm**
- **Operation speed max. 12000 rpm**
- **End shaft ø12 mm, hollow shaft ø6 mm**
- **Versatile mounting accessories**

Technical data - electrical ratings

Voltage supply	5 VDC ±10 % 10...30 VDC
Consumption w/o load (typ.)	60 mA (5 VDC) 30 mA (24 VDC)
Resolution (steps/turn)	10...2048
Reference signal	Zero pulse, width 90°
Sensing method	Optical
Output frequency	≤100 kHz
Output signals	A 90° B, N + inverted
Output circuit	Linedriver/RS422 Push-pull short-circuit proof
Interference immunity	DIN EN 61000-6-2
Emitted interference	DIN EN 61000-6-3
Approval	UL approval / E217823

Technical data - mechanical design

Dimensions (flange)	ø40 mm
Shaft	ø6 mm hollow shaft ø12 mm end shaft
Protection DIN EN 60529	IP 42, IP 65
Operating speed	≤12000 rpm
Operating torque typ.	0.0021 Nm (IP 42) 0.0075 Nm (IP 64)
Materials	Housing: polyamide black Flange: aluminium
Operating temperature	-20...+85 °C
Relative humidity	95 % non-condensing
Resistance	DIN EN 60068-2-6 Vibration 10 g, 10-200 Hz DIN EN 60068-2-27 Shock 50 g, 11 ms
Connection	Connector M9, 5-pin Connector M9, 8-pin Cable 1 m

Appendix 6. Three-phase full-bridge voltage-source inverter

SEMISTACK - IGBT

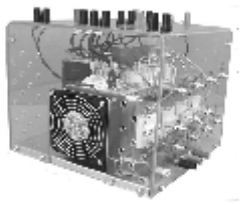

SEMITRANS Stack[1)]

Three-phase rectifier + inverter with brake chopper

SEMITEACH - IGBT
SKM 50 GB 123D
SKD 51
P3/250F

Features

- Multi-function IGBT converter
- Transparent enclosure to allow visualization of every part
- IP2x protection to minimize safety hazards
- External banana/BNC type connectors for all devices
- Integrated drive unit offering short-circuit detection/cut-off, power supply failure detection, interlock of IGBTs + galvanic isolation of the user
- Forced-air cooled heatsink

Typical Applications

- Education: One stack can simulate almost all existing industrial applications:
- 3-phase inverter+brake chopper
- Buck or boost converter
- Single phase inverter
- Single or 3-phase rectifier

[1)] Photo non-contractual

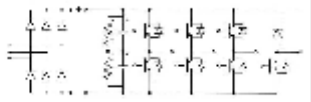

B6U + B6CI + E1CIKF

Circuit	I_{rms} (A)	V_{ac} / V_{dcmax}	Types
B6CI	30	440 / 750	SEMITEACH - IGBT

Symbol	Conditions	Values	Units
I_{rms}	no overload	30	A
	IGBT - 4x SKM 50 GB 123D		
V_{CES}		1200	V
$V_{CE(SAT)}$	I_C= 50A, V_{GE}= 15V, chip level; T_j= 25(125)°C	2,7 (3,5)	V
V_{GES}		±20	V
I_C	T_{case}= 25 (80)°C	50 (40)	A
I_{CM}	T_{case}= 25 (80)°C; t_p= 1ms	100 (80)	A
	Rectifier - 1x SKD 51/14		
$V_{in(max)}$	without filter	3 x 480	V
	with filter	3 x 380	V
	DC Capacitor bank - Electrolytic 2x 2200µF/400V		
C_{eqv}	total equivalent capacitance	1100 / 800	µF / V
V_{DCmax}	max. DC voltage applied to the capacitor bank	750	V
	Driver - 4x SKHI 22		
Power supply		0 / 15	V
Current consumption	max; per driver	16	mA
Thermal trip	Normally Open type (NO)	71	°C

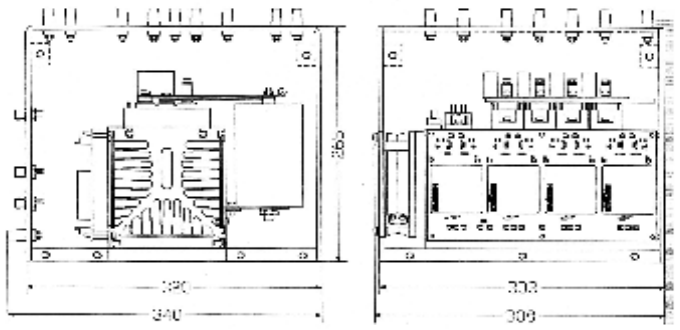

General dimensions

Appendix 7. Protection card diagram

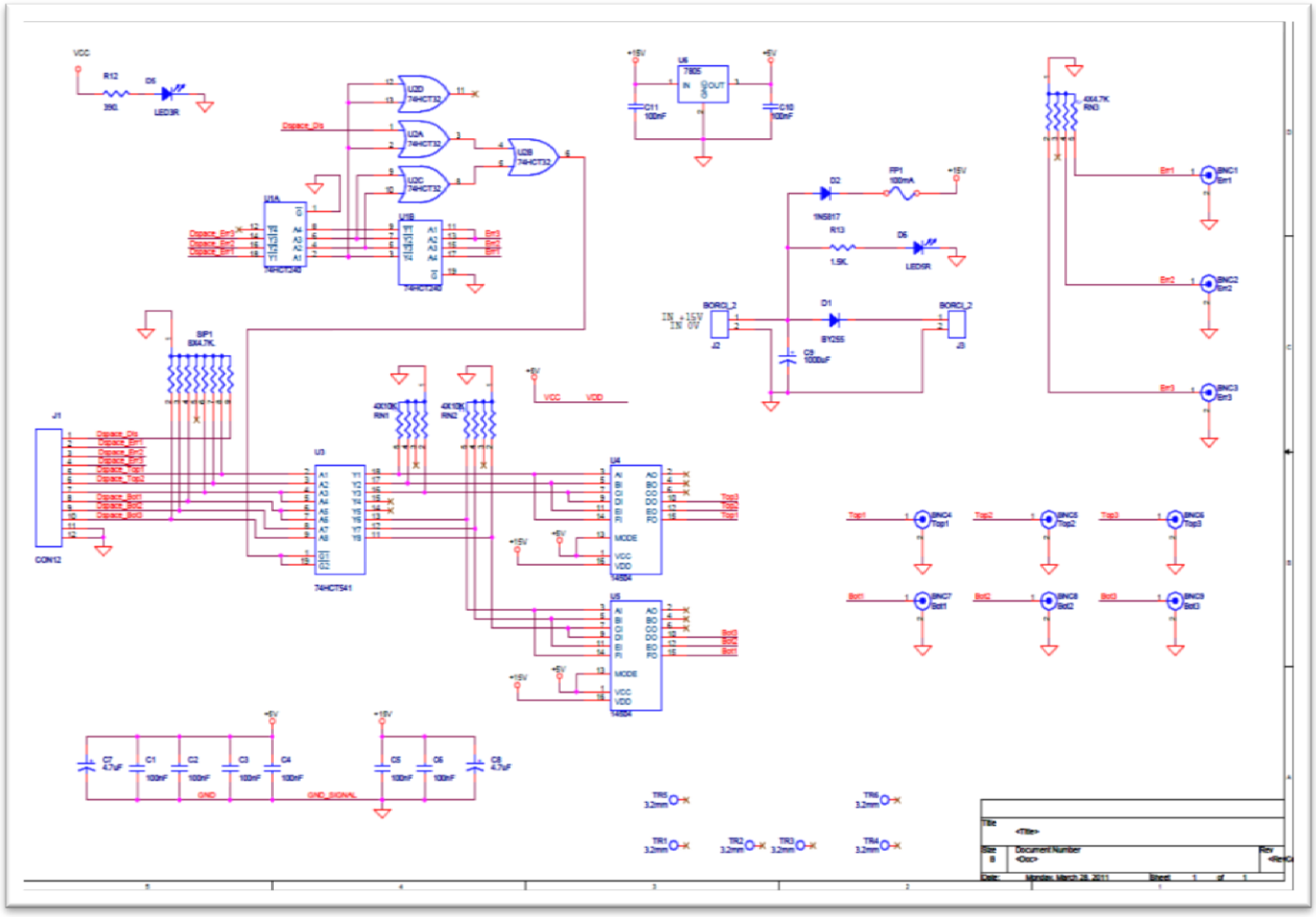

europass

Curriculum Vitae

Europass

Personal Information

First name/	**Pop Adrian Augustin**
Telephone	(+40) 749225402
E-mail	augustin.pop@mae.utcluj.ro ; adrian_augustin_pop@yahoo.com, adrian.pop@ec-lille.fr
Date of Birth	16 December 1984
Place of Birth	Cehu Silvaniei, Salaj, Romania
Nationality	Romanian

Education and Training

2009-present	Full time **Ph.D. Student** at The Technical University Cluj-Napoca, Faculty of Electrical Engineering, General Electrical Engineering, Department of Electrical Machines, Marketing and Management. Member of The Special Electric Machines and Light Electric Traction (SEMLET) Research Laboratory Faculty of Electrical Engineering, Technical University of Cluj-Napoca Full time **Ph.D. Student** at The Ecole Centrale de Lille, France, Faculty of Electrical Engineering and Power Electronics. Member of Optimization team “Laboratoire d'électrotechnique et d'électronique de puissance de Lille”-**L2EP (** Laboratory of Electrical

	Engineering and Power Electronics Research Laboratory).
	Master degree in Electrical Engineering, Department of Electrical Drives and Robots**.**
2009-2010	**Erasmus student** at Ecole Centrale de Lille, France, February-June 2009.
2004-2009	**Electrical Engineer** from The Technical University Cluj-Napoca, Romania
	Faculty of Electrical Engineering,
	Electrical Devices and Engines Specialisation 5th year (of 5)
	Graduated : June 2009
2000 - 2004	**High School graduate** at "Gheorghe Pop de Basesti", Cehu Silvaniei, Romania
	Mathematics and Informatics Classes;
	Computer Operator and Programmer Diploma
Teaching experience	
Employer	Ecole Centrale de Lille, France
Laboratory course	"Electromechanical conversion and speed control." / "Conversion Electromécanique et Variation de Vitesse."
Time period	February-August 2012
Articles reviewing experience	Conference on Electrical Machines – **ICEM 2012**, Marseille, France.
	International Aegean Conference on Electric Machines and Power Electronics – **ACEMP 2011**, Istanbul, Turkey

Languages

French	Very Good
English	Very Good
Romanian	Native
Hungarian	Beginner

Computer Skills

Programming Skills	PcOpera (Vector Fields), JMAG, Flux, SolidWorks, Optimus, MathCAD, Matlab, Microsoft Office.
	AutoCAD.

Publications

2012

Adrian Augustin POP, F. Gillon, and M.M. Radulescu, ***"Space harmonics modeling of an axial flux permanent magnet machine",*** Conférence Européenne sur les Méthodes Numériques en Electromagnétisme (NUMELEC 2012), Marseille, France

Adrian Augustin POP, F. Gillon, M.M. Radulescu, ***"Modelling and permanent magnet shape optimization of an axial- flux machine"***, Proceedings of International Conference on Electrical Machines – ICEM, 2012, Marseille, France.

Lar, Ionut Andrei ; Radulescu, Mircea ; Ritchie, Ewen ; **Adrian Augustin POP**.***"Current control methods for grid-side three-phase PWM voltage-source inverter in distributed generation systems."*** In: Proceedings of the 13th International Conference on Optimization of Electrical and Electronic Equipment, OPTIM2012. IEEE Press, 2012.

"Buck-Boost Corrector Implementing for Compact Fluorescent Lamp Applications [RF-003549] Petre-Dorel Teodosescu", Mircea Bojan, **Adrian Augustin POP**, Richard Marschalko In: Proceedings of the 13th International Conference on Optimization of Electrical and Electronic Equipment, OPTIM2012. IEEE Press, 2012.

2011	**Adrian Augustin POP**, Frédéric GILLON, Mircea M. RĂDULESCU „***Modeling and optimization of a small axial-flux brushless permanent-magnet motor for electric traction purposes",*** X International Conference, MODERN ELECTRIC TRACTION, MET'2011, 9-2011.
2010	**Adrian Augustin POP**, Mircea M. Rădulescu ***"****The dynamics performance analysis of electronically-commutated axial flux permanent magnet machine.****"***
2007	**Adrian Augustin POP**, Frédéric GILLON, Mircea M. RĂDULESCU *"Modelisation et optimization d'un moteur synchrone a aimants permanents et barriers de flux."* **Adrian Augustin POP**, Richard Marschalko *"Digital signal processing system, implemented with dsPIC* *for public network conditioning research with dc PWM converters"* 2007, Student Symposium project.
Research interests	Small electronically-commutated motors Special electric machines Special electric motor/generators: • Integrated starter/alternators for automotive applications • Integrated motor/generators for flywheel energy storage applications Permanent magnet machines Industrial Electrical Installation Design of variable speed motor applications Magnetic Field computation in electrical machines, FEA Design, Modeling and Control in electrical machines Etc.

Driving license	B category
Working address	P.O. Box 345, RO-400110 Cluj-Napoca, Romania Phone: +40 264 401829; Fax: +40 264 593117

Author's papers related to the thesis

1. **A.A. Pop**, F. Gillon, M.M. Radulescu, **Modelling and permanent magnet shape optimization of an axial-flux machine**, *Proc. XXth International Conference Electrical Machines – ICEM 2012.*
(Paper included in IEEE Xplore database *http://ieeexplore.ieee.org/stamp/stamp.jsp?tp=&arnumber=6349891*)

2. **A.A. Pop**, F. Gillon, M.M. Radulescu, **Modeling and optimization of a small axial-flux brushless permanent-magnet motor for electric traction purposes,** *Proc. Xth International Conference on Modern Electric Traction – MET '2011* (ISSN-0138-0370)

3. **A.A. Pop**, F. Gillon, M.M. Radulescu, **Space harmonics modeling of an axial-flux permanent-magnet machine,** *Proc. Conférence Européenne sur les Méthodes Numériques en Electromagnétisme – NUMELEC 2012***,** CD-ROM.

4. I.A. Lar, M.M. Radulescu, E.A. Ritchie, **A.A. Pop**, ***"Current control methods for grid-side three-phase PWM voltage-source inverter in distributed generation systems."*** *Proc. 13th International Conference on Optimization of Electrical and Electronic Equipment – OPTIM 2012.*
(Paper included in IEEE Xplore database *http://ieeexplore.ieee.org/stamp/stamp.jsp?tp=&arnumber=6231945&isnumber=6231751&tag=1*)

5. P.-D. Teodosescu, M. Bojan, **A.A. Pop**, R. Marschalko, **Buck-boost corrector implementing for compact fluorescent lamp applications [RF-003549],** *Proc. 13th International Conference on Optimization of Electrical and Electronic Equipment – OPTIM 2012.*
(Paper included in IEEE Xplore database *http://ieeexplore.ieee.org/stamp/stamp.jsp?tp=&arnumber=6231878&isnumber=6231751*)

Modeling and permanent-magnet shape optimization of an axial-flux machine

A.A. Pop, F. Gillon, M. M. Radulescu

Abstract – **This paper proposes a modeling method for axial-flux permanent-magnet machine (AFPMM) based on a finite elements analysis, and achieves a shape optimization of AFPMM poles. To solve the questions regarding the modeling of AFPMM with surface-mounted PMs, an axial 3-D to radial 2-D finite-element transformation is proposed. A special analytical method for back-emf computation is also provided. The results related to 2-D finite-element analysis are presented and compared with the experimental ones, validating the proposed approach.**

The amount of space-harmonic content in AFPMM is a primary concern to the machine designer due to its impact on the AFPMM performances. These harmonics are directly related to the flux-density and mmf distributions in the airgap, which are mainly determined by the PM excitation. Therefore, the slotless machine is analyzed. The influence of design parameters on the total harmonic distortion (THD) and the methodology to reduce space harmonics by selecting the appropriate PM shape and size are also addressed in this paper. The space-harmonic analysis is carried out according to the variety of design parameters of the finite element models.

Index Terms-- **axial-flux permanent-magnet machine, finite-element modeling and analysis, total harmonic distortion, design optimization**

I. INTRODUCTION

Axial-flux permanent magnet machines (AFPMMs) have higher torque, better power density and lower noise as compared to traditional radial-flux permanent magnet machines, and thus have gained popularity in recent years [1,2].

AFPMMs consist of a rotor-disc carrying magnets that produce the axial flux [3], and a stator-disc containing the phase windings. There are possible many variations in this basic design [4], including single-sided [5], double-sided [6], toroidal [7], and multi-disc designs [8].

The AFPMM considered in this paper is a two-stators, and one-rotor topology. The rotor is sandwiched between the two stators. The studied prototype machine is a three-phase AFPMM with one-rotor-two-stators topology and 4 pole-pairs. The rated power is 0.3 kW and the rated rotational speed is 1500 rpm. The magnets are of high-energy NdFeB-type, and are glued on the solid-iron disc-rotor. The material of the stator core is a fully-processed electrical steel sheet M600-50A. The stator has a particular construction because it is formed by 25 slots.

The torque developed by AFPMM is often affected by harmonics of various origins, such as

- space harmonics of the MMF, which are due to the non-sinusoidal distribution of the armature phase windings;
- space harmonics caused by the presence of stator slots;
- time harmonics related to the power electronic supply, and affecting the stator-armature current.

Space harmonics in AFPMMs are the main concern of the present paper. Starting from a simplified model but enough accurate and fast, the authors present a technique allowing to modify automatically the space harmonics. Finally, the shape optimization technique, as a way to solve this problem, is described and applied on the AFPMM.

II. MODELING OF AFPMMs

In modeling of AFPMMs, the fastness and accuracy of the computations are very important aspects. Using finite-element (FE) field analysis, we can take into account the 3-D structure of the machine, but performing the computations is often too hard and time-consuming. In order to evaluate quickly the performance of the AFPMM, the 2-D FE analysis, which is performed on the average radius of the machine, is a time-saving option, especially if the model will be further optimized. The main idea of the design method is to subdivide the AFPMM into independent computation planes, and to use the average radius of the machine as a design plane. This approach is sufficiently accurate to predict the motor performance, and for validation the finite element results will be compared with the experimental ones.

The airgap flux density is an important design parameter, having notable effect on the machine performances. Therefore, in order to optimize the machine, the airgap flux density must be determined correctly [9].

The airgap flux-density modeling method is based on Fourier-series development. This technique enables to identify the cross-coupling between different spatial and temporal field components, and thus provides a very useful insight into the relationship between different design variables and machine performances. For the first analysis, the effect of stator slots on the magnetic field is taking into account.

A. Axial 3-D to radial 2-D finite element transformation

From the modeling point of view, an axial flux machine has a 3D geometry but using the 2-D FEA, which is performed on the average radius of the machine, is a time saving solution and it is also providing sufficiently accurate computation results.

The method of transforming the 3-D geometry of an AFPMM into the corresponding 2-D model is illustrated in Fig.1.

The 3D rotational movement of the machine (θ_{3D}) Fig. 1. (a) is transformed into 2D linear motion (L_{2D}), Fig. 1. (c). The 3D to 2D conversion formula is:

$$L_{2D} = \theta_{3D} R_{average} \quad (1)$$

978-1-4673-0142-8/12/$26.00 ©2012 IEEE

The transformation presented in (1) is performed as follows (Fig.1.): we take a straight parallel cut to the axis of the AFPMM by an average radius; because of machine symmetry only half of model needs to be analyzed (the symmetry is fixed by a straight cut along the rotor). The extracted pole with the average computation radius ($R_{average}$) can be visualized in Fig. 1. (b).

The 2-D representative design plane is set on the average radius of the AFPMM [10]. The 3D extracted pole is than transformed into 2D linear pole (c). The discoid shape is built with a constant magnet width / pole-pitch ratio for all diameters of the machine, and thus the angular width for the magnets remain constant. The width of the slots is constant throughout the radial length of the machine, but for different diameters the angular widths of slots and teeth are variable.

The structure from Fig. 1 (c) can be analyzed with a 2D model, easier to use and much faster in computation time.

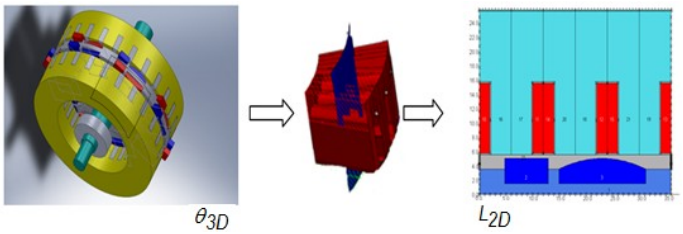

Fig. 1. (a) Design of the AFPMM under study; (b) 3-D FE-model for one magnetic pole; (c) 3-D model reduced to 2-D representative plane.

2D-model simulations can be performed in static but taking into consideration the rotation, the currents time variation and the coupling with external circuits, another transformation can be applied to create a rotating movement.

In order to use the finite-element rotation module, the model needs to be analyzed in such a way that the linear machine obtained in Fig. 2 needs to be placed at a large curvature radius from the origin. The curvature radius is chosen in such way that the rotating structure will be almost equivalent to the linear model and the rotor will be able to move without interacting with the stator.

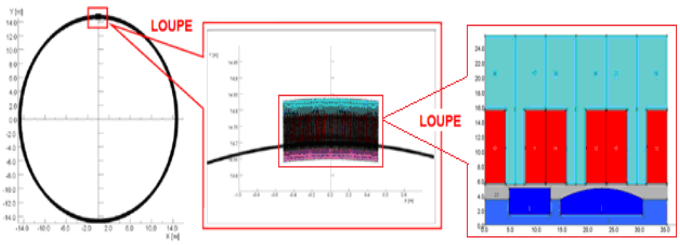

Fig. 2. Linear 2-D motion to rotating 2-D motion transformation.

The aim of this section is to obtain a 2D model which will be utilized to generate correctly, rapidly and efficiently the flux density and electromotive force waveforms of the AFPMM. Then in order to modify the space harmonics the shape of permanent magnet will be furthermore optimize.

III. MODELING RESULTS

A. Effect of nonsymmetrical pole

The effect of stator slotting on the no-load magnetic flux distribution is now investigated. The airgap flux density always drops at stator slot openings, and this effect has a significant influence on the values of the flux and back-emf. For this reason, it is important to accurately analyze the airgap flux density. The rotor-PM arrangement is shown in Fig.3. It can be seen that there are 16 magnets glued on the rotor body. There are two separated PMs for each pole. Due to this PM arrangement, the flux density distribution has an unusual waveform. The first PM has a rectangular geometry and the second PM has an arch form. The PMs of one pole are shown in Fig.4. This rotor-PM arrangement needs a special approach in order to analyze correctly the AFPMM airgap flux density.

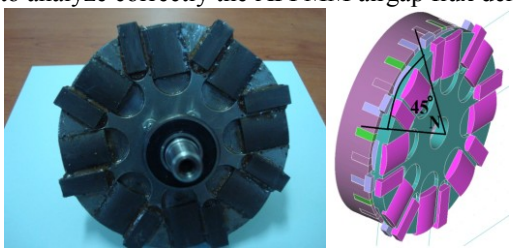

Fig.3 (a) The rotor with permanent magnets (b) One of the two stators and the rotor with its PM arrangement.

The 2-D representation of one pole of the AFPMM, and the no-load magnetic flux distribution in the airgap are shown in Fig.4. *A* and *A'* represent the winding of the phase *A*, and *B* denotes the PM-created flux density in the airgap. The superposition of the flux density with the AFPMM geometry allows pointing out the effect of the slots on the flux-density waveform.

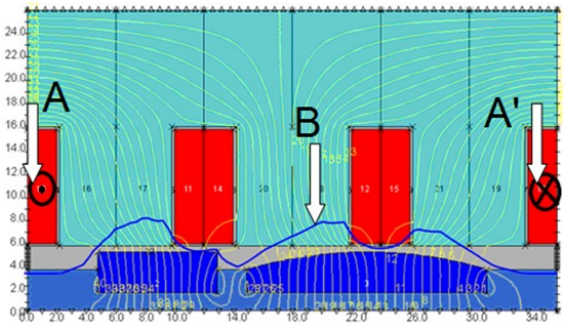

Fig. 4. No-load magnetic flux distribution for one PM-rotor pole.

The angular variation of the airgap flux density due to the rectangular and arch-shaped rotor-PMs for one pole is shown in Fig.5. The first curve of the flux density in the airgap is due to the shape of rectangular magnet and the second curvature is due to the arc shape magnet. The stator slotting effect has a large impact on the flux density shape. We can see a flux density decreasing in the areas where the flux density crosses the slots. There the flux density amplitude is oscillating due to the slotting effect. In the FE model the flux captured by the coils of one phase is computed with the subtraction between the vector potential in the slot with the go conductor (A) and the return conductor (A') multiplied by the length. The captured magnetic flux is presented in Fig. 6.

Using Faraday's law, emf is the time derivative of flux presented in Fig. 7. These computations allow us to see the interconnection between the airgap magnetic flux-density (Fig. 5), flux distribution (Fig. 6) and electromotive force (Fig. 7).

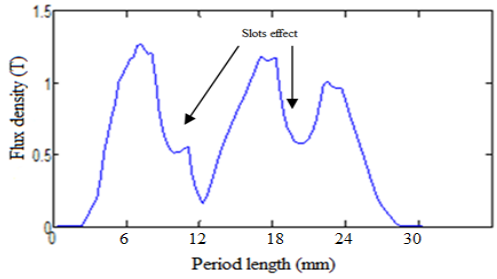

Fig. 5. Airgap magnetic flux-density due to rotor-PMs.

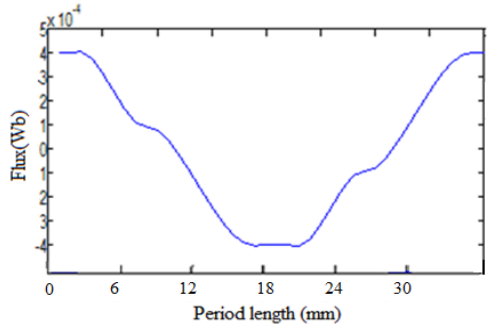

Fig. 6. Flux distribution in the stator core.

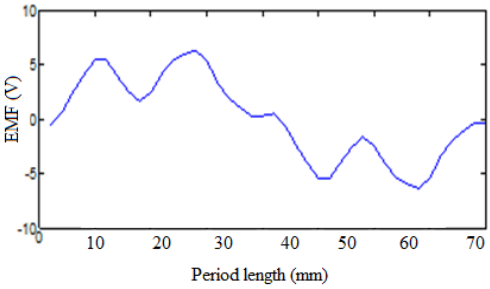

Fig. 7. FE-computed back-emf waveform.

B. Back-emf computation

In order to minimize de cogging torque the AFPMM is composed of 25 teeth. The 2D finite element simulation has been performed for 3 teeth/pole.

An important simulation result is related to the back-emf waveform (Fig.7). It is to be pointed out that the pole-pitch is $\frac{2\cdot\pi}{8}$, whereas the coil pitch is $\frac{2\cdot\pi}{25}\cdot 3$. The phase shift between these two angles defines the phase shift that's need to be add between each electromotive forces Fig. 8. The phase difference between the coil pitch and magnetic pole is 1.8 degrees. The signal obtained is shifted by 1.8 degrees for all 8 poles of the machine. The coils with a phase shift of 1.8 degree are allowing making an estimation of the phase back-emf (Fig. 9). Finally, composed signals are collected and divided by the number of coils. The obtained back-emf signal is presented in Fig. 10.

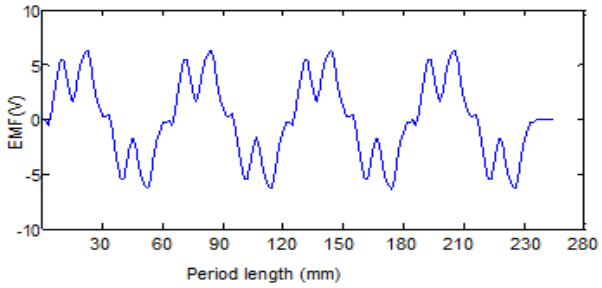

Fig. 8. Analytically-obtained back-emf waveform.

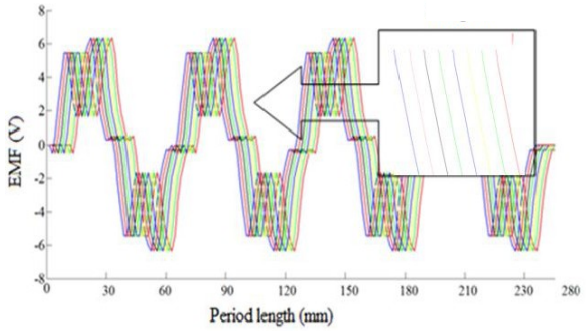

Fig. 9. Analytically-obtained open-circuit (no-load) back-emf.

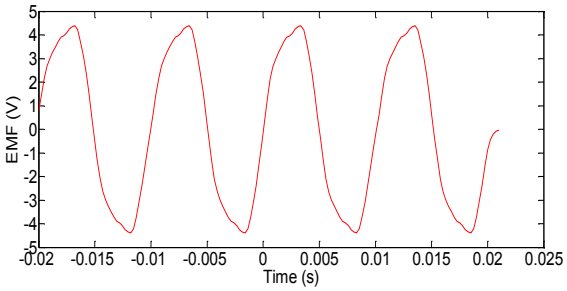

Fig. 10. Analytically-computed open-circuit (no-load) back-emf signal.

If we take a closer look at the Fig. 9 and Fig. 10 we can see that the flux oscillations disappear, and the new signal obtained is close to an ideal sinusoidal waveform.

In this section, a special analytical method for back-emf computation was provided. In order to validate the results obtained by 2-D finite element analysis, the computations will be compared with experimental tests.

C. Testing the prototype

A comparison between FE-computed flux-related values and the experimental ones is provided. Hence, no-load tests were performed under open-circuit (generator-mode) conditions using the DC machine drive as a prime mover. The no-load test was done to evaluate the back-emf values.

The back-emf measurements were carried out for a nominal speed of 1500 rpm. The voltage measurements are made with the high-precision voltage oscilloscope probe. The test results captured on the oscilloscope are presented in Fig.11. The colored signals represent the induced voltage for the three stator phases. The open-circuit back-emfs for forward and reverse rotation are presented in Fig.12 and Fig.13, respectively. It can be observed that the back-emf waveforms have the amplitude equal to 4.4 V. Depending on the rotation

sense the shape of those waveforms have different shapes; this is attributable to the rotor-PM arrangement.

In order to compare the computed and experimental results, the corresponding back-emf waveforms are superposed in Fig.14, which shows a good agreement.

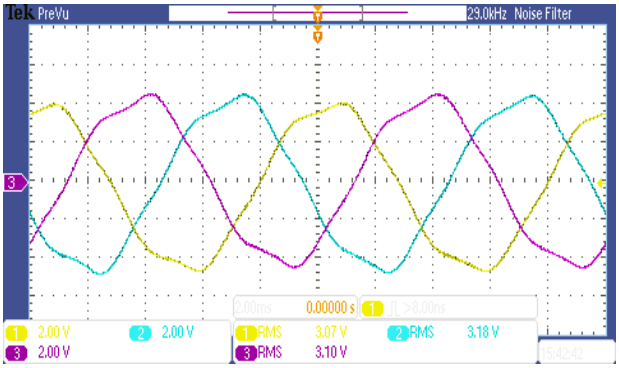

Fig. 11. Experimental open-circuit (no-load) back-emf waveform

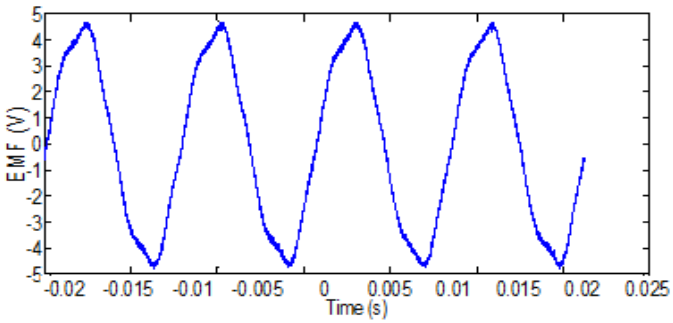

Fig. 12. Experimental open-circuit (no-load) back-emf for clockwise rotation.

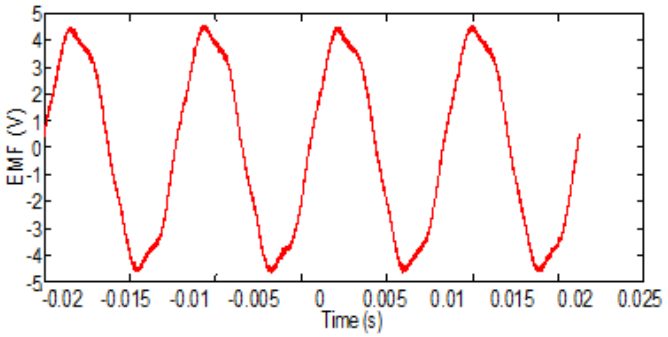

Fig. 13. Experimental open-circuit (no-load) back-emf for counter-clockwise rotation.

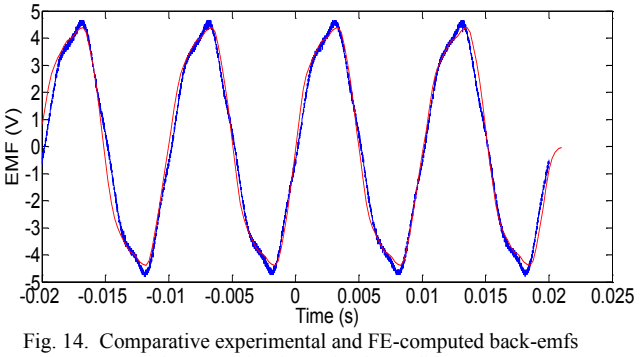

Fig. 14. Comparative experimental and FE-computed back-emfs under open-circuit (no-load) condition.

IV. SPACE HARMONICS IMPROVEMENT BY DESIGN OPTIMIZATION

The harmonics of electromotive force are due to the windings and the shape of the permanent magnets. In order to have a lower distribution of space harmonics in flux density the shape of permanent magnet needs to be optimized. To analyze the flux density harmonics the effect of stator slots is not taken into account. Finding the exponential harmonics in the flux density waveform, it will be possible to decrease them by optimizing the rotor-PM shape. Optimizing the PM size allow us to obtain a flux-density waveform with reduced space harmonics distribution.

A. Slotless AFPMM analysis

The pulsations of torque in permanent magnet machines are the result of the interaction of electromotive force harmonics and current harmonics [11]:

$$C_{elmg} = \frac{3E_1 \cdot I}{2 \cdot \Omega} + \frac{3 \cdot I}{2 \cdot \Omega} \cdot \sum_{i=1}^{3} \left[\left(E_{6k-1} + E_{6k+1} \right) \cos(6k\theta) \right] \quad (2)$$

E represents the electromotive force and I the phase current.

In the first instance of our work we will take into account the two important torque components like flux density and electromotive force. Our study will focused on analysis of those two components in order to modify the space harmonics distribution. Modifying the space harmonics distribution of flux density and EMF will have an important impact in improving the electromagnetic torque as it's possible to see in (2).

Supposing an ideal stator-winding, the back-emf results as

$$e = n\frac{\partial \varphi}{\partial t} = n\frac{\partial \int BdS}{\partial t} = n\frac{\partial \int BLRd\theta}{\partial t} \quad (3)$$

φ is the flux density in the airgap, L and R are, respectively, the length of the machine and the radius of the rotor.

So, one may write:

$$e = n\frac{\partial \int BLRd\theta}{\partial t}\frac{dt}{d\theta}\Omega = nB(\theta)LR\Omega \quad (4)$$

Neglecting the effect of the winding, the harmonics of the EMF are those of the flux density $nLR\Omega$, reducing these harmonics will permit to reduce the harmonics of the EMF. The objective will be to find a proper way to optimize the flux density harmonics.

The influence of rotor magnets design parameters on the magnetic flux distribution and its total harmonic distortion (THD) in surface-type AFPMM is very important to our work.

The flux density distribution in the AFPMM under study is presented in Fig. 15. The AFPMM was simulated under no-load condition to monitor the airgap flux pattern. This signal is the subject of Fast Fourier Transformation. This technique considers the time-space distribution of electromagnetic variables so that it enables to identify the cross-coupling between different spatial and temporal field components. Therefore, it provides a very interesting insight into the correlation between different design variables and machine performances. The shape of the spatial waveform is defined

by solving in polar coordinates the magnetic potential quations in the air-gap.

The airgap flux density can be expressed in Fourier series as:

$$B(\theta) = \sum_{n=1}^{\infty} (a_n \cos(n\theta) + b_n \sin(n\theta)) = \sqrt{a_n^2 + b_n^2} \cdot e^{j\varphi} \quad (5)$$

where n=1 corresponds to the fundamental component. The objective is to reduce the airgap flux-density harmonics and thus the back-emf harmonics.

The frequency spectrum of flux density is displayed in Fig.16. The axial component of the no-load airgap flux density due to rotor-PMs in the middle of the airgap plane is emphasized. It shows that the main harmonic in the flux-density spectrum is the first-order harmonic and then the third harmonic. Fifth- and seventh-order airgap flux-density harmonics are also significant. The study only considers the harmonic orders less than 50, whilst only the orders less than 15 are presented in figure.

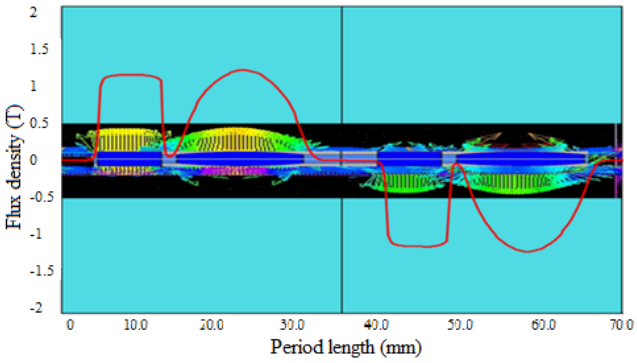

Fig. 15. Flux-density distribution in the airgap of the AFPMM under study.

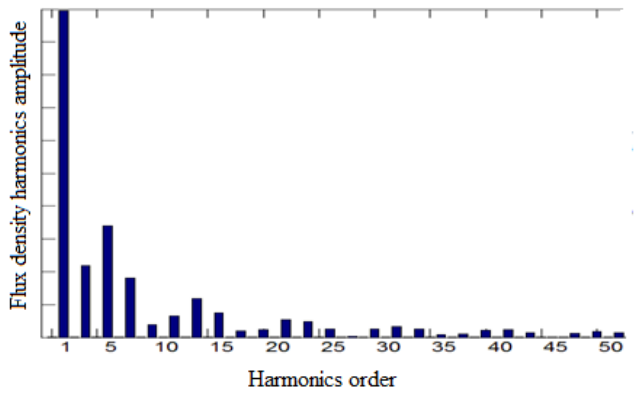

Fig. 16. Frequency spectrum of the flux-density harmonics of the AFPMM under study.

The airgap flux density distribution produced by rectangular and sinusoidal magnets in a surface-mounted AFPM machine (neglecting the slot effect) is a square and sinusoidal waveform consisting of all odd harmonics.

The amount of distortion in the AFPMM back-emf, quantified by the total harmonic distortion (THD), is defined by

$$THD = \frac{\sqrt{\sum_{h=3,5,7...13}^{\infty} B_h^2}}{\sqrt{B_1^2}} \quad (6)$$

From (5) and (6), we know that the harmonic component of B_h is inversely proportional to the harmonic order h, so the distortion is mainly determined by the low harmonics.
Knowing the distribution of representative harmonics in the flux density, the shape of permanent magnets will be furthermore optimize in order to modify those harmonics.

B. Rotor-PM shape optimization

As with conventional synchronous machines, and for a variety of reasons, sinusoidal flux density waveforms are also desirable for many permanent magnet machine applications. Because of the low magnet permeability, which is comparable to that of air, the shape of the airgap flux density depends not only on the airgap length, but also on the shape and dimensions o f the magnet itself.

The purpose of this section is to achieve a design optimization with two objectives as:

- First, optimization objective is to minimize the total harmonic distortion (THD) of the airgap flux density.
- The second objective is to find alternative magnet design that would minimize the amplitude of odd harmonics and maximize the fundamental.

Accordingly, an optimization method is introduced that allows improving the rotor-PM shape and dimensions in order to minimize key harmonic components that exist in the given design. The analysis aimed at the rotor structure, especially at rotor-PM shape is presented in Fig. 17.

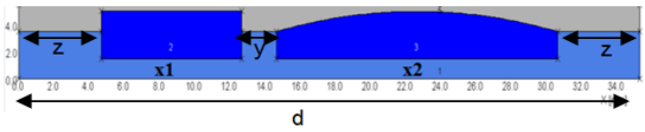

Fig. 17. Initial rotor structure of the AFPM.

The optimization is performed using GA (genetic algorithm) method to explore global space solutions.

In searching for PM dimensions alternatives both magnet length x1 and x2 are varied in the limits of Table I, subject to the geometrical constraint given by Eq. (7). The shape and height of the rectangular and arc-shaped PM remain constant. The objective function is described by Eq. (7).

TABLE I
OPTIMIZATION VARIABLES

Variables	Rated values	Variation interval	Units	Name
x1	8	2.99<x1<16	mm	First Magnet length
x2	16	2<x2<16	mm	Second Magnet length
y	1.95	1.95	mm	Space between the magnets
z	-	-	mm	The left and right extremities of the rotor pole
d	33.34	33.34	mm	Length of one rotor pole

The optimization problem is formulated as:

$$\begin{cases} \min THD(x_1, x_2) \\ x_{1\min} \le x_1 \le x_{1\max} \\ x_{2\min} \le x_2 \le x_{2\max} \end{cases} \quad (7)$$

Global space solution is explored using GA method. Optimal result is given after 3000 iterations, as provided by Table II.

TABLE II
GA OPTIMIZATION RESULT

Population size	Number of generation	X1	X2	F
30	100	15.995	4.769	0.39

The THD obtained from the original AFPMM model, with the given geometrical PM shapes, was 0.47. It can be notice an improvement of THD to 0.39.

The optimized PM-rotor geometry is presented in Fig.18. It can be seen that the PM dimensions have been successfully changed in order to minimize the flux-density THD. The GA convergence is shown in Fig.19.

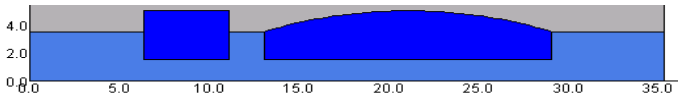

Fig. 18. Optimized rotor structure of AFPM.

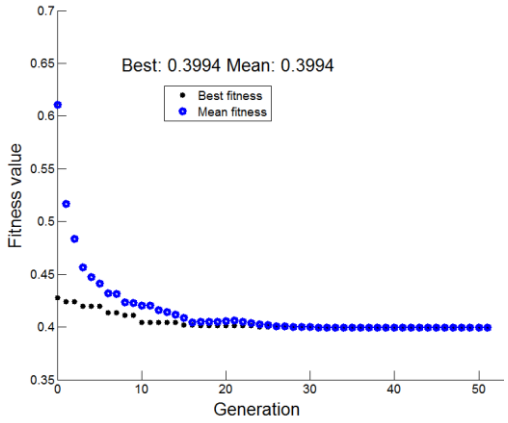

Fig. 19. Fitness generation.

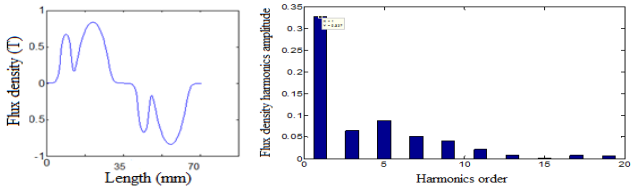

(a) *(b)*

Fig. 20. (a) Optimized flux density waveform; (b) Flux-density harmonics order.

Numerical optimization method has been applied to identify optimal permanent magnets design in order to reduce the total harmonic distortion. The optimize flux density waveform and the fast Fourier transformation of the signal is presented in Fig. 20. Furthermore, optimal permanent magnet design in order to minimize the odd harmonics components and maximize the fundamental harmonic amplitude will be further investigated using multi-objective methods.

C. Multi-objective optimization

Taking into account the geometrical constraints given by (5) the objective function is defined by

$$F_{obj} = \begin{bmatrix} \sqrt{\sum_{h=3,5,7...13}^{\infty} B_h^2} = Numerator \\ \left(\sqrt{B_1^2}\right) = Deno\,min\,ator \end{bmatrix} \quad (8)$$

The objective is to minimize the amplitude of odd harmonics and to maximize the fundamental.

The 3-D representation of *Numerator* as a function of PM length is presented in Fig. 21.

The optimal results are displayed in Fig.21. Here the 3D Pareto front, for the optimization problem (two objectives) is pointed out. The dots marked with (blue) circles are Pareto solutions, while the (red) stars are the tested points. It can be seen that the extreme Pareto front intersection gives a relative solution for the two search objectives. Thus, the *Numerator* (representing the odd harmonics) is 0.12, while the *Denominator* is increased to 1.32.

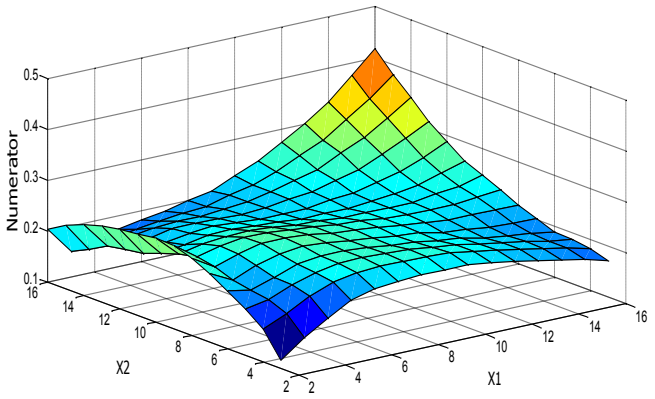

Fig. 21. The odd harmonics in function of x1 and x2.

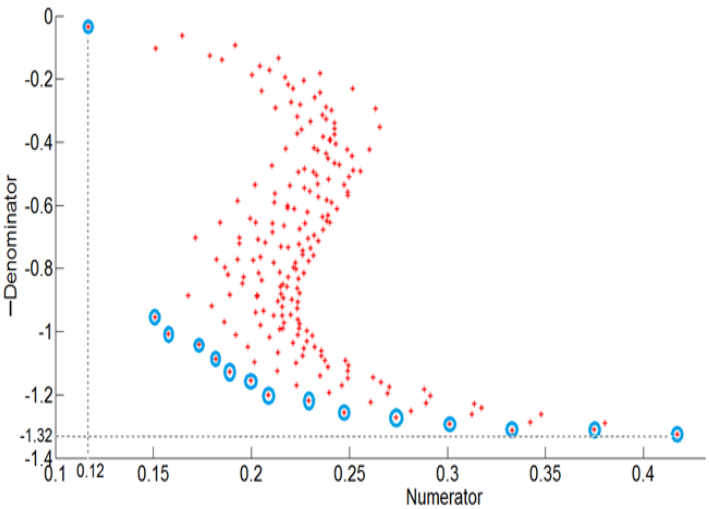

Fig. 22. Pareto front.

V. CONCLUSIONS

A small double-sided AFPMM has been presented in this paper.

To solve the questions regarding the modeling of axial-flux surface-mounted PM machines, an axial 3-D to radial 2-D finite-element transformation has been proposed. A special analytical method for back-emf computation was provided. An important aspect of this computation is regarding the flux density to back-emf waveform transformation. From an oscillating flux-density waveform a close to ideal sinusoidal back-emf waveform was obtained. The FE field analysis models have been developed in order to predict the AFPMM flux density distribution. FE-computed and measured results, for the open-circuit (no-load) back-emf have been compared, showing good agreement. The no-load tests were performed under open-circuit (generator-mode) conditions.

The possibility of reducing the harmonic content of the airgap flux density waveforms in surface-mounted PM machines has been presented. This approach was primarily formulated from the mathematical point of view and then formulated into a minimization problem. Computerized minimization optimization techniques were applied to systematically modify a composite function of odd harmonics contents while simultaneously maximizing the fundamental component.

REFERENCES

[1] J.F. Gieras, R. Wang, and M.J. Kamper, *"Axial-flux permanent-magnet brushless machines"*, Springer, The Netherlands, 2nd edition, 2008.

[2] Patterson, D.J.; Colton, J.L.; Mularcik, B.; Kennedy, B.J.; Camilleri, S.; Rohoza, R.; , "A comparison of radial and axial flux structures in electrical machines," *Electric Machines and Drives Conference, 2009. IEMDC '09. IEEE International*, pp.1029-1035, 3-6 May 2009

[3] S. Tounsi, F. Gillon, S. Brisset, P. Brochet, R. Neji, "Design of an axial flux brushless DC motor for electric vehicle", *Proceedings of International Conference on Electrical Machines – ICEM,* 2002, CD-ROM.

[4] A. Parviainen, *"Design of axial-flux permanent magnet low-speed machines and performance comparison between radial-flux and axial-flux machines"*, Ph.D. Thesis, Lappeenranta University of Technology, Finland, 2005.

[5] S.M Mirimani,, A Vahedi, F Marignetti, "Effect of inclined static eccentricity fault in single stator-single rotor axial flux permanent magnet machines"*, IEEE Transactions on Magnetics*, vol.48, no.1, pp.143-149, 2012

[6] T.-F. Chan, W. Wang, L.-L. Lai, "Analysis of an axial-flux permanent-magnet synchronous generator with a double-sided rotor," *Electromagnetic Field Computation (CEFC), 2010 14th Biennial IEEE Conference on* , 9-12 May 2010

[7] A. Mahmoudi, H.W. Ping, N.A. Rahim, "A comparison between the TORUS and AFIR axial-flux permanent-magnet machine using finite element analysis," *Electric Machines & Drives Conference (IEMDC), 2011 IEEE International* , pp.242-247, 15-18 May 2011

[9] A. Egea, G. Almandoz1, J.Poza, A.Gonzalez, "Analytic model of axial flux permanent magnet machines considering spatial harmonics", *Proc. International Symposium on Power Electronics, Electrical Drives, Automation and Motion – SPEEDAM,* 2010.

[11] D. Vizireanu, S. Brisset, P. Brochet, Y. Milet, D. Laloy, "Study of Current and Electromotive Force Waveforms in Order to Improve the Performance of Large PM Synchronous Wind Generator", in *Recent Developments of Electrical Devices,* Springer, The Netherlands, 2006, pp. 397-413

BIOGRAPHIES

Adrian A. POP was born in Romania in 1984. He received the Dipl. Ing. degree from Faculty of Electrical Engineering, Technical University of Cluj-Napoca, Cluj-Napoca, Romania, in 2009. Since October 2009, he pursues a three-year full-time Ph.D. study program at the Technical University of Cluj Napoca under international co-supervision of Ecole Centrale de Lille, France. He is a member of the Special Electric Machines and Light Electric Traction (SEMLET) Research Laboratory, Technical University of Cluj-Napoca, Romania and of the Laboratory of Electrical Engineering and Power Electronics Research Laboratory (L2EP), Ecole Centrale de Lille, France. His research interests are in special electric machines for automotive applications and railway propulsion systems.

Frédéric GILLON was born in France in 1967. He obtained an Engineer Diploma in 1992 and a Ph.D. in 1997 at Université des Sciences et Technologies de Lille. He is Associated Professor at Ecole Centrale de Lille, since 1999. His research area is optimal design of electric motor drive systems. The applications are linear motors, axial- and radial-flux synchronous motors, and railway propulsion systems.

Mircea M. RADULESCU (IEEE Senior Member 99) received the Dipl.Ing. degree in electrical engineering (with honors) from the Technical University of Cluj-Napoca, Cluj-Napoca, Romania, in 1978, and the Ph.D. degree in electrical engineering from the Polytechnic University of Timisoara, Timisoara, Romania, in 1993. Since 1983, he has been with the Faculty of Electrical Engineering, Technical University of Cluj-Napoca, where he is currently Full Professor in the Department of Electric Machines and Head of the Special Electric Machines and Light Electric Traction (SEMLET) Research Laboratory. He is the author or coauthor of more than 120 published scientific papers in refereed technical journals and international conference and symposium proceedings. He is an Associate Editor of the international scientific quarterly *Electromotion*. His biography is listed in several editions of *Who's Who in the World* and *Who's Who in Science and Engineering*. His teaching and research activities include computer-aided design of electro-mechanical devices, field analysis of electro-magnetic structures, the design and control of small electric motors, actuators and mechatronic drives, and light electric traction systems. Prof. Radulescu is a member of the International Steering Committees of several conferences and symposia in the field of electric motor drives and electric traction.

Space harmonics modeling of an axial flux permanent magnet machine

A.A. POP[1,2,3], F. GILLON[1,2], M. M. RADULESCU[3], I. LAR[3], P.D. TEODOSESCU[3]
[1] Univ. Lille Nord de France, F-59000, Lille, France
[2] EC-Lille, L2EP, F-59650, Villeneuve d'Ascq, France
[3] Technical University of Cluj-Napoca, SEMLET Group, RO-400114, Cluj-Napoca, Romania

***Abstract* –The content of space-harmonic in axial flux permanent magnet machine (AFPMM) is a important concern to the machine designer because to its impact on the performance. In AFPMMs, the harmonics are related to the flux-density and the MMF distributions in the airgap, which are mainly determined by the permanent magnets excitation. This paper proposes two different approaches to modelize the flux density in the airgap. The finite element and analytical method are developed in tandem in order to modelize, compare and optimize the flux density waveforms. Many optimization methods have been proposed in order to optimize the design of permanent magnet machines. In this paper, the authors investigate the optimal permanent magnet design in order to minimize the space harmonics distribution using the sequential quadratic programming (SQP) optimization algorithm. By selecting the appropriate PM shape and size it is possible to reduce the desired exponential harmonics. Taking into account the SQP, the shape of the permanent magnets is optimized and the harmonics content is reduced. The optimal solutions given by the analytical and finite element model are then validated.**

1 Introduction

Axial-Flux Permanent Magnet Machines (AFPMMs), also called the disc-type machine, is an attractive alternative to the cylindrical radial flux permanent magnet (RFPM) machine because of its higher torque, better power density compact construction and lower noise, and thus have gained popularity in recent years [1]. This machine represents another benefit -the axial length wich is small compared with the clasical radial machines.

The AFPMM considered in this paper is a two-stators, and one-rotor topology. The rotor is sandwiched between the two stators. The studied prototype machine is a three-phase AFPMM with one-rotor-two-stators topology and 4 pole-pairs. The rated power of this machine is 0.3 kW with rated rotational speed of 1500 rpm with aplication in light electrical traction. The magnets are of high-energy NdFeB-type, and are glued on the solid-iron disc-rotor. The material of the stator core is a fully-processed electrical steel sheet M600-50A. The stator has a particular construction because it is formed by 25 slots. The rotor-PM arrangement is shown in Fig.1. It can be seen that there are 16 magnets glued on the rotor body. There are two separated PMs for each pole. Due to this PM arrangement, the flux density distribution has an unusual waveform. The first PM has a rectangular geometry and the second is a arc shaped magnet [2].

The torque developed by AFPMM is affected by harmonics of various origins, such as:

- Space harmonics caused by the stator slots;
- Space harmonics of the MMF, which are caused by non-sinusoidal distribution of the armature phase windings; [3]
- Time harmonics related to the power electronic supply, and affecting the stator-armature current.

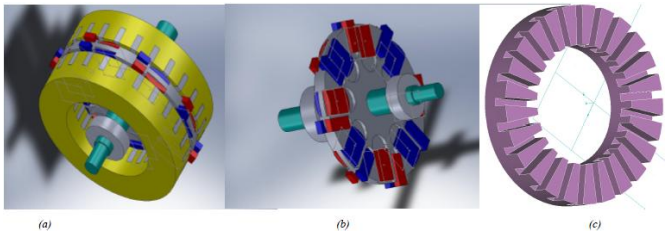

Fig. 1. (a) 3D representation of AFBPMM (b) The rotor with permanent magnets (c) One of the two stators.

2 The influence of magnetic parameters on torque computation

Torque pulsations in permanent magnet machines are due to the interaction between electromotive force harmonics and current:

$$C_{elmg} = \frac{3E_1 \cdot I}{2 \cdot \Omega} + \frac{3 \cdot I}{2 \cdot \Omega} \cdot \sum_{i=1}^{3} \left[\left(E_{6k-1} + E_{6k+1} \right) \cos\left(6k\theta \right) \right] \qquad (1)$$

I is the phase current, E represents the electromotive force. The currents are considered perfectly sinusoidal.

The space harmonics distribution and his interaction with the torque is the objective of our work. Minimizing the space harmonics distribution of flux density will improve the electromagnetic torque can be seen in (1).

If we suppose that stator winding is ideal, the back-emf results to be as follows:

$$e = n\frac{\partial \varphi}{\partial t} = n\frac{\partial \int BdS}{\partial t} = n\frac{\partial \int BLRd\theta}{\partial t} \qquad (2)$$

φ is the flux density in the airgap, R is the radius of the rotor and L the length of the machine.

It can be seen that:

$$e = n\frac{\partial \int BLRd\theta}{\partial t}\frac{dt}{d\theta}\Omega = nB(\theta)LR\Omega \qquad (3)$$

If we don't take in consideration the winding effect, the harmonics of the EMF are those of the flux density. Reducing these harmonics will permit to reduce the harmonics of the EMF.

An interesting method in controlling the flux spacial repartition and total harmonic distortion (THD) is to modify the shape of rotor magnets.

3 Flux density modeling using finite element method

Taking into account the 3-D structure of the machine is often too hard and too time-consuming. In order to evaluate quickly the performance of the AFPMM, the 2-D FE analysis is a time saver solution compared with the 3D FE analysis. In order to obtained rapidly the airgap flux density distribution the 2D FE model is recommended- Fig. 2.

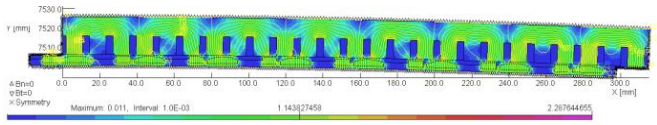

Fig. 2 2-D representation of AFPMM

This simulation is made for a slotless machine therefore the slots impact on the flux density repartition is not taken into account Fig. 3. In this figure we can notice the airgap flux density repartition generated by the permanent magnets.

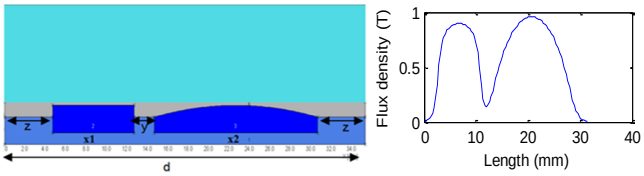

(a) *(b)*

Fig. 3 (a) One pole representation of the AFPMM (b) Flux density distribution for an half period.

This first simulation of the AFPMM was made under no-load condition in order to monitorize the airgap flux pattern. This technique considers the time-space distribution of electromagnetic variables so that it enables to identify the cross-coupling between different spatial and temporal field components. Therefore, it provides a very interesting insight into the correlation between different design variables and machine performances.

The airgap flux density harmonics representation can be obtained by being developed into Fourier series:

$$B(\theta) = \sum_{n=1}^{\infty} (a_n \cos(n\theta) + b_n \sin(n\theta)) = \sqrt{a_n^2 + b_n^2} \cdot e^{j\varphi} \qquad (4)$$

where n=1 corresponds to the fundamental component.

4 Flux density modeling using analytical method

The second model which is taking into account is the analytical model. Using analytical model we are able to reduce more of computation time compared with the FE method. This method could give us a quick inside look regarding the flux density harmonics distribution.

The model is developed in Matlab with the help of trigonometric functions and nonlinear regression.

Improving the rotor-PM shape enables the minimization of key harmonic components that exist in the given design.

The results obtained from the finite element model and from analytical model are now compared in order to verify our computation accuracy. In Fig.4 we represent the flux density obtained by finite element and analytical method. The solid line represents the flux density from finite element model and the dash dot line represents the flux density obtained from analytical model. The computed signals show good agreement.

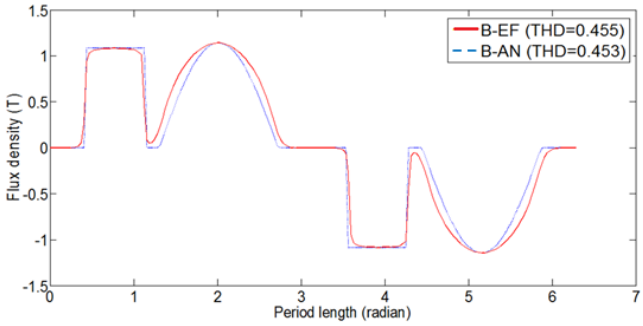

Fig. 4. Airgap flux density distribution of the AFPMM.

Furthermore the optimization will be made using the analytical and finite element model. Computerized minimization optimization techniques will be applied to systematically modify the composite function of odd harmonics contents, modifying the permanent magnets geometry.

5 Flux density harmonics optimization using FE model

In order to reduce undesired flux density harmonics several steps need to be made. In Fig. 5 we represent the coupling and the information flux between optimization algorithm (SQP) and finite element model- Opera 2D. The roles of the different modules from Fig. 5, are presented in Table I.

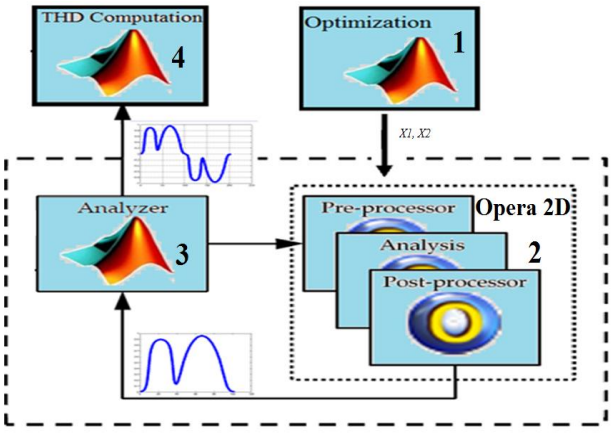

Fig. 5 The optimization process of the AFPMM using FE model

Table I. Role of the different modules in AFPMM optimization process

Module	Role
(1)SQP optimization	perform optimization on a low-budget of FEM evaluations
(2)Opera 2D	perform FEM evaluation (pre, post-processing and analysis)
(3)Analyzer	launch FEM evaluation, recompose the flux density signal and export the results to THD computation block
(4)THD computation	Fast Fourier Transformation (fft-Matlab) and THD computation

The AFPMM optimization process starts with (1) and then launched within Matlab. The SQP algorithm makes regular calls to the finite element model of the AFPMM, throughout a Matlab developed bridge. The AFPMM model evaluation is done using the commercial finite element optimization software Opera 2D.

The FE model evaluation implies three distinct phases: pre-processing (the mesh is generated for the given geometrical configuration), analysis (a static analysis (ST) is performed for the model, generating a results file) and post processing (analysis results are extracted and made available to the Matlab model launching function by the Matlab-Opera bridge). Depending on the geometrical configuration, one FE model evaluation (pre, post-processing and analysis) takes about 15 seconds.

The Matlab model is launching the function then exports the results to the Analyzer. The flux density signal is recomposed for entire period. Then the signal passes to the THD computation block. Here the signal is the subject of Fast Fourier Transformation (fft). The THD is now computed. Once the optimization process has finished, the optimization results are managed and analyzed in Matlab.

5.1 Optimization

The first block represents the optimization algorithm implementation. *X1* represents the length of first permanent magnet (Fig.3) and *X2* the length of second permanent magnet. The values of this variable will be optimized in order to reduce the total harmonics distribution. In which concerns the permanent magnet shape optimization, a classical optimization algorithm is used: the SQP (Sequential Quadratic Programming) method. This algorithm is applied with the commercial software Matlab.

The SQP algorithm attempts to approximate the objective function using a quadratic model and the constraint functions using a linear model of the optimization variables. SQP has excellent local convergence properties and is shown to be faster than most other gradient based optimizers on a large set of test problems [4].

The SQP is used to speed-up the search process and obtain an improvement in the objective function value as quickly as possible.

5.2 Finite element model

A finite element model (FEM) of the AFPMM has been developed in 2D using the commercial FE software Opera. The model construction through command lines allows the automated modification of the parameters of the device within an optimization process. The mesh of the geometry is also parameterized, depending on the different values of the geometrical parameters for a given configuration of the AFPMM.

A finite elements software consists of three parts called commonly: “pre-processor”, “processor”, and “post-processor”.

5.2.1 The pre-processor

The pre-processor is used to draw the geometry of AFPMM, to define materials and model borders. Here a parameterized model is realized in order to use it in optimization process. The model of AFPMM is composed of three tasks:

a) Draw: here the one pole of AFPMM was constructed for an unslotted stator.

b) Materials: the physical characteristics of the geometrical areas previously drawn in their assigning properties (magnetic linear, nonlinear) was assigned.

d) Boundary conditions: the normal, tangential and symmetric conditions were applied to the external lines of the geometry.

5.2.2 The processor

The “processor” is the element where the partial differential equation it is solve on discrete form. It solves a linear system by a given method of resolution. For our nonlinear problem, the processor solves in an iterative way until the required precision is reached. The processor makes possible to find magnetic potential vector values in each node and then a linear approximation inside each element. When this variable is found, the magnetic field can be found and flux density distribution which is the main objective for our problem.

5.2.3 The post-processor

The “post-processor” is the element where the results are analyzed. A visualization aspect is often useful for the comprehension of the results. The role of this block is to visualize the airgap flux density and then to be redirected to an output file.

5.3 Analyzer

The analyzer is used for recomposing the flux density signal for an entire period. Also this block serves to make a bridge between FE model and Matlab. The computation results are then exported to the THD block.

5.4 THD computation

Like the conventional synchronous machines the sinusoidal flux density waveforms are desirable for many

permanent magnet machine applications. Because of the low magnet permeability, which is comparable to that of air, the shape of the airgap flux density depends not only on the airgap length, but also on the shape and dimensions of the magnet itself.

The total harmonic distortion, or THD, of a signal is a measurement of the harmonic distortion and is defined as the ratio of the sum of the powers of all harmonic components to the power of the fundamental frequency Eq. 5.

$$THD = \frac{\sqrt{\sum_{h=3,5,7\ldots13}^{\infty} B_h^2}}{\sqrt{B_1^2}} \quad (5)$$

Accordingly, an optimization method is introduced that allows improving the rotor-PM shape and dimensions in order to minimize key harmonic components that exist in the given design. The analysis aimed at the rotor structure, especially at rotor-PM shape is presented in Fig. 6.

The optimization problem is formulated as:

$$\begin{cases} \min THD(x_1, x_2) \\ x_{1\min} \le x_1 \le x_{1\max} \\ x_{2\min} \le x_2 \le x_{2\max} \end{cases} \quad (6)$$

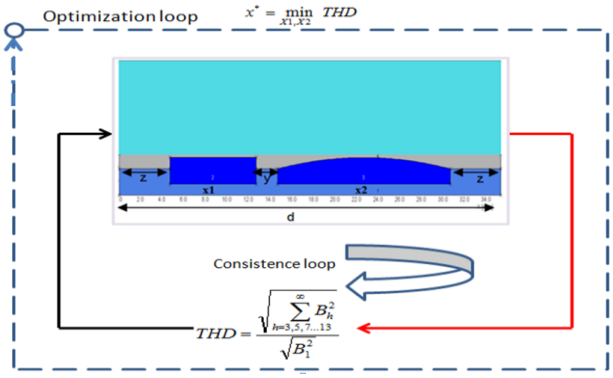

Fig. 6 Mono-objective optimization problem

6 Flux density harmonics optimization using AN model

In order to optimize the flux density harmonics an analytical model was constructed and analyzed. The optimization process using an AN model is a time saver option.

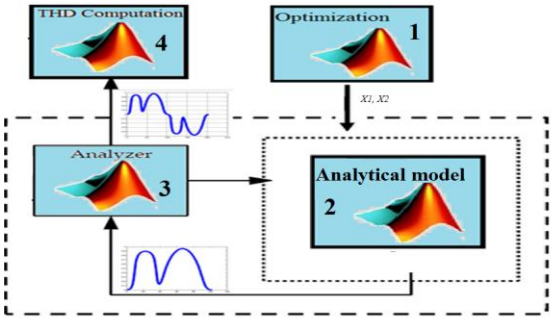

Fig. 7 The optimization process of the AFPMM using FE model

In Fig. 7 the coupling and the information flux between optimization algorithm (SQP) and AFPMM modeled by analytical model (AN) are presented. We can notice that the information flux difference between FE and AN model can be found in the second block where the flux density signal is computed. The optimization process is taking place in the same manner with the FE model only difference is made by second block.

In order to validate FE and AN models a convergence simulation has been made. In Fig. 8 a simulation of 400 points is presented. Here it can be noticed that converge tendency for both models is similar for optimum solutions.

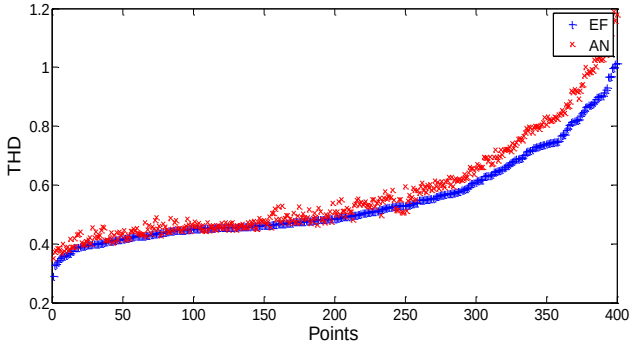

Fig. 8 Finite element and analytical model optimal solutions convergence.

7 Optimization results

Numerical optimization method has been applied to identify optimal permanent magnets design in order to reduce the total harmonic distortion. In Table. 2 the optimization results are presented.

Table 2. Optimization results

Parameters	Rated values	Variation interval	Optimized values	Units
x1	8	2<x1<19	2	Mm
x2	16	3<x2<10	19	Mm
y	1.95	1.95	constant	Mm
z	computed	computed	computed	Mm
d	31.41	31.41	constant	Mm
THD EF	0.455	-	0.27	-
THD AN	0.453	-	0.33	-

The first permanent magnet length *X1* is reduced to 2mm and the second permanent magnet length *X2* is maximized to 19 mm. The flux density produced by the optimized permanent magnets is represented in Fig. 9. We can notice that both optimized models FE and AN generate same values for the permanent magnets. Also it can be seen that the THD is minimized to 0.27 for the FE model and 0.33 for the AN model.

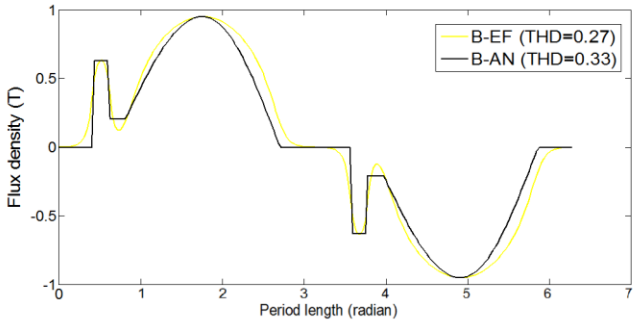

Fig. 9 Optimization flux density results for the Analytical and Finite element model

In Fig.10 the flux density harmonics are presented. It shows that the main harmonic in the flux-density spectrum is the first-order harmonic and then the third harmonic. Fifth- and seventh-order airgap flux-density harmonics are also significant. The study only considers the first 20 harmonics. orders. The red bars represent the harmonics of the flux density obtained from FE model. Blue bars represent the flux density harmonics from analytical model. The harmonics of flux density obtained using the analytical model are represented by the blue bars. The yellow and black bars represent the optimize flux density harmonics for the FE and AN model. It can be seen that the odd harmonics was succesfully reduced and so as the THD.

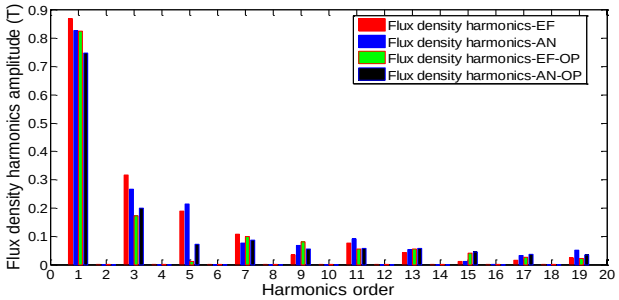

Fig. 10. Frequency spectrum of the flux-density harmonics of the AFBPMM under study for a half period.

In Fig.11 we represented the influence of *X1* and *X2* variables to THD computation. It can observe that the optimization process is trying to minimize the length of the first permanent magnet and maximize the second. The blue regions represent the optimum solutions and the red regions the undesirable solutions.

For the AN model the tendency is similar with the FE model. In Fig. 12 it can be notice that the minimum value of THD is reached for the same values of permanent magnets lengths 2 and 19, respectively.

In Fig. 13 it can be verify the FE and AN models behavior for objective function. Both models have almost the same tendency for the optimum solutions but it can be seen that for the unfeasible solutions starts to have different repartitions.

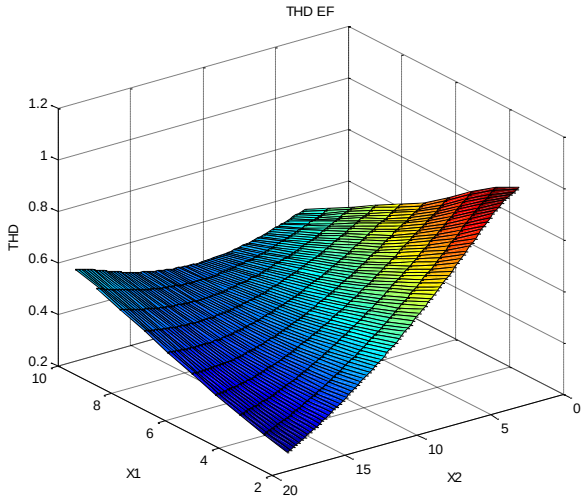

Fig. 11 THD 3-D representation as a function of *X1* and *X2* variables for FE model

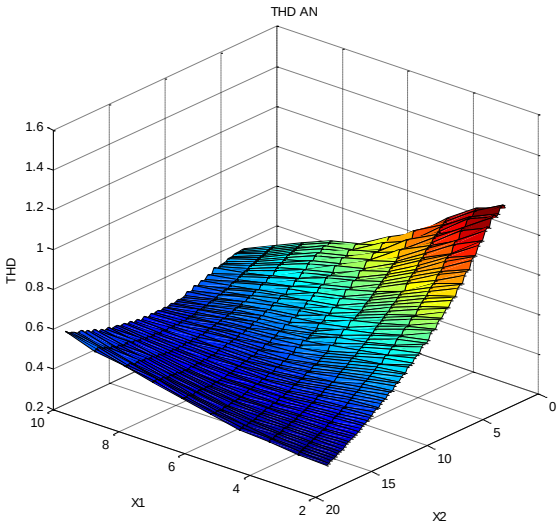

Fig. 12 THD 3-D representation as a function of *X1* and *X2* variables for AN model

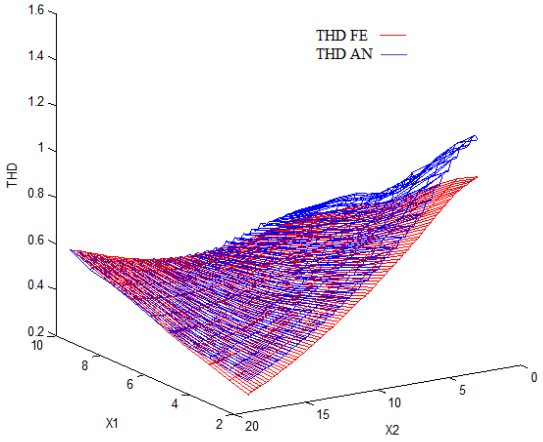

Fig. 13 THD 3-D representation as a function of *X1* and *X2* variables for FE and AN model.

CONCLUSIONS

In this paper a small double-sided AFPMM has been presented. A FE model was developed in order to predict the airgap flux density distribution.

The possibility of reducing the harmonic content of the airgap flux density waveforms in surface mounted PM machines has been presented. The approach was primarily formulated from the mathematical point of view and then transposed into a minimization problem. Minimization optimization techniques were applied to systematically modify a composite function of odd harmonics contents.

FE model can get precise solutions, but usually in a time-consuming manner. So, in order to optimize the AFPMM performances, it was necessary to have a fast computation model. An analytical model was developed is order to solve this time costing problem. The AN model is a time saver option but not so accurate as the FE model. This inconvenient can be eliminated if furthermore in the optimization process the output space mapping [5] will be utilized.

This algorithm could attain the optimization goal by building an approximate link (mapping function) between the design variables of the two models (FE and AN). The FE- "fine" model (accurate but difficult to evaluate) and AN-"coarse" model (easy to evaluate but inaccurate).

REFERENCES

[1] Patterson, D.J.; Colton, J.L.; Mularcik, B.; Kennedy, B.J.; Camilleri, S.; Rohoza, R.; , "A comparison of radial and axial flux structures in electrical machines," *Electric Machines and Drives Conference, 2009. IEMDC '09. IEEE International*, pp.1029-1035, 3-6 May 2009

[2] A.A POP, F. Gillon, M. M. Radulescu, *"Modeling and permanent magnet shape optimization of an axial- flux machine"*, Proceedings of International Conference on Electrical Machines – ICEM, 2012, Marseille, France. *To be published*

[3] Nguyen, T.D.; Tseng, K.J.; Chi Zhang; Shao Zhang; , "Loss study of a novel axial flux permanent magnet machine," *Electric Machines & Drives Conference (IEMDC), 2011 IEEE International* , vol., no., pp.1143-1148, 15-18 May 2011

[4] Tiwari, S.; Fadel, G.; Koch, P.; Deb, K.; , "Performance assessment of the hybrid Archive-based Micro Genetic Algorithm (AMGA) on the CEC09 test problems," *Evolutionary Computation, 2009. CEC '09*

[5] Zhai Guofo; Wang Qiya; Ren Wanbin; , "An Output Space-Mapping Algorithm to Optimize the Dimensional Parameter of Electromagnetic Relay," *Magnetics, IEEE Transactions on* , vol.47, no.9, pp.2194-2199, Sept. 2011

Résumé étendu

Les travaux de recherches exposés dans le mémoire de cette thèse de doctorat se sont déroulés dans le cadre d'une collaboration internationale associant l'Ecole Centrale de Lille à l'Université Technique de Cluj-Napoca en Roumanie. Ces travaux portent sur les petites machines à aimants permanents, à flux axial à auto-commutation électronique, et ayant un rotor-disque intérieur avec des aimants NdFeB montés en surface et possédant deux stators extérieurs, identiques avec des enroulements triphasés, distribués dans les encoches. L'application de telles machines à l'entraînement direct et basse vitesse sont envisagées. Cependant, dans de telles applications, la qualité du couple électromagnétique développé exige des concepteurs la minimisation du couple de détente et du contenu harmoniques de la f.é.m. à vide, en vue de diminuer les ondulations de couple dynamique qui peuvent induire des contraintes mécaniques ou des mouvements parasites.

Le sujet traité concerne la conception et le fonctionnement des machines à flux axial à forte puissance massique et à faible vitesse de rotation. Ce type de machine est difficiles à étudier (à cause des grandeurs magnétiques qui évoluent dans les trois dimensions de l'espace).

Dans ce contexte, le premier objectif de cette thèse est de proposer une approche électromagnétique du dimensionnement préliminaire des petites machines à aimants permanents, à flux axial (MAPFA) en topologie un rotor intérieur-deux stators extérieurs (1R-2S), dont les résultats ont été validés par un prototype démonstrateur conçu et construit dans la première étape des travaux de recherche doctorale.

Le second objectif est de développer une modélisation 2D de champ à symétrie axiale par éléments finis pour le prototype de petite MAPFA 1R-2S en vue d'une optimisation de la forme des aimants du rotor afin d'améliorer la qualité du couple électromagnétique développé.

Le dernier objectif de la thèse est d'effectuer des expériences pratiques sur le prototype, pour tester, d'une part, la modélisation numérique par éléments finis, et,

d’autre part, la faisabilité de la technique de commutation et de commande électroniques de la machine.

Le mémoire de cette thèse comporte 138 pages de contenu et des annexes composées de :

- deux articles scientifiques, issus de la recherche doctorale,
- les propriétés physiques du matériau ferromagnétique utilisé dans le prototype de machine électrique étudié,
- les caractéristiques pratiques de certains composants du banc d’essai développé (accessoires machine, capteur de position, module de l’électronique de puissance et de commande, schéma synoptique de la carte électronique),
- un logiciel MATLAB, définissant l’approche analytique de la modélisation magnétique de l’actionneur étudié,
- les lignes de commandes du logiciel OPERA de calcul numérique de champ par éléments finis, en vue de l’automatisation des procédures.

Chapitre 1 : Petites machines à aimants permanents à flux axial et à commutation électronique

Dans le premier chapitre, après un bref rappel sur les topologies candidates des petites MAPFA pour applications à entraînement direct et basse vitesse, on décrit les caractéristiques d’une telle machine de type 1R-2S par le biais d’un prototype triphasé construit pour la recherche et qui sera développée ensuite dans la thèse.

La petite MAPFA utilisée est un actionneur à double stator, chacun d’entre eux encadrant un rotor monodisque portant sur chacune de ses faces des aimants permanents NdFeB à aimantation axiale.

Dans ce chapitre les avantages et les inconvénients liés à l’encochage statorique sont présentés, à savoir la tenue mécanique des bobines, l’effet sur l’épaisseur de l’entrefer et l’effet sur les ondulations du couple.

Les études théorique et expérimentale d'un prototype de petite MAPFA 1R-2S, constituent le cœur de la thèse. La description de ce prototype révèle deux particularités :

- au niveau du rotor, pour chaque pôle (et pour chaque face du rotor), deux aimants permanents de dimensions et de formes différentes sont placés côte à côte ;
- le bobinage statorique (triphasé) est distribué dans 24 encoches, laissant une 25-ème encoche vide dans la culasse du stator.

Enfin, la dernière partie du premier chapitre présente les différentes parties traitées dans le mémoire de thèse.

Chapitre 2 : Dimensionnement analytique des petites MAPFA

Le deuxième chapitre présente les développements théoriques pour la construction d'un modèle analytique de dimensionnement de la MAPFA caractérisée dans le chapitre précédent.

La modélisation, basée sur l'hypothèse de la linéarité du circuit magnétique et négligeant certains phénomènes comme les flux de fuites magnétiques, les pertes fer et les pertes Joule, établit des formulations reliant les dimensions géométriques à la puissance ou au couple de la machine.

Dans cette modélisation, la puissance mécanique (puissance utile, en mode moteur) est exprimée en fonction du rapport des diamètres externe et interne de la machine, pour une disposition simplifiée des aimants permanents, ainsi que pour une certaine alimentation statorique, en négligeant les chutes de tension et fuites magnétiques. Le modèle analytique de dimensionnement est d'une grande complexité, compte tenu du nombre important de variables mises en jeu dans les multiples relations introduites. Les résultats numériques présentés en fin de chapitre correspondent à la configuration ayant servi à la construction du prototype de MAPFA.

Chapitre 3 : Modélisation par éléments finis et optimisation du dimensionnement des petites MAPFA

Dans le troisième chapitre, qui est la clef de voûte de la thèse, on développe la modélisation magnétique 2D par éléments finis et l'optimisation géométrique des aimants rotorique du prototype de petite MAPFA 1R-2S, pour réduire les harmoniques d'espace du champ dans l'entrefer et le couple de détente de la machine. Des méthodes originales sont développées pour le dimensionnement optimal des aimants rotoriques, permettant d'éliminer un nombre cible d'harmoniques d'espace du champ magnétique dans l'entrefer. Elles sont ensuite validées par des mesures expérimentales sur le prototype.

Dans le cas de rotor non-conventionnel, on étudie la répartition de l'induction magnétique dans l'entrefer d'abord pour l'induit statorique sans encochage, et, puis, en tenant compte des encoches. L'induction est ensuite représentée par une fonction spatiale paramétrée, qui servira dans l'optimisation géométrique des aimants rotoriques.

La partie suivante de ce chapitre présente la problématique de la présence d'harmoniques dans certaines formes d'ondes importantes vis-à-vis du comportement dynamique de la petite MAPFA. Ainsi, le cas des évolutions temporelles de la f.é.m. et de l'induction magnétique dans l'entrefer est présenté.

Différentes approches de modélisation sont présentées, d'abord par simplification des géométries des aimants et de l'encochage statorique, et ensuite par prise en compte de la forme 'réelle', déterminée numériquement, de la fonction de l'induction dans l'entrefer de la machine, compte tenu de la forme et de la position des aimants rotoriques. A ce stade, une première paramétrisation du positionnement et des dimensions des deux aimants polaires est proposée.

Compte tenu des trajets tridimensionnels des grandeurs magnétiques au sein de la machine, une modélisation 3D de la MAPFA est présentée. Sa définition est réalisée dans le logiciel JMAG-Studio, afin d'être exploitée dans le cadre de simulations éléments finis.

Dans la suite, la démarche utilisée est présentée pour la conception d'une modélisation 2D équivalente par éléments finis de de la petite MAPFA. Ainsi, le programme OPERA a été utilisé, permettant une modélisation avec le mouvement de rotation, et un couplage avec des circuits électriques extérieurs. Dans ce cadre, la présence ou non d'encoches statoriques est étudiée, notamment du point de vue du contenu harmonique des variations de la f.é.m. et de l'induction dans l'entrefer. Pour cette dernière fonction, une comparaison est réalisée entre les évolutions calculées numériquement par éléments finis et celles estimées par la modélisation analytique.

La mise au point, manifestement délicate, de la modélisation 2D équivalente par éléments finis constitue une part essentielle des travaux de thèse.

Le reste du chapitre se concentre sur l'optimisation du dimensionnement de la MAPFA par l'emploi de deux méthodes. En utilisant soit la modélisation analytique, soit celle numérique 2D par éléments finis. Les résultats d'optimisation obtenus par l'application des algorithmes SQP ('*Sequential Quadratic Programming*') et GA ('*Genetic Algorithm*') sont donnés.

Pour les premiers cas d'étude, les optimisations restent monocritère, l'objectif correspondant au taux de distorsion harmonique de l'induction magnétique dans l'entrefer. La méthode SQP donne des résultats similaires, quel que soit le modèle utilisé (analytique ou par éléments finis bidimensionnels). En appliquant la méthode GA d'optimisation sur le même problème mono-objectif, le résultat d'optimisation est voisin de celui obtenu par SQP. Pour une seconde formulation, bi-critères, du problème d'optimisation, l'application de la méthode GA vise la construction d'un front de Pareto.

Chapitre 4 : Caractérisation expérimentale et commande électronique du prototype de petite MAPFA

Le quatrième chapitre présente l'étude expérimentale sur le banc d'essais du prototype MAPFA 1R-2S et de son alimentation et commande électroniques. La machine est alimentée par un onduleur triphasé en pont complet dans une technique de commutation à 120 dégrées. Le contrôle de l'onduleur est fait en temps réel à l'aide

d’une plateforme dSPACE 1104 et la commande électronique de la machine est implémentée sous MATLAB/Simulink.

Le banc d’essais comporte le prototype MAPFA 1R-2S, un onduleur à IGBT en pont triphasé, un couple-mètre et une unité de contrôle-commande. Les premiers essais sont effectués à vide et montrent des f.é.m. compatibles avec celles obtenues par simulations numériques.

Le banc d’essais permet la validation des choix opérés (machine à flux axial, structure non-conventionnelle du rotor, modélisation analytique). La mesure du couple est effectuée et les formes d’ondes des courants sont montrées pour plusieurs points de fonctionnement.

Les essais, en mode générateur à vide, permettent de démontrer la qualité des approches de modélisation de la f.é.m. présentées dans le troisième chapitre, en vertu de la bonne concordance des mesures avec les prévisions théoriques.

La dernière partie de ce chapitre expose différents relevés expérimentaux extraits de l’utilisation du banc décrit. Des nombreux tests expérimentaux sont effectués sur le prototype de MAPFA 1R-2S pour vérifier la faisabilité de la stratégie d’auto-commutation et de commande électroniques.

Chapitre 5 : Conclusion générale et perspectives

Le dernier chapitre est consacré aux conclusions générales sur le travail de recherche de la thèse, en soulignant les contributions originales de l’auteur. Les perspectives de la thèse, en termes de recherches futures, sont finalement exposées.

Les références bibliographiques sont réunies à la fin de chacun des quatre chapitres de la thèse.

Contributions à l'étude des petites machines électriques à aimants permanents, à flux axial et à auto-commutation électronique

Résumé : Les travaux de recherche présentés dans cette thèse concernent les petites machines à aimants permanents, à flux axial et à auto-commutation électronique ayant la topologie d'un rotor intérieur discoïdal avec des aimants Nd-Fe-B montés en surface et de deux stators extérieurs identiques, chacun avec enroulement triphasé distribué dans des encoches. Après l'examen des topologies candidates pour applications d'entraînement direct basse-vitesse, une modélisation électromagnétique analytique de pré-dimensionnement d'un prototype de telles machines est réalisée. Ensuite, une approche numérique originale est développée et couplée à l'optimisation géométrique des aimants rotoriques en vue de réduire les harmoniques d'espace de l'induction magnétique dans l'entrefer et aussi les ondulations du couple électromagnétique. Des nombreux tests expérimentaux sont effectués sur le prototype de machine pour vérifier son dimensionnement ainsi que pour valider la stratégie d'auto-commutation électronique et de contrôle de base.

Mots-clefs : petites machines à aimants permanents à flux axial, topologie un-rotor-deux-stators, modélisation, optimisation géométrique, auto-commutation électronique, contrôle électronique de base, entraînement direct basse-vitesse

Contributions to the study of small electronically-commutated axial-flux permanent-magnet machines

Abstract: The research work presented in this thesis is concerned with small electronically-commutated axial-flux permanent-magnet (AFPM) machines having the double-sided topology of an inner rotor with surface-mounted Nd-Fe-B magnets, sandwiched between two outer slotted stators with distributed three-phase windings. After reviewing the small double-sided AFPM machine candidate topologies for low-speed direct-drive applications, the thesis hinges on the size equations and the analytical electromagnetic design of the inner-rotor AFPM (AFIPM) machine topology under study. Original methods of modeling and design optimization of a small prototype AFIPM machine are then proposed with the view to reducing the airgap flux density space-harmonics and the torque ripple by rotor-PM shape modification. Extensive experimental tests are carried out on the small three-phase AFIPM machine prototype in order to validate its proper design and to check its electronic commutation and basic control technique.

Key words: small axial-flux permanent-magnet machine, double-sided inner-rotor topology, modeling, design optimization, electronic commutation, basic electronic control, low-speed direct drive